BAJECE

e-mail: bajece@hotmail.com

Balkan Journal of Electrical & Computer Engineering

An International Peer Reviewed, Referred, Indexed and Open Access Journal

www.bajece.com

Vol : 8
No : 3
Year : 2020
ISSN : 2147 - 284X

It is abstracted and indexed in, Index Google Scholarship, the PSCR, Cross ref, DOAJ, Research Bible, Indian Open Access Journals (OAJ), Institutional Repositories (IR), J-Gate (Informatics India), Ulrich's, International Society of Universal Research in Sciences, DRJI, EyeSource, Cosmos Impact Factor, Cite Factor, SIS SIS Scientific Indexing Service, IIJIF, iiiFactor. ULAKBİM-TR Dizin.

General Publication Director & Editor-in-Chief
Musa Yılmaz, Batman University, Turkey.

Vice Editor
Hamidreza Nazaripouya, University of California Riverside, USA

Scientific Committee
Abhishek Shukla (India)
Abraham Lomi (Indonesia)
Aleksandar Georgiev (Bulgaria)
Arunas Lipnickas (Lithuania)
Audrius Senulis (Lithuania)
Belle R. Upadhyaya (USA)
Brijender Kahanwal (India)
Chandar Kumar Chanda (India)
Daniela Dzhonova-Atanasova (Bulgaria)
Deris Stiawan (Indonesia)
Emel Onal (Turkey)
Emine Ayaz (Turkey)
Enver Hatimi (Kosovo)
Ferhat Sahin (USA)
Gursel Alici (Australia)
Hakan Temeltaş (Turkey)
Ibrahim Akduman (Turkey)
Jan Izykowski (Poland)
Javier Bilbao Landatxe (Spain)
Jelena Dikun (Lithuania)
Karol Kyslan (Slovakia)
Kunihiko Nabeshima (Japan)
Lambros Ekonomou (Greece)
Lazhar Rahmani (Algerie)
Marcel Istrate (Romania)
Marija Eidukeviciute (Lithuania)
Milena Lazarova (Bulgaria)
Muhammad Hadi (Australia)
Muhamed Turkanović (Slovenia)
Mourad Houabes (Algerie)
Murari Mohan Saha (Sweden)
Nick Papanikolaou (Greece)
Okyay Kaynak (Turkey)
Osman Nuri Ucan (Turkey)
Ozgur E. Mustecaplioglu (Turkey)
Padmanaban Sanjeevikumar (India)
Ramazan Caglar (Turkey)
Rumen Popov (Bulgaria)
Tarek Bouktir (Algeria)
Sead Berberovic (Croatia)
Seta Bogosyan (USA)
Savvas G. Vassiliadis (Greece)
Suwarno (Indonesia)
Tulay Adali (USA)
Yogeshwarsing Calleecharan (Mauritius)
YangQuan Chen (USA)
Youcef Soufi (Algeria)

Aim & Scope
The journal publishes original papers in the extensive field of Electrical-Electronics and Computer engineering. It accepts contributions which are fundamental for the development of electrical engineering, computer engineering and its applications, including overlaps to physics. Manuscripts on both theoretical and experimental work are welcome. Review articles and letters to the editors are also included.
Application areas include (but are not limited to): Electrical & Electronics Engineering, Computer Engineering, Software Engineering, Biomedical Engineering, Electrical Power Engineering, Control Engineering, Signal and Image Processing, Communications & Networking, Sensors, Actuators, Remote Sensing, Consumer Electronics, Fiber-Optics, Radar and Sonar Systems, Artificial Intelligence and its applications, Expert Systems, Medical Imaging, Biomedical Analysis and its applications, Computer Vision, Pattern Recognition, Robotics, Industrial Automation.

BAJECE
Balkan Journal of Electrical & Computer Engineering
An International Peer Reviewed, Indexed and Open Access Journal

ISSN: 2147- 284X
Vol: 8
No : 3
Year: July 2020

CONTENTS

M. A. Gungor; Analyzing the Fluid Flow of Transit-Time Ultrasonic Flowmeter with Image Processing Technique and Developing a Quality Metric Depending on Pipe Profile,……..**193-200**

V. Ozduran; LDPCC and OFDM Based Cooperative Communication for Wireless Sensor Networks, ……..**201-208**

O. Aydin and R.G. Cinbis; Single-Image Super-Resolution Analysis in DCT Spectral Domain,……**209-217**

H. Yetis, T. Goktas; Comparative Design of Permanent Magnet Synchronous Motors for Low-Power Industrial Applications, ...**218-224**

A. Gundogdu, F. Ata, B. Dandil;Design of Neuro-Fuzzy Based Torque Controller for Torque Ripple Reduction of Asynchronous Motor,**225-234**

H. Oğraş and Ş. Fidan; Performance Comparison of ACM and GRP Methods for Image Permutation, ..……**235-241**

E. Buber, O.K. Sahingoz; Blockchain Based Information Sharing Mechanism for Cyber Threat Intelligence,……**242-253**

G. Boztas; Optimization of an Input Filter for a Three-Phase Matrix Converter,……**254-259**

I. Kaya; Optimal and Analytical Tuning of I-PD Controllers for Controlling Stable Processes with Inverse Response,……**260-265**

D. Olanloye, R. Olasunkanmi and E. Oduntan; Comparison of Support Vector Machine Models in the Classification of Susceptibility to Schistosomiasis,……**266-271**

B. Kara and A. Özgövde; Effect of RSU Placement on Autonomous Vehicle V2I Scenarios,……..**272-284**

BALKAN JOURNAL OF ELECTRICAL & COMPUTER ENGINEERING
(An International Peer Reviewed, Indexed and Open Access Journal**)**
Contact
Batman University
Department of Electrical-Electronics Engineering
Bati Raman Campus Batman-Turkey

Web: http://dergipark.gov.tr/bajece
https://www.bajece.com
e-mail: bajece@hotmail.com

Analyzing the Fluid Flow of Transit-Time Ultrasonic Flowmeter with Image Processing Technique and Developing a Quality Metric Depending on Pipe Profile

M. A. GUNGOR

***Abstract*— The ultrasonic transit-time method measures the velocity and quantity of fluids in circular type pipes by using the difference of transit time between the ultrasonic pulses propagating with and against the flow direction. This method gives the average velocity of the fluid along a particular acoustic path. At least two ultrasonic transducers are used for an acoustic path. The multipath ultrasonic flowmeters have more acoustic paths. In this paper, the acoustic path between two transducers is described as pixels for the turbulent flow and formed a flow map for ideal flow conditions such as no elbow or bend depending on pipe profile. This map is used to analyze the fluid flow for different Reynolds numbers. Additionally, for any acoustic path between two transducers, the average fluid velocity is calculated using the obtained pixel values. Thus, a quality metric is developed in this paper. This metric calculates the ideal average fluid velocity ratio between the acoustic paths. The developed metric can be used to evaluate the quality of the ultrasonic flowmeter in the domain of turbulent flow.**

Index Terms— **Fluid Flow, Image Processing, Quality Index, Ultrasonic Flowmeter**

I. INTRODUCTION

ACCORDING TO the measurement principle, the ultrasonic flowmeters are divided into two groups: Transit-Time Difference (TTD) and Doppler methods. The Doppler method is used for fluids containing particles such as bubbles and sand. This method relies on particles flowing through the fluid. Generally, this method is considered as having low performance due to the fact that the particle velocity is different from the fluid velocity. TTD ultrasonic flowmeter is used for homogeneous fluids that do not contain particles and has many advantages such as high accuracy, low maintenance and economical.

Many techniques have been developed to enhance the precision of TTD ultrasonic flowmeters, some of which find the optimal transducer angle [1], design the pipe [2], filter the signals [3, 4] and use FPGA [5, 6]. Zero-crossing and correlation methods are the most commonly used methods to find TTD [7]. Some of the scientists have studied to increase the "sensitivity for the zero-crossing method [8, 9]. Least-square-sine-fitting technique is considered as an alternative method to obtain TTD [10].

To increase the accuracy in measuring, the multipath design has different acoustic paths. The calculation method for multipath ultrasonic flowmeter is described as follows: The fluid velocity is calculated for each path as in the one-path ultrasonic flowmeter. The average velocity is calculated by multiplying the calculated velocity value with the weight value for each path. The simplest way to calculate the weight value is the averaged method involving an equally weighted average of the path velocities [11]. In another method, the weight values are determined according to the geometric position of the transducers [12]. In this method, weight values are calculated by reference to the distance of the transducers from the pipe center. The transducer, which is close to the center, has a higher weight value. It has less weight value as it moves away from the center. Several path arrangement designs exist with weights to prescribe the position of acoustic paths, and an integration method is used such as Gauss-Jacobi and Optimal Weighted Integration for Circular Sections (OWICS) [13-15]. The major disadvantage of these methods is that weights are calculated based on fixed transducer positions. Researchers have focused on eliminating such disadvantages and increasing the accuracy by using a different algorithm such as Generalized Inverse Matrix, Levenberg-Marquardt, and variances of path velocities [16-18].

Although there are many studies on TTD ultrasonic flowmeters, research continues. This paper presents a flow map for ideal flow condition (FMIFC). FMIFC is formed in the domain of turbulent flow (i.e., Reynolds number (Re) > 4000) of transit-time ultrasonic flowmeter depending on pipe profile. Thus, researchers can analyze the fluid flow depending on Re. Furthermore, using FMIFC, a quality metric is developed. The developed metric calculates the ideal average fluid velocity ratio between the acoustic paths to obtain a reference value for ideal flow conditions. For the multiple

MURAT ALPARSLAN GUNGOR, is with Department of Electrical and Electronics Engineering University of Hitit, Corum, Turkey,(e-mail: alparslangungor@hitit.edu.tr).

https://orcid.org/0000-0001-7446-7808

Manuscript received December 02, 2019; accepted June 03, 2020.
DOI: 10.17694/bajece.654414

acoustic paths, researchers can compare the application values with the reference values to evaluate their designs. In this paper, the following section presents the measurement principle of the transit-time ultrasonic flowmeter. FMIFC and the proposed quality metric are considered in Section III. Results and discussion are presented in Section IV. Finally, Section V concludes this paper.

II. OPERATING PRINCIPLE OF TRANSIT-TIME ULTRASONIC FLOWMETER

Due to the simplicity of the measurement principle, TTD method is often used in industrial applications [19]. At least two ultrasonic transducers are placed on the surface of the pipe. The transducers send ultrasonic pulses to each other. The fluid flow velocity is calculated by using the propagation time of the received pulses. The operating principle of the TTD method is shown in Fig. 1.

In Fig. 1, r_0 is the pipe radius, t_{AB} and t_{BA} are the transit times, θ is the angle between the pipe and the direction of the ultrasonic wave and v_m is the velocity on the center. In TTD method, the ultrasonic flowmeter measures the average velocity along the path between the ultrasonic transducers. Two ultrasonic transducers (shown as transducer A and transducer B in Fig. 1) send pulses propagating into and against the direction of the fluid flow. The transit time from transducer B to transducer A (t_{BA}) is greater than the transit time from transducer A to transducer B (t_{AB}) and they are calculated as follows:

$$t_{AB} = \frac{L}{c + v\cos\theta} \tag{1}$$

$$t_{BA} = \frac{L}{c - v\cos\theta} \tag{2}$$

where L is the distance between the transducer A and transducer B, v is the fluid flow velocity and c is the ultrasound speed in the fluid. The TTD is calculated as follows:

$$\Delta t = t_{BA} - t_{AB} = \frac{L}{c - v\cos\theta} - \frac{L}{c + v\cos\theta} \tag{3}$$

From the Eq. (3), we can obtain the v:

$$v = \frac{L}{2\cos\theta}\left(\frac{1}{t_{AB}} - \frac{1}{t_{BA}}\right) = \frac{r_o}{\sin\theta\cos\theta}\left(\frac{1}{t_{AB}} - \frac{1}{t_{BA}}\right) = \frac{r_o \Delta t}{\sin\theta\cos\theta t_{AB} t_{BA}} \tag{4}$$

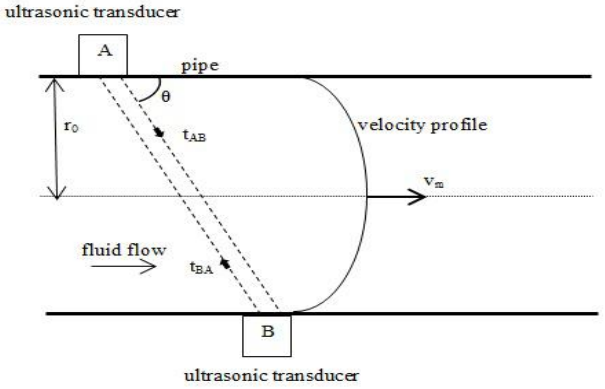

Fig.1. The principle of transit-time method

At low fluid flow velocities, the flow tends to be dominated by laminar flow, while at high fluid flow velocities flow is referred to as the turbulent flow. This paper is about the turbulent flow, i.e., Re > 4000. In the domain of turbulent flow, the velocity profile is called the "pipe profile" given by [20, 21]:

$$v(r) = v_m\left(1 - \frac{r}{r_0}\right)^p \tag{5}$$

where r is the distance from the center and p is a parameter as chosen [21, 22]:

$$p = 0.25 - 0.023\log_{10}\mathrm{Re} \tag{6}$$

Remark that this parameter decreases with increasing Re and hereby v(r) approaches to v_m. Therefore, the ratio of v(r) to v_m can be calculated depending on the Re.

III. FMIFC AND THE PROPOSED QUALITY METRIC

At first, in this paper, the fluid flow in circular type pipe for ultrasonic flowmeter application is described as pixels. The schematic of an ultrasonic flowmeter is shown in Fig. 2. The fluid flow direction in Fig. 1 corresponds to the x-direction (axial direction) in Fig. 2. The y and z directions correspond to horizontal and vertical directions, respectively. When the fluid flow in Fig. 2 is described by pixels, the pixel values along the axial direction have the same values. Thus, the pixel values are obtained along the horizontal and vertical directions to describe the fluid flow in this paper.

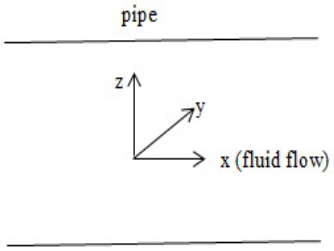

(a)

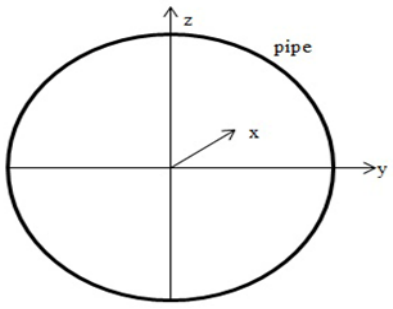

(b)

Fig.2. Schematic of an ultrasonic flowmeter (a) Longitudinal cross-section (b) Transverse cross-section

The pipe profile in Eq. (5) gives the velocity profile on the horizontal direction as shown in Fig. 1 and Fig. 2. If the ultrasonic transducers are placed on both ends of the y-axis shown in Fig. 2b, the acoustic path between these transducers can be described as pixels in Fig. 3.

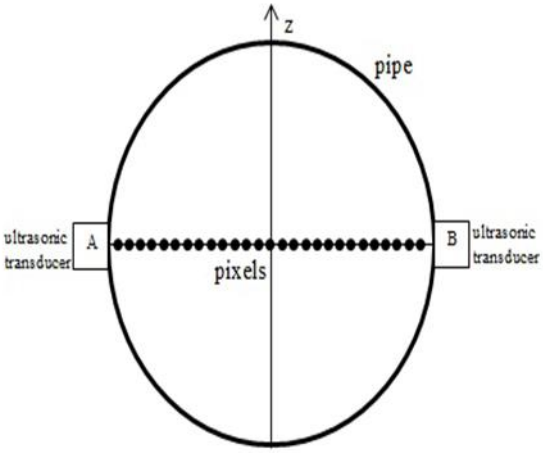

Fig.3. The acoustic path in the middle of the pipe

Any pixel value shown in Fig. 3 is between 0-255 and depends on fluid velocity. The greater fluid velocity means the bigger pixel value. Each pixel value can be calculated using Eq. (5). $r=r_0$ corresponds to the pipe surface where the velocity equals zero ($v(r) = 0$) and pixel value is zero. The pixels, which is close to the center, has a bigger value. $r=0$ corresponds to the center of the pipe where velocity is the maximum ($v(r) = v_m$) and pixel value is 255. As mentioned above, for the larger Re, $v(r)$ approaches to v_m, resulting in bigger pixel value. After calculating each pixel value on the acoustic path, the average fluid velocity on the acoustic path can be obtained by averaging the calculated pixel values.

The velocity v given by Eq. (4), corresponding to the average fluid velocity on the acoustic path between the ultrasonic transducers shown in Fig. 3, can be obtained by using v_m as follows [21]:

$$v = \frac{v_m}{1+p} \tag{7}$$

v values are calculated by using both pixels shown in Fig. 3 and Eq. (7) between Re=4000 and Re=1000000. The obtained values are normalized with v_m and shown in Fig. 4. Instead of handling the entire distance between the two transducers, shown in Fig. 3, only the pixels between the ultrasonic transducer A and center are handled to avoid extra processing.

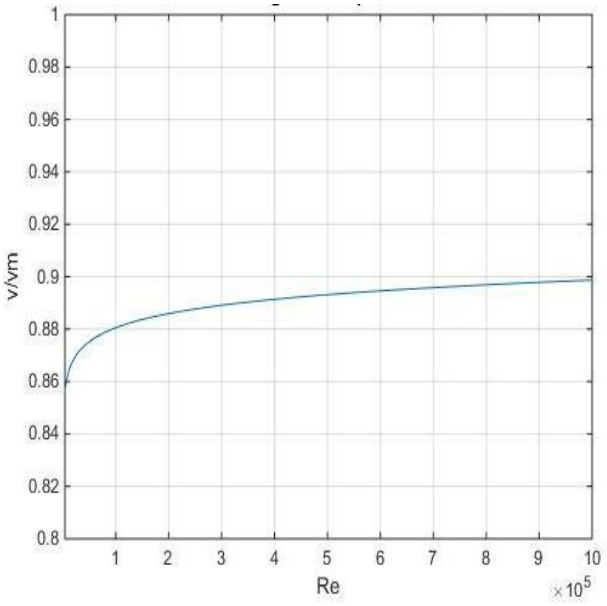

(a)

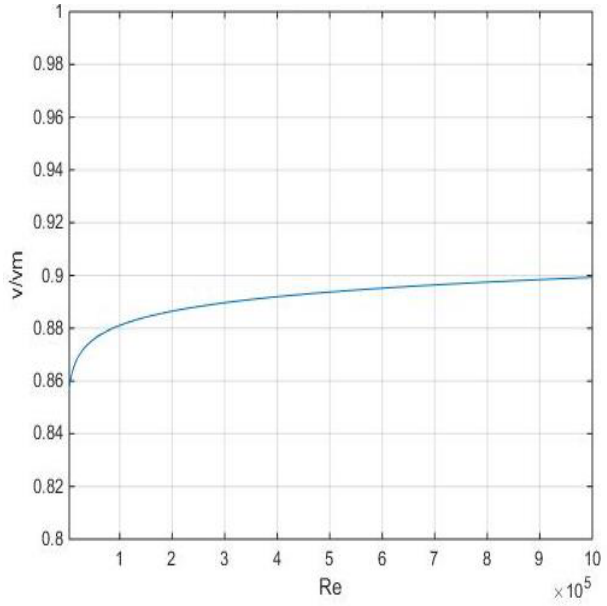

(b)

Fig.4. Obtained normalized average flow velocity vs. different Re values on the acoustic path in the middle of the pipe by using (a) Pixels (b) Eq. (7)

As shown in Fig. 4b, the normalized v value for the Re= 4000 is 0.856. It is approaching v_m as the Re increases, and this value is 0.899 for the Re=1000000. Comparing Fig. 4a and Fig. 4b, the normalized values obtained by pixels and Eq. (7) are equal to each other. If we consider the acoustic path in Fig. 3 as in Fig. 5, the pixel values of the acoustic path between each ultrasonic transducer pair and average flow velocity for

the corresponding acoustic path can be calculated by the method mentioned above.

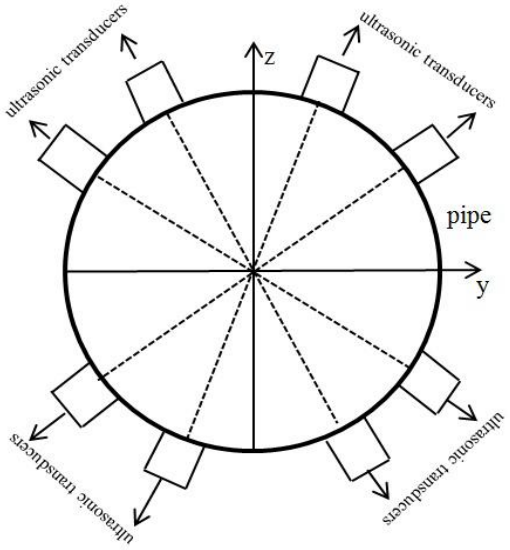

Fig.5. The transducers placed around the pipe

Usually, for ultrasonic flowmeter applications in the industry, ultrasonic transducers have a design as shown in Fig. 6.

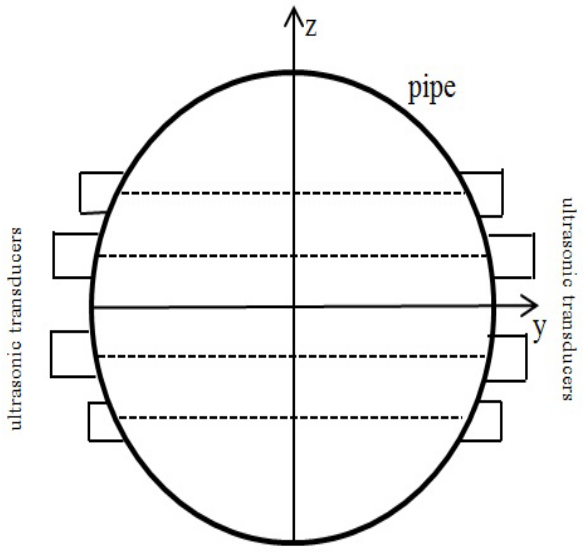

Fig.6. Ultrasonic transducers located in the z-direction

The ultrasonic transducers may be located in the middle of the pipe (as shown in Fig. 3) or at any point in the z-direction (as shown in Fig. 6). Thus, each transducer pair has a different velocity and acoustic path length information. In this paper, the normalized average flow velocity value of each acoustic path shown in Fig. 6 is calculated using pixels. For this purpose, the acoustic paths between the ultrasonic transducers are first illustrated by pixels as shown in Fig. 7. Instead of handling the entire distance between two transducers, only the pixels between the ultrasonic transducer A and center (as shown in Fig. 3) are handled to avoid extra processing.

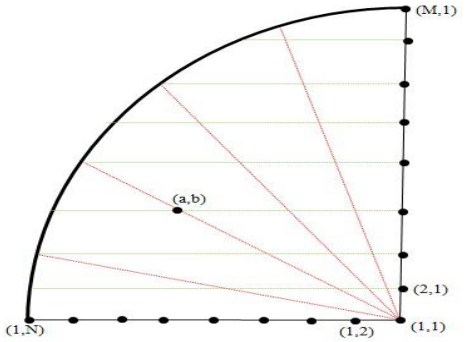

Fig.7. Finding pixel value on the acoustic path at any point in the z-direction

The pixel values of the red acoustic paths can be calculated as previously stated in this paper. The green acoustic paths indicate the acoustic paths between the ultrasonic transducers located in the z-direction as shown in Fig. 6. While N represents the number of pixels in each acoustic path, M indicates the acoustic path number. Increasing the number of M and N means more precise result but more processing. So, in this study, M and N values are chosen as 1000 (that means the image shown in Fig. 7 has 1000*1000 pixels). a and b are the vertical and horizontal positions of the pixel to be calculated, respectively. To find the pixel (a, b) value, the following algorithm is applied:

- Calculating the transducer distance = $\sqrt{r_o^2 - (a-1)^2}$ (8)
- Calculating the point distance =

$$\text{transducer distance} * \frac{b-1}{r_0} \quad (9)$$

- Calculating the r distance =

$$\sqrt{(\text{point distance})^2 + (a-1)^2} \quad (10)$$

- $$v(a,b) = v_m\left(1 - \frac{\text{r distance}}{r_0}\right)^p \quad (11)$$

where v (a, b) is the pixel value at (a, b). Transducer distance, point distance, and r distance shown in Eqs. (8-11) are indicated in Fig. 8:

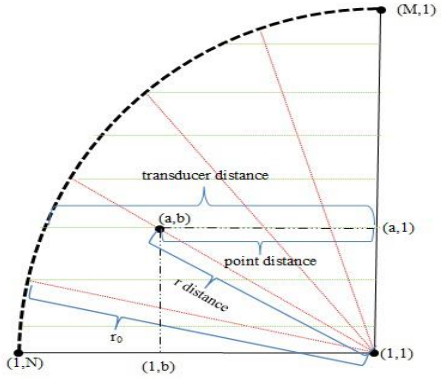

Fig.8. Transducer distance, point distance, and r distance

The lengths of the vertical position and horizontal position of the pixel (a, b) are (a-1) and (b-1), respectively. The value

of the r_0 is M-1 or N-1. All pixel values on the green acoustic paths shown in Fig. 7 can be calculated by using Eqs. (8-11) to obtain FMIFC. The r distance is calculated using Eqs. (8-10) to obtain any v (a, b) value in the image. For example, let the image has 10*10 pixels and calculate the r distance for v (3, 8). In this case, the transducer distance is the distance from (3, 10) to (3, 1), while the point distance is the distance from (3, 8) to (3, 1). Thus the r distance is the distance from (3, 8) to (1, 1). After calculating the r distance, v (a, b) value is obtained using Eq. (11). v_m which is pixel value at (1, 1) is 255. As stated in Eq. (6), parameter p shown in Eq. (11) depends on the Re. Thus, FMIFC can be obtained for each Re. Fig. 9 shows FMIFC having 1000*1000 pixels for Re=100000.

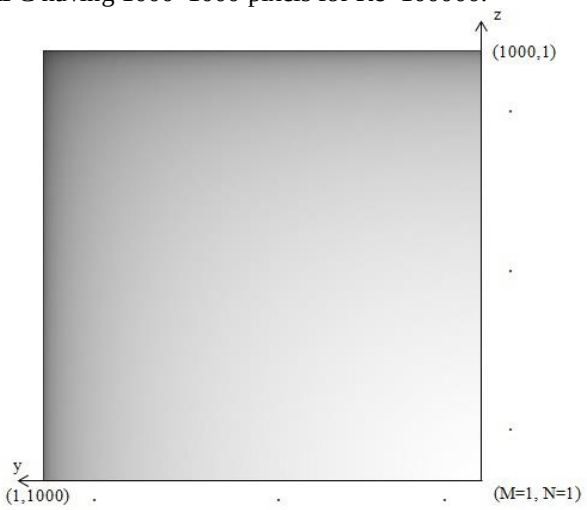

Fig.9. FMIFC for Re=100000

Fig. 9 is the diagram showing the rectangular form of Fig. 7 after calculating the pixels on the acoustic paths shown in Fig. 7. There are 1000 acoustic paths and each acoustic path has 1000 pixels in Fig. 9. The pixel at (M=1, N=1) corresponds to the v_m. The pixels at M=1000 or N=1000 correspond to the pipe surface. FMIFC can be used to analyze fluid flow for different Re values. Besides, FMIFC can be used to obtain the ideal average fluid velocity ratio between the acoustic paths in the z-direction. The average fluid velocity, for any acoustic path in the z-direction, is calculated by averaging the obtained pixels on this acoustic path. Thus, a quality metric is obtained in this paper, which indicates the ratio of the average fluid velocities of different acoustic paths. The quality metric based on pixel (Q_{bp}) is calculated as follows:

$$Q_{bp} = \frac{Q_{bpr}}{Q_a} \tag{12}$$

where Q_{bpr} and Q_a are the quality metrics for reference and application, respectively and defined as

$$Q_{bpr} = \frac{v_{bp1}}{v_{bp2}} \tag{13}$$

$$Q_a = \frac{v_1}{v_2} \tag{14}$$

where v_{bp1} and v_{bp2} are the normalized average fluid velocities based on pixel for reference, v_1 and v_2 are the average fluid velocities for the application. A researcher places the ultrasonic transducers in any positions along the z-direction on the pipe. To obtain two different flow velocities, v_1 and v_2, from two different transducer pairs, the average fluid flow velocity on the acoustic path between each ultrasonic transducer pair is measured for turbulent flow and ideal flow conditions. v_{bp1} and v_{bp2} are obtained by the method mentioned above for reference. If there is problem such as the placement of transducers in the design, the ratio between Q_{bpr} and Q_a is different from 1. That the ideal value of Q_{bp} is 1 indicates excellent compatibility between the transducer pairs. Thus, this metric can be used to assess the quality of the ultrasonic flowmeter for turbulent flow.

IV. Results and Discussion

In this paper, FMIFC is obtained in MATLAB environment to analyze fluid flow for different Re values. Fig. 10 shows FMIFC for Re=10000, 100000 and 1000000.

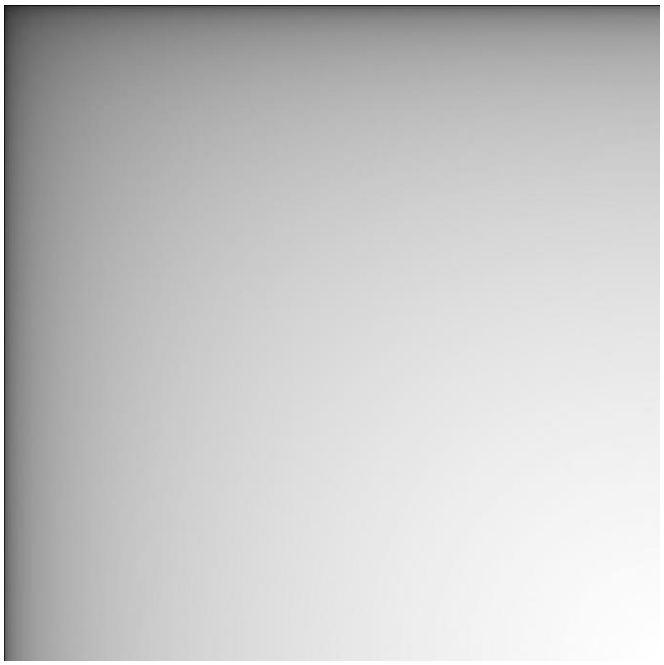

(a)

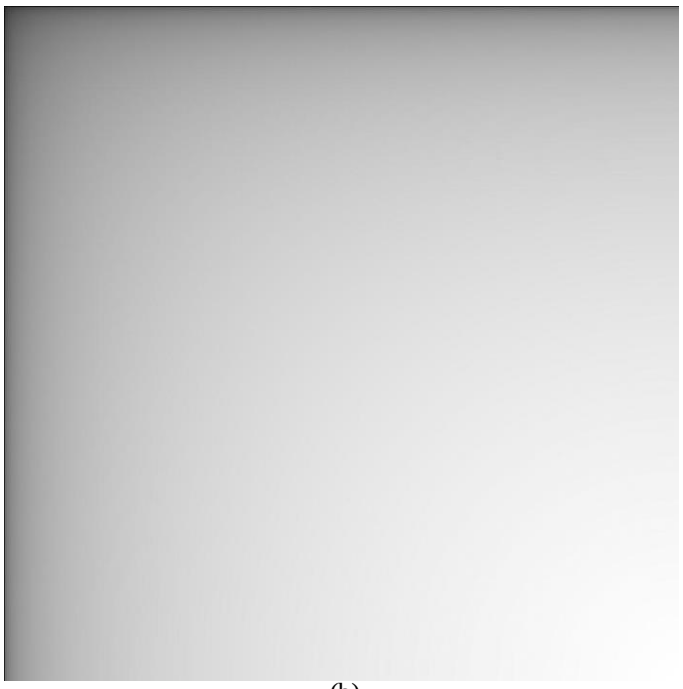

(b)

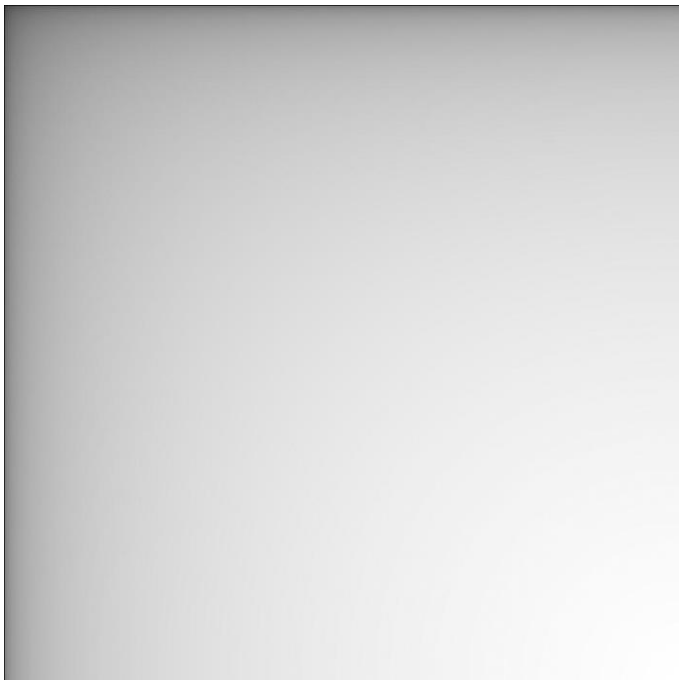

(c)

Fig.10. FMIFC for Re is (a) 10000 (b) 100000 (c) 1000000

As mentioned above, subfigures in Fig. 10 have 1000*1000 pixels (i.e., they have 1000 acoustic paths and each acoustic path has 1000 pixels). The value of the pixel at (M=1, N=1) is 255 for each figure. Comparing the subfigures in Fig. 10, FMIFC has whiter pixels for the larger Re. That means any acoustic path in the z-direction has greater velocity (larger pixel value) for larger Re. By using FMIFC, the normalized fluid velocities are obtained for M=1, 500, 1000 and Re=10000, 100000 and 1000000 (shown in Fig. 11).

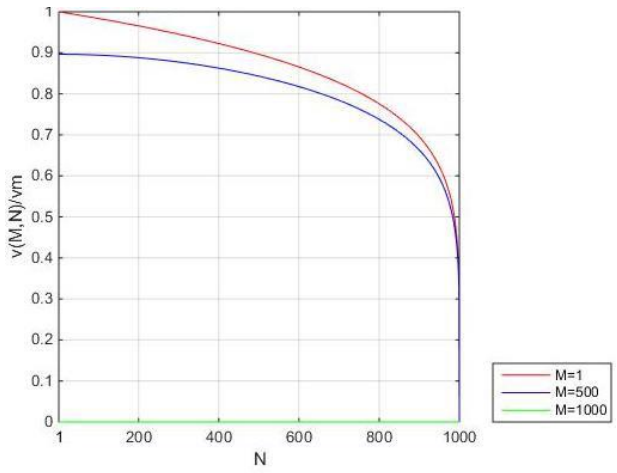

(a)

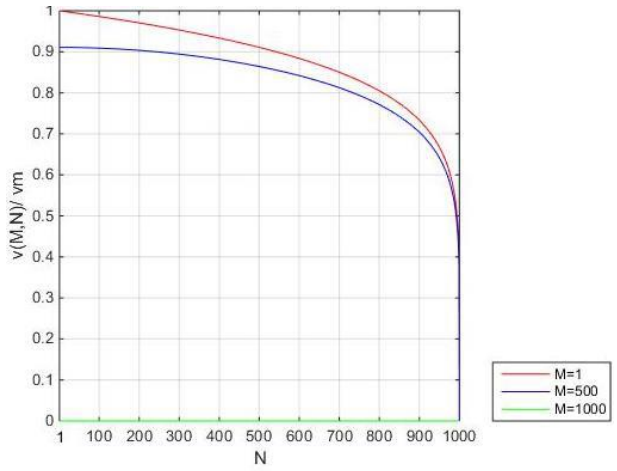

(b)

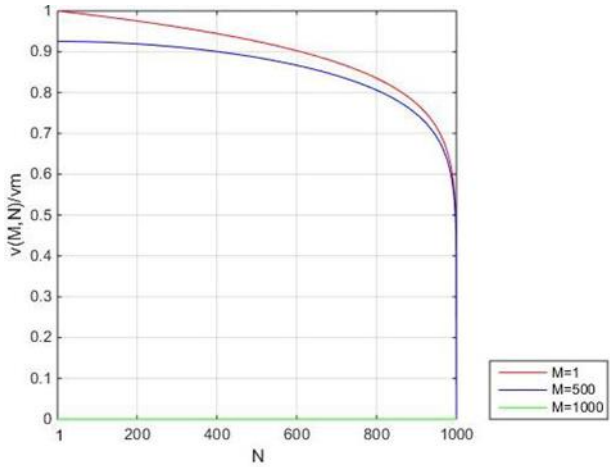

(c)

Fig.11. Normalized fluid velocity for M=1, 500 and 1000. (a) Re=10000 (b) Re=100000 (c) Re=1000000

v (M, N) shown in Fig. 11 indicates the pixel value of the fluid velocity at the position (M, N). The v (1, 1) value (i.e. M=1 and N=1) is equal to v_m in three figures. While normalized v (500, 1) is 0.896 for Re=10000, it is 0.911 and

0.925 for Re=100000 and 1000000, respectively. The pixels at M=1 or N=1 are also calculated with Eq. (5) but other pixels are calculated with pixel-based calculation method. To find normalized v (1,600) (whose values are 0.865, 0.884 and 0.903 for Re=10000, 100000 and 1000000, respectively), both Eq. (5) and pixel-based method are used. To find normalized v (500,600) (whose values are 0.818, 0.842 and 0.867 for Re=10000, 100000 and 1000000, respectively), only the pixel-based method is used in this paper. M=1000 or N=1000 indicates the pipe surface and the values of v are zero for these positions. Fig. 11 is also used to calculate Q_{bpr} which is indicated in Eq. (13). For any acoustic path in the z-direction, v_{bp} is obtained by averaging the pixels. Fig. 12 shows the obtained v_{bp} values for different acoustic paths.

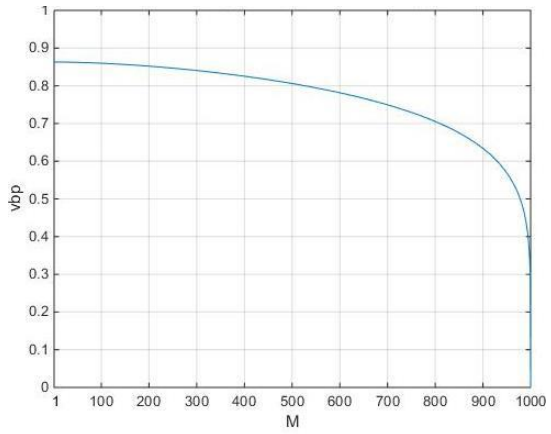

(a)

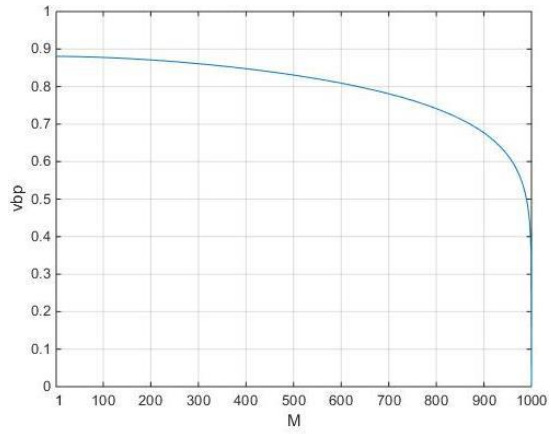

(b)

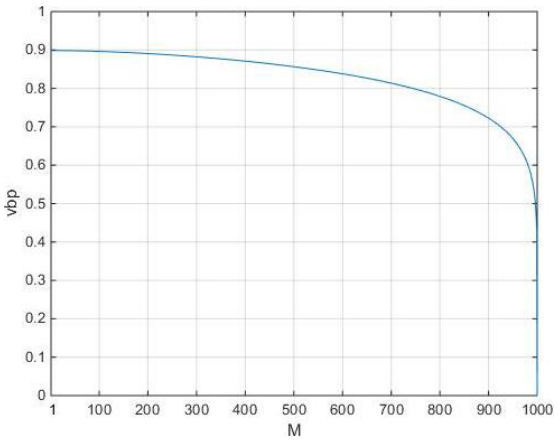

(c)

Fig.12. Obtained v_{bp} values for different acoustic paths (a) Re=10000 (b) Re=100000 (c) Re=1000000

In Fig. 12, M=1 indicates the acoustic path in the middle of the pipe. In this position, v_{bp} is 0.863, 0.881 and 0.899 for Re=10000, 100000 and 1000000, respectively. These values are also shown in Fig. 4 and can also be obtained with Eq. (7). But for other acoustic paths, the values of v_{bp} are obtained with the pixel-based calculation method. These values are used to evaluate the quality of the ultrasonic flow meter systems. If the ultrasonic transducers are placed in positions M=309 and M=809, we obtain that v_{bp1} is 0.839 for the position M=309 and v_{bp2} is 0.7 for the position M=809 as shown in Fig. 12a for Re=10000. According to Eq. (13), Q_{bpr} is 1.199. To evaluate the design, Q_{bpr} is used for reference value. The researcher calculates Q_{bp} by using the results of the application (v_1 and v_2 shown in Eq. (14)). The value of Q_{bp} shows the compatibility between the ultrasonic transducers. The ideal value of Q_{bp} is 1. For example, the researcher designs the ultrasonic flowmeter and calculates Q_{bp} with the method given in this paper, and then changes the design and recalculates Q_{bp}. If the value of the recalculated Q_{bp} is closer to 1 after the operation, this means the change has improved the design. Otherwise, the change has damaged the performance of the design. Thus, Q_{bp} can be used to analyze the design for any Re and acoustic path.

V. CONCLUSION

TTD method measures the average velocity of the fluid along the acoustic path between the two ultrasonic transducers. Currently, there are many studies on TTD ultrasonic flowmeters. For researchers, it is very important to analyze their designs. This paper presents FMIFC to analyze the fluid flow depending on Re for the ideal flow conditions and the turbulent flow. FMIFC is obtained with the pixels describing the acoustic paths. FMIFC in this paper has 1000*1000 pixels which represent the number of acoustic paths and the number of pixels in each acoustic path. Any pixel in FMIFC has a greater grey level value for greater velocity. Furthermore, a quality metric is developed by using the obtained FMIFC. This metric indicates the reference ratio of the average fluid velocity of different acoustic paths. The results show that the proposed metric is easy to use for any acoustic path or Re.

Thus, it is recommended as a useful alternative metric to evaluate the performance of the ultrasonic flowmeter.

REFERENCES

[1] Y. Inoue, H. Kikura, H. Murakawa, M. Aritomi, M. Mori, "A study of ultrasonic propagation for ultrasonic flow rate measurement.", Flow Measurement and Instrumentation, vol.19. 3-4, 2008, pp. 223-232.

[2] Y. Yu, G. Zong, "Design and simulation of an ultrasonic flow meter for thin pipe", In 2011 IEEE International Conference on Mechatronics and Automation, August 2011, pp. 1115-1119.

[3] L. Mingwei, L. Guosheng, H. Yanguo, "Research on improving the accuracy of the ultrasonic flow-meter with time difference method", In 2010 International Conference on Electrical and Control Engineering, June 2010, pp. 1704-1707.

[4] L. Svilainis, P. Kabisius, A. Aleksandrovas, A. Chaziachmetovas, "Excitation signal's influence on ultrasonic transit time flow meter's performance", In IOP Conference Series: Materials Science and Engineering, vol. 42. 1, 2012, pp. 012047.

[5] S. V. Kulkarni, M. M. Sonkhaskar, S. D. Pardeshi, "Test bench development for acquisition module FPGA of Ultrasonic flow meter", In 2015 International Conference on Pervasive Computing (ICPC), January 2015, pp. 1-6.

[6] Y. Wang, "New-type ultrasonic flow meter design based on FPGA high-speed data sampling", In 2009 9th International Conference on Electronic Measurement & Instruments, August 2009, pp. 1-509-512.

[7] Y. Bo, C. Li, "Electronic circuit design for reciprocal operation of transit-time ultrasonic flow meters.", Flow Measurement and Instrumentation, vol.32, 2013, pp.5-13.

[8] J. Berrebi, P. E. Martinsson, M. Willatzen, J. Delsing, "Ultrasonic flow metering errors due to pulsating flow.", Flow Measurement and Instrumentation, vol. 15.3, 2004, pp. 179-185.

[9] Z. Chen, Z. Li, "Robust precise time difference estimation based on digital zero-crossing detection algorithm.", IEEE Transactions on Instrumentation and Measurement, vol. 65.8, 2016, pp.1739-1748.

[10] A. Hamouda, O. Manck, M. Hafiane, N. E. Bouguechal, "An enhanced technique for ultrasonic flow metering featuring very low jitter and offset.", Sensors, vol. 16.7, 2016, pp.1008.

[11] I. Gryshanova, I. Korobko, P. Pogrebniy, "Increasing of accuracy of multipath ultrasonic flow meters by intelligent correction.", Measurement Automation Monitoring, vol. 62,2016, pp.411-416.

[12] K. Zanker, "Diagnostic ability of the daniel four-path ultrasonic flow meter.", In Southeast Asia Flow Measurement Workshop, March 2003.

[13] T. Tresch, P. Gruber, T. Staubli, "Comparison of integration methods for multipath acoustic discharge measurements.", In proc. IGHEM, July 2006, pp. 1-16.

[14] T. Tresch, B. Lüscher, T. Staubli, P. Gruber, "Presentation of optimized integration methods and weighting corrections for the acoustic discharge measurement.", In International conference on hydraulic efficiency measurements, September 2008.

[15] A. Voser, "Analyse und Fehleroptimierung der mehrpfadigen akustischen Durchflussmessung in Wasserkraftanlagen", Doctoral dissertation, ETH Zurich, 1999.

[16] L. Qin, L. Hu, K. Mao, W. Chen, X. Fu, "Flowrate Determination for Arbitrary Multipath Arrangement Based on Generalized Inverse of Matrix.", IEEE Sensors Journal, vol.17.12, 2017, pp. 3625-3634.

[17] X. Tang, X. Xie, H. Zhang, H. Zhou, "Data integration for multi-path ultrasonic flowmeter based on Levenberg–Marquardt algorithm.", IET Science, Measurement & Technology, vol.9.8, 2015, pp. 909-920.

[18] L. Peng, B. Zhang, H. Zhao, S. A. Stephane, H. Ishikawa, K. Shimizu, "Data integration method for multipath ultrasonic flowmeter.", IEEE Sensors Journal, vol.12.9, 2012, pp. 2866-2874.

[19] L. C. Lynnworth, *Ultrasonic Measurements for Process Control*, Academic Press, Inc., 1989.

[20] J. T. Davies, *Turbulence Phenomena*, Academic Press, New York, 1972.

[21] B. Iooss, C. Lhuillier, H. Jeanneau, "Numerical simulation of transit-time ultrasonic flowmeters: uncertainties due to flow profile and fluid turbulence.", Ultrasonics, vol.40.9, 2002, pp. 1009-1015.

[22] G. Jossinet, "Mesure du debit des liquides par debitmetre accrochable a ultrasons.", NT EDF/DER, HP-12/91.26, 1991.

BIOGRAPHY

Murat Alparslan Gungor received the B.S. degree in Electronics Engineering from Istanbul University, Istanbul, in 2000, M.S. and Ph. D degrees in Electrical and Electronics Engineering from Gazi University, Ankara, Turkey, in 2008 and 2015, respectively. He became the Assistant Professor at Hitit University in 2015. He is currently Assistant Professor in the Electrical and Electronics Engineering Department of Hitit University. His research interests include signal processing, image processing, medical imaging systems and ultrasonic flowmeters.

LDPCC and OFDM based cooperative communication for wireless sensor networks

Volkan Ozduran, *Member*, *IEEE*

***Abstract*—This paper investigates the low-density parity-check codes and orthogonal frequency division multiplexing technique effects on the relay assisted sensor networks. The investigation utilizes Rician and Rayleigh fading environments for the performance analysis. The investigation also considers two different types of information exchange processes, which are direct and relay assisted cases. In the relay assisted case, the relay terminal operates in amplify-and-forward and decode-and-forward modes. Monte-Carlo based computer simulations reveal that 10^{-5} bit error rate value is reached at 16.50 dB for low density parity check coded orthogonal frequency division multiplexing over Rician fading environment in decode-and-forward relay protocol. Similarly, 10^{-5} bit error rate value is reached at 0.36 dB for the low density parity check coded orthogonal frequency division multiplexing over Rician fading environment in amplify-and-forward relay protocol and finally 10^{-5} bit error rate value is reached at -5.30 dB for low density parity check coded orthogonal frequency division multiplexing over Rician fading environment without relay protocols.**

***Index Terms*—Low-density parity check-codes, OFDM, Cooperative communications, Wireless sensor networks**

I. INTRODUCTION

WITH THE helping hand of advances in the sensor technology, wireless sensor networks have got a lot of usage areas in recent years. These usage areas can be summarized as: military, meteorological, biomedical, security, space exploration, monitoring, environmental, and home applications [1]. Although commonly usage of sensors, they have got some disadvantages. One of the main disadvantages of the sensors is the battery problem. These tiny creatures have got limited battery capacity. This negative way of the sensors effects to make better communication in low signal-to-noise ratio (SNR) values. Many researchers are dealing with this negative effect. One of the main desires for the communication systems is to achieve better communication values at lower power levels. In a classical point to point communication method, signals may lose in channel because of the fading effects. To prevent losing signal, it must be sent with high SNR values at transmitter side. This causes more energy consumption to reach better communication values.

On the other hand, cooperative communications [2] have got advantages over classical point to point communications. The basic idea behind cooperative communications is terminals share their resources to mitigate the fading and interference effects over signals. There are several cooperative relay strategies proposed in literature such as, amplify-and-forward (AF) [3], decode-and-forward (DF) [4], compress-and-forward [5], coded cooperation [6], and filter-and-forward [7]. One of the main objectives of these cooperation techniques is to use the relay node effectively. At each relay node, signals regenerate from the relay process and this minimizes the effect of the channels over signals and provides reliable and robust communications in low power values. In [8], authors proposed a joint network-channel coding in cooperative communications model and one of the main aim of their proposed model is to achieve better bit error rate (BER) performance values. In this proposed model, both source and relay nodes have to send their data to the destination node. Similarly, in [9], the authors proposed a model to reduce the power consumption effectively. In this proposed model, each source node behaves as a single carrier transmitter and the other nodes, which are near the source node, work as relay nodes, which shift the signal from the source node to specific frequencies. Moreover, in [10] the authors designed a model for energy efficient rural applications in wireless sensor networks and they reached sufficient results for a cluster head to data gather node transmission through Nakagami-*n* channel in wireless sensor network.

So as to minimize the energy consumption, [11] utilizes cooperative multiple-input multiple-output (MIMO) orthogonal frequency division multiplexing (OFDM) system model structure for wireless sensor networks. Likewise, [12] also deals with the energy minimization for sensor networks applications. Apart from the aforementioned studies, [12] takes into consideration the circuit energy consumption as well. In addition, [12] also shows that single input single output (SISO) systems may outperform the MIMO systems when the data rate and modulation scheme are fixed. In order to minimize the overall transmit power, [13] proposes and analyses joint power control and bit rate assignment for OFDM modulated two-way AF relay wireless sensor networks. [14] utilizes Low-Density Parity-Check (LDPC) error correcting codes for channel coding and investigates the various types of multi-carrier modulation techniques, which are single-carrier frequency division multiple access (SC-FDMA) and orthogonal frequency division multiple access (OFDMA), effect on system total power consumption. [15] provides a systematic literature review regarding error correcting codes for wireless sensor networks. [15] seeks answers for the importance of the error correction codes for wireless sensor network applications in terms of energy, power, and performance. [16] utilizes quasi-cyclic LDPC code for improving the complexity of the encoder in wireless sensor node.

VOLKAN OZDURAN is with Department of Electrical and Electronics Engineering, Istanbul University-Cerrahpasa, Istanbul, Turkey, (email: volkan@istanbul.edu.tr).
https://orcid.org/0000-0002-9442-9099

Manuscript received February 12, 2020; accepted June 08, 2020.
DOI: 10.17694/bajece.688294

Reference [17] considers wavelet based compress-and-forward relay protocol and investigates the wavelet compression families Haar and Daubechies-4 techniques' performance evaluations in wireless sensor networks. In addition, [17] utilizes LDPC error correction codes at transmitter side and maximum-ratio combining (MRC) technique at receiver side. Results in [17] reveal that Haar achieves better performance than Daubechies-4. [18] provides performance comparison of the binary phase shift keying (BPSK) modulated error correction codes in additive white Gaussian noise (AWGN) environment. [18] shows that Reed-Solomon code achieves better BER performance than its counterparts. [19] proposes serially concatenated LDPC and turbo codes scheme for wireless sensor networks. [20] seeks an answer for the distance and frequency effects on the error correction codes' energy efficiency in wireless sensor networks.

Differently from aforementioned studies, in order to minimize the overall energy consumption, this paper utilizes LDPC error correcting codes for channel coding process. BPSK modulation and OFDM multicarrier modulation techniques are chosen to achieve better communication values at low SNR. The MRC technique is utilized at the receiver side to combine the received signals, which are coming from source and relay terminals. This proposed model is performed with and without OFDM and relay nodes over various channel types to measure the robustness and overall power consumption of the designed model.

The rest of the paper is organized as follows. In Section 2, the LDPC codes, which are used for channel coding, are briefly described. In Section 3, the OFDM technique is briefly described. In Section 4, purposed cooperative communication system model is described. In section 5, simulation results are presented and finally in Section 6, performance results are briefly discussed.

II. LOW DENSITY PARITY CHECK CODES

LDPC codes are known as a linear block codes and was first introduced by Gallager [21] in 1962. But it has not been used for a long time until McKay and Neal [22] brought it to the light in 1992. After 1992, LDPC codes has found a lot of usage areas in literature and in daily life. LDPC codes have got two types. The first one is regular LDPC codes, which is introduced by Gallager in 1962, and the other one is irregular LDPC codes [23]. The differences between regular and irregular LDPC codes are the structure of the parity check matrix, H. In regular LDPC codes, the parity check matrix's columns and weights are produced constantly. On the other hand, in irregular LDPC codes, the parity check matrix's columns and weights are produced non-constantly. Irregular LDPC codes perform better than regular LDPC codes because of the distribution of 1 and 0 bits.

III. ORTHOGONAL FREQUENCY DIVISION MULTIPLEXING

Over the last decade, with the improvements on the Digital Signal Processers (DSP), OFDM has found a lot of usage areas in wideband communication over mobile radio FM channels, asymmetric digital subscriber lines (ADSL), high-speed digital subscriber lines (HDSL), very high-speed digital subscriber lines (VHDSL), digital audio broadcasting (DAB), digital video broadcasting (DVB) and HDTV terrestrial broadcasting [24]. In a single-carrier data transmission technique, the information bit sequences are sent on a single-carrier modulation system and if there is a burst occurring in a bit sequence it affects all the bit sequences. To overcome this negative effect Frequency Division Multiplexing (FDM) method is proposed. FDM divides the frequency bands into several sub channels and these sub channels are non-overlapping each other. This enables to use the frequency spectrum efficiently. In 1966 Chang [25] proposed orthogonality and overlapping methods for multicarrier modulation to use the frequency spectrum efficiently. OFDM is a special type of FDM technique and the concept of the OFDM is to divide the communication channel into several sub channels which is called in commonly subcarriers. These subcarriers are orthogonal and overlapping between each other. This orthogonality and overlapping enable to use spectrum very efficiently. Each subcarrier carries the one bit of the total information bits [26, 27]. The OFDM transmitter and receiver structures are depicted in figure 1 (a) and (b), respectively [24].

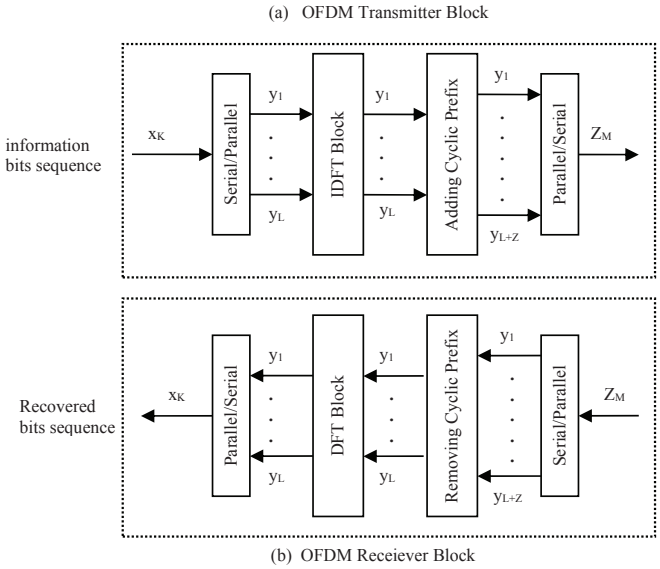

Fig. 1: Overview of OFDM scheme.

At transmitter side, a group of serial data sequences are made parallel by using serial to parallel converter and are sent to the IDFT block to modulate each separate parallel data sequences. Then these modulated bit sequences are sent to the cyclic prefix (CP) block to add bits from end of the line to avoid the inter-symbol interference (ISI) and inter-carrier interference (ICI) effects. After this process, these parallel bit sequences are sent to the parallel to serial blocks to be a serial data sequence. Finally, these data sequences are sent to the channel. At receiver side, serial data sequences are received

and forwarded to the serial to parallel blocks and then sent to the removing CP block to remove added bits which are added at transmitter side to avoid the ISI and ICI. Then these bits are sent to the DFT blocks to demodulate and then sent to the parallel to serial block to handle serial data sequence.

IV. SYSTEM MODEL

In proposed communication system models, which are depicted in figure 2 and 3, the investigation considers with relay node and without relay node over various channel types such as, AWGN environment, fading environment both for Rician and Rayleigh types in wireless sensor networks. The investigation considers that the sensor nodes, which are presented in figure 2 and 3, are placed in a small cluster with equal distance. The investigation utilizes LDPC codes for channel coding process instead of classical communication systems. This channel encoder helps to reach Shannon [28] theoretical communication limit at low signal to noise ratios. Since the relay terminal operates in half-duplex mode, the information exchange process can be completed in two phases, which are phase I and Phase II.

The received signals at relay and destination terminals for figure 2 and 3 can be written as:

$$y_{s,r} = \sqrt{P_1} h_{s,r} x + n_{s,r} \tag{1}$$

$$y_{s,d} = \sqrt{P_1} h_{s,d} x + n_{s,d} \tag{2}$$

where $y_{s,d}$ and $y_{s,r}$ are received signals at destination and relay terminals, respectively. P_1 is the transmit power at source terminal. x is the transmit information. $h_{s,d}$ and $h_{s,r}$ are channel impulse responses between source $\rightarrow$ destination and source $\rightarrow$ relay, respectively. $n_{s,d}$ and $n_{s,r}$ are AWGN at destination and relay terminals, respectively.

In the case that relay terminal operates in AF mode, the relay terminal amplifies the received signal, which is coming from the source terminal, with G amplification factor and forwards it to the destination terminal. The G amplification factor can be calculated as:

$$G = \sqrt{\frac{\mathrm{P}_2}{\mathrm{P}_1 |h_{s,r}|^2 + N_0}} \tag{3}$$

where P_2 is the relay terminal's transmit power and N_0 is the noise variance at relay terminal. After this amplification process, the received signal at destination terminal can be written as:

$$y_{r,d} = G\sqrt{\mathrm{P}_2} h_{r,d} y_{s,r} + n_{r,d} \tag{4}$$

In the case that relay terminal operates in DF mode, the relay node receives coded signal coming from the source node and decodes the received signal and then transmits the decoded signal to the destination node. The received signal at destination terminal can be written as:

$$y_{r,d} = \sqrt{\mathrm{P}_2} h_{r,d} \hat{x} + n_{r,d} \tag{5}$$

where $\hat{x}$ is the decoded information. At destination node, the signals coming both from the source node and the relay nodes are combined by using MRC [29] or maximum-likelihood (ML) receiver [30]. The combined signal at the MRC detector can be written as in [29, 31]

$$y = a_1 y_{s,d} + a_2 y_{r,d} \tag{6}$$

Here, y is the received signal both coming from the source node and the relay node. a_1 and a_2 factors can be formulated with the help of [29, 31] as:

$$a_1 = \frac{\sqrt{\mathrm{P}_1} h_{s,d}}{N_0} \tag{7}$$

$$a_2 = \frac{\sqrt{\mathrm{P}_2} h_{r,d}}{N_0} \tag{8}$$

Cooperative communication system is designed based on following assumptions:

- (a) For LDPC structure, Generator matrix, G is $302x1200$ bits and parity check matrix, H is $900x1200$ bits length and regular LDPC codes are used.
- (b) For OFDM structure, serial to parallel block divides the signal by 10 to make parallel and for the CP block takes 5 of the signal. For this model, 60 bits of the 1200 bits length of the signal for both adding CP and removing CP blocks.
- (c) For the channel type, when the communication system performed with the OFDM technique, noise is normalized with 0.08 coefficient.
- (d) For AF and DF cooperative relay protocols, transmit powers, $\mathrm{P}_1 = 0.6P$ and $\mathrm{P}_2 = 0.4P$ are chosen.
- (e) Both for AF and DF relay protocols 8 relay nodes are utilized for cooperative communication.

For no relay node model, communication system is designed by using LDPC codes with and without using OFDM technique and is performed over various environments such as AWGN environment, fading environment both for Rayleigh and Rician cases. This model is classical communication model and communication takes place between source node and destination node. At source node, 302 bit length source data is sent to the LDPC encoder block, after encoding process according to the assumption (a) at LDPC block, 302 bit length signal become 1200 bit length and sent to the BPSK modulation. The mathematical formulation for BPSK can be written as:

$$z = 2x - 1 \tag{9}$$

Here, x is the 1200 bit length LDPC coded signal and z is the output of the BPSK modulation. In BPSK modulation block "0" bits are converted to "-1" and "1" bits are converted to the "1" and sent to the OFDM block. In OFDM block, modulated serial bits are converted to the parallel bits according to the assumption (b) at serial to parallel block. 1200 bits length signal is divided by "10" and we have $120x10$ matrix and then this matrix block sent to the IDFT block. At IDFT block modulation process takes place here. After IDFT block, this signal set is sent to the CP block to add bits according to the assumption (b), which is stated above. The reason why these bits are added at CP block is to mitigate the effect of

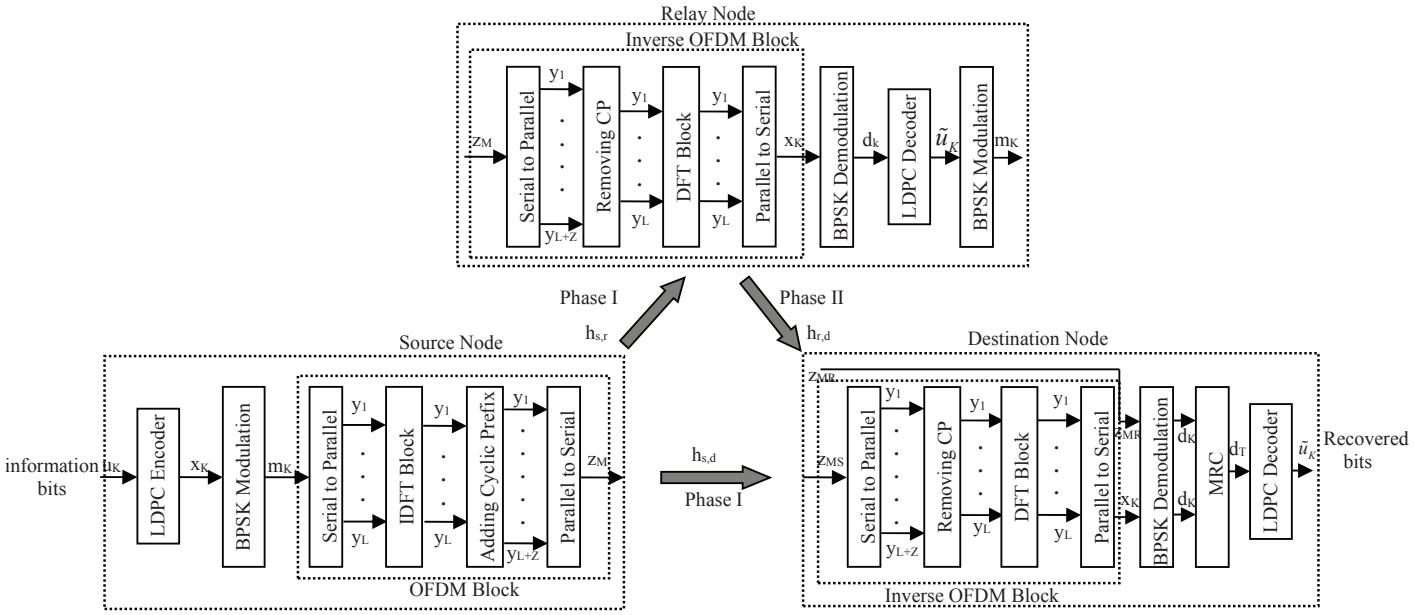

Fig. 2: DF based proposed cooperative communication model.

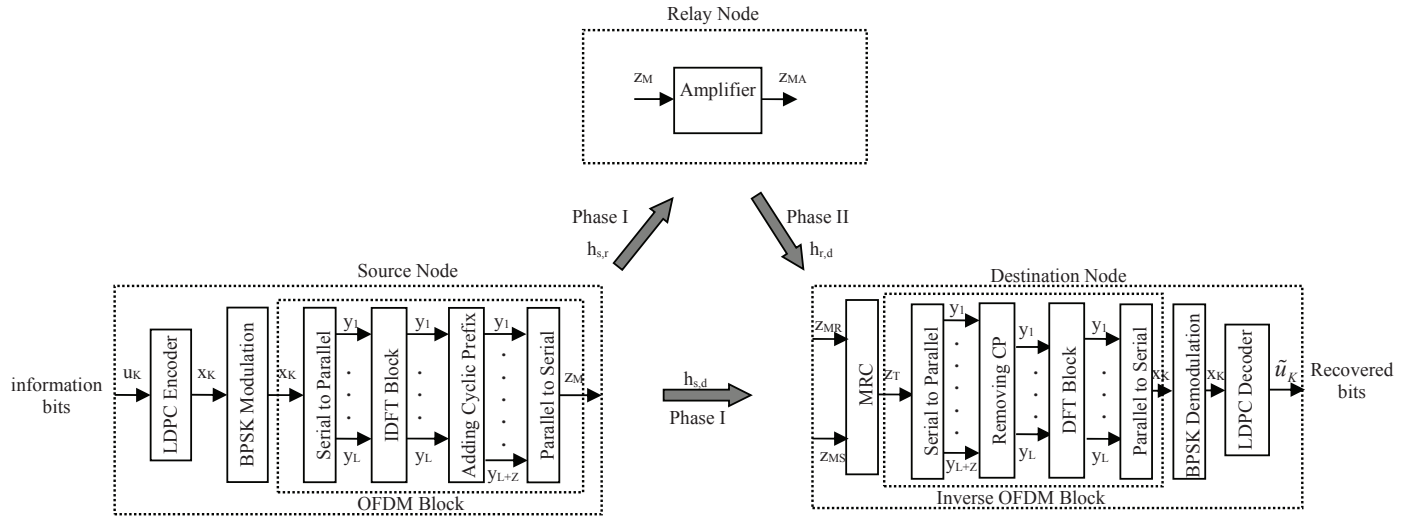

Fig. 3: AF based proposed cooperative communication model.

the ISI and ICI. After adding CP block, signal set become a $126x10$ matrix and this parallel block is converted to serial bit set by parallel to serial block. This 1260 length bit set is sent to the channel. At channel the system is performed with AWGN environment and fading environment both for Rician and Rayleigh fading cases. When the communication system is performed with OFDM block, channel noise is normalized with 0.08 coefficient based on the assumption (c).

At receiver side, inverse OFDM block receives 1260 bit length noisy signal from channel. The first process in inverse OFDM block is to convert this 1260 bit length serial data stream into the parallel based on the assumption (b). After the serial to parallel block, signal set is become a $126x10$ matrix and is sent to the removing CP block to remove the CP bits, which is 60 bits. After the removing CP block signal set is become a $120x10$ matrix. This parallel block is converted to serial data stream by parallel to serial block and is become 1200 bit length. This block is the last block for the inverse OFDM block. 1200 bit length bit stream is demodulated with BPSK demodulation block and forward to the LDPC decoder block to handle the recovered bits. At LDPC decoder, Message Passing Algorithm (MPA) [32] is used for decoding process. After decoding process, recovered bit sequences are handled. For this proposed communication model, simulation results are presented in table 1 and figure 4.

For DF cooperative communication, system model is depicted in figure 2 and communication takes place in 2 phases, Phase I and Phase II. For phase I situation, source node is designed based on assumptions and likewise no relay model. Source node sends 1260 bit length bit stream to the relay node and destination node simultaneously according to (1) and (2), respectively. When the relay node receives noisy signal from source node, inverse OFDM block processes the signal and at the end of the inverse OFDM block, 1200 bit length set is handled and forwarded to the BPSK demodulation block. After demodulation process, LDPC decoder receives it and decodes it by using MPA and recovered bits are modulated with BPSK modulation block according to (9). For phase II situation, BPSK modulated signal is forwarded to the destination node according to (5).

Destination node receives these signals coming both from source node-phase I and Relay nodes-Phase II. These signals are different between each other, such as source node signal is LDPC coded OFDM signal and the relay node signal is decoded signal, so destination node process these signals separately. When the destination node receives noisy source signal from phase I case, it forwards to the inverse OFDM block and when the destination node receives decoded signal from relay nodes it forwards to the BPSK modulation block. These signal sets are demodulated separately and combined at MRC according to (6) and forwarded to the LDPC decoder. LDPC decoder decodes them using MPA and recovered bits are handled. Simulation results are presented in table 1 and figure 5.

For AF cooperative communication, system model is illustrated in figure 3 and it is designed based on assumptions. Communication takes place in 2 phases, Phase I and Phase II as in DF protocols. Source node is similar with no relay model and DF model and for Phase I case, source node sends 1260 bit length bit stream to the relay node and destination node simultaneously according to (1) and (2), respectively. When the relay nodes receive noisy signal from source node they simply amplifies the noisy signal with (3) and forwards to the destination node according to (4) in Phase II case. Destination node receives signals both from source node and relay nodes and it combines these signals by using MRC according to (6) which is constructed based on (7) and (8). MRC block forwards to the inverse OFDM block and after the inverse OFDM blocks, 1260 bits length signal is become 1200 bits length and is forwarded to the BPSK demodulation block. Demodulated signal is sent to the LDPC decoder and it is decoded by using MPA and finally recovered bit sequences are handled. Simulation results are presented in table 1 and figure 6.

V. SIMULATION RESULTS AND DISCUSSION

In this study, LDPC codes and OFDM techniques are utilized for cooperative wireless sensor networks. AF and DF relay protocols are chosen for cooperative communication model. The investigation is also modeled and performed LDPC coded OFDM and without OFDM technique with AWGN, fading environment both for Rician and Rayleigh cases without using any relay node. For no relay node case, the Shannon theoretical limit value, 10^{-5} BER, is reached at -0.50 dB for LDPC coded AWGN environment, -3.20 dB for LDPC coded OFDM over AWGN environment. The effect of the OFDM systems over performance evaluation can be clearly seen from performance curves. 2.70 dB gain is achieved by using OFDM system. Similarly when the LDPC coded signal is performed over fading environment, 10^{-5} BER value is reached at 2.30 dB for Rayleigh fading case (K=0), -4.30 dB for LDPC coded OFDM over Rayleigh fading case. Here, 6.60 dB gain is reached by using OFDM system. For Rician fading case (K=10), 10^{-5} BER value is reached with LDPC coded signal at -0.10 dB and -5.30 dB for LDPC coded OFDM system. Here, 6.40 dB gain is reached by using OFDM system. These performance evaluation curves are presented in figure 4. For DF, communication model is presented in figure 2. The investigation is performed with and without OFDM systems. Here, 10^{-5} BER value is reached at 33.00 dB for LDPC coded Rayleigh fading environment case (K=0) and 30.00 dB for LDPC coded OFDM over Rayleigh fading environment. 3.00 dB gain is obtained by using OFDM. For Rician case (K=10), 10^{-5} BER value is reached at 19.00 dB for LDPC coded version and 10^{-5} BER value is reached at 16.50 dB for LDPC coded OFDM over Rician fading environment. By using OFDM, 2.50 dB gain is obtained. Performance evaluation curves are presented in figure 5. For AF relay protocol, cooperative communication model is depicted in figure 3. The investigation is performed with and without OFDM techniques. Performance curves are shown in figure 6. Here, 10^{-5} BER value is reached at 1.42 dB for LDPC coded Rayleigh fading environment case (K=0). On the other hand, 0.75 dB is reached for LDPC coded OFDM over Rayleigh fading environment. In these cooperative communication schemes, by using OFDM,

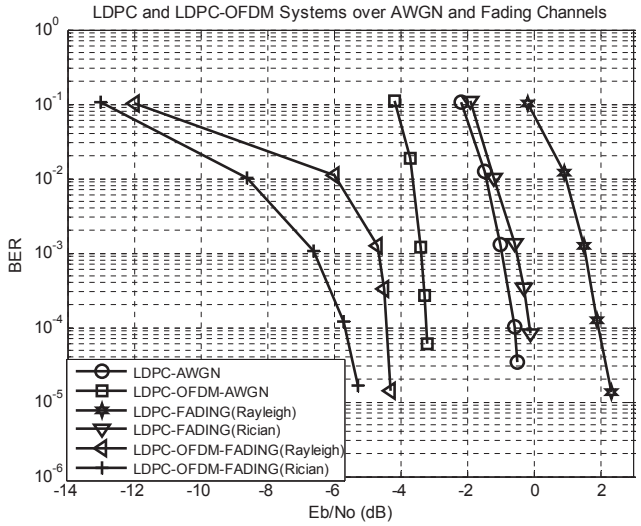

Fig. 4: Performance of LDPC and LDPC-OFDM Systems over AWGN and Fading Channels.

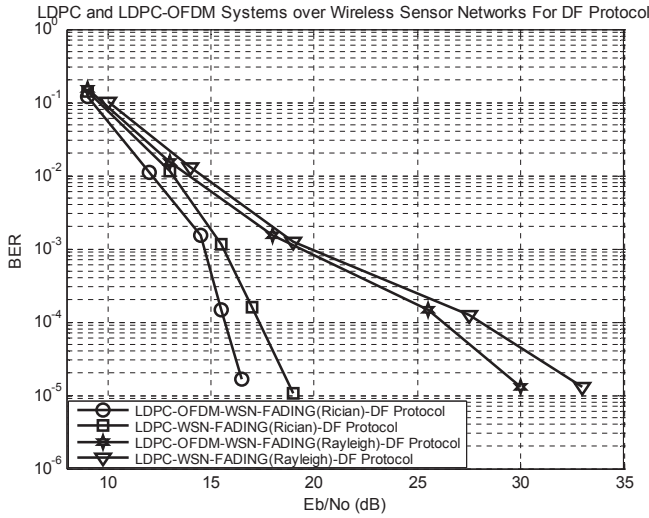

Fig. 5: Performance of LDPC and LDPC-OFDM systems over wireless sensor networks for DF relay protocols.

0.67 dB gain is obtained. For Rician fading case (K=10), 10^{-5} BER value is reached at 1.09 dB for LDPC coded version and 10^{-5} BER value is reached at 0.36 dB for LDPC coded OFDM over Rician fading environment. By using OFDM, 0.73 dB gain is obtained. Performance evaluation curves are presented in figure 6.

According to the above simulation results, it can be clearly seen the effect of the OFDM systems over communication models. It is also observed from the figures that significant coding gain can be achieved by using OFDM and LDPCC techniques. When the relay protocols are performed in Rician

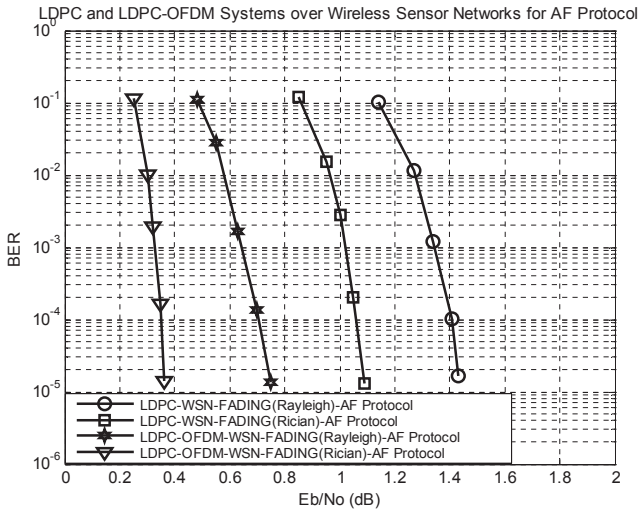

Fig. 6: Performance of LDPC and LDPC-OFDM systems over wireless sensor networks for AF relay protocols.

and Rayleigh fading cases, the best value is reached in AF relay protocol.

Consequently, for practical applications, AF relay protocol is better than DF relay protocol because of its lower complexity and lower power consumption.

VI. Conclusion

This paper have proposed a communication model which utilizes LDPC encoder, OFDM, and communication protocols for the relay process, which are AF and DF protocols. The investigation have achieved significant coding gain by using OFDM technique. The results are clearly stated and observed the effect of the OFDM in the simulation results.

In future works, the proposed model can be compared by using different coding techniques, relay protocols and the multiplexing method, which is non-orthogonal multiple access, to achieve a better performance values in lower power consumption.

References

[1] I. Akyildiz, W. Su, Y. Sankarasubramaniam, and E. Cayirci, "Wireless sensor networks: a survey," *Computer Networks*, vol. 38, no. 4, pp. 393 – 422, 2002.

[2] A. Nosratinia, T. E. Hunter, and A. Hedayat, "Cooperative communication in wireless networks," *IEEE Communications Magazine*, vol. 42, no. 10, pp. 74–80, Oct 2004.

[3] M. Torabi, W. Ajib, and D. Haccoun, "Performance analysis of amplify-and-forward cooperative networks with relay selection over rayleigh fading channels," in *VTC Spring 2009 - IEEE 69th Vehicular Technology Conference*, April 2009, pp. 1–5.

[4] J. N. Laneman and G. W. Wornell, "Distributed space-time-coded protocols for exploiting cooperative diversity in wireless networks," *IEEE Transactions on Information Theory*, vol. 49, no. 10, pp. 2415–2425, Oct 2003.

[5] S. Simoens, O. Munoz-Medina, J. Vidal, and A. Del Coso, "Compress-and-forward cooperative mimo relaying with full

	AWGN Environment			Fading Environment					
				Rayleigh Case (K=0)			Rician Case (K=10)		
	LDPCC	LDPCC+OFDM	Gain	LDPCC	LDPCC+OFDM	Gain	LDPCC	LDPCC+OFDM	Gain
No Relay	-0.50	-3.20	2.70	2.30	-4.30	6.60	-0.10	-5.30	6.40
AF Relay	-	-	-	1.42	0.75	0.67	1.09	0.36	0.73
DF Relay	-	-	-	33.00	30.00	3.00	19.00	16.50	2.50

* This table is constructed based on the Shannon theoretical limits 10^{-5} Bit Error Rate (BER) value.

Fig. 7: The comparison results of without using any relay node, AF and DF protocols both for AWGN and Fading environments (in dB)

channel state information," *IEEE Transactions on Signal Processing*, vol. 58, no. 2, pp. 781–791, Feb 2010.

[6] T. E. Hunter and A. Nosratinia, "Performance analysis of coded cooperation diversity," in *IEEE International Conference on Communications, 2003. ICC '03.*, vol. 4, May 2003, pp. 2688–2692 vol.4.

[7] H. Chen, A. B. Gershman, and S. Shahbazpanahi, "Filter-and-forward distributed beamforming in relay networks with frequency selective fading," *IEEE Transactions on Signal Processing*, vol. 58, no. 3, pp. 1251–1262, March 2010.

[8] Du Bing and Zhang Jun, "Design and optimization of joint network-channel ldpc code for wireless cooperative communications," in *2008 11th IEEE Singapore International Conference on Communication Systems*, Nov 2008, pp. 1625–1629.

[9] Weiguo Tang and Lei Wang, "Cooperative ofdm for energy-efficient wireless sensor networks," in *2008 IEEE Workshop on Signal Processing Systems*, Oct 2008, pp. 77–82.

[10] M. R. Islam and J. Kim, "Capacity and ber analysis for nakagami-n channel in ldpc coded wireless sensor network," in *2008 International Conference on Intelligent Sensors, Sensor Networks and Information Processing*, Dec 2008, pp. 167–172.

[11] D. S. Singh A.K., Mishra S.K., "Energy efficiency in wireless sensor networks: Cooperative mimo-ofdm," *Recent Trends in Communication, Computing, and Electronics. Lecture Notes in Electrical Engineering*, vol. 524, no. -, pp. 147–154, December 2018.

[12] Shuguang Cui, A. J. Goldsmith, and A. Bahai, "Energy-efficiency of mimo and cooperative mimo techniques in sensor networks," *IEEE Journal on Selected Areas in Communications*, vol. 22, no. 6, pp. 1089–1098, Aug 2004.

[13] X. Ji, Z. Bao, and C. Xu, "Power minimization for ofdm modulated two-way amplify-and-forward relay wireless sensor networks," *J Wireless Com Network*, vol. 70, no. -, pp. 1–8, April 2017.

[14] V. Ozduran and N. Ozdemir, "3gpp long term evolution (lte) based cooperative communication in wireless sensor networks," in *2012 IV International Congress on Ultra Modern Telecommunications and Control Systems*, Oct 2012, pp. 900–905.

[15] M. Bettayeb, S. Ghunaim, N. Mohamed, and Q. Nasir, "Error correction codes in wireless sensor networks: A systematic literature review," in *2019 Intern. Conf. on Commun., Signal Processing, and their Applications (ICCSPA)*, 2019, pp. 1–6.

[16] S. Choi and B. Moon, "Implementation of energy efficient ldpc code for wireless sensor node," *Kim T. et al. (eds) Communication and Networking. FGCN 2011. Communications in Computer and Information Science, Springer*, vol. 266, no. -, pp. –, 2011.

[17] V. Ozduran and O. N. Ucan, "Wavelet based compress-and-forward relay protocol for cooperative communication in wireless sensor networks," in *Computational Intelligence and Bioinformatics / 755: Modelling, Simulation, and Identification*, 2011.

[18] I. Ez-zazi, M. Arioua, A. el Oualkadi, and Y. el Assari, "Performance analysis of efficient coding schemes for wireless sensor networks," in *2015 Third International Workshop on RFID And Adaptive Wireless Sensor Networks (RAWSN)*, 2015, pp. 42–47.

[19] M. M. Salah and A. A. Elrahman, "Energy efficiency based concatenated ldpc and turbo codes for wireless sensor networks," in *2015 IEEE International Conference on Signal Processing, Communications and Computing (ICSPCC)*, 2015, pp. 1–6.

[20] S. Howard, C. Schlegel, and K. Iniewski, "Error control coding in low-power wireless sensor networks: When is ecc energy-efficient?" *J. Wireless Com Network, Springer*, vol. -, no. -, pp. 1–14, 2006.

[21] R. Gallager, "Low-density parity-check codes," *IRE Transactions on Information Theory*, vol. 8, no. 1, pp. 21–28, January 1962.

[22] D. J. C. MacKay and R. M. Neal, "Near shannon limit performance of low density parity check codes," *Electronics Letters*, vol. 32, no. 18, pp. 1645–, Aug 1996.

[23] T. J. Richardson, M. A. Shokrollahi, and R. L. Urbanke, "Design of capacity-approaching irregular low-density parity-check codes," *IEEE Transactions on Information Theory*, vol. 47, no. 2, pp. 619–637, Feb 2001.

[24] A. Pandharipande, "Principles of ofdm," *IEEE Potentials*, vol. 21, no. 2, pp. 16–19, April 2002.

[25] R. W. Chang, "Synthesis of band-limited orthogonal signals for multichannel data transmission," *The Bell System Technical Journal*, vol. 45, no. 10, pp. 1775–1796, Dec 1966.

[26] L. Litwin and M. Pugel, "The principles of ofdm," *RF signal processing*, vol. -, no. 10, pp. 30–48, Jan 2001.

[27] H. Lotia, "Modeling a multicarrier wireless communication transceiver," *Embedded Software systems literature survey*,

2004.
[28] C. E. Shannon, "A mathematical theory of communication," *Bell System Technical Journal*, vol. 27, no. 3, pp. 379–423, 1948.
[29] D. G. Brennan, "Linear diversity combining techniques," *Proceedings of the IRE*, vol. 47, no. 6, pp. 1075–1102, June 1959.
[30] X. Liu and W. Su, "Ber performance analysis of the optimum ml receiver for decode-and-forward cooperative protocol," in *2007 IEEE International Conference on Acoustics, Speech and Signal Processing - ICASSP '07*, vol. 3, April 2007, pp. III–485–III–488.
[31] W. Su, A. Sadek, and K. Ray Liu, "Cooperative communication protocols in wireless networks: Performance analysis and optimum power allocation," *Wireless Pers Commun*, vol. -, no. -, p. 181217, 2008.
[32] S. Arora, C. Daskalakis, and D. Steurer, "Message-passing algorithms and improved lp decoding," *IEEE Transactions on Information Theory*, vol. 58, no. 12, pp. 7260–7271, Dec 2012.

Volkan Ozduran graduated from department of Electronics at Soke Technical High School, Aydin, Turkey in 1997. He received his A.Sc. degree in Industrial Electronics, B.Sc., M.Sc. and Ph.D. degrees are in Electrical and Electronics Engineering from Istanbul University, Istanbul, Turkey in 2002, 2005, 2008 and 2015 respectively. During his Ph.D. studies he visited Stanford University, Stanford, CA, USA department of Electrical Engineering, Space, Telecommunications, and Radioscience Laboratory, Dynamic Spectrum Management (DSM) Research group as a visiting student researcher between April 2012 and October 2012 under the supervision of Prof. Dr. John M. CIOFFI, the best known father of DSL. Prof. CIOFFI was his formal second advisor in his PhD studies. During his Ph.D. studies he also had some short visits to California Institue of Technology (CALTECH), Pasadena, CA, USA and Princeton University, Princeton, NJ, USA, department of Electrical Engineering in April 2013 and November 2014, respectively. His current research interests area more on cooperative communications, interference mitigation, massive MIMO and signal processing for wireless communications. He is an active Reviewer in various IEEE conferences and Transactions Journals

Single-Image Super-Resolution Analysis in DCT Spectral Domain

O. AYDIN and R.G. CINBIS

***Abstract*—Advances in deep learning techniques have lead to drastic changes in contemporary methods used for a diverse number of computer vision problems. Single-image super-resolution is one of these problems that has been significantly and positively influenced by these trends. The mainstream state-of-the-art methods for super-resolution learn a non-linear mapping from low-resolution images to high-resolution images in the spatial domain, parameterized through convolution and transposed-convolution layers. In this paper, we explore the use of spectral representations for deep learning based super-resolution. More specifically, we propose an approach that operates in the space of discrete cosine transform based spectral representations. Additionally, to reduce the artifacts resulting from spectral processing, we propose to use a noise reduction network as a post-processing step. Notably, our approach allows using a universal super-resolution model for a range of scaling factors. We evaluate our approach in detail through quantitative and qualitative results.**

***Index Terms*—Super resolution, deep learning, image process.**

I. Introduction

THE primary goal of single-image super-resolution (SR) is to reconstruct a high-resolution (HR) image from a single low-resolution (LR) image with maximum perceptual affinity. Single-image SR has recently attracted a great interest due to its possible applications in a variety of areas, including medical imaging, remote sensing, consumer photo enhancement, and video surveillance. However, SR remains as an unsolved problem mainly due to its ill-posed nature: there can be infinitely many scenes yielding the same LR image. Therefore, in SR, the goal is to find the perceptually most plausible HR image(s) corresponding to a given LR image.

From a machine learning perspective, LR-to-HR mapping is a regression problem. To tackle this problem, a variety of traditional machine learning approaches have previously been proposed, such as local linear regression [1], dictionary learning [2] and random forests [3]. More recently, the progress in SR has been dominated by deep learning (DL) based approaches, leading to significant improvements in the state-of-the-art models thanks to learning better nonlinear mappings, e.g. [4]–[6].

ONUR AYDIN, is with the Department of Computer Engineering, Bilkent University, Ankara, 06800, Turkey, (e-mail: onuralg@gmail.com).
https://orcid.org/0000-0002-9304-0647

RAMAZAN GOKBERK CINBIS, is with the Department of Computer Engineering, METU, Ankara, 06800, Turkey, (e-mail: gcinbis@ceng.metu.edu.tr).
https://orcid.org/0000-0003-0962-7101

Manuscript received April 03, 2020; accepted July 14, 2020.
DOI: 10.17694/bajece.714293

Two mainstream ways of utilizing deep learning techniques in super-resolution problem are available. In the first approach, the input image is resized to the target scale using a basic method, such as bicubic interpolation. Then, the SR problem degrades to learning a non-linear transformation that enhances the image quality of the HR image. In the second one, the upscaling transform is directly learned within the deep learning architecture, typically using *transposed convolution* layer(s) [7]. In both cases, LR - HR image pairs are typically required during model training. Once the training is complete, the model is used to predict the HR versions of novel LR image inputs.

In designing an SR approach, there are arguably three primary concerns. *Precision* which demonstrates how accurately target high-resolution image is reconstructed is the main factor. The second one is *efficiency*, which refers to the inference-time computational requirements. Efficiency can especially be critical in applications requiring real-time processing and/or inference on low-power devices. The third one is *flexibility* in terms of selecting an output scale factor at test time, which determines the area ratio between the output and input image. Utilizing a separate network for every scale factor is inherently costly, inefficient and impractical. Furthermore, since model training gets more difficult as the scale factor increases, it is also not plausible to learn a model that is trained only for the largest scaling factor of interest and then down-scale from its output as needed.

To tackle the SR problem, we focus on the use of frequency domain deep learning approaches. The frequency-based representations are relatively little studied in the domain of deep learning. A prominent study in this area is Rippel et al. [8], which shows that convolutional neural networks (CNNs) can be used to learn image classification models in the Fourier domain. Wang et al. [9] shows that discrete cosine transform (DCT) can be used to compress weights of CNNs while preserving the prediction accuracy. Kumar et al. [10] shows that CNNs can be trained to predict wavelet coefficients to improve SR performance. Only in recent works [11] and [12] Fourier domain CNNs have been explored for SR.

In our work, we are approaching single-image super-resolution problem via learning a deep neural network in DCT based frequency domain. More specifically, we train deep neural networks to learn how to transform input low-resolution images into high resolution ones, within the DCT frequency representation. Then, in the spatial domain, a pre-trained artifact reduction model is utilized to eliminate unintended effects appearing when the resulting frequency domain representation is transformed back to the spatial domain. We comprehensively

evaluate our approach on benchmark datasets and discuss its benefits and drawbacks. Our formulation provides us a fast and efficient approach, and, gets rid of the necessity to train a separate model for arbitrary scale factors, i.e. a single model can be used for super resolution to a variety of scaling factors.

Outline. In Section II, we provide a brief overview of deep learning based single-image SR. In Section III, we present our analysis on the use of DCT domain for SR and the details of our approach. In Section IV, we provide our experimental results with detailed evaluations and comparisons to contemporary deep SR approaches. In Section V, we conclude with a summary of our observations and discussion on possible future work directions.

II. Related work

In this section, we present an overview of well-known spatial domain and recent frequency domain approaches for SR. A more comprehensive overview of deep learning based methods for SR can be found in the recent survey by Anwar et al. [7].

Super-Resolution Convolutional Neural Network (SRCNN) [4] proposes one of the first deep learning architectures for single-image SR. It applies a 3-layer CNN on the output of bicubic interpolation output. The model is trained using ℓ_2 reconstruction loss between the SR output and the target HR image. One disadvantage of the SRCNN model is that for every scaling factor, a different model is trained. While SRCNN is not the state-of-the-art on benchmark datasets anymore, it is still a good reference for DL-based SR due to its simplicity.

Several papers propose improvements over the SRCNN approach. For example, Faster Super-Resolution Convolutional Neural Network (FSRCNN) [13] proposes a deeper architecture that uses a transposed convolution layer, instead of upsampling using bicubic interpolation as a preprocessing step. More specifically, in FSRCNN architecture, seven convolutional layers and single transposed-convolution layer is used. Like SRCNN, the model is trained over the ℓ_2 reconstruction loss. Very Deep Super Resolution (VDSR) [5] improves the SRCNN architecture by stacking 20 convolutional layers and adding residual connections. In addition, using *scale augmentation*, the approach trains one model for all scaling factors. Super-Resolution Generative Adversarial Networks (SRGAN) [14] uses adversarial training for improving SR outputs. The SR model contains a *generator*, and a *discriminator* network is used to enforce the generator to produce SR outputs indistinguishable from real HR images. The approach uses *perceptual loss*, i.e. reconstruction loss in convolutional feature space, in addition to the adversarial loss. Laplacian Super-Resolution Networks (LapSRN) [6] proposes to progressively increase the image resolution over a Laplacian pyramid, via 27 convolutional layers with residual connections. The model is trained using *Charbonnier loss*, which is a robust reconstruction loss function that handles outliers better than ℓ_2 loss.

In the recent work of Dai et al. [15], it is highlighted that most SR approaches neglect correlations of intermediate layers. This work proposes the *second-order attention network* to model correlations in intermediate layers and to learn more discriminative representations by adaptive re-scaling of features. Additionally, a non-locally enhanced residual group scheme is proposed in order to capture long-distance spatial information and local-source residual attention groups are proposed to learn abstract feature representations.

Another open problem in SR is effective training on deep architectures, especially for large scaling factors. Towards tackling this problem, Wang et al. [16] proposes a progressive learning approach. Combined with an adversarial training scheme, this method obtains significant improvements, especially for high scaling factors.

Kumar et al. [10] proposes the Wavelet Domain Super-Resolution (CNNWSR) model, which aims to directly predict discrete wavelet transform coefficients of the high-resolution target image. The predicted wavelet coefficients are utilized to reconstruct high-resolution images via two-dimensional inverse DWT. Unlike SRCNN which reconstructs a single-image, CNNWSR architecture is using convolutional layers to predict three separate images that contain all wavelet coefficients. This architecture is the first solution that fuses the deep learning and spectral approaches for SR problem. Nevertheless, the core issue of the CNNWSR architecture is limited to select arbitrary scale factors which is caused from the nature of wavelet transform. Frequency Domain Super Resolution (FNNSR) [11] and Improved-FNNSR (IFNNSR) [12] are two recently proposed Fourier domain SR approaches. FNNSR formulates a deep neural network that parameterizes convolutions as point-wise multiplications in the spectral domain using single convolutional layers to approximate ReLU activations. IFNNSR improves this approach mainly by (i) using Hartley transform instead of Fourier transform, (ii) utilizing multiple convolutional layers to better approximate ReLU activations and (iii) proposing a novel weighted Euclidean loss that emphasizes the errors at high frequency components.

There are a couple of major differences between our approach and the aforementioned frequency domain SR approaches. First of all, while we train a fully connected super-resolution network for predicting carefully-selected frequency terms, other frequency domain approaches define convolutional networks in the frequency domain and predict all frequency terms. Secondly, while we are training a single model for any scale factor, in other spectral-domain SR methods, a separate network is needed for each scale factor. Third, we use DCT as the spectral representation, mainly for its well-known representational power that does not require complex numbers.

III. Method

In this section, we first give a summary of the discrete cosine transform (DCT). In Section III-B, we present our analysis and observations on DCT based super-resolution. Then, in Section III-C, we present our DCT-based super-resolution approach in detail. Finally, in Section III-D, we present the post-processing approach based on an artifact reduction network that aims to eliminate the ringing artifacts.

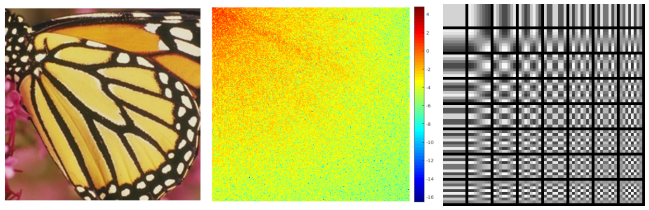

(a) (b)

Figure 1: (a) 2D DCT example, (b) 2D DCT bases shown as images.

A. Discrete Cosine Transform

The spectral domain transforms convert a time (spatial) domain signal to the frequency domain without any information loss. Arguably, the most well-known discrete transform is the Discrete Fourier Transform (DFT). However, even if the input signal is real, DFT yields a representation involving complex numbers. While it is possible to handle complex numbers in a compute graph, the involvement of complex number arithmetic naturally introduces complexity, which may lead to difficulties especially when deploying to low-cost inference devices.

Therefore, in our work, we focus on the Discrete Cosine Transform (DCT). DCT decomposes a signal into cosine functions oscillating at various frequencies and yields only real-valued numbers in the spectral representation. For a two dimensional discrete signal f and its frequency domain representation F, two-dimensional DCT is described as follows [17]:

$$F[u,v] = a(u)a(v)\sum_{x=0}^{N-1}\sum_{y=0}^{M-1} f[x,y]\gamma(x,y,u,v) \quad (1)$$

where $\gamma(x,y,u,v)$ is defined as

$$\gamma(x,y,u,v) = \cos\left(\frac{\pi(2x+1)u}{2N}\right)\cos\left(\frac{\pi(2y+1)v}{2M}\right) \quad (2)$$

and $a(u)$ is defined as:

$$a(u) = \left\{ \begin{array}{ll} \sqrt{\frac{1}{N}}, & u=0 \\ \sqrt{\frac{2}{N}}, & u\neq 0 \end{array} \right\} \quad (3)$$

The signal transformed to frequency domain is reconstructed back via two-dimensional Inverse DCT which is described as follows:

$$f[x,y] = \sum_{u=0}^{N-1}\sum_{v=0}^{M-1} a(u)a(v)F[u,v]\gamma(x,y,u,v). \quad (4)$$

In the Figure 1a, 2-D DCT of an example image is provided. On the one hand, as can be seen in the figure, the resulting DCT spectral representation is difficult to understand directly due to the "loss" (i.e. transformation) of spatial structure. On the other hand, DCT spectral representation allows easily exploring the distribution of information across various frequency components. The top-left corner values correspond to lower frequencies and bottom-right corner values correspond to higher frequencies. As it can be seen through this example, a notable feature of DCT is its energy compaction property. Thanks to this property, DCT preserves substantially more information in lower frequency components [18]. In this context, the relationship between DCT and Karhunen-Loéve transform, which is known to provide the optimal bases for linear approximations of stochastic processes under certain assumptions, is notable [19].

Furthermore, in the Figure 1b, the basis functions for 2-D DCT is given. Each basis function is a 2-D representation of the mixture of two cosine functions which are oscillated at different frequencies. The first basis function located at the top left corner is the DC term. From top to bottom and from left to right, the frequencies of cosine functions increase.

B. Super-resolution in DCT spectral domain

In this section, we present our analysis of the problem of SR on the DCT spectral representation domain. We use the analysis and our main observations presented in this section to design and construct our SR network.

In our approach, we utilize bicubic interpolation to resize a given low-resolution image to the target image size as a pre-processing step, e.g. we up-scale by a factor of $2\times, 3\times, 4\times$ or similar. Thereafter, the image is split to fixed-sized patches with a stride of patch size. Throughout our study, we fix the input patch size 16×16 pixels. The goal is to synthesize HR patches from these LR patches, therefore, we use bicubic interpolation to obtain initial output patches, e.g. of size $32 \times 32, 48 \times 48, 64 \times 64$ for the scaling factors $2\times, 3\times, 4\times$, respectively.

After obtaining the initial output patches, we compute their spectral representations using 2-d discrete cosine transform. Then, to better understand the problem, we compute the squared error between bicubic interpolated patches and true HR patches over the DCT coefficients of the patches, and, average these errors across a large sample of patches from our training set (see Section IV). We show the resulting mean square errors values for three different scale factors in Figure 2a, 2b and 2c. In these images, each pixel represents a frequency value. Following the ordering in Figure 1, while the top left corner stands for low frequencies, the bottom right corner stands for high frequencies and the remaining regions stand for mid-frequencies.

If we interpret these mean squared error values as distribution of error in the space of DCT coefficients, we observe that lower-mid range contains the largest problematic region (we simply refer to this region as mid-frequencies for brevity), instead of low-frequencies or higher frequencies. We also observe that this error distribution in the DCT coefficient space is consistent across all three scaling factors.

Following these observations, we focus on minimizing the coefficient errors on the most problematic DCT components by applying a neural network architecture to the DCT representations of bicubic interpolation output. We emphasize the importance of the observation that the error accumulates in the same DCT components: this leads us to construct a single model for all scaling factors, thanks to the fact that higher frequency DCT components have relatively low importance. Therefore, by focusing on only the mid-frequency terms, one

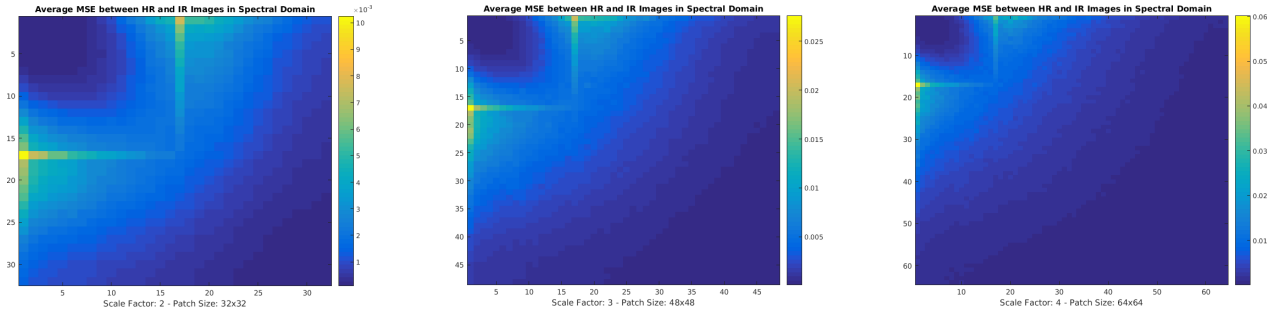

(a) 2× scaling (b) 3× scaling (c) 4× scaling

Figure 2: Mean squared error of DCT coefficients between bicubic interpolated patches and HR patches at three different scaling factors.

can deploy a single model that does can be utilized for a range of scaling factors.

C. Our super-resolution network

The primary purpose of our neural network architecture is learning a mapping from bicubic interpolated image patches to ground truth HR image patches. Additionally, we aim to make the model applicable for various scale factors. Hence, input and output dimensions shall be coherent for all scale factors. Towards meeting these goals, we observe that if the network is trained to map all DCT coefficients, as the number of coefficients varies depending on the number of inputs, the network will need to be trained for each scale factor separately. Therefore, we instead focus on specific frequency components that are available above all scaling factors larger than a minimum (2× in our case) factor.

To realize this approach, following our observations made in the previous section, we focus on the problem of mapping mid-frequency DCT coefficients of LR inputs to values closer to those of true HR patches. We select the target frequency components by finding the most problematic 512 frequency values, according to the mean square error analysis results. These frequency components naturally fall into the mid-frequencies band.

We illustrate our overall approach in Figure 3. The model first converts the input LR image into its DCT spectral representation. Then we take the selected frequency components and feed them to the neural network. Here, the binary mask shown in the figure corresponds to the 512 mid-frequency components that we truly use in our experiments. We replace these coefficients with those produced by the network and reconstruct the SR image through inverse DCT (IDCT).

In training our SR network, we use mean square error as our loss function. The error is measured between the coefficients produced by the SR network and those of the target HR patches. As our network architecture, we use a feed-forward fully connected neural network. Our choice of fully-connected layers instead of convolutional layers is motivated by the observation that local structure is repetitive and it is hard to apply the same mapping onto different regions in the spectral domain, unlike the spatial domain. In addition, the use of fully-connected layers allows us to choose arbitrary frequency components for processing, without requiring an image-like structure.

In the network architecture, we use a four-layered fully connected neural network with 512 neurons per layer. In total, the network contains 1050624 parameters. To prevent from overfitting, after every fully connected layer, we place a dropout layer [20]. Since discrete cosine transform typically yields numbers in the range from -1 to 1 (except the DC term), we use a hyperbolic tangent function as the activation function. We use Xavier initializer [21] for model initialization and use Adam optimizer [22] for optimization. We use a batch-size of 128 in training. Overall, we observe relatively little variance in training loss and validation performance scores with respect to changes made in architectural details and other hyper-parameters.

D. Artifact reduction in spatial domain

It is well known that manipulations on spectral image representations easily lead to apparent artifacts in the spatial domain. This is essentially due to the fact that manipulation of a single spectral coefficient corresponds to jointly manipulating all pixels, at varying wave-like degrees parameterized by a periodic function. Given that our SR algorithm corresponds to manipulation of only a subset of coefficients by design, we observe ringing artifacts on the SR output.

To reduce the resulting ringing artifacts, we apply an artifact reduction solution as a post-processing step. In our experiments, we use a pre-trained AR-CNN model [23], which uses an SRCNN-like convolutional neural network architecture. This network is trained to learn a mapping from JPEG compressed images to pre-compression images to learn to reduce compression artifacts. The model is trained using mean-square error, on a newly built dataset called *dataA*. We observe that even if the AR-CNN model is trained on a entirely different dataset, it leads to a significant artifact reduction on our SR image results. We show its effect through an example on Figure 4, where the intermediate steps (bicubic interpolation, spectral super-resolution and artifact reduction) of our complete single-image super-resolution approach can be seen. The corresponding improvements in PSNR scores can also be seen in this figure.

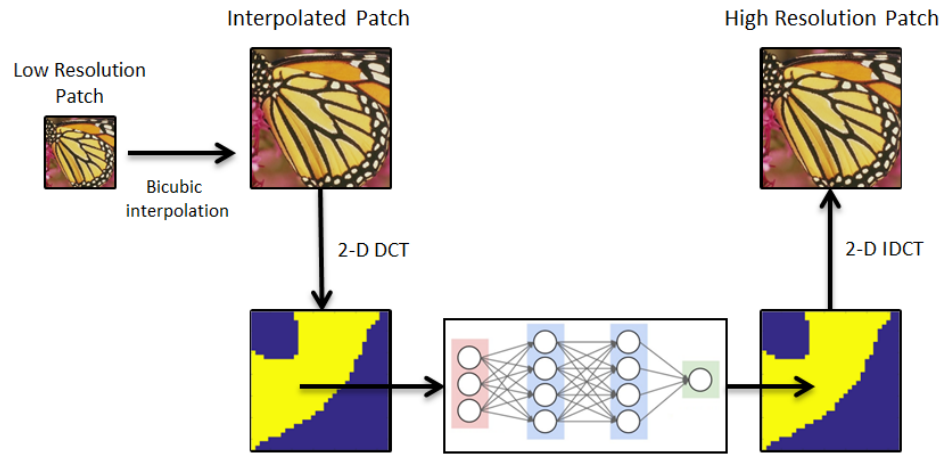

Figure 3: Our Spectral Super Resolution approach.

Algorithm 1 Spectral Super-Resolution

Input: Low-resolution input image (I_{LR}).
Input: Target HR scale (α).
Output: Predicted output image.
$I_{HR}^{Bicubic} \leftarrow$ BicubicInterpolation(I_{LR},α)
patches $\leftarrow$ SplitToPatches($I_{HR}^{Bicubic}$)
for index **in** 1 . . . Count(patches) **do**
    $S_{patch} \leftarrow$ DCT(patches[index])
    S_{patch}[FreqMask] $\leftarrow$ SRNetwork(S_{patch}[FreqMask])
    patches[index] $\leftarrow$ InverseDCT(S_{patch})
$I_{HR}^{SR} \leftarrow$ MergePatches(patches)
$I_{HR}^{PostProcessed} \leftarrow$ ARCNN(I_{HR}^{SR})
return $I_{HR}^{PostProcessed}$

We give the summary of complete super-resolution inference steps in Algorithm 1. The algorithm takes a low-resolution image and a scale factor which indicates how much the image should be resized. Initially, the input image is resized with bicubic interpolation to the given scale factor. Then, the resized image is divided into patches and each patch is processed separately. Here, each patch is first transformed into the frequency domain using discrete cosine transform, and problematic frequency regions are improved using our super-resolution network. Then, the improved patches are transformed back to the spatial domain and each patch is located back to their original place. In the post-processing step, the complete super-resolved image is given to the ARCNN model to reduce the artifacts resulting from spectral domain processing.

IV. Experiments

Our experimental setup and results with detailed analyses are given in this stage. In Section IV-A, experimental setup and implementation details are explained. In Section IV-B, we present our experimental results.

A. Experimental setup

In this section, we present (i) the details of train, validation and test datasets, (ii) the evaluation metrics and (iii) the model selection details.

Datasets. In the training phase, we use the widely used BSDS200, General100, and T91 datasets, which contain 200, 100 and 91 images, respectively. Following the common practice, e.g. [6], we use the combination of these three datasets and obtain 391 training images in total. For evaluation, we use four separate datasets: Set5 [24], Set14 [25], BSDS100 [26], and Urban100 [27]. These datasets contain 5, 14, 100 and 100 images, respectively. We use Set5 as our validation set for architecture and hyper-parameter selection and use the remaining three datasets for test evaluation.

Performance metrics. For quantitative evaluation of the SR results, we use the *Peak Signal-to-Noise Ratio* (PSNR) and *Structural Similarity Index* (SSIM) [28] evaluation metrics, following the common practice [7]. We note that while higher PSNR and SSIM values are desirable in theory, these metrics are not fully correlated with true perceptual quality [14]. Utilizing a better evaluation metric for the super-resolution problem remains as an open problem in SR.

Model selection. We use performance scores on the validation set for architecture and hyper-parameter tuning. To optimize over the hyper-parameter combinations, we use grid search over the learning rate and the number of neurons per layer. As the learning rate candidates, we use the set $\{10^{-4}, 10^{-5}, 10^{-6}\}$. As the number of neurons per layer (i.e.number of hidden units), we use the candidate set $\{256, 512, 1024\}$.

In our experiments, we have obtained very similar training curves across varying learning rates and varying number of neurons per layer. We have observed that while training speeds up for higher learning rates, the model converges to nearly the same training loss and validation performance values. Similarly, we have observed that while converge delays as

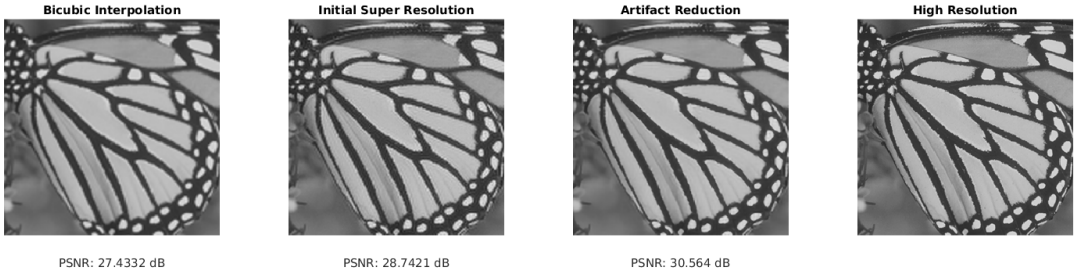

Figure 4: Intermediate Steps of Our Super Resolution System

Table I: Quantitative evaluation of state-of-the-art SR solutions (PSNR - SSIM score pairs).

Algorithm	Scale	Set5 [24]	Set14 [25]	BSDS100 [26]	Urban100 [27]
Bicubic	2	33.69 - 0.931	30.25 - 0.870	29.57 - 0.844	26.89 - 0.841
FNNSR [11]	2	35.20 - 0.943	31.40 - 0.895	30.58 - 0.877	-
Ours	2	**35.53 - 0.953**	**31.64 - 0.904**	**30.64 - 0.884**	**28.15 - 0.882**
RFL [3]	2	36.59 - 0.954	32.29 - 0.905	31.18 - 0.885	29.14 - 0.891
SelfExSR [27]	2	36.60 - 0.955	32.24 - 0.904	31.20 - 0.887	29.55 - 0.898
SRCNN [4]	2	36.72 - 0.955	32.51 - 0.908	31.38 - 0.889	29.53 - 0.896
FSRCNN [13]	2	37.05 - 0.956	32.66 - 0.909	31.53 - 0.892	29.88 - 0.902
VDSR [5]	2	37.53 - 0.959	33.05 - 0.913	31.90 - 0.896	30.77 - 0.914
LapSRN [6]	2	37.52 - 0.959	33.08 - 0.913	31.80 - 0.895	30.41 - 0.910
Bicubic	3	30.41 - 0.869	27.55 - 0.775	27.22 - 0.741	24.47 - 0.737
FNNSR [11]	3	31.42 - 0.883	28.32 - 0.802	27.79 - 0.772	-
Ours	3	**31.44 - 0.906**	**28.41 - 0.828**	**27.78 - 0.788**	**24.78 - 0.781**
RFL [3]	3	32.47 - 0.906	29.07 - 0.818	28.23 - 0.782	25.88 - 0.792
SelfExSR [27]	3	32.66 - 0.910	29.18 - 0.821	28.30 - 0.786	26.45 - 0.810
SRCNN [4]	3	32.78 - 0.909	29.32 - 0.823	28.42 - 0.788	26.25 - 0.801
FSRCNN [13]	3	33.18 - 0.914	29.37 - 0.824	28.53 - 0.791	26.43 - 0.808
VDSR [5]	3	33.67 - 0.921	29.78 - 0.832	28.83 - 0.799	27.14 - 0.829
LapSRN [6]	3	33.82 - 0.922	29.87 - 0.832	28.82 - 0.798	27.07 - 0.828
Bicubic	4	28.43 - 0.811	26.01 - 0.704	25.97 - 0.670	23.15 - 0.660
FNNSR [11]	4	29.35 - 0.827	26.62 - 0.727	26.42 - 0.696	-
Ours	4	**29.21 - 0.852**	**26.55 - 0.755**	**26.33 - 0.721**	**23.42 - 0.701**
RFL [3]	4	30.17 - 0.855	27.24 - 0.747	26.76 - 0.708	24.20 - 0.712
SelfExSR [27]	4	30.34 - 0.862	27.41 - 0.753	26.84 - 0.713	24.83 - 0.740
SRCNN [4]	4	30.50 - 0.863	27.52 - 0.753	26.91 - 0.712	24.53 - 0.725
FSRCNN [13]	4	30.72 - 0.866	27.61 - 0.755	26.98 - 0.715	24.62 - 0.728
VDSR [5]	4	31.35 - 0.883	28.02 - 0.768	27.29 - 0.726	25.18 - 0.754
LapSRN [6]	4	31.54 - 0.885	28.19 - 0.772	27.32 - 0.727	25.21 - 0.756

the number of trainable parameters gets larger, the model converges to nearly the same performance scores despite changes in the number of neurons hyper-parameter.

In the artifact reduction model (AR-CNN [23]) we use as a post-processing step, four different pre-trained models are available. Each model is trained over a different image set, constructed with different JPEG compression quality values ($Q \in \{10, 20, 30, 40\}$). We choose the best model for our post-SR processing purposes according to the PSNR values obtained on the validation set. The best PSNR value is obtained for $Q = 40$, which is the highest JPEG quality.

B. *Experimental results*

In this section, we present our main quantitative results with comparisons to contemporary deep SR approaches, analyze the effect of the artifact-reduction network in detail, give an ablative study and finally discuss our SR model through qualitative examples.

Main results. In Table I, we provide the PSNR and SSIM scores of our approach and a number of other SR approaches. The table consists of three sections, corresponding to respectively $2\times$, $3\times$ and $4\times$ scaling factors. The last four columns correspond to the performance scores obtained on the Set-5, Set-14, BSDS100, and, Urban100 datasets. For each method and each dataset value, we present the corresponding pair of PSNR - SSIM scores.

In the results shown in Table I, we observe that bicubic interpolation, which is the most basic method shown in the table and is also the first step of our SR approach, obtains the lower PSNR and SSIM results, as expected. The results of the bicubic interpolation can be seen as the baseline performance for all SR methods. We observe that our approach obtains significant improvements in PSNR and SSIM scores compared to the bicubic interpolation baseline. However, we also observe that our approach obtains relatively lower scores, especially in terms of the PSNR scores, compared to other methods, especially the spatial-domain SR techniques. This is not surprising to consider that most spatial domain SR methods directly aim to minimize the reconstruction loss, which in fact corresponds to optimizing the PSNR score. In fact, we observe that our method obtains much more competitive scores

in terms of the SSIM metric.

To improve our understanding of the DCT spectral representation for SR purposes, we repeat the identical mean square analysis in frequency domain which we made in Section III now using the SR method outputs. In the Figure 5a, 5b, 5c and 5d, we present the mean squared error analysis results for bicubic interpolation, our model, SRCNN and LapSRN, respectively. First of all, as previously discussed, we observe again that bicubic interpolation is most problematic for mid-frequency terms. While we observe significant error reductions made by the SRCNN and LapSRN models in the region between low and middle frequencies, we still observe rather large errors on the mid-frequency components. We also observe that our model is capable to correct the target problematic region coefficients considerably. However, we observe that the error reduction is not perfect, as there are still errors in relatively lower frequencies of the targeted region. Overall, we observe that for all SR methods in consideration, middle frequency DCT terms remain to be the most problematic region.

Analysis of artifact reduction. One important question that needs to be answered is the role of artifact reduction network on the SR performance scores we obtain. Therefore, in order to measure the significance of artifact reduction module, we evaluate its effect using different module combinations: using (i) only bicubic interpolation, (ii) bicubic interpolation followed by artifact reduction, and, (iii) bicubic interpolation followed by super-resolution and artifact reduction. For these three experiments, we obtain 33.69 dB, 33.82 dB and 35.53 dB PSNR scores on the Set5 dataset, respectively. These results show that even if artifact reduction solution is a deep image enhancement architecture, utilizing AR network alone improves the bicubic interpolation result by only 0.13 dB, which is far smaller than the improvement obtained by our complete approach. This result shows that the artifact reduction itself is not suitable for replacing the SR network.

Ablative study. In Table II, we present a detailed analysis on our design choices, particularly on applying artifact reduction as a post-processing step and operating only on a subset of DCT components. More specifically, the table shows results for the scaling factors $2\times$, $3\times$ and $4\times$, each one corresponding to one section. For each scaling factor, we present the PSNR and SSIM scores on three different datasets, for bicubic interpolation, our super-resolution model only, our super-resolution approach with artifact reduction and our super-resolution model operating at all 1024 DCT components.

From these results, we first see that, SR-only approach (without artifact reduction) yields significant improvements over the bicubic interpolation, consistently across the scaling factors and across the test datasets. We also see that artifact reduction provides valuable improvements over the SR model outputs. Finally, we observe that using all frequencies in super-resolution mapping yields results even below bicubic interpolation images. While the difficulty of training over all frequencies is a factor here, we have observed that poor prediction of the offset value plays a dominant role in poor performance in this case. Overall, these results confirm the design choices that we have made in our approach.

Qualitative results. In this section, we qualitatively evaluate our approach with comparisons to reference spatial-domain SR methods and ground truth HR images. For simplicity, we focus on the $3\times$ scaling factor and images from the Set14 dataset.

The sample images are shown in Figure 6. Each row shows the images obtained using SRCNN, LapSRN and our method, followed by the ground truth image. We observe that our method shows better results in capturing certain patterns in comparison to SRCNN and LapSRN, while yielding less sharp edges, as expected. For instance, in the second image, we can see that pattern on the tablecloth is reconstructed at better fidelity compared to the spatial domain methods. However, especially in the third example, it can be seen that our method tends to yield slightly more blurry images, as a result of focusing on improving mid-frequency DCT terms.

V. Conclusions

In this work, we have explored the use of spectral representations for developing a complete single-image super-resolution model. Our SR system involves of two main stages. In the first stage, we learn a super-resolution mapping from LR images to HR images entirely in the spectral domain, using DCT representation of the images. Here, we use the bicubic interpolation to initiate the output image and choose the subset of most problematic DCT frequency components at train time. Our second stage aims to remove ringing artifacts caused by spectral transformations used in the first phase, using an artifact reduction network.

Overall, our results show that, while deep SR methods formulated in the spatial domain yields better PSNR scores, there are cases where applying super-resolution in the spectral domain is advantageous, especially at reconstructing patterns. We also observe that there are specific DCT components for which the mainstream SR models yield highly erroneous estimates. These observations suggest that despite challenges of formulating super-resolution purely in the spectral domain, this line of research is promising in many aspects, and can be a way to enhance and improve, especially through developing hybrid models that jointly model the spectral and spatial domain. Additionally, towards obtaining better results, spectral super-resolution methods can potentially be enhanced through more sophisticated network designs and introducing adversarial training strategies.

References

[1] R. Timofte, V. De Smet, and L. Van Gool, "A+: Adjusted anchored neighborhood regression for fast super-resolution," in *Asian Conference on Computer Vision*. Springer, 2014, pp. 111–126.

[2] J. Yang, J. Wright, T. S. Huang, and Y. Ma, "Image super-resolution via sparse representation," *IEEE International Conference on Image Processing*, vol. 19, no. 11, pp. 2861–2873, 2010.

[3] S. Schulter, C. Leistner, and H. Bischof, "Fast and accurate image upscaling with super-resolution forests," in *IEEE Conference on Computer Vision and Pattern Recognition*, 2015, pp. 3791–3799.

[4] C. Dong, C. C. Loy, K. He, and X. Tang, "Image super-resolution using deep convolutional networks," *IEEE Transactions on Pattern Analysis and Machine Intelligence*, vol. 38, no. 2, pp. 295–307, 2016.

[5] J. Kim, J. Kwon Lee, and K. Mu Lee, "Accurate image super-resolution using very deep convolutional networks," in *IEEE Conference on Computer Vision and Pattern Recognition*, 2016, pp. 1646–1654.

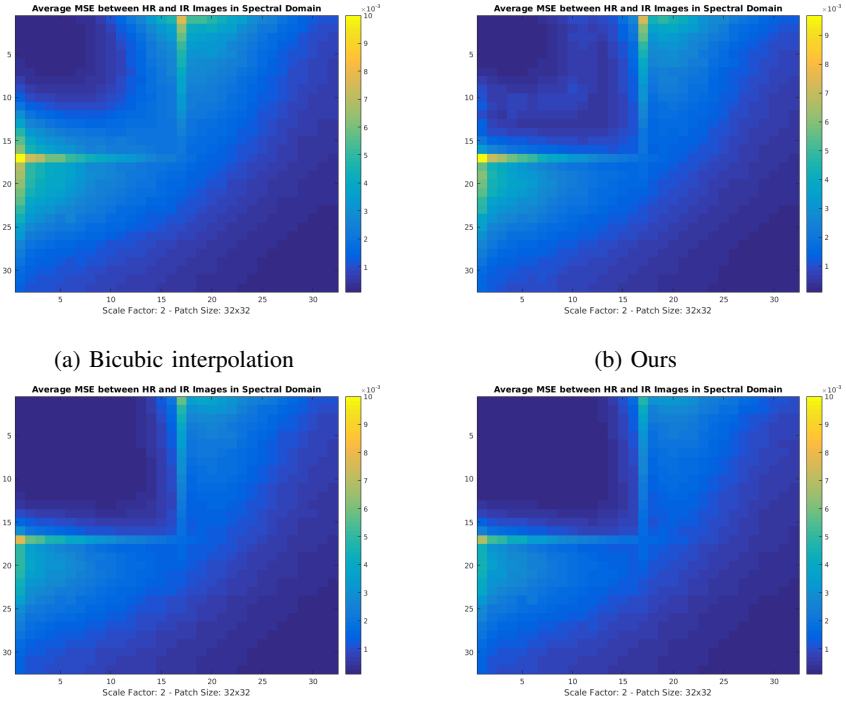

(a) Bicubic interpolation (b) Ours

(c) SRCNN (d) LapSRN

Figure 5: Mean squared error of DCT coefficients between bicubic interpolated and HR patches at the scaling factor of $2\times$.

Table II: Quantitative evaluation for analyzing the effect of artifact reduction and operating on a subset of DCT components. PSNR-SSIM score pairs are shown.

Setup	Scale	Set5 [24]		Set14 [25]		BSDS100 [26]	
Bicubic	2	33.69	0.931	30.25	0.870	29.57	0.844
SR	2	34.72	0.941	31.15	0.903	30.37	0.889
SR+AR	2	35.53	0.953	31.64	0.904	30.64	0.884
SR - all frequencies	2	27.68	0.893	25.98	0.865	24.98	0.862
Bicubic	3	30.41	0.869	27.55	0.775	27.22	0.741
SR	3	31.08	0.901	28.17	0.826	27.66	0.801
SR+AR	3	31.44	0.906	28.41	0.828	27.78	0.788
SR - all frequencies	3	24.37	0.889	21.46	0.755	21.65	0.735
Bicubic	4	28.43	0.811	26.01	0.704	25.97	0.670
SR	4	28.93	0.846	26.39	0.753	26.19	0.719
SR+AR	4	29.21	0.852	26.55	0.755	26.33	0.721
SR - all frequencies	4	22.13	0.835	21.32	0.708	20.88	0.658

[6] W.-S. Lai, J.-B. Huang, N. Ahuja, and M.-H. Yang, "Deep laplacian pyramid networks for fast and accurate super-resolution," *arXiv preprint arXiv:1704.03915*, 2017.

[7] S. Anwar, S. Khan, and N. Barnes, "A deep journey into super-resolution: A survey," *arXiv preprint arXiv:1904.07523*, 2019.

[8] O. Rippel, J. Snoek, and R. P. Adams, "Spectral representations for convolutional neural networks," in *Advances in Neural Information Processing Systems*, 2015, pp. 2449–2457.

[9] Y. Wang, C. Xu, S. You, D. Tao, and C. Xu, "Cnnpack: Packing convolutional neural networks in the frequency domain," in *Advances in Neural Information Processing Systems*, 2016, pp. 253–261.

[10] N. Kumar, R. Verma, and A. Sethi, "Convolutional neural networks for wavelet domain super resolution," *Pattern Recognition Letters*, vol. 90, pp. 65–71, 2017.

[11] J. Li, S. You, and A. Robles-Kelly, "A frequency domain neural network for fast image super-resolution," in *International Joint Conference on Neural Networks*. IEEE, 2018, pp. 1–8.

[12] S. Xue, W. Qiu, F. Liu, and X. Jin, "Faster image super-resolution by improved frequency-domain neural networks," *Signal, Image and Video Processing*, pp. 1–9, 2019.

[13] C. Dong, C. C. Loy, and X. Tang, "Accelerating the super-resolution convolutional neural network," in *European Conference on Computer Vision*. Springer, 2016, pp. 391–407.

[14] C. Ledig, L. Theis, F. Huszár, J. Caballero, A. Cunningham, A. Acosta, A. Aitken, A. Tejani, J. Totz, Z. Wang *et al.*, "Photo-realistic single image super-resolution using a generative adversarial network," *arXiv preprint arXiv:1609.04802*, 2016.

[15] T. Dai, J. Cai, Y. Zhang, S.-T. Xia, and L. Zhang, "Second-order attention network for single image super-resolution," in *IEEE Conference on Computer Vision and Pattern Recognition*, 2019, pp. 11 065–11 074.

[16] Y. Wang, F. Perazzi, B. McWilliams, A. Sorkine-Hornung, O. Sorkine-Hornung, and C. Schroers, "A fully progressive approach to single-image super-resolution," in *IEEE Conference on Computer Vision and Pattern Recognition*, 2018, pp. 864–873.

[17] A. V. Oppenheim, *Discrete-time signal processing*. Pearson Education India, 1999.

[18] K. R. Rao and P. Yip, *Discrete cosine transform: algorithms, advantages, applications*. Academic press, 2014.

[19] R. Clarke, "Relation between the karhunen loeve and cosine transforms," in *IEE Proceedings F (Communications, Radar and Signal Processing)*, vol. 128, no. 6. IET, 1981, pp. 359–360.

[20] N. Srivastava, G. E. Hinton, A. Krizhevsky, I. Sutskever, and R. Salakhutdinov, "Dropout: a simple way to prevent neural networks from overfitting." *Journal of Machine Learning Research*, vol. 15, no. 1,

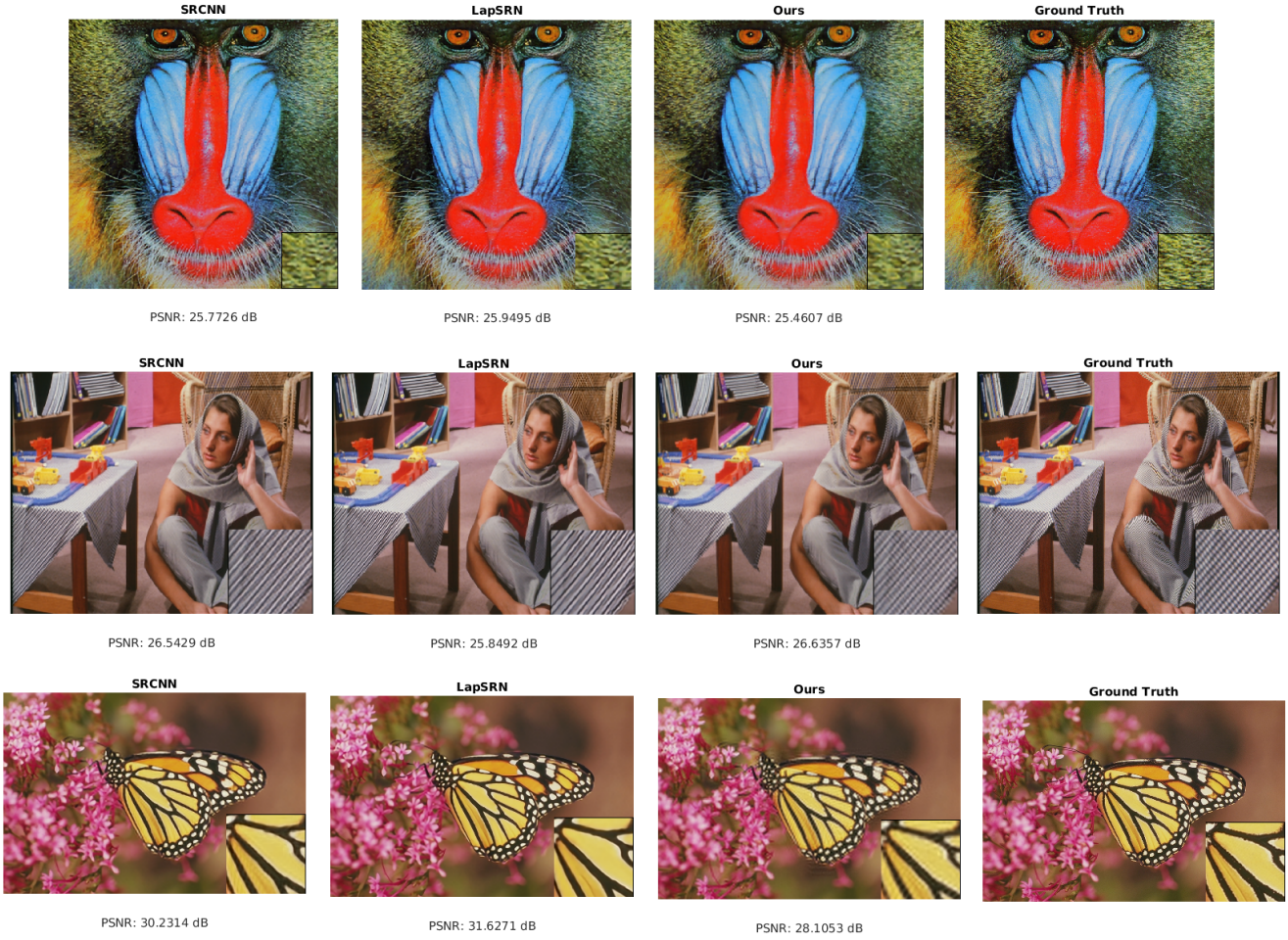

Figure 6: Example super-resolution results obtained using the SRCNN, LapSRN, our method with comparison to the ground truth high-resolution images. The images are taken from the Set14 dataset. The shown super-resolution results correspond to $3\times$ scaling factor.

pp. 1929–1958, 2014.

[21] X. Glorot and Y. Bengio, "Understanding the difficulty of training deep feedforward neural networks," in *International Conference on Artificial Intelligence and Statistics*, 2010, pp. 249–256.

[22] D. Kingma and J. Ba, "Adam: A method for stochastic optimization," *arXiv preprint arXiv:1412.6980*, 2014.

[23] C. Dong, Y. Deng, C. Change Loy, and X. Tang, "Compression artifacts reduction by a deep convolutional network," in *IEEE International Conference on Computer Vision*, 2015, pp. 576–584.

[24] M. Bevilacqua, A. Roumy, C. Guillemot, and M. L. Alberi-Morel, "Low-complexity single-image super-resolution based on nonnegative neighbor embedding," 2012.

[25] W. Shi, J. Caballero, F. Huszár, J. Totz, A. P. Aitken, R. Bishop, D. Rueckert, and Z. Wang, "Real-time single image and video super-resolution using an efficient sub-pixel convolutional neural network," in *IEEE Conference on Computer Vision and Pattern Recognition*, 2016, pp. 1874–1883.

[26] P. Arbelaez, M. Maire, C. Fowlkes, and J. Malik, "Contour detection and hierarchical image segmentation," *IEEE Transactions on Pattern Analysis and Machine Intelligence*, vol. 33, no. 5, pp. 898–916, 2010.

[27] J.-B. Huang, A. Singh, and N. Ahuja, "Single image super-resolution from transformed self-exemplars," in *IEEE Conference on Computer Vision and Pattern Recognition*, 2015, pp. 5197–5206.

[28] Zhou Wang, A. C. Bovik, H. R. Sheikh, and E. P. Simoncelli, "Image quality assessment: from error visibility to structural similarity," *IEEE Transactions on Image Processing*, vol. 13, no. 4, pp. 600–612, April 2004.

Onur Aydin Onur Aydn received the B.S. degree in Electrical and Electronics Engineering from Bilkent University, Turkey in 2014 and the M.S. degree in Computer Engineering from Bilkent University, Turkey in 2018. His research interests include machine learning and computer vision, with special interest in image enhancement and learning with weak supervision.

Ramazan Gokberk Cinbis graduated from Bilkent University, Turkey, in 2008, and received an M.A. degree from Boston University, USA, in 2010. He was a doctoral student at INRIA Grenoble, France, between 2010-2014, and received a PhD degree from Université de Grenoble, France, in 2014. He is currently an Assistant Professor at METU, Ankara, Turkey. His research interests include machine learning and computer vision, with special interest in deep learning with incomplete weak supervision.

Comparative Design of Permanent Magnet Synchronous Motors for Low-Power Industrial Applications

H. YETIS, T. GOKTAS

***Abstract*— Permanent magnet synchronous motors (PMSMs) have superior features such as less volume and weight, long-life, high performance compared to induction motors. In this study, a comparative design of PMSMs is provided by considering a 2.2 kW induction motor nameplate parameters which is commonly used in industrial applications. A parametric analysis is used in order to design stator slot and magnet geometries of Surface-Mounted Permanent Magnet Synchronous (SPM) and Interior Permanent Magnet (IPM) Motors to get the high efficiency, low torque ripple. Ansys@Maxwell-2D software using time stepping finite element method is utilized to verify the advantages of designed motors compare to induction motors. In addition, material consumptions of both PMSMs and induction motor are compared to show the effectiveness of proposed motors in mechanically. It is shown that designed SPM and IPM motors have higher efficiency, lower torque ripple and volume than that of induction motors.**

Index Terms—**Interior permanent magnet synchronous (IPM) motor, motor design, parametric analysis, permanent magnet synchronous motors (PMSMs), surface-mounted synchronous (SPM) motor**

I. INTRODUCTION

THE IDEA of obtaining the required flux from magnets to produce the necessary torque in electrical machines is based on the 20th century [1-3]. The historical development of these motors is directly related to the advances in the technology of high-density permanent-magnet materials with sufficient remanent flux density and coercivity [4]. The high performance PMSMs which have a higher torque/power ratio can be designed using highly energy intensive magnets such as Neodymium-Iron-Boron (NdFeB) and Samarium-Cobalt (SmCo) magnets [5].

The permanent magnet synchronous motors (PMSMs) have superior features compared to induction motors such as high efficiency, less mechanical noise, direct drive, high performance even at low speeds, long-life time and less volume [6-10].

The rotor has permanent magnets (PMs) to produce the required torque as well as flux instead of excitation windings in PMSMs; thus the efficiency do increase due to elimination of copper losses and the operation and maintain costs reduces in PMSMs. That's why they are highly preferred in industrial applications [11-12].

The permanent magnet synchronous motors (PMSMs) are classified as two groups such as surface-mounted synchronous (SPM) motors and interior magnet synchronous (IPM) motors based on magnet positions on the rotor [13-14]. It is known that locating the magnets on the rotor surface provide simplicity in surface-mounted motors while IPM motors are mechanically more robust since its magnets are embedded into rotor. SPM motors are very popular in industrial applications due to their stator inductances independent of rotor position, simplicity of control and construction [15]. IPM motors offer a wide constant power speed range and can be overloaded at low and high speed than SPM motors [16].

Besides its superior advantages, a common drawback of the PMSMs is torque ripple [17-18]. There are several reasons such as harmonics in the back EMF; magnetic saturation, and controller effects which cause ripple on the torque in both PMSMs. [19]. In a SPM motor, cogging torque which is caused by the interaction between the magnets on the rotor surface and the steel teethes on the stator also contributes torque ripple. [6,20]. In IPM motor, torque ripple is generated as undesirable by product of the interaction between rotor and stator MMF waveform and the variation of magnetic reluctance between the flux barriers and slot teethes [21-23]. In the design process; slot / pole combination, stator slotting, magnet geometry and rotor structure should be designed carefully to decrease torque ripple.

The objective of this paper is to present PMSMs advantages compared to induction motor for low-power industrial applications. A sensitive design process is carried out to high efficiency and low torque ripple ratio PMSMs.

For this purpose, both IPM and SPM motors are comparatively designed using ANSYS@Maxwell-2D software. The 2.2 kW induction motor is selected as reference motor [24]. The parameters of the reference induction motor and proposed PMSMs are given in Table A. In order to design the optimal PMSMs, the parametric analysis is carried out through the RMxprt@Maxwell software. The designed

HICRET YETIS is with Department Electrical and Electronics Engineering University of Inonu University, Malatya, Turkey, (e-mail: hicretyetis@gmail.com).

https://orcid.org/0000-0002-3173-5611

TANER GOKTAS, is with Department Electrical and Electronics Engineering University of Inonu University, Malatya, Turkey, (e-mail: taner.goktas@inonu.edu.tr).

https://orcid.org/0000-0002-8218-3239

Manuscript received April 30, 2020; accepted June 17, 2020.
DOI: 10.17694/bajece.729751

PMSMs are analyzed in terms of torque ripple, efficiency, flux distribution, phase current and material consumption compared using Maxwell-2D transient solver. The transient finite element analysis (FEA) results show that two PMSMs designs have less volume, higher efficiency and lower torque ripple compared to reference induction motor.

II. DESIGN PROCESS OF PERMANENT MAGNET SYNCHRONOUS MOTORS

The output torque in PMSMs strongly depends on the remanent flux density of magnet. The *d-q* equivalent circuit model is widely used since it simplifies the calculation of complex equations [25]. The electromagnetic torque (T_{em}) produced by PMSMs according to the d-q equivalent circuit model calculated as:

$$T_{em} = \frac{3}{2} p_p \left[\psi_{pm} i_q + (L_d - L_q) i_d i_q \right] \quad (1)$$

where P_p is the number of pole pairs, ψ_{pm} is the permanent magnet flux linkage. The i_d, i_q, L_d and L_q represent stator *d-q* axis currents and inductances, respectively. The terms ($\psi_{pm} i_q$) and (L_d-L_q)$i_d i_q$ in Eq. (1) are related to magnet torque and reluctance torque, respectively. The L_d and L_q inductances are independent from the rotor position and they are approximately equal to each other in SPM motors, - *but not IPM motors*.

Based on Eq. (1), the produced electromagnetic torque in SPM motors ($T_{em\text{-}SPM}$) can be modified as in Eq. (2) since L_d and L_q are equal each other, thus eliminates the second term in Eq. (1) as follows:

$$T_{em_{SPM}} = \frac{3}{2} p_p \left[\psi_{pm} i_q \right] \quad (2)$$

As seen from the Eq. (2), L_d and L_q inductances do not directly affect the torque generation in SPM motors On the contrary to SPM motors, the IPM motors can operate at high speeds due to embedding rotor magnets and have reluctance torque since L_d and L_q inductances are different from each other due to positions of magnet as shown in Fig. 1. The existence of reluctance torque in IPM motors provides high torque/power ratio at variable speed applications and it is possible to use low-cost permanent magnets which has lower magnetic energy density due to reluctance torque component [15]. It is clear that the electromagnetic torques includes the reluctance torque component as in Eq. (1) compared to that of SPM motors.

As a result, it should be considered that some electrical and mechanical parameters such as slot/pole combination, winding distribution, magnetic saturation, stator slot structure, magnet shape and dimensions to design high performance PMSMs.

A. Design Parameters

Electrical and mechanical parameters such as power, torque, speed, armature current density, rotor and stator material type, stator and rotor dimensions, etc. are taken into account in order to design both SPM and IPM motors. It is well known that the output power is proportional to stator and rotor outer diameter in any motor. The outer diameter of stator and rotor and stack length in PMSMs can be lower than that of IMs since they have their own excitation due to permanent magnets. That's why, stator and rotor outer diameters in PMSMs are selected as 122 *mm* and 63 *mm*, respectively to get the required output power. Since the reluctance torque component contributes positively to the output torque, the stack length value of the IPM motor can be chosen smaller compared to SPM motor. Thus, the stack lengths are selected as 65 *mm* and 58 *mm* for SPM and IPM motors, respectively. In both designs, *NdFe35* magnets which have high energy density have been used. The Air gap value is selected as smaller as possible mechanically such as 0.5 *mm* to minimize the leakage flux distribution in the air-gap.

TABLE I
PARAMETERS OF DESIGNED MOTORS

Parameter	*Unit*	SPM	IPM
Stator and rotor core material		1008	
Armature current density	A/mm^2	5.7	
Slot number		39	33
Pole number		28	10
Stator outer diameter	*mm*	122	
Rotor outer diameter	*mm*	63	
Rotor inner diameter	*mm*	26	
Air gap	*mm*	0.5	
Stator and rotor skew angle	*degree°*	0	
Stack length	*mm*	65	58

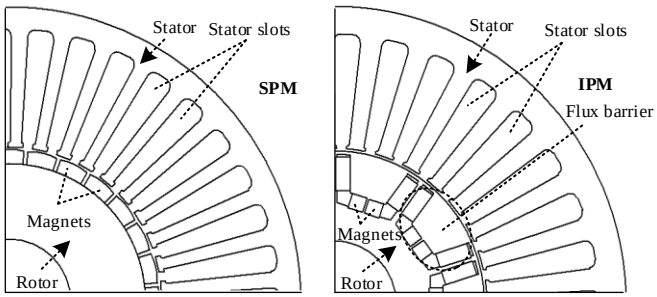

(a) (b)

Fig.1. Main geometry of designed motors; (a) SPM, (b) IPM

Each magnet forms a pole in SPM motor while each flux barrier forms a pole in IPM motor. Since the area on the inner surface of the IPM rotor is limited, the number of poles cannot be selected as high as in the SPM motor. In addition, number of slot in PM motors should be determined according to number of pole depending on the motor type because the slot/pole ratio can affect the dynamic motor performance as well. Based on the possible pole/slot combinations [26], the number of slot and poles are selected as 39 slot / 28 pole for SPM motor and 33 slot / 10 pole for IPM motor. The coil pitch is 1 and 3 for SPM and IPM motor, respectively since it is dependent on slot/pole ratio of the designed motors. The designed motor parameters by considering electrical parameters of reference induction motor (see Appendix- Table A) are summarized at Table I.

TABLE II
THE LIMITS OF INPUT PARAMETERS AND STEP SIZE

	Unit	Ranges	Increment
Slot length (Hs2)	*mm*	15 < Hs2 < 25	Δ_{Hs2} = 0.25
Slot width-1 (Bs1)	*mm*	2.75 < Bs1 < 5	Δ_{Bs1} = 0.1
Slot width-2 (Bs2)	*mm*	3 < Bs2 < 8	Δ_{Bs2} = 0.1
Slot opening (Bs0)	*mm*	1.25 < Bs0 < 2.75	Δ_{Bs0} = 0.1
Magnet Geometry of SPM	**Unit**	**Ranges**	**Increment**
Magnet thickness (Mt)	*mm*	1.5 < Mt <5	Δ_{Mt} = 0.25
Magnet width (emb)	-	0.4 < emb <0.95	Δ_{emb} = 0.02
Magnet Geometry of IPM	**Unit**	**Ranges**	**Increment**
Magnet thickness (Mt)	*mm*	1 < Mt < 3	Δ_{B1} = 0.1
Magnet width (Mw)	*mm*	13 < Mw < 22	Δ_{Mw} = 0.1

B. *Parametric Analysis*

Parametric analysis is an approach of the influence of different geometric and physical parameters on the system performance. The effect of each input parameter on the output values is examined by changing parameters in a certain number of step. The input parameters are modified to provide the most optimal output values such as efficiency, torque and flux density in motors. In order to carry out parametric analysis, the *RMxprt* @ ANSYS software is used for both PMSMs design process. The selected input parameters for parametric analysis are slot length, slot width, slot opening, magnet thickness and magnet width since they significantly affect the motor performance in PMSMs [27-28]. The output parameters are motor efficiency and stator flux density and cogging torque to design the motor more efficiently. It should be noted that there is no cogging torque in IPM motor.

Table II shows that the limits of input parameters and incremental step size for each parameters in parametric analysis. The incremental step size of each analysis is well enough to get the optimal results. The dimensions of the stator slots are modified as to limit the current density J= 5.7 A/mm^2 and maximum flux density B_{max}= 1.8 *Tesla* in order to avoid magnetic saturation by considering B-H curve of used materials. Fig. 4. shows the parametric analysis results for PMSMs.

As can see from the Fig. 4 (Stator length (Hs2) parameter), when the slot length (Hs2) increases the efficiency raises at a certain point. In IPM motor, efficiency parameter is getting decreased after Hs2=22.5 *mm* so Hs2 value should be carefully selected considered as slot topology. Slot length (Hs2) also affects the stator flux density. As seen, when the slot length increases, stator flux density is getting lower for both SPM and IPM motors. It is clearly seen that slot length (Hs2) has no more effect on the cogging torque in SPM motor.

Slot width (Bs1) can affect the motor dynamic performance as well. As can be seen from the Fig.4 (Slot width-1 (Bs1) parameter), the efficiency gets lower values if the slot with increases whereas flux density raises depending on increasing Bs1 values. Cogging torque gets minimized while slot width-1 increases.

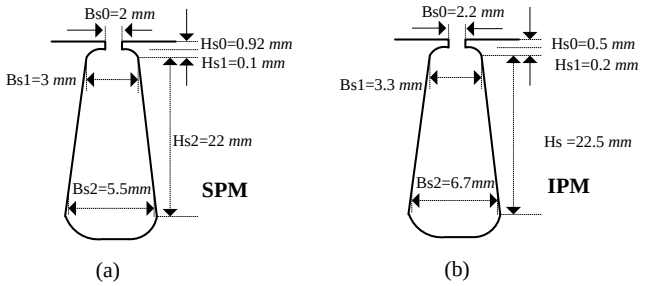

Fig.2 Slot geometries of a) SPM motor b) IPM motor

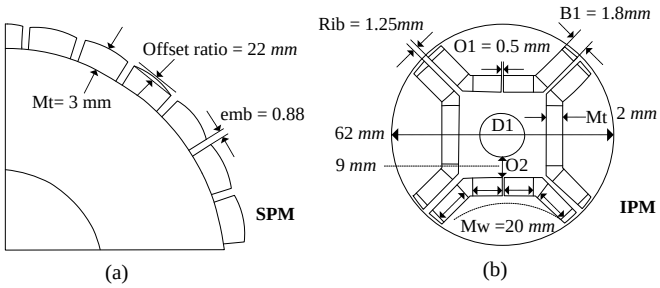

Fig.3 Magnet geometries of a) SPM motor b) IPM motor

Based on the parametric analysis results, slot width-2 (Bs2) strongly affect the stator flux density, -but not efficiency as seen Fig. 4 (Slot width-2 (Bs2) parameter). It is also seen that cogging torque in SPM motors decreases with the increasing slot width-2 (Bs2) values.

The parameter of slot opening (Bs0) has no significantly effect on efficiency and stator flux density in both PM motors as seen from the Fig.4 (Slot opening (Bs0) parameter). The cogging torque values change depending on different slot opening (Bs0) parameters.

Based on the parametric results, in order to limit B_{max}=1.8 *Tesla* to avoid the magnetic saturation, the parameters Hs2, Bs1 and Bs2 are selected as 22 *mm*, 3 *mm*, 5.5 *mm* for SPM motor and 22.5 *mm*, 3.3 *mm*, and 6.7 for IPM motor, respectively. Other slot geometry parameters are also selected through the parametric analysis results to get the optimum values of each specified motor performance parameters as seen From the Fig. 2.

Fig. 3. shows the magnet geometries for both PMSMs. The single flux barrier layered U-shape rotor type is selected as to get the high torque/power ratio for IPM motor. As seen from the figure, magnet thickness, embrace ratio, and shape of magnets are taken into account to design the rotor. It is clearly seen from the Fig.4 (Magnet thickness (Mt) parameter) that if the magnet thickness (Mt) increase, the efficiency and flux density raise up since flux density is proportional to magnet volume as known. The cogging torque is almost the same with the increasing magnet thickness values in SPM motor.

Magnet width (ebm for SPM and Mw for IPM) has also affect the motor performance. As seen from the Fig. 4. (Magnet width (ebm&Mw) parameter), if the magnet width (ebm&Mw) increase then the efficiency and stator flux density

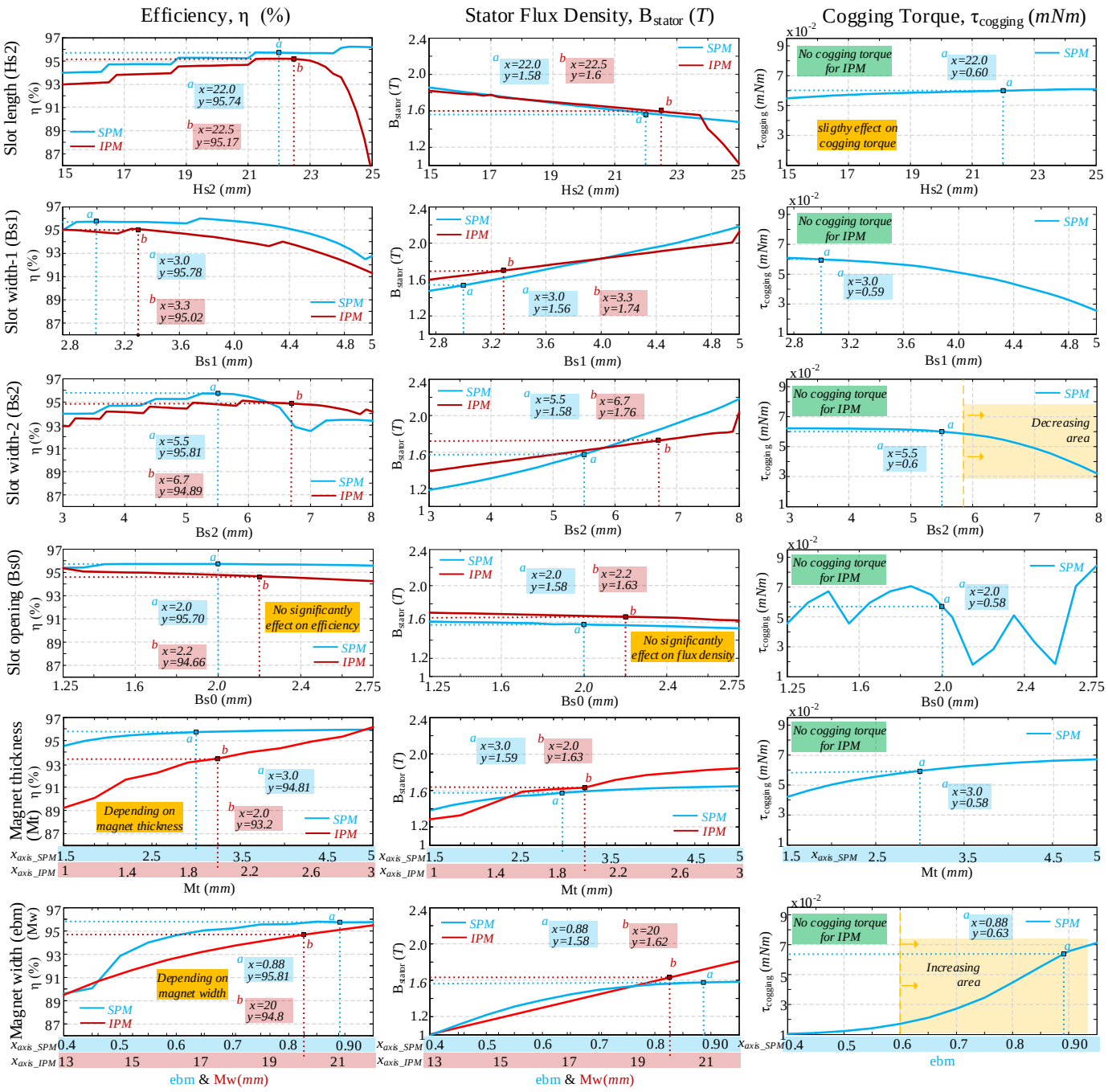

Fig. 4 Parametric analysis results of SPM (blue-solid line) and IPM (red-solid line) motor

raises depending on magnet width values. However, cogging torque is dramatically increases with the increase magnet width values.

In order to select the optimal values of these parameters, it should be considered that maximum flux density is lower than specified value 1.8 *Tesla*. The parameters Mt and ebm are selected as 3 *mm* and 0.88 for SPM motor. In IPM motor Mt and Mw are selected as 2 *mm*, 20 *mm*.

Based on the parametric analysis results, it has seen that all stator slot and rotor magnet geometries is chosen in order to limit the stator flux density at B_{max}= 1.8 *Tesla* for both two motors. It has been concluded that some of rotor parameters such as magnet thickness (Mt) and magnet width (ebm&Mw) has more impact on motor efficiency and flux density while some stator slot parameters such as slot width-2(Bs2) and slot width-1 (Bs1) affect flux density in SPM and IPM motors.

III. ANALYSIS RESULTS

In order to see the performance of designed motors compared to reference induction motor, both PM motors and induction motor have been analyzed through the ANSYS@ Maxwell software in transient time step. The time step is 0.7 *msec* to get the accurate results in simulations. Both PM motors and reference IM are driven in the same pure 3-phase sinusoidal voltage ($V_{applied}$=380 V) and loaded at the same

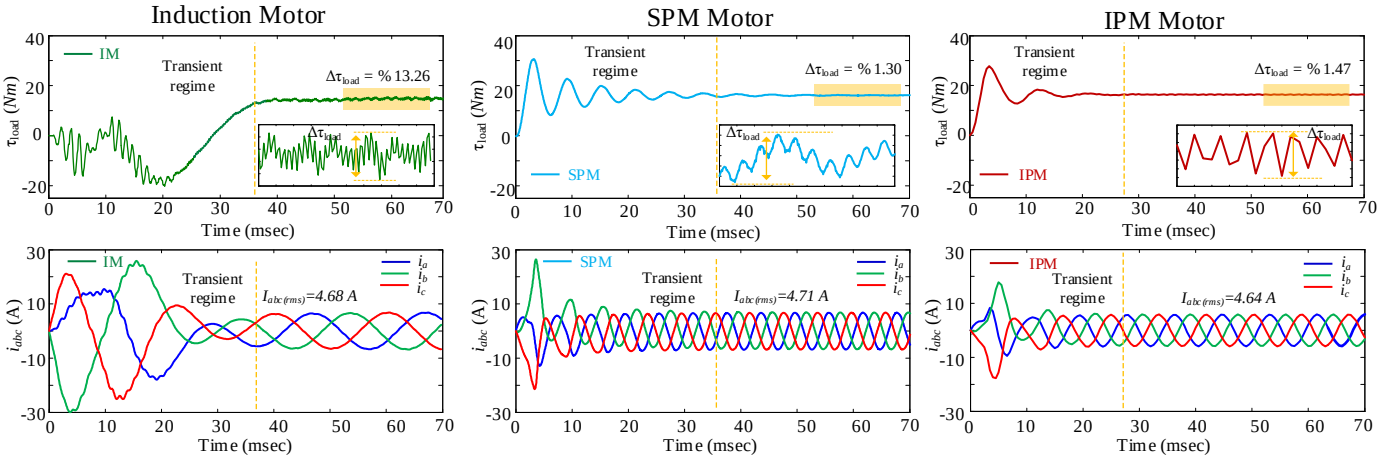

Fig. 5. Torque and Phase currents of a) Induction motor b) SPM motor c) IPM motor

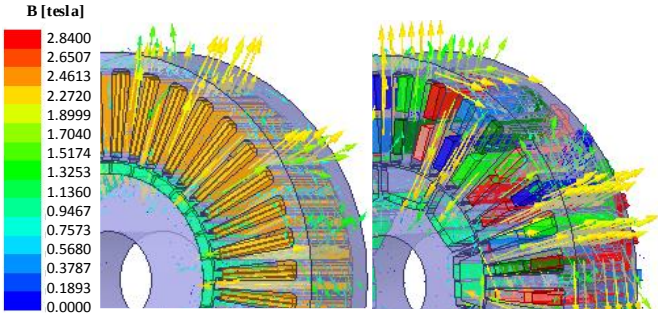

Fig. 6. The 3D view and flux vectors of a) SPM b) IPM motor

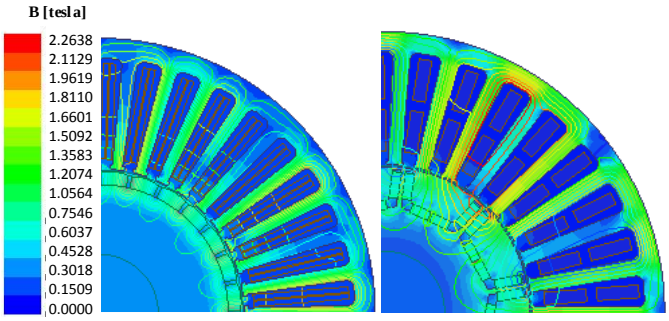

Fig. 7. Magnetic flux density of a) SPM b) IPM motor

TABLE III
PARAMETERS OF MOTORS

Parameters	*Unit*	Induction motor	SPM motor	IPM motor
Efficiency	%	88.97	95.71	94.51
Torque ripple	%	13.26	1.30	1.47
Stator outer diameter	*mm*	145	122	122
Stack length	*mm*	110	65	58

TABLE IV
METARIAL CONSUMPTION OF MOTORS

Mass	*Unit*	Induction Motor	SPM motor	IPM motor
Stator core	*kg*	6.1476	2.2359	2.081
Rotor core	*kg*	3.0647	1.0133	0.929
Stator winding	*kg*	2.3262	1.4367	1.444
Rotor bar	*kg*	0.6759	-	-
Rotor magnet	*kg*	-	0.2319	0.1716
Total	*kg*	12.211	4.9179	4.627

torque and output power to compare the dynamic performance of all motors. The torque and torque ripple, stator phase currents, efficiency and material consumption are examined for all motors to see the advantages of PM motors compare than reference induction motor.

Fig. 6 shows that 3D view of designed SPM and IPM motor. It can be seen that flux vectors in PM motors are well oriented along with the rotor poles. It is clear that designed SPM and IPM motors have lower volume and size compared than induction motor since the have their own excitation in the rotor. The stator outer diameter and stack length of PM motors are lower than that of induction motor as seen from Table III. Flux density and flux vector of designed motors are shown in Fig. 7. As can be seen from the figure that there is no magnetic saturation in designed PM motors (see Appendix- Fig. a B-H curve of used material).

Fig. 5 shows that torque and phase currents of SPM, IPM and IM motors to see the effectiveness of PM motors. As seen from the Fig.5 that the torque ripple of PM motors are lower than reference induction motor at the same loaded conditions. The phase currents approximately have the same RMS values for all motor which results to limit current density at specified value (J= 5.7 *A/mm*^{2}). If the efficiency is analyzed for all motors, it is clearly seen from the Table III. that efficiency has increased by almost 5% compared to that of IM. Table IV. shows the material consumption of designed PM motors and reference induction motor. As seen from the Table IV. that total mass of SPM and IPM motor are reduced by approximately 60% compared than the reference induction motor. However, it should be considered that the high price of magnet used (*NdFe35*) will increase the total cost of PM motors. Although the total cost increases, the additional production costs will be compensated in the medium or long term as the PM motors efficiency are higher than IMs.

It is concluded that the designed SPM and IPM motors have higher efficiency, lower torque ripple, volume and mass compared than induction motor.

IV. CONCLUSIONS

The design stages of SPM and IPM motors are described in detail and stator&rotor geometries are determined through the parametric analysis. Torque and torque ripple, efficiency, phase currents and material consumption of designed PM motors are compared to reference induction motor that is utilized for low power applications. Along with the parametric optimization process, the efficiency of PM motors has been increased while torque ripple, motor volume as well as motor weights have been decreased compared than that of induction motor. The designed PM motors enable very practical solutions due to its energy efficiency and performance in low power industrial applications.

V. APPENDIX

TABLE A
PARAMETERS OF INDUCTION MOTOR

Motor name: Induction motor	**Item**
Rated power	2.2 *kW*
Rated speed	1420 *rpm*
Rated torque	14.8 *Nm*
Number of slot/pole	36/4
Stator outer diameter	145 *mm*
Rotor outer diameter	88 *mm*
Rotor inner diameter	35 *mm*
Stack length	110 *mm*
Air gap	0.25 *mm*
Armature current density	5.7 A/mm^2
Winding type	Distributed
Coil span	8
Stator and rotor core material	1008
Stator skew angle	0 °
Rotor skew angle	12.86 °
Efficiency	88.97 %
Torque ripple	13.26 %

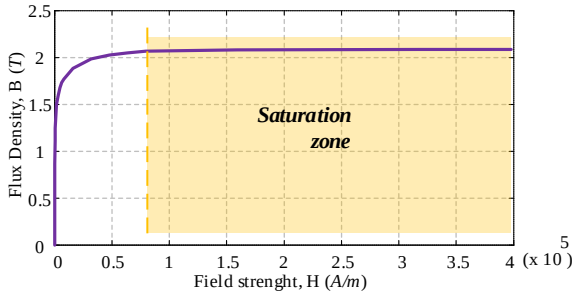

Fig. a. B-H curve of stator and rotor core material (Steel_1008)

REFERENCES

[1] T.J.E. Miller, T. W. Neumann, E Richter, "A permanent magnet excited high efficiency synchronous motor with line-start capability,"18th Ind. Appl. Soc. Annu. Meeting, 1983, pp. 455-461.

[2] G.R. Slemon, "On the Design of High-Performance Surface-Mounted PM Motors", IEEE Transactions on Industry Applications, Vol. 30, No. 1, Jan./Feb. 1994, pp. 134-140.

[3] M.A. Rahman, "Analysis of Brushless Permanent Magnet Synchronous Motors" IEEE Transactions on Industry Applications, Vol. 43, No. 2, April 1996, pp.256-267.

[4] M.A. Rahman, G. Slemon, "Promising Applications of Neodymium Boron Iron Magnets in Electrical Machines" IEEE Transactions on Magnetics, Vol. 21, No. 5, 1985, pp.1712-1716.

[5] G. Pellegrino, T.M. Jahns,N. Bianchi, W.L. Soong, F. Cupertino, "The Rediscovery of Synchronous Reluctance and Ferrite Permanent Magnet Motors", Tutorial Course Notes, Springer Nature, Switzerland, 2016.

[6] N. Bianchi, S. Bolognani, "Design Techniques for Reducing the Cogging Torque in Surface-Mounted PM Motors", IEEE Transactions on Industry Applications, Vol. 38, No. 5, Sep./Oct. 2002, pp.1259-1265.

[7] E. Carraro, M. Degano, M. Morandin, N. Bianchi, "PM Synchronous Machine Comparison for Light Electric Vehicles", IEEE International Electric Vehicle Conference (IEVC), 17-19 December 2014, Florence, pp.1-8.

[8] N. Bianchi, S. Bolognani, P. Frare, "Design Criteria for High-Efficiency SPM Synchronous Motors", IEEE Transactions on Energy Conversion, Vol. 21, No. 2, June 2006, pp.396-404.

[9] C. He, T. Wu, "Analysis and Design of Surface Permanent Magnet Synchronous Motor and Generator", CES Transactions on Electrical Machines and Systems, Vol. 3, No. 1, March 2019, pp. 94-100.

[10] R. Celikel and M. Ozdemir, "Control of a Three-Phase Boost Rectifier for High-Speed BLDC Generators Used in Flywheel Energy Storage System" International Conference on Advanced Technology & Sciences (ICAT'16), 2016, pp. 530-535.

[11] V. Sarac, D. Iliev, "Synchronous Motors of Permanent Magnet Compared to Asynchronous Induction Motor", Electrotehnica, Electronica, Automatica (EEA), Vol. 65, No. 4, 2017, pp. 51-58.

[12] R. Celikel, "Speed Control of BLDC Using NARMA-L2 Controller in Single Link Manipulator", Balkan Journal of Electrical and Computer Engineering, Vol. 7, No. 2, April 2019, pp. 141-148.

[13] Y. Yang, S. Castano, R. Yang, M. Kasprzak, B. Bilgin, A. Sathyan, H. Dadkhah, A. Emadi, "Design and Comparison of Interior Permanent Magnet Motor Topologies for Traction Applications" IEEE Transactions on Transportation Electrification, Vol, 3, No 1, 2017, pp. 87-97.

[14] H. Yetis, E. Mese, M. Biyikli, "Design and Comparison of Ferrite Based IPM and NdFeB Based SPM Synchronous Motors for Gearless Elevator Systems", International Conference on Electrical Machines (ICEM), 3-6 Sep.2018, Alexandroupoli, pp.635-641.

[15] G. Pellegrino, A. Vagati, P. Guglielmi, B. Boazzo, "Performance Comparison Between Surface-Mounted and Interior PM Motor Drives for Electric Vehicle Application", IEEE Transactions On Industry Applications, Vol. 59, No 2, 2012, pp. 803-811.

[16] A. M. El-Refaie, T. M. Jahns, "Comparison of synchronous PM machine types for wide constant-power speed range operation", 40th Conf. Rec. IEEE IAS Annu. Meeting, Oct. 2–6, 2005, vol. 2, pp. 1015–1022.

[17] R. Islam, I. Husain, A. Fardoun and K. McLaughlin, "Permanent-Magnet Synchronous Motor Magnet Designs With Skewing for Torque Ripple and Cogging Torque Reduction", IEEE Transactions on Industry Applications, Vol. 45, No. 1, 2009, pp. 152-160.

[18] R. Celikel, O. Aydogmus, "A torque ripple minimization method for brushless DC motor in high speed applications using buck boost topology" Journal of Enginering Research, Vol. 7, No. 3, September2019, pp. 200-214.

[19] M. S. Islam, S. Mir, T. Sebastian and S. Underwood, "Design considerations of sinusoidally excited permanent-magnet Machines for low-torque-ripple applications", IEEE Transactions on Industry Applications, Vol. 41, No. 4, July-Aug. 2005, pp. 955-962.

[20] T. Li and G. Slemon, "Reduction of cogging torque in permanent magnet motors IEEE Transactions on Magnetics, ,Vol. 24, No 6, Nov. 1988, pp. 2901–2903.

[21] S. H. Han, T. M. Jahns and W. L. Soong, "Torque Ripple Reduction in Interior Permanent Magnet Synchronous Machines Using the Principle of Mutual Harmonics Exclusion", IEEE Industry Applications Annual Meeting, Sep. 2007, pp.558-565.

[22] S. Han, T. M. Jahns, W. L. Soong, M. K. Güven and M. S. Illindala, "Torque Ripple Reduction in Interior Permanent Magnet Synchronous Machines Using Stators With Odd Number of Slots Per Pole Pair", IEEE Transactions on Energy Conversion, Vol. 25, No. 1, March 2010, pp. 118-127.

[23] M. Sanada, K. Hiramoto, S. Morimoto, Y. Takeda, "Torque Ripple Improvement for Synchronous Reluctance Motor Using an Asymmetric Flux Barrier Arrangement", IEEE Transactions On Industry Applications, Vol. 40, No. 4, Jul./Aug. 2004, pp. 1076-1082.
[24] T. Goktas, M. Arkan, "Diagnosis of Broken Rotor Fault in Inverter-Fed IM by Using Analytical Signal Angular Fluctuation", 16th International Power Electronics and Motion Control Conference and Exposition, 21-24 Sept 2014, Antalya, pp. 1-6.
[25] D.Y. Ohm, "Dynamic Model of PM Synchronous Motors", Drivetech, Inc., Blacksburg, Virginia, 1997.
[26] J.R. Hendershot, T.J.E. Miller, "Design of brushless permanent magnet motors", Magna Physics Publishing and Clarendon Press, Oxford,1994.
[27] M. Ayaz, M. Tezcan, E. Mese, K. Yılmaz, "Parametric Optimization of Permanent Magnet Synchronous Machines" in Proc. 6th International Conference on Control Engineering & Information Technology (CEIT), 25-27 Oct. 2018, İstanbul, pp. 1-6.
[28] C. Lu, S. Ferrari, G. Pellegrino, C. Bianchini, M. Davoli, "Parametric Design Method for SPM Machines Including Rounded PM Shape", in Proc. 2017 IEEE Energy Conversion Congress and Exposition (ECCE), 1-5 Oct. 2017, Cincinnati, pp. 4309-4315.

BIOGRAPHIES

HICRET YETIS received B.S. and M.S. degrees in electrical engineering from Yildiz Technical University, Istanbul, Turkey, in 2013, 2017, respectively. Since 2018 she has been a student of Ph.D. degree in Inonu University, Malatya, in the Electrical and Electronics Engineering department. Her research interests include design of electric machines.

TANER GOKTAS received B.S and M.S degrees in electrical engineering from Firat University, Elazig, Turkey, in 2006 and 2010, respectively, and the Ph.D. degree in Electrical Engineering from the Inonu University, Malatya, Turkey, in 2015. He was a visiting scholar in the Power Electronic and Drives Lab, University of Texas at Dallas from 2014 to 2015. Since 2016, he has been with Inonu University as Assistant Professor. His research interests include electric machines drives, condition monitoring, motor design and diagnostic techniques in electric machines.

Design of Neuro-Fuzzy Based Torque Controller for Torque Ripple Reduction of Induction Motor

A. GUNDOGDU, F. ATA and B. DANDIL

***Abstract*—Among all the control methods developed for Induction Motor (IM) drivers, the hysteresis controller based Direct Torque Control (DTC) method has an important place. This control method does not require other rotor and stator parameters except the stator resistance and does not require position or velocity sensors. However, there are some disadvantages of the DTC method, such as high torque, flux and current ripples. In this study, in order to reduce the high torque ripples occurring in an induction motor that is controlled by the hysteresis controller based conventional DTC method, a simple and effective Sugeno type Neuro-Fuzzy Torque Controller (NFTC) is proposed. This proposed controller is used instead of hysteresis controller. An experimental setup consisting of 1.1 kW induction motor, current and voltage measurement, DS1103 control card and two-level voltage source inverter was installed. To evaluate the performance of the proposed controller structure, various experimental studies were performed. Results obtained from the proposed NFTC based structure and conventional hysteresis controller based DTC structures are given comparatively. By the obtained experimental results, it was confirmed that the proposed NFTC-based controller structure considerably reduced flux and torque ripples in the motor.**

Index Terms—***Direct Torque Control, AC Drives, Neural Fuzzy Networks, Torque Ripple Reduction*.**

I. INTRODUCTION

ASYNCHRONOUS MOTORS have been largely used for many years because of their simple structure, high-strength, reliability, robustness, low cost, and high efficiency. In industrial applications, different methods have been used to control induction motors. These methods are generally implemented in two ways, vector and scalar control methods. In the scalar method, only the frequency and amplitude of current, voltage and flux space vectors are controlled. On the other hand, in the vector control method, in addition to the amplitude and frequency, the positions of these current, voltage and flux vectors are also checked [1,18]. To be able to achieve a high-performance control of the variable-speed induction motor drivers, the vector control method can be used. Vector control method ensures decoupled control of torque and flux independently of each other as in a free-excitation direct current machine.

There are two most widely used vector control methods, Direct Torque Control (DTC) and Field Oriented Control (FOC). As first, the Field Oriented Control was proposed by Blaschke [2] in 1971. Development of the conventional Direct Torque Control (DTC) was carried out by Takahashi [3] in 1986. Direct Torque Control method (DTC) has some characters such as simple control structure, high-speed torque and flux response, and robustness against parameter uncertainties [4,5]. Compared to the Field Oriented Control method, it is seen that the DTC method is less sensitive to parameter changes.

However, the conventional DTC method has some disadvantages, such as high torque, flux and current fluctuations, high acoustical noise level at low speed, variable switching frequency, difficulty in the control of flux and torque at very low speeds, and nonzero steady state torque error [6]. To be able to solve the above mentioned disadvantages of the conventional DTC, many research have been carried out by researchers on adaptive hysteresis band [5], improved switching table [7,8], space vector modulation approach and constant switching frequency [9,10,25], reduction of torque ripple [7-10,22,23], Intelligent control techniques [11,12], complex flux estimation methods [13], controller design [9,14,26,27], multilevel inverters [15], predictive control [16], genetic algorithm [19], parameter estimation with particle swarm optimization [20]. There are two fundamental problems that many researchers have been focusing on; these are high torque ripple and variable switching frequency. Different application schemes based on intelligent control techniques (e.g., fuzzy logic, genetic algorithm, neural networks, and neural-fuzzy) have been proposed to overcome these problems [21, 24].

In this study, in order to decrease the high torque ripple and obtain a switching frequency that was constant, a new Neuro-

AHMET GUNDOGDU, is with Department of Electrical Engineering University of Batman, Turkey, (e-mail: ahmet.gundogdu@batman.edu.tr).
https://orcid.org/0000-0002-8333-3083

FIKRET ATA, is with Department of Electrical Engineering University of Bingol, Bingol, Turkey, (e-mail: fata@bingol.edu.tr).
https://orcid.org/0000-0000-0000-0000

BESIR DANDIL, is with Department of Mechatronics Engineering University of Firat, Elazig, Turkey, (e-mail: bdandil@firat.edu.tr).
https://orcid.org/0000-0002-3625-5027

Manuscript received April 30, 2020; accepted May 28, 2020.
DOI: 10.17694/bajece.730311

Fuzzy Torque Controller (NFTC), which was in Sugeno type, was proposed. Torque error and the change of torque error were selected as input variables of NFTC. The output variable of this controller is the torque slope (T_{SLP}). In the 2nd part of this paper, a dynamic model of an IM is presented. In the 3rd part, torque and flux equations related to the conventional DTC is given. In part 4, the internal structure of the proposed controller is described. Finally, in the 5th part, the block diagram for the experimental design and experimental results are given.

II. THE DYNAMIC MODEL FOR AN INDUCTION MOTOR

It is possible to give the dynamic model of an IM on the stationary reference frame as below.

Stator voltage equations:

$$V_{s\alpha} = \frac{d}{dt}\varphi_{s\alpha} + R_s I_{s\alpha} \quad (1)$$

$$V_{s\beta} = \frac{d}{dt}\varphi_{s\beta} + R_s I_{s\beta} \quad (2)$$

$$\bar{V}_s = \frac{d}{dt}\bar{\varphi}_s + R_s \bar{I}_s \quad (3)$$

Stator flux equations:

$$\varphi_{s\alpha} = L_s I_{s\alpha} + L_m I_{r\alpha} \quad (4)$$

$$\varphi_{s\beta} = L_s I_{s\beta} + L_m I_{r\beta} \quad (5)$$

$$\bar{\varphi}_s = L_s \bar{I}_s + L_m \bar{I}_r \quad (6)$$

Rotor flux equations:

$$\varphi_{r\alpha} = L_r I_{r\alpha} + L_m I_{s\alpha} \quad (7)$$

$$\varphi_{r\beta} = L_r I_{r\beta} + L_m I_{s\beta} \quad (8)$$

$$\bar{\varphi}_r = L_r \bar{I}_r + L_m \bar{I}_s \quad (9)$$

In equations (1)-(9), the notations of "s" and "r" refer to the stator and rotor variables, respectively. In addition, while the stator voltages are referred by $V_{s\alpha}$ and $V_{s\beta}$, $I_{s\alpha}$ and $I_{s\beta}$ refer to stator currents, $I_{r\alpha}$ and $I_{r\beta}$ refer to rotor currents, $\varphi_{s\alpha}$ and $\varphi_{s\beta}$ refer to stator fluxes, $\varphi_{r\alpha}$ and $\varphi_{r\beta}$ refer to rotor fluxes, I_s and I_r refer to stator and rotor current vectors, R_s refers to stator winding resistance, and L_s, L_r, L_m refer to the stator and rotor inductance and common inductances of them. The motor's electromagnetic torque (T_e) can be derived as in Equations (10)-(11) by using stator and rotor flux equations given above.

$$T_e = \frac{3}{2}\frac{P}{2}\frac{L_m}{\sigma L_s L_r}\bar{\varphi}_s * \bar{\varphi}_r \quad (10)$$

$$T_e = \frac{3}{2}\frac{P}{2}\frac{L_m}{\sigma L_s L_r}|\bar{\varphi}_s|.|\bar{\varphi}_r|.sin(\gamma_s - \gamma_r) \quad (11)$$

$$\gamma_s - \gamma_r = \delta \quad (12)$$

In this equation, $\sigma = 1 - L_m^2/L_s L_r$ is the leakage factor, P is the number of double poles, γ_s , γ_r are rotor and stator flux vectors' angles, and δ is the torque angle. In equation (11), it is obviously seen that the electromagnetic torque generated by the motor is a function of the rotor and stator flux vectors. The relationship between rotor and stator flux vectors is demonstrated in Figure 1. A sudden change is followed by the rotor flux in the rotor flux $\bar{\varphi}_s$ with a certain delay. The generated electromagnetic torque is proportional to $|\bar{\varphi}_s|$, $|\bar{\varphi}_r|$ and torque angle δ.

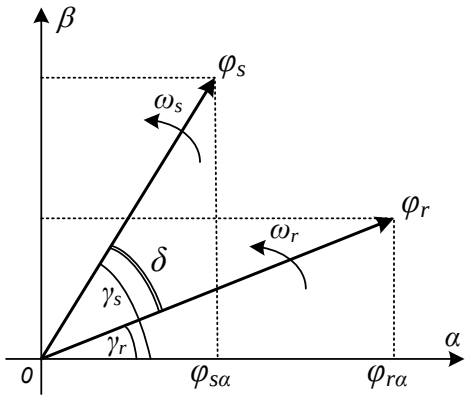

Figure 1. Rotor and stator flux vectors in αβ reference frame.

According to Figure 1, it is possible to realize the torque control of the IM via controlling the torque angle δ. In a balanced continuous sinusoidal situation, depending on operating conditions, the rotation of the rotor and stator flux vectors at a constant angular speed is observed. In this case, the torque angle δ is constant and this depends on the operating conditions. Thus, the generated electromagnetic torque becomes constant. If the flux vector $|\bar{\varphi}_s|$accelerates, the torque angle δ and the generated electromagnetic torque increase. If the flux vector $|\bar{\varphi}_s|$ slows down, the torque angle δ and the generated torque reduce.

III. TORQUE AND FLUX EQUATIONS OF CONVENTIONAL DIRECT TORQUE CONTROL METHOD

The conventional DTC method achieves decoupled control of the electromagnetic torque and the stator flux independently from each other. The fundamental principle of this method is regulating the amplitude of the stator flux and the electromagnetic torque by selecting directly the appropriate voltage vectors and their control signals. To estimate the components of the stator flux, the stator voltage model is used. Stator voltage model is generally a simple form of stator flux

estimation techniques. Following equations are used in order to calculate the components and amplitudes of the stator flux;

$$\varphi_{s\alpha} = \int (V_{s\alpha} - R_s I_{s\alpha}) dt \quad (13)$$

$$\varphi_{s\beta} = \int (V_{s\beta} - R_s I_{s\beta}) dt \quad (14)$$

$$\varphi_s = \sqrt{\varphi_{s\alpha}^2 + \varphi_{s\beta}^2} \quad (15)$$

In a practical application, stator voltage components ($V_{s\alpha}$,$V_{s\beta}$) and stator current components ($I_{s\alpha}$,$I_{s\beta}$) are obtained by applying the αβ conversion to the real 3~ voltage and currents measured from the motor terminals.

In order for estimation, only stator voltage, resistance and current are required and this estimation depends on open-loop integration of the stator back-emf. Through this way, estimation of the flux is ensured accurately at high speeds. On the other hand, noise in voltage and current measurement, stator resistance voltage drop and integration drift become significant because it causes an inaccurate estimation at low speed.

As it is presented in the equation (16), the electromagnetic torque, which the motor generates, is calculated with the help of the stator flux and currents.

$$T = \frac{3}{2} P\left(\varphi_{s\alpha} I_{s\beta} - \varphi_{s\beta} I_{s\alpha}\right) \quad (16)$$

The fundamental control diagram for the conventional DTC method proposed by Takahashi for induction motor drivers is given in Figure 2. This control structure includes torque and torque with flux hysteresis tapes, flux and angle estimation blocks, and a switching table for selection of voltage vectors.

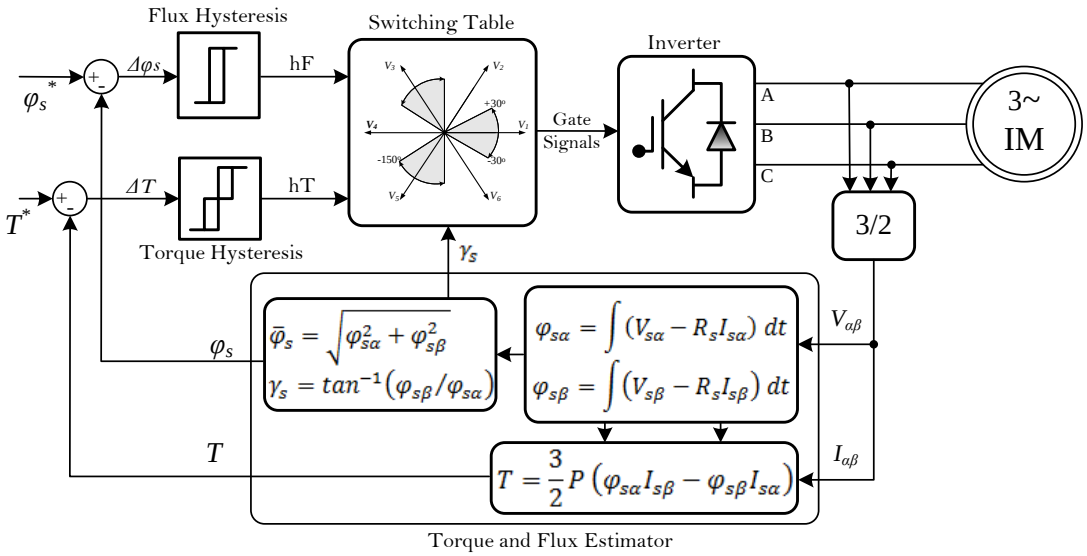

Figure 2. Basic configuration of the conventional DTC

As shown in Figure 2, there are two different cycles in which flux and torque are obtained. In the conventional DTC method, when the closed-loop process of motor driver system is performed, a PI speed controller is usually utilized for the generation of the reference torque. Torque error ΔT and flux error $\Delta\varphi_s$ are obtained by comparing the torque and flux reference values with their actual values obtained by the measurement.

$$\Delta T = T^* - T \quad (17)$$

$$\Delta\varphi_s = \varphi_s^* - \varphi_s \quad (18)$$

$$\gamma_s = tan^{-1}\left(\varphi_{s\beta}/\varphi_{s\alpha}\right) \quad (19)$$

In the equations (17) - (19) above, T^* is reference torque, φ_s^* is reference current and γ_s is the stator flux vector angle. The inverter switching signals are obtained by helping of ΔT, $\Delta\varphi_s$ and γ_s. The torque and flux errors obtained at the output of the comparison blocks are applied as input to hysteresis controllers. While the flux hysteresis controller is a two-level comparator, the torque hysteresis controller is a three-level comparator.

While the flux hysteresis controller generates hF=1, hF=0 at the output according to the flux error information at the input, the torque hysteresis controller generates hT=-1, hT=0, hT=1 at the output according to the torque error information at the input. These numerical values are then applied as input to the switching table for determining the region where the stator flux vector is located. The switching table is presented in Table 1.

TABLE I
TAKAHASHI SWITCHING TABLE

hF	*hT*	N=1	N=2	N=3	N=4	N=5	N=6
1↑	1↑	**V2**	**V3**	**V4**	**V5**	**V6**	**V1**
	0	**V7**	**V0**	**V7**	**V0**	**V7**	**V0**
	-1↓	**V6**	**V1**	**V2**	**V3**	**V4**	**V5**
0↓	1↑	**V3**	**V4**	**V5**	**V6**	**V1**	**V2**
	0	**V0**	**V7**	**V0**	**V7**	**V0**	**V7**
	-1↓	**V5**	**V6**	**V1**	**V2**	**V3**	**V4**

The orbit of the stator flux vector is divided into six different sectors. The voltage source inverter generates a total of eight voltage vectors; six active voltage vectors (V1-V6) and two zero voltage vectors (V0-V7). Representations of these voltage vectors and sectors on αβ frame are given in Figure 3.

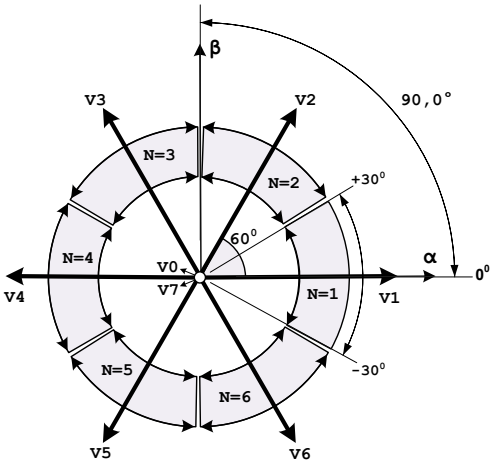

Figure 3. Inverter voltage vectors and sectors.

N=1-6 number sectors that includes the stator flux vector is determined by equation (20), and the angular position of this flux vector is determined by equation (19).

$$-\frac{\pi}{6}+(N-1)\frac{\pi}{3}\leq\gamma_s(N)<\frac{\pi}{6}-(1-N)\frac{\pi}{3} \qquad (20)$$

Depending on the hysteresis flux controllers and output of the hysteresis torque, the most suitable voltage vectors are selected from Table 1. According to Table 1, the flux decreases for hF=0 and the flux increases for hF=1. Similarly, the torque increases for hT=1, the torque decreases for hT=-1 and the torque does not change for hT=0.

IV. PROPOSED NEURO-FUZZY TORQUE CONTROLLER

In order for designing of the Neuro-Fuzzy Torque Controller, Artificial Neural Networks and Fuzzy Logic are able to be used together. To be able to obtain the first artificial neural network structure, online/offline learning processes can be used with the help of human expert knowledge. For combining artificial neural networks and fuzzy logic, one of the recommended methods is the adaptive neuro-fuzzy inference system (ANFIS) [11,12]. Instead of the torque hysteresis controller used in the conventional DTC method, a neuro-fuzzy torque controller whose block diagram is given in Figure 4 is used in this study. The proposed controller performs the same task as the conventional three-level torque hysteresis controller. For this reason, the same switching table is used for selecting the appropriate voltage vectors.

The proposed structure of the neuro-fuzzy torque controller is presented in Figure 4. This controller structure consists of two triangular carrier waves [9], two comparator blocks and a neuro-fuzzy controller. Triangular carrier waves (carr_upp and carr_low) have 180^0 phase difference.

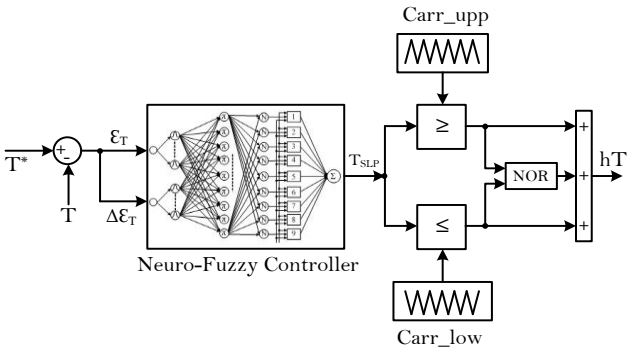

Figure 4. Proposed neuro-fuzzy torque controller.

The internal structure of the proposed neuro-fuzzy torque controller is demonstrated in Figure 5.

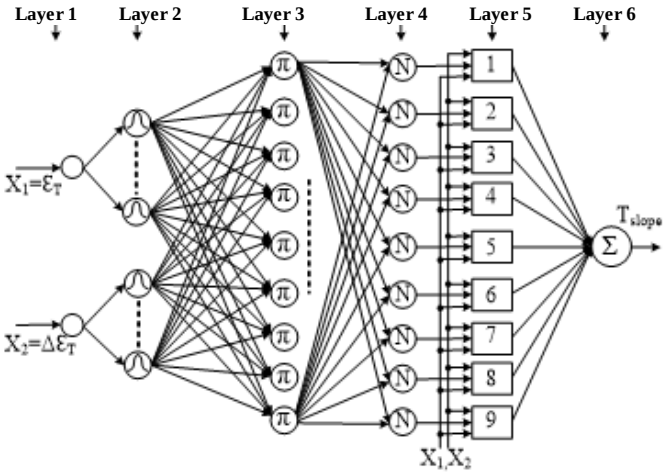

Figure 5. Two-input neuro-fuzzy controller structure.

The input variables of the controller are the torque error and the variation of this error. In addition, the torque slope T_{SLP} is the output variable of the controller. This controller is a first order sugeno type controller. It consists of functional blocks constructed by using six network layers: The layers of the controller perform fuzzification, inference and defuzzification of the fuzzy systems.

LAYER 1. In this layer, the input of the controller is selected as, $X_1=\mathcal{E}_T(t)$, $X_2=\Delta\mathcal{E}_T(t)$

LAYER 2. This layer contains the membership functions. For input variables, calculation of membership function degree is done by this layer.

LAYER 3. This layer applies the fuzzy as well as the operation. Here, the output specifies the firing strength of the rules.
LAYER 4. Here, respecting to the others, each input is being normalized.
LAYER 5. In this layer, the calculation of the consequent values is performed. Here, the output is the result of the normalized certainty of a rule and the function related to this.
LAYER 6. This is the output layer. Here, an output is generated as a collection of all incoming signals.

The torque slope T_{SLP}, which is the output of the neuro-fuzzy controller, is compared to the triangular carrier wave as shown in Figure 6.

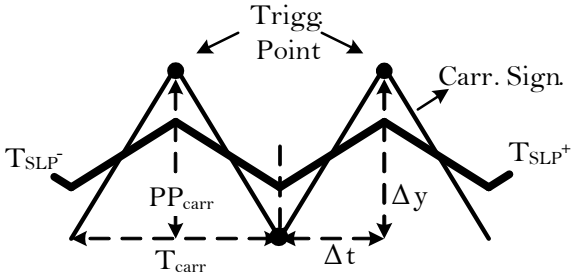

Figure 6. Triangle carrier signal and torque.

Here, PP_{car} is the top-to-top value of the triangular carrier wave and T_{car} is its period. The slope of the triangular carrier wave is calculated as in equation (21).

$$|absolute\ slope_{carr}| = \frac{\Delta_y}{\Delta_t} = \frac{PP_{carr}}{T_{carr}/2} = 2f_{carr}\,PP_{carr} \tag{21}$$

In reference [17], it is emphasized that the torque slope, the motor speed, rotor and stator fluxes, stator voltage are functions of load. The expressions for the increasing in torque(T_{SLP}^{+}) and the decreasing in torque (T_{SLP}^{-}) are given in the equations (22) and (23).

$$T_{SLP^+} = \frac{dT^+}{dt} = -A_t T + B_t V_s^{\varphi s} + K_t\left(\frac{w_e}{d} - w_r\right) \tag{22}$$

$$T_{SLP^-} = \frac{dT^-}{dt} = -A_t T - K_t w_r \tag{23}$$

where,

$$A_t = \frac{1}{\sigma\tau_{sr}} \tag{24}$$

$$B_t = \frac{3}{2}\frac{P}{2}\frac{L_m}{\sigma L_s L_r}\varphi_r \tag{25}$$

$$K_t = \frac{3}{2}\frac{P}{2}\frac{L_m}{\sigma L_s L_r}(\varphi_s\varphi_r) \tag{26}$$

The absolute slope of the T_{SLP} should not exceed the absolute slope of the triangular carrier signal.

$$T_{SLP} \le \frac{\Delta y}{\Delta t} = \frac{PP_{carr}}{T_{carr}/2} = 2f_{carr}\,PP_{carr} \tag{27}$$

The slope of the T_{SLP} in the neuro-fuzzy controller is determined by the scaling factor K_{SF}. On the other side, the scaling factor K_{SF} is obtained by using equations (22) and (23) as below.

For the positive slope, from Eq.(22);

$$K_{SF^+} \le \frac{2f_{carr}\,PP_{carr}}{T_{SLP^+}} \tag{28}$$

For the negative slope, from Eq.(23);

$$K_{SF^-} \le \frac{2f_{carr}\,PP_{carr}}{|T_{SLP^-}|} \tag{29}$$

are obtained. The output of the proposed neuro-fuzzy torque controller (hT) is given by equation (30) and it is the same as the outputs of the three-level torque hysteresis controller,

$$\mathrm{hT} = \begin{cases} 1 & T_{SLP} \ge \mathrm{carr_upp} \\ 0 & \mathrm{carr_low} < T_{SLP} < \mathrm{carr_upp} \\ -1 & T_{SLP} \le \mathrm{carr_low} \end{cases} \tag{30}$$

In addition, a flux controller is designed using a proportional gain instead of neuro-fuzzy controller or similar torque controller.

V. EXPERIMENTAL SETUP AND RESULTS

A block diagram of the experimental setup developed to implement both the conventional hysteresis controller based DTC method and the proposed neuro-fuzzy torque controller based DTC method is given in Figure 7.

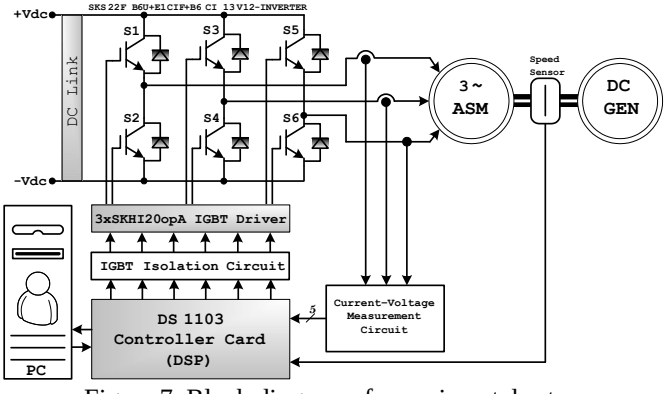

Figure 7. Block diagram of experimental setup.

The experimental setup consists of dSPACE DS1103 control card, 5000 pulse incremental encoder, Semikron SKS22F B6U model, three-phased VSI-IGBT inverter and 2-pole, 1.1 kW, 380 V, 50 Hz standard induction motor whose parameters are given in Appendix A. Figure 9 shows a photo related to the experimental setup. The DS1103 control card has PowerPC PPC750GX/1 GHz master processor and TMS320F240/20 MHz auxiliary processor.

By the help of the measured stator currents and voltages, estimation of the torque and flux, generation of the triangular carrier waves, determination of the sector where the flux vector is located, realization of the numerical calculation of the neuro-fuzzy controller and all other calculations are performed by using this control card. The control algorithm for the proposed controller structure was carried out by using the Matlab/Simulink block diagram presented in Figure 8.

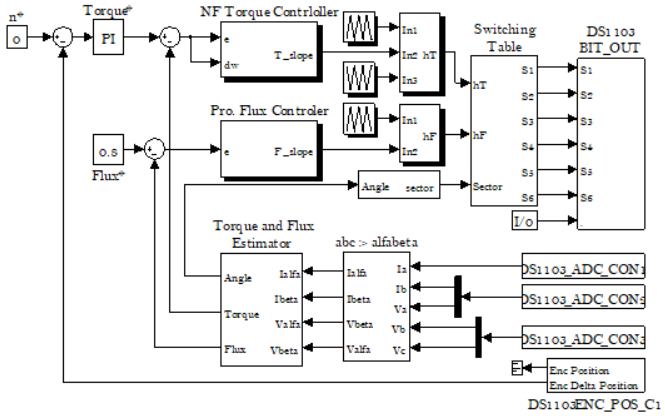

Figure 8. Matlab/Simulink block diagram of the proposed DTC with NFTC.

User interface software called Control Desk Developer (CDD) was used to display real-time measurements such as motor speed, stator voltages and currents, and to change the speed reference and controller parameters online.

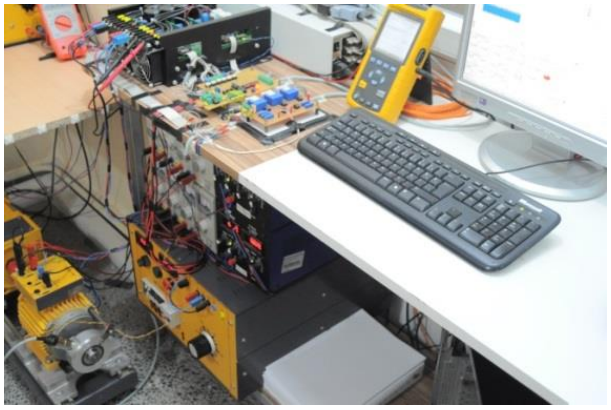

Figure 9. Photograph of the experimental setup.

In the experimental studies, it was determined that the DC bus voltage of the inverter was 520 volts, the dead time was 3 μs, the sampling period was Ts=50μs and the period of the triangular carrier signal for the torque cycle is T_{carr}=100 μs. By PI speed controller, the starting torque of the motor was limited as ± 6 Nm.

Torque hysteresis controller was set to 10% of nominal torque so that its bandwidth was 0.372 Nm. The real value of the stator flux was calculated using the stator voltage model. Its reference value was 0.8 Wb.

The flux hysteresis controller was set to 1% of the nominal flux so that its bandwidth was 0.008 Wb. The motor shaft speed was measured with a high-resolution encoder of 5000 pulses. To load the motor, a DC generator was installed on the motor shaft. Measurement of the two-phase currents were performed by two Hall-effect current sensors and the third phase current was obtained by calculation in the algorithm. The measurement of the motor peak voltages are also done by Hall-effect voltage sensors and transferred into the control structure.

Various experimental studies were carried out in order to show the performance of the proposed neuro-fuzzy torque controller, and for the both control methods, the obtained results are given below.

A. Transient Performance

The transient regime performance of the both control algorithms under the same operating conditions was analyzed by comparing torque, speed, flux and current responses. First, the graphs obtained for the unloaded state of the motor are given in Figures (10)-(11).

The speed and torque responses of the two control algorithms are shown in Figure 10. With regards to the settling time of speed and torque, transient performances are similar. Figure 11 presents speed, torque, current and flux responses obtained using proposed NFTC algorithm for the speed reversal from -2700 rpm to +2700 rpm and from +2700 rpm to -2700 rpm. The torque and phase current increased during reversal operation mode.

During this time, the amplitude of the stator flux is being fixed at 0.8 Wb. This result verifies that decoupling process between the flux and torque can deal with the four-quadrant operation mode.

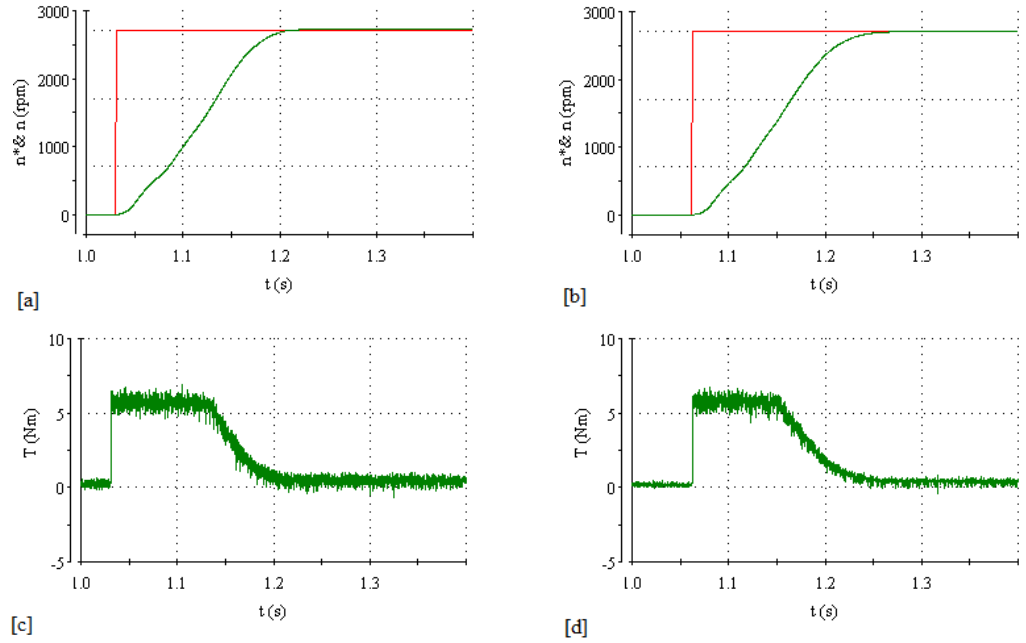

Figure 10. Experimental responses, no-load, from 0 to 2700 rpm. (a) Speed response for conventional DTC. (b) Speed response for Proposed DTC. (c) Torque response for conventional DTC. (d) Torque response for Proposed DTC.

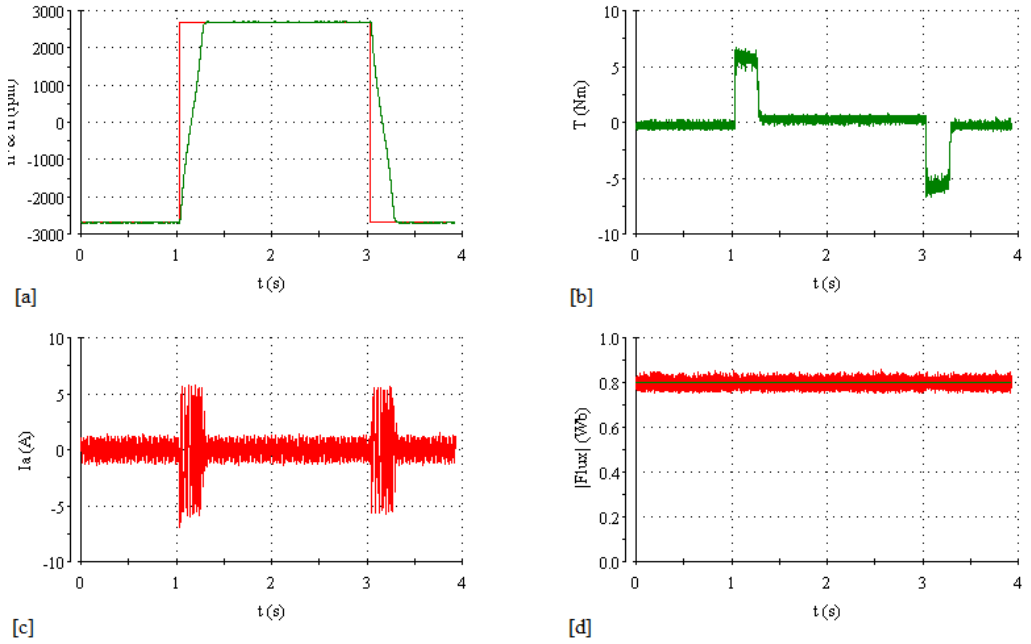

Figure 11. Experimental responses for Proposed DTC, no-load, from -2700 to +2700 rpm. (a) speed, (b) torque, (c) current, (d) flux.

B. Steady-State Performance

Evaluating the torque, speed, flux and current ripples in different conditions, the steady state performance of the two control algorithms was compared. Graphics of the steady states are presented in Figures 12-18, for no-load and with-load operation at +2700 rpm.

Figure 12 (a) and (b) demonstrates the experimental torque responses. The related rms torque ripples of the conventional DTC algorithm and proposed NFTC algorithm are 1.8 and 0.9 Nm., respectively. It is understood that a reduction in the rms torque ripple is small noticeably. Compared with the conventional DTC, this rms torque ripple level is significantly decreased.

Moreover, except torque ripple, speed and flux responses are presented in Figures 13 and 14, respectively. Figure 13 (a) and (b) show the experimental rms speed ripples of 10 and 5 rpm for the conventional DTC and proposed NFTC algorithm, respectively. Figure 14 (a) and (b) show the experimental rms flux ripples of 0.1100 and 0.0974 Wb for the conventional

DTC and proposed NFTC algorithm, respectively. It is seen that rms speed and flux ripples are reduced.

As shown in Figures 15 and 16, the stator phase current and αβ currents are nearly sinusoidal. The amplitude of current ripples in NFTC is lower than that of conventional DTC. On the other hand, in the NFTC algorithm, the oscillations are more regular and uniform.

Figures 17 and 18 show the stator αβ fluxes waveform and its circular trajectory. Compared the speed, torque, current, and flux responses of the experimental results given in Figures 12-18, it can be seen that the proposed NFTC algorithm has decreased not only the torque ripple but also the speed, flux, and current ripples.

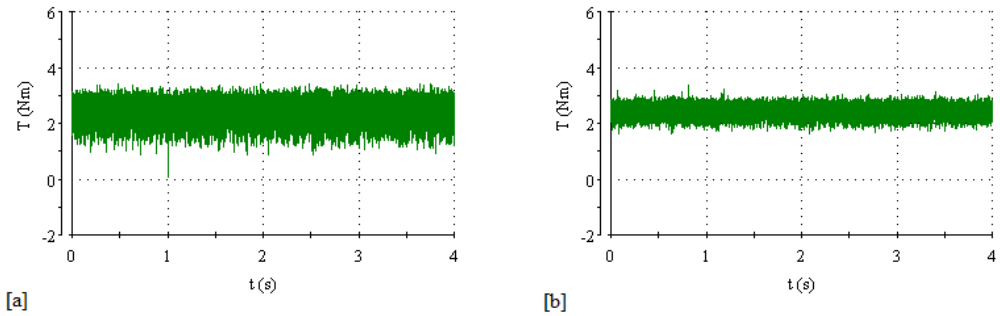

Figure 12. Experimental torque responses, with-load, at +2700 rpm. (a) Conventional DTC. (b) Proposed DTC

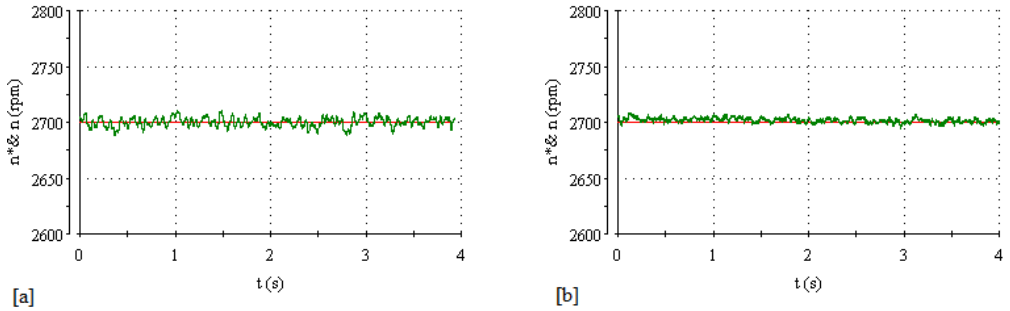

Figure 13. Experimental speed responses, no-load, at +2700 rpm. (a) Conventional DTC. (b) Proposed DTC.

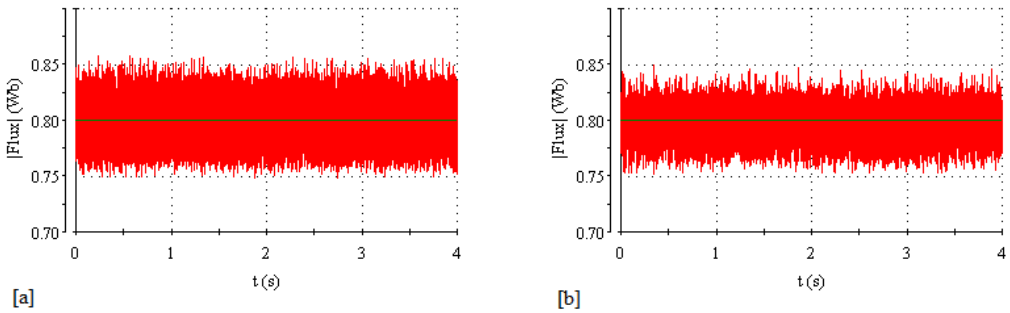

Figure 14. Experimental |Flux| responses, with-load, at +2700 rpm.(a) Conventional DTC. (b) Proposed DTC.

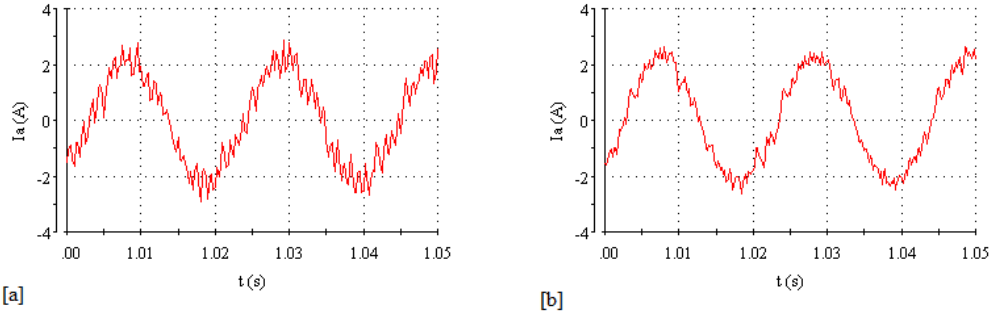

Figure 15. Experimental phase current responses, with-load, at +2700 rpm. (a) Conventional DTC. (b) Proposed DTC.

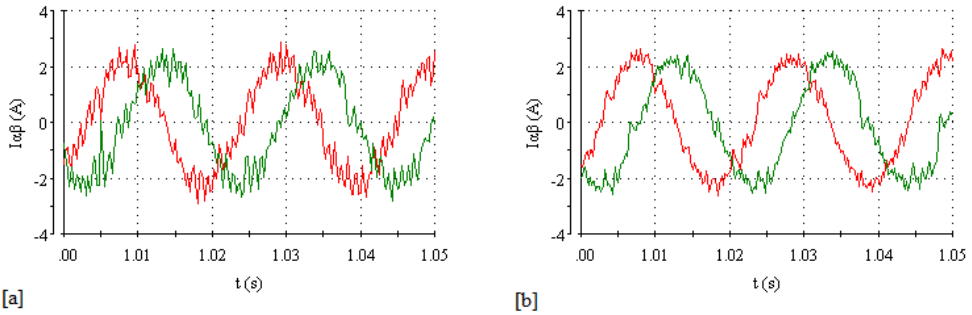

Figure 16. Experimental αβ current responses, with-load, at +2700 rpm. (a) Conventional DTC. (b) Proposed DTC.

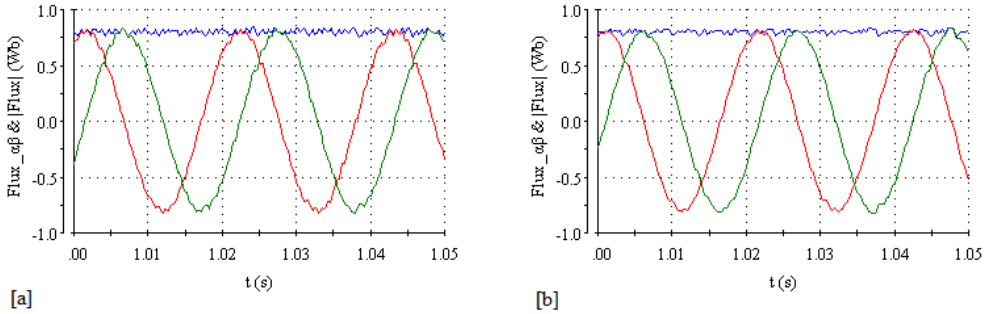

Figure 17. Experimental αβ flux responses, with-load, at +2700 rpm. (a) Conventional DTC. (b) Proposed DTC.

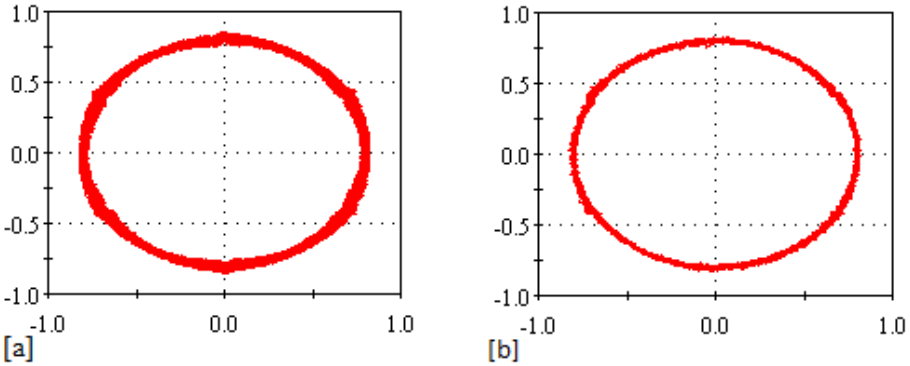

Figure 18. Experimental stator flux trajectory responses, with-load, at +2700 rpm. (a) Conventional DTC. (b) Proposed DTC

VI. CONCLUSION

Although the DTC is preferred for highly dynamic applications, it shows high torque and current ripple. In this study, a new neuro-fuzzy torque controller is proposed in order to enhance the performance of the conventional DTC and to reduce torque ripples. The efficiency of the proposed controller is demonstrated experimentally under the step speed and load changes. Looking at the experimental results, it is seen that the proposed neuro-fuzzy torque controller has a few advantages, such as torque and flux ripple reduction, low harmonic contents for currents, good performance at low-speed range, sinusoidal stator currents, and constant switching frequency. However, the performance of the controller is highly determined by the quality of the calculation of the scaling factor K_{SF}. It should be noted that the values of K_{SF}, are not optimized for all speed ranges. The scaling factor must be optimized using by advanced control techniques.

As a result of this study, transient performances of two control algorithms are similar, but the steady-state performance of the proposed NFTC control algorithm is better than the conventional DTC. While it maintains the simple structure of the DTC at the same time, the proposed neuro-fuzzy torque controller produces lower torque, speed, flux, and current ripples when compared with the conventional DTC. It is seen that the torque, speed, flux, and current ripples are significantly decreased.

ACKNOWLEDGEMENT

This study is a part of Ahmet GÜNDOĞDU's doctorate thesis, and it is supported by Firat University Scientific Research Projects Unit (FUBAP) with 1724 numbered project, titled "*Torque Ripple Reduction by Neural-Fuzzy Networks of Asynchronous Motor.*"

APPENDIX

Motor Parameters;

3 Phase; P=1.1 kW; V=220 V; f=50 Hz; 2P=2; Rs=8.231 Ω; Rr=4.46 Ω; Lm=0.5787 mH; J=0.0019 kg.m^2; B=0.000263 Nms

REFERENCES

[1] Buja G, Kazmierkowski MP. "Direct Torque Control of PWM Inverter Fed AC Motors-A Survey". *IEEE Transactions on Industrial Electronics*, 51 (4), 744-757, 2004.

[2] Blaschke F. "A New Method for the Structural Decoupling of AC Induction Machines". *In Conf. Rec. IFAC*, 1-15, 1971.

[3] Takahashi I, Noguchi T. "A New Quick-Response and High Efficiency Control Strategy of an Induction Machine". *IEEE Transactions on Industrial Applications*, 22, 820-827, 1986.

[4] Belkacem S, Naceri F, Abdessemed R. "Reduction of Torque Ripple in DTC for Induction Motor Using Input-Output Feedback Linearization". *Turkish Journal of Electrical Engineering and Computer Sciences*, 20(3), 273-285, 2012.

[5] Casadei D, Grandi G, Serra G, Tani A. "Effects of Flux and Torque Hysteresis Band Amplitude in Direct Torque Control of Induction Machines". *In Conf. Rec. IECON'94*, 299-304, 1994.

[6] Casadei D, Profumo F, Serra G, Tani A. "FOC and DTC: Two Viable Schemes for Induction Motors Torque Control". *IEEE Transactions on Industrial Electronics*, 17 (5), 779-787, 2002.

[7] Casadei D, Serra G, Tani A. "Improvement of Direct Torque Control Performance by Using a Discrete SVM Technique". *In Conf. Rec. PESC'98*, 997-1003, 1998.

[8] Galvan E, Carrasco JM, Ortega R, Escobar G, Stankovic AM. "A Family of Switching Control Strategies for the Reduction of Torque Ripple on the Direct Torque and Flux Control for Induction Motors". *The 27th Annual Conference of the IEEE Industrial Electronics Society*, 1274-1279, 2001.

[9] Idris NRN, Yatim AHM. "A Reduced Torque Ripple Controller for Direct Torque Control of Induction Machines". *Electric Power Components and Systems*, 507–524, 2002.

[10] Tripathi A, Khambadkone AM, Panda SK. "Torque Ripple Analysis and Dynamic Performance of a Space Vector Modulation Based Control Method for AC-Drives". *IEEE Transactions on Power Electronics*, 20(2), 485-492, 2005.

[11] Grabowski PZ, Blaabjerg F. "Direct Torque Neuro-Fuzzy Control of Induction Motor Drive". *DSP Implementation In Conf. Rec. IECON'98*, 657-661, 1998.

[12] Vasudevan M, Arumugam R. "High-Performance Adaptive Intelligent Direct Torque Control Schemes for Induction Motor Drives". *KMITL Sci. Tech. J*, 5(3), 559-576, 2005.

[13] Xia Y, Oghanna W. "Fuzzy Direct Torque Control of Induction Motor with Stator Flux Estimation Compensation". *In Proc.IEEE IECON'97*, 2, 505-510, 1997.

[14] Lai YS, Lin JC. "New Hybrid Fuzzy Controller for Direct Torque Control Induction Motor Drives". *IEEE Transactions on Power Electronics*, 18(5), 1211-1219, 2003.

[15] Lee KB, Song JH. "Torque Ripple Reduction in DTC of Induction Motor Driven by Three-Level Inverter With Low Switching Frequency". *IEEE Transactions on Power Electronics*, 17(2), 255–264, 2002.

[16] Miranda H, Cortes P, Yuz P, Rodriguez J. "Predictive Torque Control of Induction Machines Based on State-Space Models". *IEEE Transactions on Industrial Electronics*, 56(6), 1916–1924, 2009.

[17] Kang JK, Sul SK. "Torque Ripple Minimization Strategy for Direct Torque Control of Induction Motor". *In Conf. Rec. IEEE-IAS*, 438-443, 1998.

[18] Qutubuddin MD, Yadaiah N. "Modeling and Implementation of Brain Emotional Controller for Permanent Magnet Synchronous Motor Drive". *Engineering Applications of Artificial Intelligence*, 60, 193–203, 2017.

[19] Sangdani MH, Tavakolpour-Saleh AR, Lotfavar A. "Genetic Algorithm-Based Optimal Computed Torque Control of a Vision-Based Tracker Robot: Simulation and Experimental". *Engineering Applications of Artificial Intelligence*, 67, 24–38, 2018.

[20] Sakthivel VP, Bhuvaneswari R, Subramanian S. "Multi-Objective Parameter Estimation of Induction Motor Using Particle Swarm Optimization". *Engineering Applications of Artificial Intelligence*, 23, 302–312, 2010.

[21] Kumar RH, Iqbal A, Lenin NC. "Review of Recent Advancements of Direct Torque Control in Induction Motor Drives-A Decade of Progress". *IET Power Electronics*, 11(1), 1-15, 2018.

[22] Gowri KS, Reddy TB, Babu CS. "Direct Torque Control of Induction Motor Based on Advanced Discontinuous PWM Algorithm for Reduced Current Ripple". *Electrical Engineering*, 92, 245-255, 2010.

[23] Labiod C, Srairi K, Mahdad B, Benbouzid MEH. "A Novel Control Technique for Torque Ripple Minimization in Switched Reluctance Motor Through Destructive Interference". *Electrical Engineering*, 100(2), 481-490, 2018.

[24] Kesler S; Akpınar AS, Saygın A. "The Fuzzy Logic Based Power Injection Into Rotor Circuit For Instantaneous High Toerque And Speed Control In Induction Machines". *Pamukkale University Journal of Engineering Sciences*, 15(1), 13-23, 2009.

[25] Zaky MS. "High Performance DTC of Induction Motor Drives Over a Wide Speed Range". *Electrical Engineering*, 97(2), 139-154, 2015.

[26] Deniz E, Coteli R, Dandil B, Tuncer S, Ata F, Gencoglu MT. "Neuro-Fuzzy Current Controller for Three-Level Cascade Inverter Based D-STATCOM". *45th International Universities Power Engineering Conf. UPEC'2010*, 1-5, 2010.

[27] Coteli R, Deniz E, Dandil B, Tuncer S, Ata F. "Phase Angle Control of Three Level Inverter Based D-STATCOM Using Neuro-Fuzzy Controller". *Advances in Electrical and Computer Engineering*, 12(1), 77-84, 2012.

BIOGRAPHIES

AHMET GUNDOGDU, Elazığ in 1974. He received the B.S. and M.S. degrees in electrical teaching from the University of Firat, Elazığ, in 2004 and the Ph.D. degree in electrical engineering from Firat University, Elazığ, in 2012. From 2000 to 2012, he was a Research Assistant with the electrical teaching department. Since 2013, he has been an Assistant Professor with the Electrical Engineering Department, Batman University. His research interests include magnetic levitation, electrical machines, motor control.

FIKRET ATA, Department of Electrical Engineering, Bingol University.

BEŞİR DANDIL, Department of Mechatronic Engineering, Firat University.

Performance Comparison of ACM and GRP Methods for Image Permutation

H. OĞRAŞ and Ş. FIDAN

***Abstract*— Permutation and substitution processes of an image are most widely used in image encryption algorithms as they are thought to increase system security in cryptography. Permutation is the first process that all pixel positions in an image are shuffled in specific order or randomly in order to break strong correlation between adjacent pixels. Secondly, substitution is used to change pixel values by mixing a secret key in the permutated image. In an ordinary image, adjacent pixels have close values, so they have strong correlation and this correlation needs to be broken effectively before encryption. The degree to which this process is performed, directly affects overall system security. In this paper, performance evaluations for Group (GRP) and Arnold's Cat Map (ACM) methods are analyzed through some numerical results and their performances are compared to figure out which one is better. Experimental results consist of numerical and visual results determined in Matlab R2015a.**

Index Terms— **Image; GRP; Arnold's Cat Map; Confusion; Logistic Map**

I. INTRODUCTION

IN IMAGE cryptosystems, permutation-substitution structure is the most widely used architecture for image encryption algorithms [1-3]. After the first presentation by Fridrich in 1998, lots of studies about this structure have been proposed in image cryptography [4-8]. In most of these studies, it is emphasized that pixel positions of a source image should be replaced to another position before the encryption process for security improvements. In most ordinary image, any given pixel value can be easily predicted from the values of its neighbors. According to the Shannon's requirements, permutation and substitution are two basic processes to obscure high redundancies in an image and strong correlation of pixels in that image [7,9,10]. In order to achieve this situation, researchers use image permutation techniques to enhance security of their encryption algorithms.

HİDAYET OĞRAŞ, is with Vocational School of Technical Sciences, Electronic-Communication Programming, University of Batman, Batman, Turkey, (e-mail: hidayet.ogras@batman.edu.tr).
https://orcid.org/0000-0001-9624-7400

ŞEHMUS FİDAN, is with Vocational School of Technical Sciences, Electronic Programming, University of Batman, Batman, Turkey, (e-mail: sehmus.fidan@batman.edu.tr). https://orcid.org/0000-0002-5249-7245

Manuscript received December 30, 2019; accepted June 03, 2020.
DOI: 10.17694/bajece.667740

Due to simplicity and effectiveness, ACM is one of the most frequently used methods in chaos-based image encryption systems by researchers [11-14].The function of ACM method is that image rotates continuously resulting in a form that is not visible by the naked eye. In addition, it has a characteristic of area-preserving which means that if it is iterated enough times, then the original image reappears. Another permutation method to be examined in this paper is GRP. GRP is an important bit permutation technique in cryptography which changes the position of bits in a given sequence by employing a control bit [15]. Permutation performances between these two methods are compared in detail in this study. In this sense, average moving distance of scrambling (AMDS), number of equal pixel rate (NEPR) and correlation coefficient of adjacent pixels are considered to compare the performance of both permutation methods. The rest of the paper is organized as follows: Section 2 gives the brief overview of GRP and ACM methods. Section 3 introduces chaotic Logistic map that is used to be a control bit generator for GRP. Performance comparison of both methods is analyzed in Section 4. Finally, the conclusions are discussed.

II. MATERIALS AND METHODS

In this section, two mentioned methods for pixel replacement in an image are introduced. Then, some explanations and techniques are given about how to generate control bit from using Logistic map for GRP method. Some mathematical tests of AMDS, NEPR and CCAP are explained briefly which are used to compare performances of both methods.

A. ACM Method

ACM is a simple and invertible discrete system that is defined in (1).

$$\begin{bmatrix} x' \\ y' \end{bmatrix} = \begin{bmatrix} 1 & p \\ q & pq+1 \end{bmatrix} \begin{bmatrix} x \\ y \end{bmatrix} \bmod N \tag{1}$$

Here, (x, y) is pixel position of the source image sized in NxN and (x', y') refers corresponding pixel position. p and q are control parameters of the system which are positive integers. The inverse of ACM is determined in (2).

$$\begin{bmatrix} x \\ y \end{bmatrix} = \begin{bmatrix} pq+1 & -p \\ -q & 1 \end{bmatrix} \begin{bmatrix} x' \\ y' \end{bmatrix} \bmod N \tag{2}$$

ACM can be used as a permutation method for any image. In this technique, permutation process focuses on the position of

pixels not the pixel values in the image. In mathematically, ACM is a linear transformation with simple mod operation.

B. GRP Method

GRP method has two inputs named as data and control bits. In this technique, input data is swapped according to the control bit. Here, input data values are placed in two groups as a left group and a right group. According to the control bit, if bit i of the control bit is 0, then the value of i in data goes to the left group, otherwise it goes to the right group. This process is performed in sequential until all the control bits is checked and relative positions of the input data within the same group do not change. Figure 1 shows as an example of how the GRP instruction works on 8-bit systems.

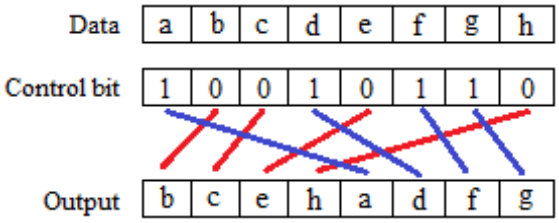

Figure 1. 8-bit GRP operation

C. Logistic Map

Logistic map is a simple non-linear discrete system [16]. It consists of an iterative equation as defined in (3).

$$x_{n+1} = r.x_n(1 - x_n) \tag{3}$$

Here, r is the control parameter and chosen as $0 < r \leq 4$; x_n is state variable of the map. For any initial value under $x_0 \in (0,1)$, the map generates sequence of values in the range of (0,1). Logistic map has very rich dynamic behaviors such as stationary, periodic and chaotic depending on control parameter. When $r \in [3.57,4]$, then the generated sequence is aperiodic, non-convergent and very sensitive to initial value which leads to chaos and resulting very complicated and unpredictable behavior. Bifurcation diagram of the Logistic map is shown in Figure 2.

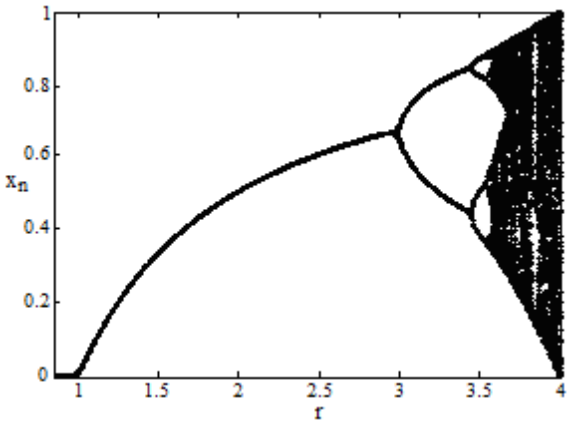

Figure 2. Bifurcation diagram of the Logistic map

D. AMDS Test

In image processing, main purpose of a permutation is to change pixel positions of an image through a specific algorithm so original pixel positions need to be moved to another positions. If a pixel has been moved farther away comparing to its original location, then the degree of permutation is higher [17]. This process can change the visuality of an image although it does not affect pixel values. The average moving distance of scrambling is defined as in (4).

$$AMDS = \frac{1}{M \times N} \sum_{i=1}^{M} \sum_{j=1}^{N} \sqrt{(w-i)^2 + (v-j)^2} \tag{4}$$

In (4), (i,j) represents original pixel coordinate in an image with a size of $(M \times N)$ and (w,v) represents permutated pixel coordinate. In ACM method, pixel positions change in diagonal direction so AMDS test can be used to calculate the displacement of pixel positions for this method. On the other hand, in GRP method, pixel positions change in one direction only. Therefore, for each line of the permutated image, position change of the pixels is calculated separately then average distance value is calculated as in (5).

$$ADS = \frac{1}{M} \sum_{l=1}^{M} D_l \tag{5}$$

For instance, means coordinate changes for the pixel address of (1,1:M) between original and permutated image. The larger value of AMDS or average distance of scrambling (ADS) means that less relation between the original image and permutated image and also higher efficiency of the permutation method. For a square image with 256 size, universal mean of the average moving distance for random permutation is 256/3=85.3 [17]. This value can be used as a criterion to compare the efficiency of the permutation for both methods.

E. NEPR Test

NEPR is related to number of the same pixel values found in specific coordinates between the original image and permutated image. It is measured in percent and defined in (6).

$$NEPR(O,S) = \frac{1}{M \times N} \sum_{i=1}^{M} \sum_{j=1}^{N} \left[T(O(i,j), S(i,j)) \right] \times 100\%$$
$$T(O(i,j), S(i,j)) = \begin{cases} 1 & , \ O(i,j) = S(i,j) \\ 0 & , \ O(i,j) \neq S(i,j) \end{cases} \tag{6}$$

NEPR shows the rate of identical pixel values at the same position between original and permutated images. If NEPR value is high, then efficiency of the scrambling is lower. If NEPR is zero, then no pixel values are equal at the same coordinate.

F. CCAP Test

In an ordinary image, an arbitrarily chosen pixel is strongly correlated with its adjacent pixels either they are vertically, horizontally or diagonally oriented.

$$cc = \frac{\sum_{i=1}^{N}(x_i - \bar{x}).(y_i - \bar{y})}{\sqrt{\left(\sum_{i=1}^{N}(x_i - \bar{x})^2\right)\left(\sum_{i=1}^{N}(y_i - \bar{y})^2\right)}} \quad (7)$$

This correlation needs to be broken after permutation process. Consequently, in the case of high-performance permutation methods, correlation coefficients of adjacent pixels are expected to be close to zero. The formula of the correlation coefficient is defined in (7).

The formula given in (7) returns a value between -1 and 1. Correlation coefficient of 1 means a strong positive relationship between two variables. Correlation coefficient of -1 indicates that for every positive increase in one variable, there is a negative decrease of proportion in the other. 0 means no relationship between two variables.

G. Generating Control Bit

GRP method uses a sequential control bit for data replacement. In this study, chaotic Logistic map is used to generate control bit for GRP method. In order to get a sequential bit, a map equation in (8) is utilized.

$$control_bit = \begin{cases} 0 \ , \ x_n < 0.5 \\ 1 \ , \ x_n \geq 0.5 \end{cases} \quad (8)$$

Using (8), a control bit value of '1' or '0' is generated for each x_n which is the output of Logistic map. For instance, generated bit values are listed in Table 1, when the system parameters are selected as x_0=0.1234 and r=4.

TABLE I
GENERATING BIT VALUES USING LOGISTIC MAP

Log. Map Output	0.4327	0.981	0.0712	0.2644	0.7781	0.6907	0.8545	0.4974
Output of the (8)	0	1	0	0	1	1	1	0

III. Experimental Results

In this section, test image of 'Peppers' with different size is used for the performance evaluation of both permutation methods. Since both permutation methods depend on pixel positions rather than pixel values, the meaning of the test image does not have much importance. However, the size of the test images may affect results of the performance analysis for both methods. In some analysis, test images with different size are taken into consideration for the performance comparison. The performances of the both methods are also compared with different iterations of permutation operation.

A. Visual Analysis

'Peppers' test image with 256x256 size is used for visual analysis. Figure 3 shows the results of ACM method applied on the test image for different number of iteration (n) with randomly selected parameters of p=5 and q=4.

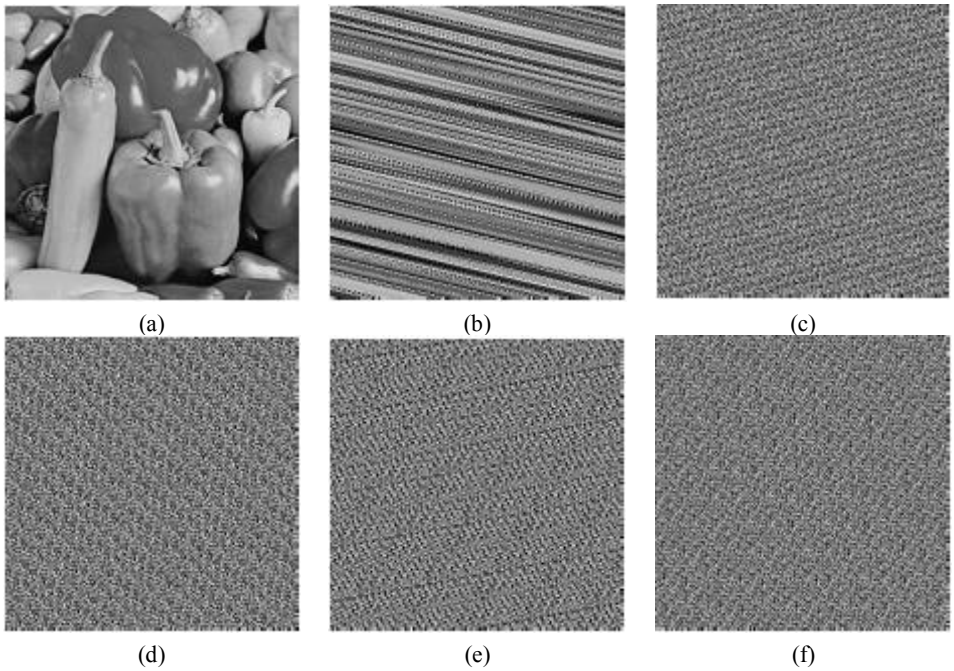

Figure 3. Results of ACM for 'Peppers' image with different number of iterations: (a) n=0 (b) n=1 (c) n=3 (d) n=8 (e) n=15 (f) n=40

Figure 4 shows the results of applying GRP-256 bit method on the 'Peppers' image for different number of n.

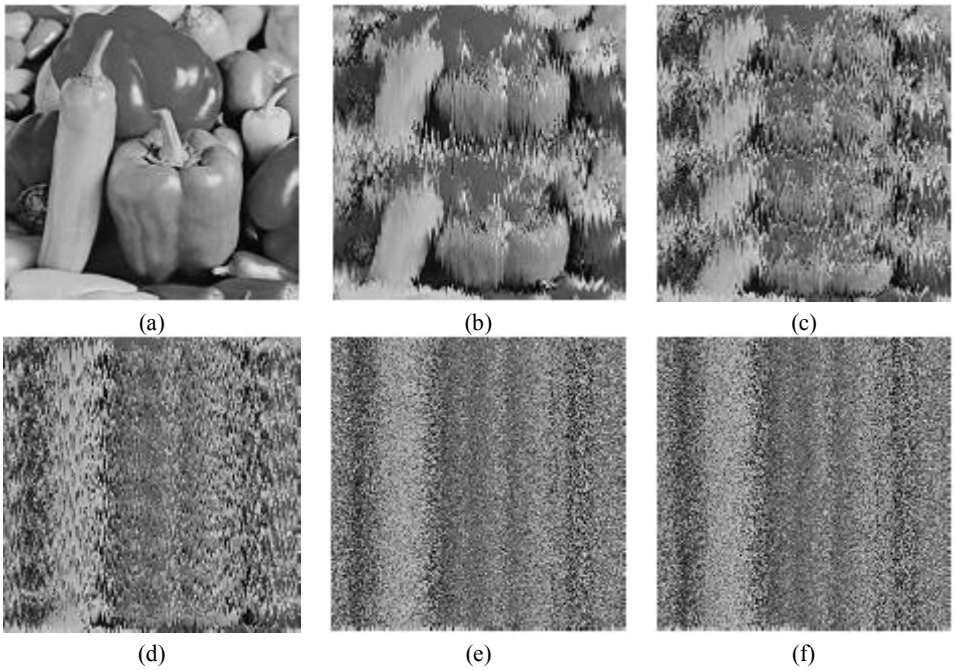

Figure 4. Results of GRP-256 bit for Peppers image with different number of iterations: (a) n=0 (b) n=1 (c) n=2 (d) n=3 (e) n=15 (f) n=40.

According to the results of Figure 3, in ACM method the test image becomes meaningless after the first iteration. This provides sufficient and effective permutation with only one iteration of the test image. On the other hand, GRP-256 bit method makes the test image meaningless completely at the end of the 3th iteration, so in GRP method, iterations must be done several times for enough complexity. It is concluded that for visual analyses, ACM shows better performance than the GRP-256 bit method.

B. AMDS Analysis

Test images with different size are used to determine AMDS values for ACM and GRP methods. AMDS values are calculated for different number of iterations for ACM and the results are listed in Table 2.

TABLE II
AMDS VALUES FOR ACM METHOD

Image size	**ACM (p=1; q=1)**	**Number of iterations**				
		n=1	n=2	n=3	n=4	n=5
128x128	AMDS	69.2	67.3	66.9	66.7	66.7
256x256	AMDS	**138.5**	**134.6**	**133.8**	**133.5**	**133.4**
512x512	AMDS	277.0	269.2	267.7	267.0	266.9

TABLE III
ADS VALUES FOR GRP METHOD

Image size	**GRP**	**Number of iterations**				
		n=1	n=2	n=3	n=4	n=5
128x128	ADS	37.1	39.2	40.4	41.8	43.0
256x256	ADS	63.6	78.1	81.7	83.9	**87.2**
512x512	ADS	127.9	156.0	159.8	163.2	167.1

ADS values are calculated for test images with different sizes and number of iterations for GRP method. Results are listed in Table 3.

According to the Table 2 results, AMDS values decrease slightly as the number of iterations increases in ACM method. However, the calculated values (written in bold) are significantly higher than the critical level. This indicates a sufficient permutation of the ACM method. On the other hand, according to the Table 3, the values obtained from GRP are much lower than the ACM values for all iterations. Furthermore, if the number of iteration increases, then ADS value also increases significantly. Hence, enough number of iterations is needed for effective permutation in GRP method. For instance, an image with a size of 256x256 requires 5 iterations for ADS to be greater than the critical value of 85.3. In addition, as the size of the test images increases, both AMDS and ADS values also increase proportionally. As a result, in ACM method, the degree of displacement of pixel positions is much better than the GRP method.

C. *NEPR Test*

After an effective permutation process, number of equal pixels for the same pixel coordinates between original and permutated images should be very low. NEPR test is applied for ACM method for different iterations of the permutated version of the image and results are listed in Table 4.

TABLE IV
NEPR VALUES FOR ACM METHOD

Image size	**ACM (p=1; q=1)**	**Number of iterations**				
		n=1	n=2	n=3	n=4	n=5
128x128	NEP	83	93	108	109	112
	Rate (%)	**0.51**	0.57	0.66	0.66	0.68
256x256	NEP	345	367	417	396	404
	Rate (%)	0.53	0.56	0.64	0.60	0.62
512x512	NEP	1802	1811	2003	2157	2059
	Rate (%)	0.69	0.69	0.76	0.82	0.78

TABLE V
NEPR VALUES FOR GRP METHOD

Image size	**GRP**	**Number of iterations**				
		n=1	n=2	n=3	n=4	n=5
128x128	NEP	537	578	603	649	592
	Rate (%)	3.28	3.53	3.68	3.96	3.61
256x256	NEP	1714	1696	1794	1859	1759
	Rate (%)	2.62	2.59	2.74	2.84	2.68
512x512	NEP	5953	5812	5792	6067	5825
	Rate (%)	2.27	2.22	**2.21**	2.31	2.22

NEPR values are calculated for test images having different sizes for GRP method. Results are listed in Table 5.

According to the NEPR results for both methods, the overall performance of ACM is better than the GRP. For ACM method, the minimum NEPR value occurs in the first iteration of a 128x128 image, while in GRP method, the minimum NEPR value occurs in the third iteration of the 512x512 test image. This confirms that ACM method has a great permutation effect on the test image for small number of iterations. In addition, GRP requires several times of iteration for sufficient permutation of the test image. All NEPR results in GRP are significantly bigger than the results of ACM for all sizes and number of iterations.

D. *CCAP Test*

In a good permutated image, an arbitrarily chosen pixel is weakly correlated with its adjacent pixel. Correlation coefficient value between original and permutated images should be small in an effective permutation. ACM and GRP methods are applied to the test image of 'Peppers' and then CCAP test is performed in vertical (V), horizontal (H) and diagonal (D) directions to compare the performance of both methods. The average results are listed in Table 6 and Table 7. Minimum values of CCAP are written in bold.

TABLE VI
CCAP VALUES FOR ACM METHOD

Image size	ACM (p=1; q=1)	Direction	Number of iterations				
			n=1	n=2	n=3	n=4	n=5
128x128	CCAP	V	-0.3243	-0.1071	0.1582	-0.0452	0.1299
		H	0.0164	-0.3370	**0.0091**	0.2463	0.1251
		D	-0.1144	-0.2151	-0.1077	-0.0674	**-0.0496**
256x256	CCAP	V	-0.3116	-0.1112	0.1744	-0.0647	0.0838
		H	**0.0323**	-0.3386	-0.0688	0.1711	0.0741
		D	-0.1289	-0.1891	-0.1400	**-0.0983**	-0.1035
512x512	CCAP	V	-0.3569	0.1041	0.0535	-0 0301	**0.0195**
		H	0.0318	0.0613	-0.1473	**0.0132**	-0.0568
		D	-0.1123	**-0.0082**	-0.1317	-0.0546	-0.0856

TABLE VII
CCAP VALUES FOR GRP METHOD

Image size	GRP	Direction	Number of iterations				
			n=1	n=2	n=3	n=4	n=5
128x128	CCAP	V	0.1319	-0.1014	**0.0389**	0.0410	-0.1776
		H	0.0858	0.3265	0.4179	0.3992	0.2571
		D	0.3420	0.2472	0.0983	0.1953	0.0776
256x256	CCAP	V	0.1082	-0.0977	**-0.0292**	0.1042	0.1088
		H	0.1296	0.0899	0.1784	0.2803	0.3324
		D	0.3142	0.1473	0.1153	0.2484	0.1846
512x512	CCAP	V	0.2721	-0.1169	-0.1040	-0.0513	0.0552
		H	0.1240	0.1160	0.1616	0.1838	0.2292
		D	0.4996	0.2458	0.1757	0.2370	0.1674

According to the CCAP test results, ACM method shows better performance than GRP method. If all numerical and visual analyses are considered for both methods, ACM is a better choice against GRP in order to break correlation of adjacent pixels in an image.

IV. CONCLUSIONS

In this paper, performance evaluation of two important permutation methods used in image processing are concerned in order to compare their performances through visual and numerical analyses. In both visual and numerical analyses, ACM method shows better performance than the GRP method. AMDS and NEPR test results are critical points under the numerical analyses for the performance evaluation of the both methods. These results demonstrate that ACM changes pixel positions more effective as well as bigger in size with respect to the GRP method for all iterations. Although the total displacement of pixels is smaller in the GRP method, the average pixel distance between the previous and next iteration of the permutation are bigger than the ACM method.

REFERENCES

[1] Patidar, V., Pareek, N. K., Purohit, G., & Sud, K. K. (2011). A robust and secure chaotic standard map based pseudorandom permutation-substitution scheme for image encryption. *Optics communications*, *284*(19), 4331-4339.

[2] Enayatifar, R., Abdullah, A. H., Isnin, I. F., Altameem, A., & Lee, M. (2017). Image encryption using a synchronous permutation-diffusion technique. *Optics and Lasers in Engineering*, *90*, 146-154.

[3] Huang, L., Cai, S., Xiong, X., & Xiao, M. (2019). On symmetric color image encryption system with permutation-diffusion simultaneous operation. *Optics and Lasers in Engineering*, *115*, 7-20.

[4] Belazi, A., El-Latif, A. A. A., & Belghith, S. (2016). A novel image encryption scheme based on substitution-permutation network and chaos. *Signal Processing*, *128*, 155-170.

[5] Patro, K. A. K., & Acharya, B. (2019). An efficient colour image encryption scheme based on 1-D chaotic maps. *Journal of Information Security and Applications*, *46*, 23-41.

[6] Huang, H., He, X., Xiang, Y., Wen, W., & Zhang, Y. (2018). A compression-diffusion-permutation strategy for securing image. *Signal Processing*, *150*, 183-190.

[7] Oğraş, H., & Türk, M. (2017). A Robust Chaos-Based Image Cryptosystem with an Improved Key Generator and Plain Image Sensitivity Mechanism. *J. Inf. Secur*, *8*, 23-41.

[8] Patro, K. A. K., & Acharya, B. (2018). Secure multi–level permutation operation based multiple colour image encryption. *Journal of information security and applications*, *40*, 111-133.

[9] Ping, P., Xu, F., Mao, Y., & Wang, Z. (2018). Designing permutation–substitution image encryption networks with Henon map. *Neurocomputing*, *283*, 53-63.

[10] Oğraş, H., & Türk, M. (2016). A Secure Chaos-based Image Cryptosystem with an Improved Sine Key Generator. *American Journal of Signal Processing*, *6*(3), 67-76.

[11] Chen, F., Wong, K. W., Liao, X., & Xiang, T. (2014). Period distribution of generalized discrete Arnold cat map. *Theoretical Computer Science*, *552*, 13-25.

[12] Abbas, N. A. (2016). Image encryption based on independent component analysis and arnold's cat map. *Egyptian informatics journal*, *17*(1), 139-146.

[13] Chai, X., Fu, X., Gan, Z., Lu, Y., & Chen, Y. (2019). A color image cryptosystem based on dynamic DNA encryption and chaos. *Signal Processing*, *155*, 44-62.

[14] Dhall, S., Pal, S. K., & Sharma, K. (2018). A chaos-based probabilistic block cipher for image encryption. *Journal of King Saud University-Computer and Information Sciences*.

[15] Nazari, S., Moin, M. S., & Kanan, H. R. (2016). A face template protection approach using chaos and GRP permutation. *Security and Communication Networks*, *9*(18), 4957-4972.
[16] Hua, Z., & Zhou, Y. (2016). Image encryption using 2D Logistic-adjusted-Sine map. *Information Sciences*, *339*, 237-253.
[17] Xiangdong, L. I. U., Junxing, Z., Jinhai, Z., & Xiqin, H. (2008). Image scrambling algorithm based on chaos theory and sorting transformation. *IJCSNS International Journal of Computer Science and Network Security*, *8*(1), 64-68.

BIOGRAPHIES

HIDAYET OGRAS received his Ph.D degree in Electrical and Electronics Engineering from the University of Firat, Elazig, Turkey, in 2017. He is currently an Assistant Professor at department of Electronics Communication in Batman University and his research interests cover chaos-based Cryptography and Steganography. He is also interested in Secure Communication Systems and Signal Processing.

FIDAN ŞEHMUS is an assistant professor at department of electronic technology in Batman University. He received his bachelor's degree in Electric Education from University of Gazi, Ankara, Turkey. In 2010 he completed his graduate education at Afyon Kocatepe University, Turkey. He received Ph.D. degree in Electrical and Electronics Engineering from the University of Firat, Elazig, Turkey, in 2018. His works focuses control systems and power electronics of Wind Turbine. He is also interested in machine learning and its real application.

Blockchain Based Information Sharing Mechanism for Cyber Threat Intelligence

E. BUBER, O.K. SAHINGOZ

***Abstract*— In recent years, networked computers are extensively used in every aspect of our daily lives. Besides, the anonymous structure of the Internet results in an increase in the number of attacks not only for individual users but also for local area networks. Current attacks are more sophisticated, and they are developed by experienced intruders with the use of automated malware production methods. These organized intrusions can go over the defense lines of the systems due to the weakness of the detection/prevention mechanisms or carelessness of individual users. After sneaking into the system, these attacks can work until they are detected, and they can access many critical resources of the company. Earlier detection of these attacks is very trivial issue for the security admins. This can be accomplished by acquiring the signature (critical information) of the newest attacks as early as possible. One suggested solution is the use of a *Threat Information Sharing* system, which is set up between security firms and authorities. This approach enables the distribution of the marks of the recent (zero-day) attacks and the development of some proactive prevention mechanisms for them. The use of both peer to peer and centralized sharing mechanisms have some inherited deficiencies. Therefore, in this paper, a pure decentralized cybersecurity information sharing system is proposed with the use of blockchain technology. A controlled decision-making mechanism, authorization termination, and rule-sets maintenance are proposed to make distributed decisions within the system. For making a decision, two smart contracts should be used in the blockchain. One holds the positive votes while the other holds the negative ones. Members of the system are able to access cyber threat data by using company-related queries. The system can facilitate the integration of many data sources into cybersecurity management system. Additionally, it enables us to collect in a single repository that can be accessed for implementing real-time cybersecurity applications.**

Index Terms— **blockchain, cyber threat intelligence, information sharing, controlled decision-making mechanism, smart contract.**

EBUBEKIR BUBER, is with Department of Computer Engineering at Yildiz Technical University, Istanbul, Turkey (e-mail: ebubekirbbr@gmail.com).

https://orcid.org/0000-0002-0586-7514

OZGUR KORAY SAHINGOZ, is with Department of Computer Engineering at Istanbul Kultur University, Istanbul, Turkey, (e-mail: o.sahingoz@iku.edu.tr).

https://orcid.org/0000-0002-1588-8220

Manuscript received November 10, 2019; accepted June 10, 2020.
DOI: 10.17694/bajece.644948

I. INTRODUCTION

IN RECENT years, computer technologies have been developed rapidly and continue to evolve. This development has also brought some negative effects with it. Parallel to this enhancement, there is a steady increase in cyber-attacks.

As a result of digitalization, not only the huge companies but also the small ones (even single users) have become more sensitive to the privacy and security of their data where much of their personal information is stored in the cyberworld.

In the 2019 report of Ninth Annual Cost of Cybercrime Study of Accenture [1], the average loss of companies exposed to cyber-attack in 2018 increased to $ 13.0 M, compared to $ 11.7 M in 2017. According to the report, the increase in the last year is about 12% and the increase in the last 5 years is about 72%. For the next five years, the total value at risk from cybercrime is expected as $5.2 trillion. Therefore, to preserve the companies, some additional protection mechanisms should be constructed.

In traditional way the security of the network can be established with the use of firewall mechanisms and intrusion detection mechanisms (IDSs)[2][3][4]. Although the use of these systems is very efficient, the success of them directly related with the definition of threats and attacks in a quick and up to date way for catching the zero-day type attacks.

Many companies do research on detection and prevention systems to make their systems more secure against cyber-attacks. Their experiences are stored as a knowledgebase in their systems that construct intelligence. This intelligence can either be gained after encountering some type of attacks or by accessing this information over some servers, which are maintained and shared by some security firms or agencies. This shared information is called *Cyber Threat Intelligence*. For example, Phishtank [5] shares URL addresses that are used in a phishing attack to anyone. Some additional ones can be listed as follows; IBM X-Force Exchange [6], Palo Alto Networks Auto Focus [7], LogRhythm Threat Lifecycle Management [8], FireEye iSIGHT [9], LookingGlass Cyber Solutions [10], Normshield Inc. [11], Firehol IP Lists [12].

There are 3 different groups of companies who share their cyber threat information as follows.

- Companies, which share the information free of charge (e.g., government agencies)
- Companies, which share the information with a fee (e.g., some commercial firms)
- Companies, which provide the information to users free

of charge after a certain period from the detection of threat, while charging for up to date sharing (e.g., some commercial firms)

These companies can share the information either via their web pages or through an API. Many companies prefer the second method, and their cyber threat information can be accessed from a single centralized platform by using an API. In order to collect data from different platforms, users must perform some additional efforts for each cyber threat information server.

For the threat information sharing companies, the amount of data stream is quite high. This data sharing can be either in peer to peer communication model or in a client server architecture. Each of them has some specific deficiencies. Collecting and distributing data from a single data center slow down the system and make it difficult to scale. It is thought that sharing information with a distributed structure should be more efficient than gathering and sharing in a single center. Therefore, in this study, a blockchain-based approach was proposed to share the cyber threat information data in a distributed way.

Blockchain technology emerged as an acceptable solution for a distributed solution. Setting up a blockchain network gives trust to the information distribution service, which can be on untrusted sources. The system also combines easy access from anywhere in the world by using a global network like the Internet, with cryptographic security to give each member a fast and safe way to verify critical information by establishing trust between them. Members (companies) can easily add threat information for being accessible by each member in the system. However, some information should only be accessible by authorized users depending on their membership type.

In this paper, a distributed cybersecurity information system is proposed to keep the protection mechanism of the system up to date. The system is designed with the blockchain technology to enable a cryptographic security mechanism in a distributed structure. Not only the reliability but also the up to date cyber threat information are very critical for security admins. An axiom for incorrect cyber threat information can have very bad consequences. Cyber threat information can be verified, and information can be extracted about the reliability of this information, with the proposed blockchain mechanism. Many companies can enter data about the same asset (e.g., IP). They can enter cyber threat information for the same malicious IP address. This makes it easier to analyze assets that are false positive, while those that are harmful stand out. The information added to the chain cannot be changed or deleted due to the blockchain structure. This means that the cyber threat information data for the system to be designed should be stored continuously in a historical way.

In the proposal, some decisions need to be taken at some stages. Therefore, a controlled decision-making mechanism is designed to make the necessary decisions to ensure the functioning of the system. This mechanism is built on a voting-based system. Decision-making is carried out on a distributed structure within the system. Smart Contracts are generally preferred to solve his situation used.

The rest of the paper is organized as follows: In the next Section, the background information on blockchain technology is explained. The proposed blockchain structure for the cyber threat information system and detailed analysis of this system is detailed in section III and Section IV, respectively. Finally, the discussion and conclusion about the topic are drawn.

II. Literature Review

Cybersecurity is a very critical issue not only in civil life but also in the military field [13]. Cyberpower and abilities are among the most important power elements among states today. Accordingly, we started to see blockchain technology more and more every day in the military field as well as the other fields [14]. The protection of personal data has become a very important issue for all applications today. There are many application areas where blockchain technology is applied in the field of cybersecurity [15]. With the proliferation of the Internet of Things (IoT), the small devices we use in our daily lives have become connected to the internet and can communicate with each other. The security of data transfer between these devices is a very important issue. IoT related studies on networks and machine visualization, public-key cryptography, web applications, certification schemes, and the secure storage of Personally Identifiable Information (PII) are included in the literature.

Systematic integration of the IoT and Cyber-Physical Systems (CPS) into the supply chain has also brought new complexities to the threat environment to increase operational efficiency and quality. And IoT devices can be easily targeted by attackers. [16] introduced an innovative blockchain-based secure and privacy-preserving data sharing mechanism for IoT devices (specifically for smart cities). Identifying cyber threats and planning the axioms required for possible cyber incidents are routine procedures for many computer network systems. Blockchain technology can be applied to intrusion detection systems as it maintains data integrity and provides transaction transparency [17].

For the threat information sharing companies, the amount of data stream is quite high. This data sharing can be either in peer to peer communication model or in a client server architecture. Each of them has some specific deficiencies. Some institutions share cyber intelligence data to reduce the cost of cyber-attacks on a global scale. Integration of these shared data into cybersecurity products and keeping these data up to date can be costly. As a solution to this situation, studies in which blockchain-based cyber intelligence data are shared are proposed [18][19][20].

Blockchain-based systems have risks, as with any application, associated with cyber-attacks [21]. For example, weaknesses arising from blockchain code, vulnerabilities that may result in end-user applications, weaknesses arising from the application environment where blockchain application is run, etc. These risks should be considered in the system to be developed and should be minimized. Besides, blockchain can also be used for cybersecurity such as visualization for security management [22], cyber insurance for cyber risk

management [23], and cyber forensics analysis [24].

Similar to these works, this technology can also be applied in some new and popular concepts such as smart cities for setting up an dynamic and distributes security mechanism by also using different data transfer models such as publish subscribe communication paradigm [25][26].

III. BLOCKCHAIN

Blockchain technology has become more popular in recent years, with Bitcoin [27] and Ethereum [28]. Bitcoin and other virtual currencies are built on blockchain technology briefly are a distributed (decentralized) and common data recording system [29]. This structure provides security, transparency, reliability, and precision for storing data. The transfer between members is done with a smart contract, which is a computerized transaction protocol that fulfills the terms of the contract whose terms have been determined by the contractor [34]. A blockchain is the name given to a chain of consecutive blocks. Each block is linked to the previous and next blocks. The blockchain has recently managed to attract attention. Many researchers from the business and academic backgrounds have begun researching applications that can be developed on this technology [31] [32].

The blockchain can be summarized as a data storage platform that serves as a public ledger. Transaction performed in blockchain technology is written into blocks in a chain. When a new chain is added, this chain grows continuously. The main advantage of the blockchain is its cryptographic security. It is almost impossible to change a block written to the chain. Additionally, a blockchain has features such as decentralization, persistency, and auditability.

The blockchain can operate in a decentralized environment by integrating many key technologies such as cryptographic hash, digital signature (based on asymmetric cryptography), and distributed consensus mechanism. With blockchain technology, a transaction is approved and published in a decentralized manner. For example, money can be transferred between two accounts without any central authority (bank). This decentralized structure, which eliminates central authority, can reduce costs, and increase productivity.

Blockchain can be used for money transfer as well as many other financial applications such as online payment [33] and managing digital assets. In addition, blockchain can also be used in applications such as; smart contract [34], public services [35], Internet of Things (IoT) [36], reputation systems [37] and security services [38].

A. Chain Structure

In the blockchain, all blocks except the first block have a parent. Each block holds the address of the parent block. A representative diagram that shows the mechanism is depicted in Figure 1.

Fig.1. Blockchain Representation

Each block has a hash value, which is calculated by using the stored data in the block. Therefore, if data in the block is changed, this hash should also be changed. This is used as a validation mechanism for not changing the data in the block. The hash of each block is held by its following block. In this way, a blockchain with a linked list structure is created. In addition to the hash, some values are kept in the block for the operation of the system, and necessary security measures can be taken.

A block consists of two parts: the block header and the block body. The block header contains the following information [39];

- Block version: Specifies which block validation rules to follow.
- The hash of parental block: A 256-bit hash that points to the previous / parent block.
- The hash of the Merkle tree: The hash value of all operations in the block.
- Timestamp: The current timestamp.
- nBits: current hash target in a compact format.
- Nonce: A 4-byte field that usually starts with 0 and shows increments for each hash.

An example image of the information contained in a block header is given in Figure 2.

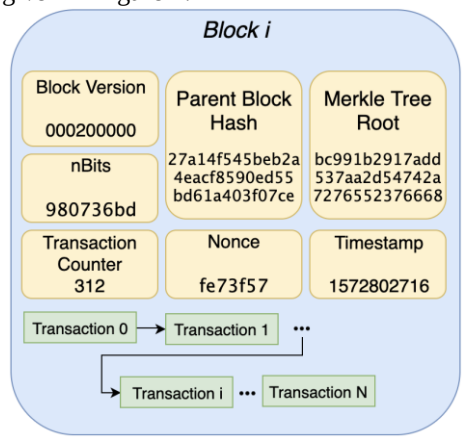

Fig. 2. Block Structure

The block body consists of a transaction counter and transactions. The maximum number of transactions in a block depends on the size of the block and the size of each transaction. The blockchain uses an asymmetric cryptography mechanism to verify transactions [40].

For the blockchain system to work, the entered block data must be validated by all miners (nodes). Consistent reconciliation between all nodes is required. Reconciliation between miners is called Consensus. To establish continuous consensus between many nodes is critical in the highly dynamic blockchain structure. The blocks are prepared and added to the chain, and the consensus is ensured among the miners.

How to reach the Consensus between miners is a trivial problem that must be solved in such a dynamic environment where different miners are constantly being produced and added data to the chain. There is no central node in the blockchain that ensures that the ledger in the distributed nodes is the same. Nodes do not need to trust other ones. Therefore,

some protocols are required to ensure that the ledger on different nodes is consistent. There are many protocols developed in the literature to solve this problem. Two of these are PoW (Proof of Work) [27] and PoS (Proof of Stake) [32]. PoW is the protocol used for Bitcoin Consensus. PoS is an energy-efficient version of PoW. In addition to these protocols, many methods have been developed in the literature to achieve consensus [39].

B. *Smart Contract*

Smart Contract (SC) is a programmable transaction protocol that fulfills the terms of the contract whose terms are determined by the contractors [34]. A smart contract in a blockchain is a piece of code that can be executed automatically by miners. Smart contracts have been integrated into many blockchain mechanisms, such as the Ethereum [28].

Smart contracts can be defined as a block of programming code containing streams of if-else components. Smart contracts are added to the blockchain like an ordinary block. An SC is a new generation contract type with distributed working mechanism, continuity, and traceability provided by blockchain structure. Smart contracts added to the chain can be operated automatically when the specified conditions are met, or they can also be operated manually.

Smart contracts are prepared / programmed after cryptographic agreements between contractors and signed cryptographically and entered to the blockchain. Loaded smart contracts can interact with other components on the blockchain. This interaction can be the initiation of a transaction or the sending / receiving of information. When contractual situations occur (such as receiving a specific message), smart contracts automatically execute the contract terms defined in it.

For example, a smart contract for a forward transaction can trigger mutual share transfer and payment transactions between contractors if the transaction price of the share reaches a predetermined value. A smart contract for insurance can use the weather information to trigger the corresponding insurance payment to the contractor in case the rain rate falls below (or above) a certain level. A smart contract for a postdated check may trigger the payment to the contractor when the collection date is reached and, if there is not enough balance in the account to be paid, it may trigger the freezing of the smart contract. With the rapid development of blockchain technology, the use of many smart contracted applications in daily life is expected to become widespread.

IV. The Proposed System

In this paper, a blockchain-based cyber threat information sharing system is proposed. In this system, anyone, either as an individual or as a security company, can access the blockchain with read-permission. However, information can only be entered into the blockchain by trusted partners. Therefore, different user roles are needed in the proposed system. In order to ensure the distributed functioning of the system, trusted partners must be identified and authorized within the blockchain.

Additionally, some rule-sets should be issued and implemented in order to maintain the continuity of the system. These rule-sets needed to be used for small scale blockchain systems. But over time, there may be a need for new rule-sets to be used for large scale blockchain systems. Therefore, it is for such a system to be able to define rule-set definitions that can be updated over time. Updateable rule-sets allows the system to be scaled more easily.

A partner who is authorized to write to the blockchain can enter cyber threat information into the blockchain. However, the fact that the obtained authorization, which lasts for a lifetime, may cause some problems. For example, a partner can gain permission to write the blockchain. Then after a certain period, this partner may enter incorrect information into the system for various reasons. It is thought that the lifetime use of the given authorizations may create negative effects that prevent the system from functioning properly. Therefore, an authorization mechanism is needed to be designed in an updatable manner. This system should be designed that can be overwritten by a partner who is authorized.

Partners who are registered to the information sharing system in the blockchain mechanism may be non-commercial organizations or institutions with commercial aims. The later may request some money from the clients who want to access this information from the sharing system. It is thought that the existence of a kind of payment mechanism may increase the preferability of the system.

There may be many partners who have write-permission to the system. Some of them may be leading companies in the field or companies that have just started to serve in this field and whose services are still under development. Evaluating these companies which are different in terms of reliability at the same level, can make it difficult to use the provided information efficiently. Therefore, designing a mechanism that demonstrates the reliability and experience levels of firms should facilitate the more efficient use of cyber intelligence data by users.

Only trusted partners can add new blocks in the chain. The number of trusted partners is expected to be much less than the number of users who have reading-permission. It takes some time for all miners to validate the information written to the blockchain. Since the number of users performing a write operation to the chain should be small, it is expected that information added in the chain should be quickly verified. Rapid processing and validation of information are crucial to take immediate preventions against cyber-attacks.

The authorization mechanism and the update of the rule-sets should be made through controlled decisions taken by trusted partners. The proposed platform should also enable other companies to verify the added information. Thus, the accuracy of cyber threat information can be evaluated.

A. *Authorizations and User Roles*

The system is designed with a User-Based Access Control model. There are be 3 different types of privileges in the system. User profiles can have at least one of these privileges

are "*Read", "Write" and "Vote"*.

The data in the blockchain can be readable by all users. This means that all users have the reading privilege. Write authorization is needed to write cyber threat information to the blockchain. Controlled decisions are required within the system in order to continue the operation of the blockchain mechanism. These decisions are built on a voting-based system. Some users who are authorized to write also have the right to vote in the decision-making mechanism. Voting authority is not an authorization granted to all users who have write-authority. This privilege is granted only to users who are trusted partner.

There are 5 different user roles in the system, which are listed as follows;

- *Reader:* Only users who want to read the information in the blockchain are included in this user profile. This user profile is only authorized to read.
- *Standard Partner:* Users who have both read and write privileges in the system are included in this profile.
- *Standard Partner Candidate*: It is the profile of the users who want to become a standard partner during the review stage. Users with this profile do not have write-privileges on the main chain but have write-authorizations on the test chain. This write authorization obtained on the test chain expires after a certain period.
- *Trusted Partner:* Users who have access to the system with read, write, and vote-privileges are included in this profile.
- *Founder Partner:* Trusted Partners who are responsible for carrying out initialization operations for the system to start are included in this profile.

A user can first access the system in the Reader profile except for Founder Partners. If the user fulfills the necessary conditions, he can obtain other privileges and switch to other profiles. Similarly, a user can be downgraded from the Standard Partner profile to the Reader profile with Controlled Decision-Making Mechanism (CDMM). Operations such as user authorization are carried out with a controlled decision mechanism in the system. CDMM can be implemented within the framework of certain rules. The rules for operation are defined in the rule-sets.

B. Initialization

A user must collect a number of votes, in order to be authorized within a CDMM. Many trusted partners are needed for voting. Since the system doesn't have any trusted partner defined in the system at the beginning time, it was necessary to design an initial state for the system to start working.

Initially, there are N trusted partners who must come together to undertake the initialization steps necessary for the system to operate in the initial state. These partners are included in the Founding Partner profile in the system. Founder Partners should add a pair of SCs to the chain, just like any other user to be defined in the system. 3 different types of SCs are used for the operation of the system. These are;

- Positive Vote Contact (PVC)
- Negative Vote Contract (NVC)
- Control Contract (CC)

CC verifies that the requirements for the decision-making mechanism are met. PVC and NVC are used for counting votes whose mechanism is detailed in the ongoing parts.

In the initial state, all the founding partners are needed to vote by running the PVC of all other founding partners except himself. In this way, each founding partner should have N-1 positive votes. The initial state in which the founding partners voted each other is represented in Figure 3.

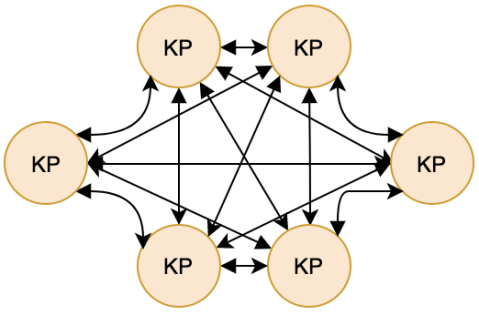

Fig.3. Initial Situation in which Founding Partners Vote for Each Other

The founding partners add the first CC to the blockchain to get the system up and running.

The first CC added to the system is called the Master Control Contract (MCC). The MCC maintains the addresses of other control contracts. The founding partners add only one MCC to the system. Each founding partner then creates its own CC and adds it under to the MCC.

CCs are designed as a tree structure. Each CC is derived from another CC. The first control contract defined in the system is the MCC. Each founding partner then adds its own CC to the system under the MCC. When the initial state is completed, the system has one MCC and one control contract as much as the number of founding partners. The tree structure of the control contract is given in Figure 4.

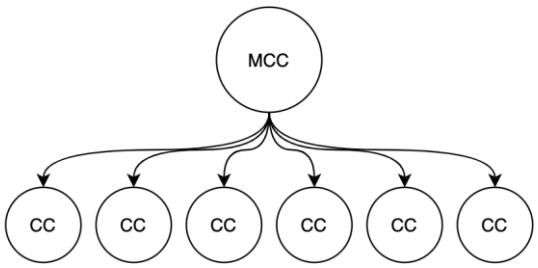

Fig. 4. Tree Structure of Control Contracts

After the initial state, the user authorization steps with the Controlled Decision-Making Mechanism (CDMM) are executed for the users who want to have authority in the system.

Each CC verifies that the requirements for the authorization mechanism are met. Each CC holds the addresses of the users it authorizes and the addresses of the other CC under it. It is much more difficult to de-authorize users who have a founding partner profile. The parameters used for the termination of authorization for the founding partners shall be

separate from those used for other users. These parameters are also defined in the rule-sets.

C. Controlled Decision-Making Mechanism (CCDM)

After the blockchain mechanism started to operate, some decisions are needed to be taken by the community. This decision-making mechanism plays important roles in the operation of the system, such as user authorization and the determination of new rule-sets. CDMM works according to some hyperparameters defined in the rule-set. Some of these parameters are;

- Enough positive votes to increase the authority
- Enough negative votes for termination of authorization
- Time to continue voting (e.g., 1 week, 1 month)

In this study, the decision-making mechanism is designed as a voting-based system. A decision process that receives enough votes within the community is approved and processed in the blockchain. Deciding that enough votes are obtained is made according to the values defined in the rule-set. For example, if enough votes are defined as 50% in the rule-set to increase user authorization, 50% of the trusted partners must vote as positive to increase the authority of the user. A decision that fails to obtain enough negative votes is rejected and cannot be active in the system. Voting is not an activity that can be performed by all users. Only users with Trusted Partners can vote on the system. For the voting system to work successfully, it is assumed that the trusted partners do not vote for bad or harmful purposes but perform fair voting only in legal cases. In order to meet these requirements, the selection of trusted partners must be selective. Voting is carried out with SCs (PVC, NVC) in the controlled decision mechanism designed, as mentioned before.

D. Voting

To keep the SC structure simple, PVC and NVC must be added to the system in the system for voting. This is shown in Figure 5. These two SCs are identical in structure. However, the intended use is different. One of the SCs is used to count positive votes, while the other is used to count negative votes. These two contracts are connected to each other. One voting contract shall hold the address of the other one.

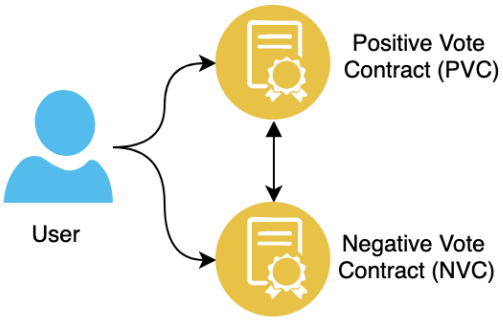

Fig.5. Voting Contracts Added to the System

Vote Contracts basically keep the number of votes and the people who vote. Therefore, a counter is held in the application code. Each time the SC is executed, this counter value is increased by 1, and the address of the trusted partner running the SC is stored in the block. Each of the trusted partners who have the authority to vote cannot vote more than one vote for a decision. However, votes can be changed. The pseudocode for the voting process is shown in Algorithm 1.

Algorithm 1: Voting Algorithm

```
IF SC is run AND the user is not in the users' list
THEN
   counter += 1
   save user address in the block
ENDIF
```

Voting for a user who has not previously vote positive or negative for an SC is executed by the Voting Algorithm. The given algorithm is used for both positive and negative votes. The registered user lists for positive and negative users are different.

A trusted partner who votes positive for a standard partner candidate may want to change its mind over time and turn its vote to negative. In this case, the trusted partner who wants to change the vote is just executed NVC. With this process, the address of the trusted partner who changed the process is deleted from the PVC and written to NVC. As a result, the number of positive votes decreases by 1, while the number of negative votes increases by 1 as shown in Algorithm 2.

Algorithm 2: Vote Change Algorithm

```
IF one tries to change the vote THEN
  Delete user address from the current list
  Decrease previous vote count by one
  Save user address to new vote list
  Increase vote counter
ENDIF
```

In this way, it can be ensured that the positive votes given are non-lifetime and can be changed over time. It is also possible to reverse this process, that is, to turn a negative vote into a positive vote. The information contained in the SCs to be used is kept in 3 different parts: header, code, and memory.

The header section includes the following parts;

- SC Address
- Previous SC Address (if applicable)
- Rule-set Version Number
- Peer Voting Contract Address (NVC address for PVC / PVC address for NVC)
- Timestamp

Certain definition of rules is needed in order to carry out the CDMM. The rules consist of preliminary information to be used in the mechanism of the system, such as determining the number of votes enough for the decision to be taken. Rules are defined in rule-sets, and all SCs must comply with the rules in the rule-set. The number of votes defined in the rule-set must be provided in the PVC in order to complete the decision-making mechanism. Otherwise, the decision should be rejected.

E. User Authorization with CDMM

A standard partner candidate must receive enough votes from trusted partners in the system according to the values

defined in the rule-set. The standard partner candidate must contact the trusted partners and ask them to review and vote on them. The first trusted partner to which the user applies to examine raises this user to the standard partner candidate profile, as depicted in Algorithm 3.

Algorithm 3: Authorization Algorithm

```
The user completes the requirements.
The user applies to trusted partners for voting.
Trusted partners examine the user.
IF suitable for a positive vote THEN
  The trusted partner runs the candidate's PVC.
ELSE
  The trusted partner does not vote or give
  negative vote using NVC.
ENDIF
```

Trusted partners require some information from the user to review the applicant. The user is then upgraded to the standard partner candidate level, allowing the user to write to the test chain, which is a small copy of the main blockchain. The candidate user is asked to enter the sample data of cyber threat intelligence information to this test chain. When the candidate user enters the sample data into the test chain, the examination process begins.

Trusted partners examine the standard partner candidate to be voted in terms of the information they provide and the cyber threat intelligence they enter in the test chain. Then, it is concluded whether the candidate user can provide reliable cyber threat intelligence information. The trusted partner who completes the review phase executes the PVC or NVC added by the candidate user to the system. If the user meets the requirements, the trusted partner will run one of these vote contracts of the user. Visual representation of user authorization and inclusion in the system are given in Figure 6.

Several cases are analyzed that will have a detrimental effect on the SC code or the unfair treatment of the number of votes when examining VCs. If the VCs code is designed in accordance with standards, the trusted partner will run the partner candidate's PVC once. Since the analysis and SC execution are transactions for a certain fee, the partner candidate will have to pay a certain application fee when he / she applies to the trusted partners in order to get votes.

It is not obligatory to vote after the examination phase. It is also possible that a user who does not have the qualification to vote positively is not allowed to vote at all. For a candidate to become a standard partner or a standard partner to become a trusted partner, he must receive enough votes and meet certain requirements. The necessary conditions will be defined in the rule-sets.

The conditions are first checked by the user's PVC. As soon as the PVC determines that the conditions are met, it applies to any Control Contract. If the Control Contract gives approval after performing the necessary checks, the user is raised to an upper profile. Similarly, the conditions for termination of authorization are controlled by NVC.

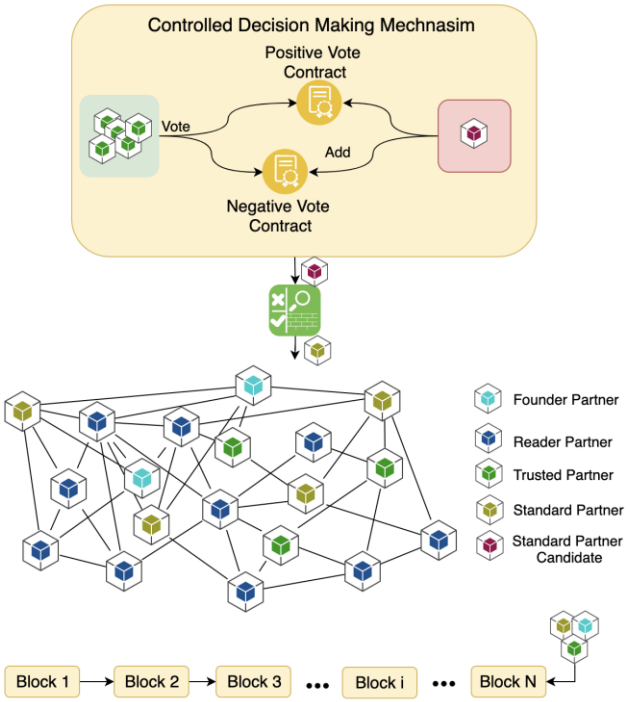

Fig 6. User Authorization with CDMM

In the Standard Partner profile, a user can enter the correct cyber threat information into the system for a while and start to enter incorrect information after a certain period or may exhibit behaviors that may adversely affect system operation. When such situations are encountered, it is necessary to de-authorize the relevant partner. This process is called authorization termination. In the case of a user whose authorization is to be terminated, trusted partners vote for this user's NVC. The profile of the user who has received enough negative votes according to the rules defined in the rule-set is reduced to a lower profile. With this method, a trusted partner level can also be reduced to the standard partner level.

In this case, the CC is applied. After checking with the Control Contract, which checks the necessary conditions for the termination of authorization, the profile of the partner concerned is reduced to a lower level, as depicted in Algorithm 4.

Algorithm 4: Termination of Authorization

```
Trusted partners vote negative for a user if they
consider it necessary

IF requirements are met THEN
  The user's privileges are dropped

ENDIF
```

The parameters required for the termination of authorization are defined in the rule-set. CCs are SCs that are added to the system by trusted partners. These contracts are derived from the tree structure. CCs ensure that the requirements for authorization have been met. Authorization and termination of authorization are carried out by CC. Each of the trusted partners is responsible for adding one CC to the system. Each CC is established as a node under the CC to which the trusted

partner is authorized. In this way, the tree structure of the CCs is preserved. A user who wishes to increase his authorization may apply to any CC. Each CC maintains the addresses of the users it authorizes and the addresses of the other CCs under it.

The structure of the CC is standard. The first CC is entered into the system by the Founder Partners. All CCs added to the system are copies of the contracts added by the founding partners to the system. It is important that each trusted partner adds a CC to the system so that the authentication verification step can be performed in a distributed architecture. In this way, even if some of the CCs have been damaged for various reasons, the system continues to operate smoothly.

Since the authorization and termination of the authorization are important steps, it is considered that an extra verification mechanism and CCs will contribute to the sustainability of the system. CCs also play an important role in updating rule-sets.

A separate blockchain will be used to examine the information that the standard partner candidate will enter the system. This chain is called the Test Chain. A standard partner candidate cannot enter data into the main chain until it is included in the standard partner profile; only data can be entered the test chain. The test chain can only be read by trusted partners. The authority to write data to the test chain is also defined for a certain period. The time definition is defined in the rule-sets. These steps are shown in Figure 7.

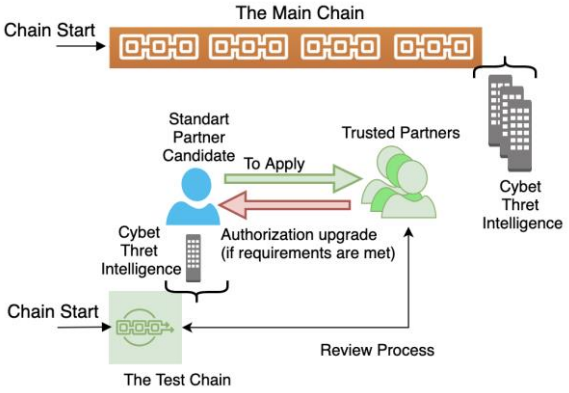

Fig 7. Standard Partner Candidate Review Steps

With the authorization termination process, the privileges granted to the users are not available for the lifetime. A user who has write-privileges in the system can be disqualified if he does not enter useful information as promised in the system. In this way, problems that may occur in the system are minimized.

F. Rule Sets

Some rules should be defined in CDMM and at other points. For example, the number of votes required for decision-making in a CDMM is one of these rules. The rules to be determined must meet the system requirements. Some of the rules that can be included in the rule-set are as follows;

- Percentage of positive votes required to become a trusted partner (positive vote count/ all trusted partner count)
- Percentage of negative votes required to authorize a trusted partner (negative vote count/ all trusted partner count)
- Percentage of negative votes required to authorize a standard partner (negative vote count/ all trusted partner count)
- Enough percentage of votes to update rule-set (positive vote count/ all trusted partner count)
- The default value for voting time

Since the defined rule-sets can be updated over time, the version information of the rule-set must be kept in each partner's Vote Contracts. If the rule-set version is changed, users are informed that the new rule-set has been changed.

G. Updating Rule Set with CDMM

The update of the rule-sets can be tracked by version numbers. Vote Contracts operate according to the rules in the currently defined and accepted rule-set. All SCs of all partners in the system must be renewed, and the version number of the new rule-set must be entered in these SCs, in order to update the rule-set. When renewing SCs, the address of the previous SC is entered into new contracts. This creates a link between SCs.

Each of the trusted partners in the system can propose a new set of rules. The trusted partner who makes the rule-set suggestion should add the system with the candidate rule-set on a pair of Vote Contracts. The steps in CCMM are performed using VCs entered into the system with the new suggested rule-set.

The rule-set that succeeds in getting the required number of votes to update can now be used in the system.

Announcing Updated Rule-set

Notifying users of the rule-set update and triggering the renewal of the required VCs is a crucial step in the functioning of the system.

It is first checked by the VCs associated with the rule-set to see if the requirements for updating the rule-set are met. If the necessary conditions are met, PVC applies to the Master CC. Once a CC confirms that the necessary requirements have been met, it reports the situation to the Master CC. The main CC is announced to the CCs under it. Each CC that receives the relevant announcement transmits the information to the VCs and CCs under it.

CCs are in a tree structure. Each CC is derived from a CC. The first CC defined in the system is the master CC. In case there are many users in the system, the tree structure of the CCs is given in Figure 8.

After the announcement, a new VC pair is created on the system for each user, even if their memory space is not full. The system operation is continued by entering the address of the previous SC, and the new rule-set version to the new SC created.

Users who do not renew their VC is downgraded from the standard partner or trusted partner profile to the Reader profile until they renew their contracts.

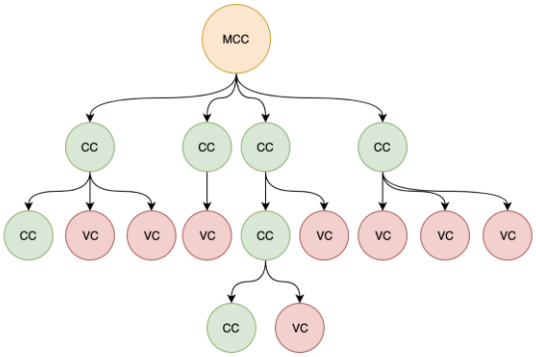

Fig 8. Tree Structure of Control Contracts

The ability to update the set of rules is very important to make it easier to scale the system over time and is a very costly process. Because of the cost, it is expected that rule-set updates are not operated very often, but only when necessary at a critical level.

V. Analysis of the System

In this study, a blockchain-based approach to cybersecurity information sharing is proposed. A decentralized decision-making mechanism is needed to ensure the distributed functioning of the system. The CDMM is also proposed to make decisions within the system. This mechanism is executed with a voting-based approach. A standard partner candidate can be promoted to the standard partner profile; he must collect enough votes. An initial situation is designed where there are no users with voting rights in the startup phase. In the first case there are N founding partners. Founding partners also have trusted partner privileges. The founding partners are also responsible for performing a few operations of the system. These operations are;

- Each founding partner votes for the other founding partners. In this way, each founding partner should have n-1 votes.
- The founding partners create and add a set of rules to be executed for the initial state.
- Founding Partners add one master CC to the system.
- Each founding partner adds its own CC under the main CC.
- Some of the initialized parameters in the rule-set created by the founding partners are as follows;
  - Percentage of positive votes to be obtained from trusted partners to become standard partners.
  - Percentage of positive votes required to become a trusted partner
  - Percentage of negative votes required to authorize a trusted partner
  - Percentage of negative votes required to authorize a standard partner
  - Enough percentage to update rule-set
  - The default value for voting time

When the system initialization phase is completed, the founding partners start to enter cyber threat intelligence information in the chain. Anyone can read this information and can now add standard partner users to the system.

CDMM is carried out in order to decide to increase authority. The candidate user adds a pair of VCs to the system to become a standard partner. One of the voting contracts holds positive votes, while the other one is used to count negative votes. The candidate user applies to the trusted partner level users in the system after the VC added to the system. At the time of application, a few documents are submitted to trusted partners. The documents contain information about the user as well as information about the cyber threat information obtained. In addition, the candidate user transmits a few documents on how he obtains cyber threat information data to the trusted partners during the application.

The first of the trusted partners applied to gives this candidate the authority to write to the test chain. The candidate user is then expected to enter some cyber information data into this test chain. After the candidate enters data in the test chain, the trusted partners applied for review the data entered by the candidate user in the test chain and the documents submitted by the candidate to the trusted partners during the application. Trusted partners who decide that the entered cyber threat information data are useful and consistent, run the Positive Vote Contract (PVC) of the relevant candidate, and vote positive. Trusted partners who do not feel that the candidate is qualified to vote positively may not vote at all or vote negative.

The candidate user who succeeds in obtaining the number of votes defined in the rule-set from the trusted partners currently present in the system is upgraded to the standard partner level. If the percentage of votes required to become a standard partner in the rule-set is 50% and the number of currently trusted partners is 10, the candidate user must receive at least 5 positive votes. First, the voting contracts of the candidate are checked whether the necessary conditions are met. The candidate user who meets the requirements defined in the rule-set to become a standard partner applies to any CC in the system. If the CC confirms that the necessary conditions are met, the candidate user is promoted to the standard user authorization, and the address of the user's VCs is added to the CC that authorizes the user.

Similarly, if the trusted partner meets the conditions set in the rule-set, he / she rises to the trusted partner level. The required conditions are first checked by the voting partner of the trusted partner candidate. The voting contract applies to any CC for the authorization upgrade when the necessary conditions are met. If the CC confirms that the necessary requirements are met, the trusted partner candidate is raised to the trusted partner level. The user who reaches the trusted partner level creates a CC. The created CC is added to the CC, which authorized from.

With this approach, CC has a tree structure. The top node is the master CC that the founding partners add to the system. At the first level, there are CCs entered by the founding partners. Two types of data can be found in CC.

These are;

- Address of the voted partners of the authorized standard

partners
- Address of the CC of authorized partners

The tree structure of the CCs grows over time by branching, as in Figure 8.

These steps are repeated for each standard partner and trusted partner. Over time, many standard partners and trusted partner-level users are created in the system.

The list of trusted partners running VCs is saved into the VCs memory area. VCs are entities with limited memory space. Storing a number of addresses results in high memory usage in VCs. If the SC becomes out of memory space so that the contracts do not function due to the memory space being filled, a new VC is created, and the address of the previous VC is entered into the new VC. For example, when there is no space in the memory area of the PVC for a decision, a new PVC is automatically added to the system. The address of the previous PVC is entered into the newly created PVC. This makes it easier to scale the system. Adding the new VC to the system and entering the old VC address into the new VC is coded / defined into the code area of VC. That is to say, the processes required to fill the memory space and the entry of new contracts into the system are performed automatically when the appropriate conditions are met.

The requirements of the system may change over time, or some additions may be needed to make the system more secure. The requirements for operating a system with 100 partners may differ from those required for a system with 1,000,000 partners.

For example, If there are 100 trusted partners in the system and the percentage of enough votes is decided as 50%, At least 50 trusted partners' votes are needed to increase the authority. However, in the system with 1,000,000 trusted partners, if the percentage of enough votes is 50%, 500,000 trusted partners must vote. When the system is getting growth, decreasing the percentage value of enough votes can increase the sustainability of the system. In order to overcome this, the rulesets are designed to be updated timely.

Updating the rule-set can be done by assigning new values to existing rules or adding new rules to the rule-set. In this way, it can easily adapt to changing conditions. The rule-set is updatable; It is an important step in terms of scalability of the system and adaptation of the system to changing conditions.

Any trusted partner can make suggestions for updating the rule-set. For the update process, the steps of the control decision-making mechanism proposed in this study are carried out. The trusted partner who suggests adds the proposed set of rules and a pair of VCs to the system. Then, they announce their proposal to all trusted partners. Trusted partners review and vote for a new set of rules. The rule-set, which receives enough votes defined in the rule-set, can be used in the system in this step. Proposing a new set of rules can be considered as a collective decision rather than an individual activity. A community of trusted partners can decide on the rules in the proposed rule-set, as a result of extensive analysis, the rules can be proposed, as well as through the surveys carried out among trusted partners, and update recommendations can be suggested.

After it is decided to update the rule-set, all SCs in the system must operate according to the rules in the new rule-set. Therefore, the update of the rule-set should be announced to SCs. The announcement of rule-sets is an important step for system operation. The announcements for the rule-set update is made by the CCs. Since the authorization process is carried out through CC, each partner must add a CC to the blockchain. The standard partner level users' voting contract address, and the trusted partner level user CC address is kept in the CC. This allows CCs to dominate a tree structure, as given in Figure 8. If enough votes for the rule-set update are collected, the situation is announced to the MCC. The MCC informs the CCs under it. Each CC shall inform the VCs and other CCs under it. Whenever it communicates to all assets under each CC, the system is informed of the use of the new set of rules in all VCs.

The new rule-set can be very different from the previous rule-set. Therefore, when the rule-set is updated, the current status of the VCs may not meet the requirements for the operation of the rules in the new rule-set. In order to avoid this situation, VCs are updated in every rule-set update. A new SC is created for each SC, and the address of the current rule-set and the addresses of the previous SC have entered the new SC. With the completion of all these processes, the updated set of rules becomes active.

Operations such as the execution of VCs and the creation of new SCs are transactions with a certain cost. These costs need to be covered in some way. Otherwise, operations cannot be performed. Due to the nature of the system, the costs of running SCs are collected from the person who runs the contract. VCs must be run many times for voting.

Standard partner candidates need votes to increase their authority. They must also apply to trusted partners for voting purposes. The standard partner candidate pays a certain fee to the trusted partner to whom he applies. The trusted partner reviews the standard partner candidate for this fee and, if deemed necessary, runs the candidate's SC. Although the cost of the SC that is run for the standard partner candidate to collect votes is paid by the trusted partner, who votes, this cost is covered by the standard partner candidate.

SCs may need to be renewed because the memory space is full. In this case, a new SC is created and associated with the old SC. By creating a new SC, the costs associated with the old SC are covered by the SC owner. For example, user A's positive PVC has been filled, and a new PVC has been created. In this case, the necessary fee is covered by person A.

Updating the rule-set is a process to improve system operation. The improvement achieved by updating the rule-set applies to all users in the system. Therefore, in order to update the rule-set, the full cost of the transactions is not charged to the trusted partner who proposes to update the rule-set. All users who vote for the new set of rules must pay for their own votes.

When the reader users want to read cyber threat information data from the system, they can make company-based queries or data-based queries. For example, user A can filter all cyber

threat information entered the system by company C, as well as all cyber threat information entered for the IP address x.x.x.x. In addition, statistical information such as which partner enters the blockchain can be displayed in the system.

VI. Discussion and Conclusion

In order to protect the systems against new cyber-attacks, their signatures (information) should be reached as early as possible. This information can be accessed either when it is encountered in the system, or when this information is gotten from other signature servers, which share their knowledgebase to others. The latter one is preferred by the security admins, and they can contact others either in peer to peer model, or in a client server manner. Both these approaches have some negative effects, especially in maintenance.

Therefore, in this paper, a blockchain based cyber threat information sharing system is proposed. The use of blockchain technology enables cryptographic security and distributed structure for us, which are two trivial issues that are needed to be solved for the scalability of the system. The design details are detailed by showing the structure of block/data adding mechanisms with the use of a Voting mechanism and Smart Contracts.

The blockchain mechanism is set up by partners as companies, government agencies, or computer security firms. The dynamic addition of partners/users is also enabled. A candidate user must collect some votes for the authorization upgrade. The candidate user applies to trusted partners to collect votes. Trusted partners may vote positively or negatively if they deem necessary after reviewing the candidate user. The authority of the candidate user who receives enough votes is increased. Adequate votes are defined in the rule-sets. Rule-sets can be updated so that the system can adapt to changing conditions. CCs are used to validate the authorization process and to announce the update of the rule-set.

The proposed system is in the design phase. In the ongoing studies, the design of the system is aimed to be implemented. Additionally, the payment system is very important for the preferability of this system. It is thought that commercial firms may want to use a common platform where they can sell their products. It is planned to make improvements to the proposed system to increase preferability and sustainability. In addition, it is planned to conduct research to extract the experience and reliability levels among the trusted partners in the following studies. In this way, the reliability of the shared information can be accepted as a measurable metric.

References

[1] Ninth Annual Cost Of Cybercrime Study, THE COST OF CYBERCRIME, https://www.accenture.com/_acnmedia/pdf-6/accenture-2019-cost-of-cybercrime-study-final.pdf, The Last Access: May 2020

[2] G. Karatas, O. Demir and O. K. Sahingoz, "A Deep Learning Based Intrusion Detection System on GPUs," 2019 11th International Conference on Electronics, Computers and Artificial Intelligence (ECAI), Pitesti, Romania, 2019, pp. 1-6, doi: 10.1109/ECAI46879.2019.9042132.

[3] B. Reis, S. B. Kaya, O. K. Sahingoz, "A Clustering Approach for Intrusion Detection with Big Data Processing on Parallel Computing Platform", Balkan Journal of Electrical and Computer Engineering Volume 7 , Issue 3, Pages 286 - 293, 2019

[4] B. Reis, S. B. Kaya, G. Karatas and O. K. Sahingoz, "Intrusion Detection Systems with GPU-Accelerated Deep Neural Networks and Effect of the Depth," 2018 6th International Conference on Control Engineering & Information Technology (CEIT), Istanbul, Turkey, 2018, pp. 1-8, doi: 10.1109/CEIT.2018.8751784.

[5] PhishTank | Join the fight against phishing, https://www.phishtank.com/ , The Last Access: May 2020

[6] IBM X-Force Exchange, https://exchange.xforce.ibmcloud.com/, The Last Access: May 2020

[7] AutoFocus Threat Intelligence, https://www.paloaltonetworks.com/products/secure-the-network/subscriptions/autofocus , The Last Access: May 2020

[8] LogRhythm Threat Lifecycle Management (TLM) Platform, https://logrhythm.com/products/threat-lifecycle-management-platform/, The Last Access: May 2020

[9] iSIGHT Intelligence Subscriptions, https://www.fireeye.com/products/isight-cyber-threat-intelligence-subscriptions.html, The Last Access: May 2020

[10] LookingGlass Cyber Solutions, https://www.lookingglasscyber.com/ , The Last Access: May 2020

[11] Normshield Free Cyber Threat Intelligence, https://services.normshield.com/honeypotfeed , The Last Access: June 2020

[12] FireHOL IP Lists | IP Blacklists | IP Blocklists | IP Reputation, http://iplists.firehol.org/, The Last Access: October 2019

[13] R. Koch, & M. Golling, (2018, May). The cyber decade: cyber defence at a x-ing point. In 2018 10th International Conference on Cyber Conflict (CyCon) (pp. 159-186). IEEE.

[14] T. R. Vance, & A. Vance (2019, October). Cybersecurity in the Blockchain Era: A Survey on Examining Critical Infrastructure Protection with Blockchain-Based Technology. In 2019 IEEE International Scientific-Practical Conference Problems of Infocommunications, Science and Technology (PIC S&T) (pp. 107-112). IEEE.

[15] P. J. Taylor, T. Dargahi, A. Dehghantanha, R. M. Parizi, & K. K. R. Choo, (2019). A systematic literature review of blockchain cyber security. Digital Communications and Networks.

[16] I. Makhdoom, I. Zhou, M. Abolhasan, J. Lipman, & W. Ni, (2020). PrivySharing: A blockchain-based framework for privacy-preserving and secure data sharing in smart cities. Computers & Security, 88, 101653.

[17] Meng, W., Tischhauser, E. W., Wang, Q., Wang, Y., & Han, J. (2018). When intrusion detection meets blockchain technology: a review. Ieee Access, 6, 10179-10188.

[18] R. Graf, & R. King, (2018, May). Neural network and blockchain based technique for cyber threat intelligence and situational awareness. In 2018 10th International Conference on Cyber Conflict (CyCon) (pp. 409-426). IEEE.

[19] D. Homan, I. Shiel, & C. Thorpe (2019, June). A New Network Model for Cyber Threat Intelligence Sharing using Blockchain Technology. In 2019 10th IFIP International Conference on New Technologies, Mobility and Security (NTMS) (pp. 1-6). IEEE.

[20] Y. Wu, Y. Qiao, Y. Ye, & B. Lee (2019, October). Towards Improved Trust in Threat Intelligence Sharing using Blockchain and Trusted Computing. In 2019 Sixth International Conference on Internet of Things: Systems, Management and Security (IOTSMS) (pp. 474-481). IEEE.

[21] C. Killer, B. Rodrigues, & B. Stiller, (2019, May). Security Management and Visualization in a Blockchain-based Collaborative Defense. In 2019 IEEE International Conference on Blockchain and Cryptocurrency (ICBC) (pp. 108-111). IEEE.
[22] Cybersecurity Tech Basics: Blockchain Technology Cyber Risks and Issues: Overview, https://www.steptoe.com/images/content/1/8/v2/189187/Cybersecurity-Tech-Basics-Blockchain-Technology-Cyber-Risks-and.pdf, The Last Access: June 2020
[23] Feng, S., Xiong, Z., Niyato, D., Wang, P., Wang, S. S., & Zhang, Y. (2018, December). Cyber Risk Management with Risk Aware Cyber-Insurance in Blockchain Networks. In 2018 IEEE Global Communications Conference (GLOBECOM) (pp. 1-7). IEEE.
[24] G. Ahmadi-Assalemi, H. M. Al-Khateeb, G. Epiphaniou, J. Cosson, H. Jahankhani, & P. Pillai (2019, January). Federated blockchain-based tracking and liability attribution framework for employees and cyber-physical objects in a smart workplace. In 2019 IEEE 12th International Conference on Global Security, Safety and Sustainability (ICGS3) (pp. 1-9). IEEE.
[25] R. Yetis and O. K. Sahingoz, "Blockchain Based Secure Communication for IoT Devices in Smart Cities," 2019 7th International Istanbul Smart Grids and Cities Congress and Fair (ICSG), Istanbul, Turkey, 2019, pp. 134-138, doi: 10.1109/SGCF.2019.8782285.
[26] G. Dinc and O. K. Sahingoz, "Smart Home Security with the use of WSNs on Future Intelligent Cities," 2019 7th International Istanbul Smart Grids and Cities Congress and Fair (ICSG), Istanbul, Turkey, 2019, pp. 164-168, doi: 10.1109/SGCF.2019.8782396.
[27] S. Nakamoto. "Bitcoin: A peer-to-peer electronic cash system.", 2008.
[28] G. Wood. "Ethereum: A secure decentralized generalized transaction ledger.", Ethereum Project Yellow Paper, 2014.
[29] G. Foroglou, A. L. Tsilidou, "Further applications of the blockchain.", In 12th Student Conference on Managerial Science and Technology, 2015.
[30] S. Sayeed, H. Marco-Gisbert and T. Caira, "Smart Contract: Attacks and Protections," in IEEE Access, vol. 8, pp. 24416-24427, 2020, doi: 10.1109/ACCESS.2020.2970495.
[31] K. Lee, J. I. James, T. G. Ejeta, H. J. Kim, "Electronic voting service using block-chain.", The Journal of Digital Forensics, Security and Law: JDFSL, 11(2), 123, 2016
[32] Z. Zheng, S. Xie, H. N. Dai, H. Wang, "Blockchain challenges and opportunities: A survey.", International Journal of Web and Grid Services, 14(4), 352-375, 2018
[33] R. Adams, G. Parry, P. Godsiff, P. Ward. The future of money and further applications of the blockchain. Strategic Change. 2017; 26: 417– 422. https://doi.org/10.1002/jsc.2141.
[34] A. Kosba, A. Miller, E. Shi, Z. Wen, C. Papamanthou, "Hawk: The blockchain model of cryptography and privacy-preserving smart contracts.", In Proceedings of IEEE Symposium on Security and Privacy (SP), pages 839–858, San Jose, CA, USA, 2016.
[35] B. W. Akins, J. L. Chapman, J. M. Gordon, "A whole new world: Income tax considerations of the bitcoin economy.", 2013.
[36] Y. Zhang, J. Wen, "An IOT electric business model based on the protocol of bitcoin.", In Proceedings of 18th International Conference on Intelligence in Next Generation Networks (ICIN), pages 184–191, Paris, France, 2015.
[37] M. Sharples, J. Domingue, "The blockchain and kudos: A distributed system for educational record, reputation and reward.", In Proceedings of 11th European Conference on Technology Enhanced Learning (EC-TEL 2015), pages 490–496, Lyon, France, 2015.
[38] C. Noyes, "Bitav: Fast anti-malware by distributed blockchain consensus and feedforward scanning.", arXiv preprint arXiv:1601.01405, 2016.
[39] Z. Zheng, S. Xie, H. N. Dai, H. Wang, "Blockchain challenges and opportunities: A survey. Work Pap", 2016.
[40] NRI, "Survey on blockchain technologies and related services. Technical report", 2015.

BIOGRAPHIES

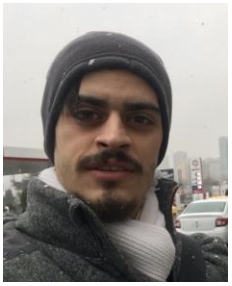

EBUBEKIR BUBER He received the B.S. and M.S. degrees in Computer Engineering from Yildiz Technical University, Istanbul, Turkey. He is currently a student of Ph.D. at Yildiz Technical University since 2019. His research interest are cybersecurity focused artificial intelligence applications and cybersecurity related blockchain systems.

OZGUR KORAY SAHINGOZ received the B.S. degree from the Computer Engineering Department, Boğaziçi University, in 1993, and the M.S. and Ph.D. degrees from the Computer Engineering Department, Istanbul Technical University, in 1998 and 2006, respectively.

He is currently working as an Associate Professor with the Computer Engineering Department, Istanbul Kültür University. He is the author of more than 100 articles. He has been working in two research projects. He graduated more than 13 M.Sc. students and supervised around six Ph.D. students. He has reviewed more than 80 national projects especially related to TUBITAK, KOSGEB-Ministry of Industry and Technology, Turkey. He is also a regular Reviewer for more than 40 Science Citation Index (/Expanded) international journals. His research interests include artificial intelligence, machine/deep learning, data science, software engineering, and UAV networking.

Dr. Sahingoz has also been very active in scientific conferences, organized and/or works as program committee members more than 100 conferences/workshops on different research areas, especially on artificial intelligence and information sciences. He has developed and taught around 20 different academic courses.

Optimization of an Input Filter for a Three-Phase Matrix Converter

G.BOZTAS

***Abstract*— This study includes an optimization of the input filter for three-phase matrix converters. An input filter effects on the power factor while improving the Total Harmonic Distortion (THD) of the input current. Unity power factor being one of the most important advantages of matrix converters will be eliminated if this is not taken into consideration. For this reason, an optimization was used by taking both parameters into consideration in this study. A Particle Swarm Optimization (PSO) algorithm was used in order to reduce the THD of the input current about 3 % with nearly unit power factor as 0.985. The first of the optimization objective functions is to decrease the THD of the input current, and the second is to increase the power factor. The matrix converter was used for a constant frequency and modulation by using the switching strategy of Venturini Method and feeds an RL load. The optimized input filter was analyzed in detail in MATLAB/SimPowerSystems environment and examined in the results. Additionally, FFT spectra of the input and output waveforms are given in the results. Thus, the most suitable input filter was obtained for this system.**

Index Terms—**Matrix converter, Venturini Method, Power Factor, Input Filter, Harmonic Distortion.**

I. INTRODUCTION

MATRIX CONVERTER obtained with the development of the forced commutated cycloconverter based on bidirectional fully controlled switches consists of semiconductor elements and converts three-phase AC line voltages to three-phase variable voltage and frequency outputs [1], [2]. This converter consisting of 9 bidirectional switches is arranged in order to connect any of the output lines of the converter to any of the input lines. The topology of the matrix converter was first proposed by Gyugi in 1976 [3]. The matrix converter was not very popular in the industry in the past due to current commutation problems between switches, using much number of component and difficulties in the control algorithm. Many researchers developed matrix converter control algorithms based on mathematical principles after Venturini's first matrix converter study in 1980. PWM modulation strategies of the matrix converter are based on the studies of Alesina and Venturini.

GULLU BOZTAS, is with Department of Electrical & Electronics Engineering, Faculty of Technology, Firat University, Elazig, Turkey, (e-mail: gulluboztas@gmail.com).

https://orcid.org/0000-0002-1720-1285

Manuscript received July 03, 2020; accepted July 30, 2020.
DOI: 10.17694/bajece.763403

The matrix converters have a more advanced potential compared to conventional voltage source inverters [4], [5]. The output waveform of the matrix converter is obtained by using a suitable PWM signal, similar to a standard inverter. However, in matrix converters, the input of the converter is fed from a three-phase constant frequency and voltage AC source instead of a fixed DC voltage source. These converters have no DC connection. The output voltages of the matrix converter are generated directly from the input voltages due to the lack of energy storage elements between input and output of the converter [6]. These converters have higher reliability, longer life and smaller design than inverters due to the lack of large reactive energy storage components such as bulky and limited-life electrolytic capacitors.[1], [7], [8]. These converters are able to naturally transfer regenerative energy back to the source without the need for any additional components or algorithms because matrix converters have bidirectional switches [9]–[11]. These converters can operate at all four quadrants of the torque-speed region due to their regeneration features [4], [12]. The matrix converter has a sinusoidal input current and this converter can operate at the unit displacement factor by depending on the modulation technique regardless of the power factor of the load. These converters can be used in large energy conversion systems such as motor drives, variable frequency wind generators and aircraft applications.

Output waveforms of the converter are affected from high frequency distortion in the input current of the converter. Input filters are often used to improve input current quality and reduce input voltage distortion in power converters. The effect of the filters between the input side of a power supply and input side of a matrix converter has become a major issue of matrix converter researches [13]. Input current filters are placed in the input of the matrix converter in order to prevent unwanted high frequency current components [7], [8], [12], [14], [15]. Passive LC filter is used as matrix converter input filter. Input filter designs for the matrix converter provide unity power factor on the power supply side by improving the quality of the main currents having sinusoidal waveforms containing low harmonic components and reducing the distortion of the input voltages provided to the Matrix converter module [5], [16]–[19]. Additionally, the input filter significantly reduces electromagnetic interference in the matrix converter [7], [12], [20].

Optimization techniques are widely in order obtain optimum parameters for the systems used in many engineering applications. Optimization is basically a mathematical technique for finding the maximum or minimum points of the

functions in some feasible regions. Today, many different optimization techniques are used in many areas [21]–[26]. Particle Swarm Optimization (PSO) is a powerful optimization method shown experimentally. This method provides good results for most optimization problems. PSO has obtained increasing popularity in the last two decades [27]. PSO is a valuable meta-heuristic approach used in scientific fields with complex optimization problems. Thanks to its simplicity, PSO has an algorithm network that can be used easily even by non-expert researchers. This situation led to increased popularity of PSO. It also allows for easy parallelization using modern high-performance computer systems. It was first proposed by Eberhart and Kennedy in 1995 [28]–[30]. PSO algorithm is very popular due to simple calculation and sharing of information. Using an optimization method such as PSO, the solution can be produced without using the gradient of the function to be optimized. It is a great advantage to use such a method if the gradient is troublesome to derived in the algorithm [31]. The PSO algorithm has two different stages. The other is called as the update phase while the first is called as the start phase. Particles called as individuals spread into a multi-dimensional search space in the algorithm. Each individual shows a suitable solution for the problem which can be optimized. The performance function of the problem represents the fitness function of the PSO algorithm [32].

In this study, the PSO algorithm is used to optimize the power factor together with the input current harmonics of a matrix converter. The difficulty of this optimization problem; it negatively effects the power factor while increasing the component values of the input filter to improve the input current harmonic of the matrix converter. The matrix converter can operate on a unit power factor due to its nature. However, the filter used at the input makes it impossible to operate on the unit power factor. In this paper, a matrix converter input filter was optimized for the input current Total Harmonic Distortion (THD) value below 5%, which can operate close to the unit power factor. The input filter optimized for the matrix converter was tested for different output frequencies and 0.98 power factor value with 3% current THD value was obtained in this study. It is shown that the THD value remains constant in all cases when the output voltage and current of the converter is analyzed. Additionally, all swarm formation during optimization were examined graphically and they were shown to reach the optimum point. This study provides a suitable solution for one of the engineering problems. In the design of such nonlinear systems, quite demanding mathematical analysis is required. However, this study has shown that optimization methods are very useful solutions for such applications.

II. MATRIX CONVERTER

The structure of the matrix converter consisting of 9 bi-directional common collector switches that allow any output phase to be connected to any input phase is given in Fig.1.

The output voltages of the matrix converter are generated directly from the input voltages due to the lack of energy storage elements between inputs and outputs of the converter. The absence of a DC-link capacitor is one of the main advantages of the matrix converter because DC-link capacitor increases cost and volume of the system. This converter can transfer regenerative energy back to the source without the need for any additional elements or algorithms because the converter has bidirectional switches. The amplitude of the matrix converter output voltage limits to 86.6 % amplitude of input voltage. However, higher output voltages can be obtained with overmodulation causing input current distortion.

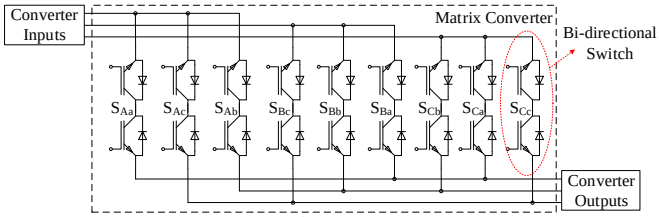

Fig.1. Structure of three-phase matrix converter

It is necessary to determine turn on/off times with sequences of the switches in order to obtain from a constant amplitude and frequency source to an adjustable amplitude and frequency output. Additionally, it is desirable to be able to operate with maximum amplitude and low total harmonic distortion. Therefore, some modulation algorithms were developed for matrix converter. Modulation algorithms used in matrix converter can be listed as Venturini, Scalar and Space Vector. In this paper, it is used switching strategy of Venturini algorithm [33].

Venturini method provides full control of output voltages and input power factor. Maximum voltage transfer ratio of the Venturini algorithm is 0.866 and this algorithm needs to output power factor information in order to control input power factor [34]. The output voltage and the duty cycle for the switch connected between the input phase β and the output phase γ in the unit input displacement factor are given in Eq. (1)-(3).

$$T_{\beta\gamma} = T_s\left[\frac{1}{3} + \frac{2V_{o\gamma}V_{i\beta}}{3V_{im}^2} + \frac{2q}{9q_m}\sin(\omega_i t + \psi_\beta)\sin(3\omega_i t)\right] \quad (1)$$

$$V_{o\gamma} = qV_{im}\cos(\omega_o t + \psi_\gamma) - \frac{q}{6}V_{im}\cos(\omega_o t) + \frac{q}{4q_m}V_{im}\cos(\omega_i t) \quad (2)$$

$$V_{im} = \sqrt{\frac{V_A^2 + V_B^2 + V_C^2}{1.5}} \quad (3)$$

where maximum voltage ratio and desired voltage ratio are q_m and q. ψ_β and ψ_γ are 0, 2π/3, 4π/3 input phase difference and output phase difference, respectively. ω_o is angular velocity of the output frequency while ω_i is angular velocity of the input frequency. V_A, V_B, and V_c are instantaneous input voltage and V_{im} is maximum input voltage.

Matrix converters generate current harmonics injected back into the AC system. The current harmonics can cause voltage distortion of the AC system. Input filter obtained with reactive energy storage component is used in order to reduce harmonics generated by matrix converters [35].

III. PSO ALGORITHM FOR FILTER OPTIMIZATION

A standard PSO algorithm performs searching using particle swarm during the iteration. In order to find the optimum solution, each particle is moved to its best position in the previous step [36]. The previous best position and the best global position are determined in Eq. (4).

$$pbest(i,t) = \underset{k=1,\ldots,t}{\arg\min}\left[f(P_i(k)) \right] \; i \in \left\{1,2,\ldots,N_p\right\} \tag{4}$$

$$gbest(i,t) = \underset{\substack{i=1,\ldots,N_p \\ k=1,\ldots,t}}{\arg\min}\left[f(P_i(k)) \right] \tag{5}$$

where i is the particle index, N_p is the total number of particles, t is the present iteration number, f is the fitness function, and P is the position of the particle. The velocity and position of particles are calculated using Eq. (6) and Eq. (7).

$$V_i(t+1) = \omega V_i(t) + c_1 r_1 (pbest(i,t) - V_i(t)) + c_2 r_2 (pbest(t) - P_i(t)) \tag{6}$$

$$P_i(t+1) = P_i(t) + V_i(t+1) \tag{7}$$

The velocity denotes as V and the inertia weight used to balance the global exploration and local exploitation denotes with ω. Uniformly distributed random variables denote r_1 and r_2. Positive constant parameters called "acceleration coefficients" which are denoted as c_1 and c_2.

PSO algorithm can be examined in 8 steps as given below;

Step 1. Each particle is started randomly $P_i(0) \sim U$(Lower Bounds, Upper Bounds).

Step 2. Fitness function is evaluated.

Step 3. The fitness function is calculated.

Step 4. Particles are sorted and the best position of each particle is determined at each iteration.

Step 5. The position and velocity of each particle are modified.

Step 6. New positions of the particles are evaluated.

Step 7. If (the number of iterations < maximum) go to Step 1.

Step 8. Choose the particle that gets the best performance ($gbest(t)=P_i(t)$).

A simulation environment was created using MATLAB for a three-phase matrix converter for optimization process. This simulation system consists of a three-phase fixed voltage source, network filter (input filter), matrix converter, and RL load as shown in Fig.2. The matrix converter was operated for a constant 0.8 modulation index by using the modified Venturini algorithm during optimization process. 380 Vrms (phase-phase), 50 Hz voltage source was used as input voltage. The input filter has a widely preferred LC filter connection structure as shown in the figure. The L inductance and C capacitor values were optimized by using two objective function. One of them is determined by approximating THD value to zero and the other is determined by approximating power factor value to 1. The objective (fitness) function is given in Eq. (8).

$$f(t) = 0.5(1 - PF) + 0.5 I_{THD} / 100 \tag{8}$$

The structure of the optimization loop is given in Fig.3. First, the PSO operates the system with a random initial LC value. Then, based on the PSO progression, an online structure is obtained by sending the analysis results to the PSO algorithm for each new LC value. The results of the progress obtained with optimization are presented in the Fig.4. As seen in the optimization results, the THD value of the input current is decreased while the power factor value is increased to 1. As a result of optimization, inductance and capacitor values of the input filter were obtained as 9.99 mH and 12.8055 µF, respectively.

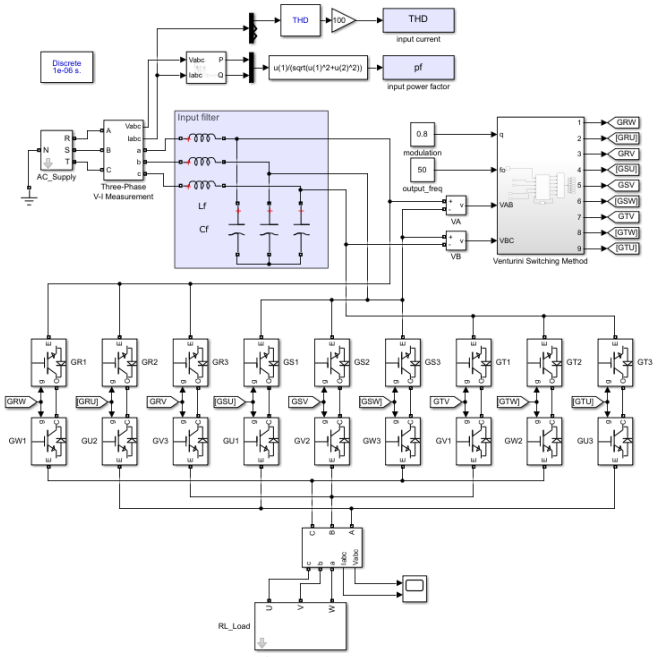

Fig.2. Structure of three-phase matrix converter

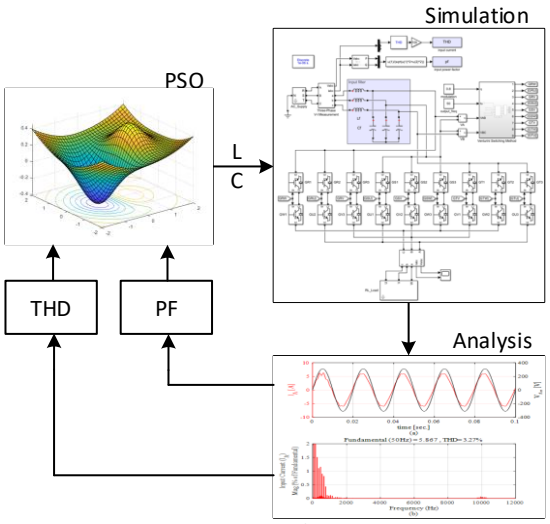

Fig.3. Structure of optimization loop

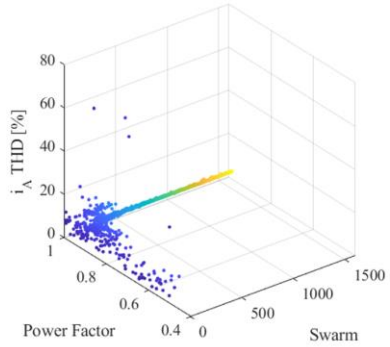

a)

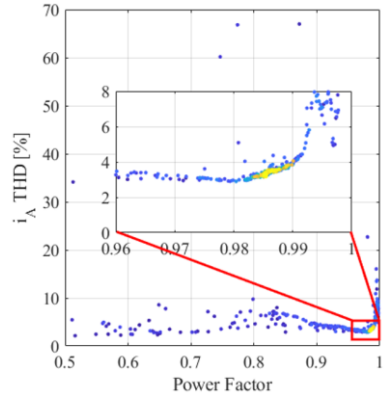

b)

Fig.4. a) Progression of power factor and I_A THD according to PSO, b) Progression of fitness functions

IV. Analysis of Optimized System

The waveforms of the input current and input voltage of the system operated without input filter are given in Fig.5. The input current signal has a very high harmonic content. The distortion of the input current mostly occurs around the switching frequency of 10 kHz when the harmonic spectrum is analyzed as seen in Fig.5a. The THD value of the input current is calculated around 67 %. The input current THD value is generally around 90 %, because of the uncontrolled rectifier structure on the input side of the inverters. Therefore, this value can be said to be quite low compared to input current THD of a standard inverter.

IEEE Std 519-1992 report provides harmonic content limits in power systems. Additionally, detailed information about harmonics can be accessed using *IEEE Recommended Practice and Requirements for Harmonic Control in Electric Power Systems* report [37], [38]. The current harmonic limits are determined according to the short circuit current strength of the system. Additionally, Total Demand Distortion (TDD) value is analyzed instead of THD value while determining these values. TDD can be defined as harmonic current distortion in % of maximum demand load current about 30-minute demand. It can be seen that the acceptable value for this system is 5 %. when the report is analyzed.

The inductance and capacitor values can be used as about 10 mH and 12 µF when the optimized values of the filter are organized as engineering notation. The system is operated with the filter values obtained as a result of optimization. The input waveforms of the matrix converter are analyzed in Fig.6. As seen in Figure 6a, current and voltage revisions oscillate

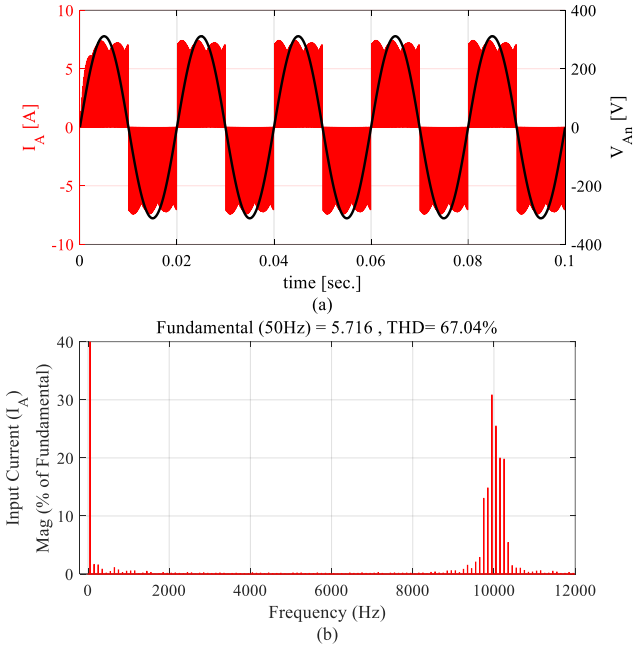

Fig.5. Without input filter; a) Waveform of input current with grid voltage, b) Harmonic spectrum of input current

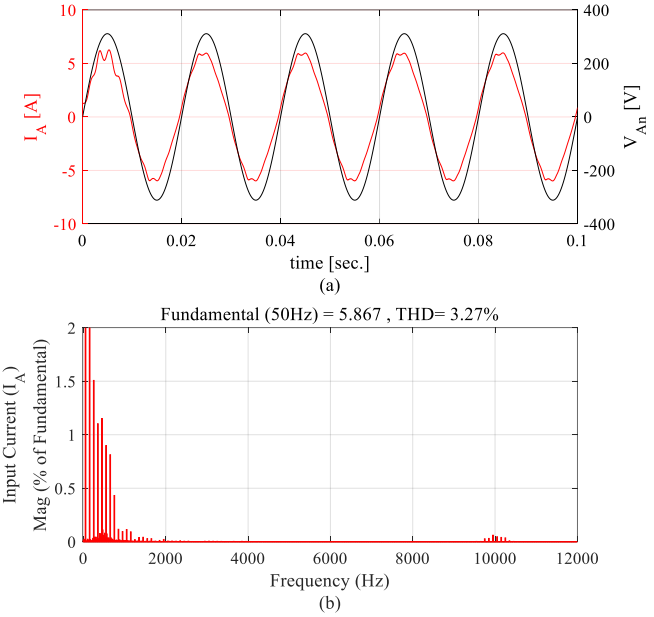

Fig.6. With optimized input filter; a) Waveform of input current with grid voltage, b) Harmonic spectrum of input current

nearly overlap. The power factor of the system was calculated as 0.985. The reason for a small notch at the top of the current signal in the first period is the nonlinear structure in the system in the transient state. It can be seen that symmetrical oscillation is obtained in later periods. It is seen that a very low THD value can be obtained around 3 % when the harmonic of the current signal is analyzed as shown in Fig.6b. The harmonic magnitude being closest to the fundamental harmonic is approximately 2 % of the fundamental harmonic value. The most dominant harmonic magnitude value is nearly 30 % of the fundamental harmonic value when the input filter was not used as shown in Fig.5b. Therefore, it is necessary to

say that the switching frequency is dominant in the non-filter condition. Additionally, the system is analyzed for different output frequency from 10 Hz to 70 Hz as shown in Table 1. As expected, the THD values of both input and output signals are similar. The input current THD value is remained below 3 % for different output frequencies. The power factor values are obtained close to the unit power factor value. Thus, in this study, the aimed low input current harmonic content and unit power factor value were successfully obtained by using an appropriate optimization. As the modulation index increases, THD values of the output voltage and output current decrease while the power factor the input current THD increase. As the modulation index decrease, THD values of the output voltage, output current and input current increase while the power factor decreases.

TABLE I
ANALYSIS OF INPUT FILTER FOR DIFFERENT OUTPUT FREQUENCY

Output Frequency	*Converter Input*		*Converter Output*	
	I_A THD	**Power Factor**	**V_{ab} THD**	**I_a THD**
Hz	**%**	**-**	**%**	**%**
10	4.09	0.989	64.04	2.72
20	4.16	0.993	64.03	2.24
30	4.75	0.988	63.42	1.96
40	3.95	0.988	63.30	1.94
50	3.27	0.985	64.81	1.90
60	4.63	0.984	64.69	2.16
70	4.30	0.9834	62.31	2.22

V. CONCLUSION

A study was carried out to improve the power factor and current harmonic content values, which are important parameters for power electronics systems. These parameters can be improved in order to obtain desired values using a passive input filter with inductance and capacitor. This conversion cannot be performed in one step by using an inverter if AC-AC conversion is to be obtained using a voltage-source inverter. Therefore, the input filter used in this conversion must be quite large. In this study, a matrix converter structure with many advantages was preferred. This system can provide a converter structure with very low input harmonic content and unit power factor, especially by using very small input filter.

It is generally preferred in order to calculate the natural frequency value in order to determine the inductance and capacitor values in the input filter. However, this approach improves the harmonic content in the input current while significantly reducing the power factor. This eliminates the ability to operate on the unit power factor being one of the most important features of the matrix converter. Therefore, filter values were optimized by using the PSO algorithm in this study. The optimization goal is to reduce the THD value of the input current and keep the power factor close to the unit power factor value. An optimization algorithm was performed in order to obtain a realistic value by operating with a simulation environment created online. The system was analyzed for optimized L and C values and different output frequencies. As a result of the analysis, it was shown that the input current THD value can be kept under the 3 % while the power factor value can be kept close to 1.

Consequently, it can be said that the optimized input filter can give the desired results without disrupting the inherent properties of the matrix converter.

REFERENCES

[1] M. Hamouda, H. F. Blanchette, and K. Al-Haddad, "Unity Power Factor Operation of Indirect Matrix Converter Tied to Unbalanced Grid," *IEEE Trans. Power Electron.*, vol. 31, 2, 2016, pp. 1095–1107,

[2] R. Kumar, A. V. Goyal, S. Srivastava, S. P. Singh, and N. Singh, "Modelling and simulation of matrix converter based DC-DC converter," in *2013 International Conference on Energy Efficient Technologies for Sustainability, ICEETS 2013*, 2013, pp. 134–138.

[3] L. Gyugyi and B. R. Pelly, "Static power frequency changers: Theory, performance, and application," Computer Science, 1976.

[4] E. Watanabe, S. Ishii, E. Yamamoto, H. Hara, J. K. Kang, and A. M. Hava, "High performance motor drive using matrix converter," in *IEE Colloquium (Digest)*, no. 72, 2000, pp. 33–38.

[5] P. Wheeler and D. Grant, "Optimised input filter design and low-loss switching techniques for a practical matrix converter," *IEE Proc. Electr. Power Appl.*, vol. 144, 1, 1997, pp. 53–60.

[6] A. Alesina and M. G. B. Venturini, "Analysis and Design of Optimum-Amplitude Nine-Switch Direct AC–AC Converters," *IEEE Trans. Power Electron.*, vol. 4, 1, 1989, pp. 101–112.

[7] A. K. Sahoo, K. Basu, and N. Mohan, "Systematic input filter design of matrix converter by analytical estimation of RMS current ripple," *IEEE Trans. Ind. Electron.*, vol. 62, 1, 2015, pp. 132–143.

[8] P. Wheeler, J. Clare, L. Empringham, M. Apap, and M. Bland, "Matrix converters," *Power Eng. J.*, vol. 16, 6, 2002, pp. 273–282.

[9] K. You, D. Xiao, M. F. Rahman, and M. N. Uddin, "Applying reduced general direct space vector modulation approach of AC-AC matrix converter theory to achieve direct power factor controlled three-phase AC-DC matrix rectifier," in *IEEE Transactions on Industry Applications*, vol. 50, 3, 2014, pp. 2243–2257.

[10] O. Aydogmus and E. Deniz, "Design and implementation of two-phase permanent magnet synchronous motor fed by a matrix converter," *IET Power Electron.*, vol. 10, 9, 2017, pp. 1054–1060.

[11] E. Deniz and Ö. Aydoğmuş, "Design and implementation of two-phase matrix converter," *J. Fac. Eng. Archit. Gazi Univ.*, vol. 32, 1, 2017, pp. 9–20.

[12] H. M. Nguyen, H. H. Lee, and T. W. Chun, "Input power factor compensation algorithms using a new direct-SVM method for matrix converter," *IEEE Trans. Ind. Electron.*, vol. 58, 1, 2011, pp. 232–243.

[13] H. H. Lee, H. M. Nguyen, and T. W. Chun, "New direct-SVM method for matrix converter with main input power factor compensation," in *IECON Proceedings (Industrial Electronics Conference)*, 2008, pp. 1281–1286.

[14] H. Wu, H. Ge, Y. Xu, and W. Zhang, "The power factor correction of three-phase to single-phase matrix converter with an active power decoupling capacity," in *IEEE Transportation Electrification Conference and Expo, ITEC Asia-Pacific 2014 - Conference Proceedings*, 2014.

[15] D. Borojević, "Space Vector Modulated Three-Phase to Three-Phase Matrix Converter with Input Power Factor Correction," *IEEE Trans. Ind. Appl.*, vol. 31, 6, 1995, pp. 1234–1246.

[16] D. Casadei, G. Serra, A. Tani, A. Trentin, and L. Zarri, "Theoretical and experimental investigation on the stability of matrix converters," *IEEE Trans. Ind. Electron.*, vol. 52, 5, 2005, pp. 1409–1419.

[17] D. Casadei, G. Serra, A. Tani, and L. Zarri, "Effects of input voltage measurement on stability of matrix converter drive system," *IEE Proc. Electr. Power Appl.*, vol. 151, 4, 2004, pp. 487–497.

[18] D. Casadei *et al.*, "Large-signal model for the stability analysis of matrix converters," *IEEE Trans. Ind. Electron.*, vol. 54, 2, 2007, pp. 939–950.

[19] J. W. Kolar, F. Schafmeister, S. D. Round, and H. Ertl, "Novel three-Phase AC-AC sparse matrix converters," *IEEE Trans. Power Electron.*, vol. 22, 5, 2007, pp. 1649–1661.

[20] K. Yamada *et al.*, "Integrated filters and their combined effects in matrix converter," in *Conference Record - IAS Annual Meeting (IEEE Industry Applications Society)*, 2005, vol. 2, pp. 1406–1413.

[21] F. B. Demir, T. Tuncer, and A. F. Kocamaz, "Lojistik-Gauss Harita Tabanlı Yeni Bir Kaotik Sürü Optimizasyon Yöntemi," *Anatol. J. Comput. Sci.*, vol. 4, 1, 2019, pp. 47–53.

[22] F. B. Demir, T. Tuncer, A. F. Kocamaz, and F. Ertam, "A survival classification method for hepatocellular carcinoma patients with chaotic Darcy optimization method based feature selection," *Med. Hypotheses*, vol. 139, 2020.
[23] F. B. Demir, T. Tuncer, and A. F. Kocamaz, "A chaotic optimization method based on logistic-sine map for numerical function optimization," *Neural Comput. Appl.*, 2020, pp. 1–13.
[24] F. B. Demir, T. Tuncer, and A. F. Kocamaz, "Lojistik-singer harita tabanli yeni bir kaotik sürü optimizasyon yöntemi," in *2019 International Conference on Artificial Intelligence and Data Processing Symposium, IDAP 2019*, 2019.
[25] R. Çelikel and M. Özdemir, "A method for current control of the flywheel energy storage system used in satellites," *Teh. Vjesn.*, vol. 26, 3, 2019, pp. 631–638.
[26] M. GEDİKPINAR and Ö. ATDOĞMUŞ, "Design of a self-starting hybrid permanent magnet hysteresis synchronous motor connected directly to the grid," *TURKISH J. Electr. Eng. Comput. Sci.*, vol. 25, 2017, pp. 1657–1668.
[27] K. E. Parsopoulos, "Particle Swarm Methods," in *Handbook of Heuristics*, Springer International Publishing, 2015, pp. 1–47.
[28] J. Kennedy ; R. Eberhart, "Particle swarm optimization," in *In: Proceedings of the IEEE international joint conference on neural networks*, 1995, vol. 4, no. 6, pp. 1942–1948.
[29] Y. Shi and R. Eberhart, "Modified particle swarm optimizer," in *Proceedings of the IEEE Conference on Evolutionary Computation, ICEC*, 1998, pp. 69–73.
[30] R. Eberhart and J. Kennedy, "New optimizer using particle swarm theory," in *Proceedings of the International Symposium on Micro Machine and Human Science*, 1995, pp. 39–43.
[31] M. Erik and H. Pedersen, "Good Parameters for Particle Swarm Optimization," Technical Report no. HL1001, 2010.
[32] M. Agrawal, M. Mishra, and S. P. S. Kushwah, "Association rules optimization using improved PSO algorithm," 2015 International Conference on Communication Networks (ICCN), 2015, pp. 395–398.
[33] M. G. B. Venturini, "Solid-State Power Conversion: A Fourier Analysis Approach to Generalized Transformer Synthesis," *IEEE Trans. Circuits Syst.*, vol. 28, 4, 1981, pp. 319–330.
[34] O. Aydogmus and S. Sünter, "Implementation of EKF based sensorless drive system using vector controlled PMSM fed by a matrix converter," *Int. J. Electr. Power Energy Syst.*, vol. 43, 1, 2012, pp. 736–743.
[35] A. Popovici, V. Popescu, M. I. Băbăiţă, D. Lascu, and D. Negoitescu, "Modeling, Simulation and Design of Input Filter for Matrix Converters," in *2005 WSEAS Int. Conf. on on Dynamıcal Systems and Control*, 2005, pp. 439–444.
[36] Y. Zhang, S. Balochian, P. Agarwal, V. Bhatnaga, and O. J. Housheya, "Artificial Intelligence and Its Applications," *Math. Probl. Eng.*, vol. 2014, 2014, pp. 1–10.
[37] T. M. Blooming and D. J. Carnovale, "Application of IEEE STD 519-1992 harmonic limits," in *IEEE Conference Record of Annual Pulp and Paper Industry Technical Conference*, 2006.
[38] D. Committee, I. Power, and E. Society, "IEEE Std 519-2014 (Revision of IEEE Std 519-1992)," *IEEE Std 519-2014 (Revision IEEE Std 519-1992)*, vol. 2014, 2014, pp. 1–29.

BIOGRAPHIES

GULLU BOZTAS received the B.S. (2011), M.S. (2015), and Ph.D. (2019) degree in electric-electronics engineering from the University of Firat. Since 2013, she has been a Research Assistant in Department of Electrical & Electronics Engineering, Faculty of Technology, Firat University, Elazig, Turkey. Her research interests include power electronics and electric machines.

I-PD Controller Design Based on Analytical Rules for Stable Processes with Inverse Response

I. KAYA

***Abstract*— Inverse response characteristic makes the control of a process more challenging. In this study, simple and analytical expressions have been obtained to evaluate optimum settings of I-PD controllers for controlling open loop stable processes with time delay and a positive zero. Time weighted versions of Integral of Squared Error (ISE) criterion, namely ISTE, IST^{2}E and IST^{3}E criteria, which have been proved to be leading to very adequate closed loop responses, have been exploited to obtain mentioned optimum settings. Simulation examples have been considered to for evaluating the effectiveness of obtained tuning rules.**

Index Terms—**PID, I-PD, Stable process, Time delay, Inverse response, Integral performance indices.**

I. INTRODUCTION

IT HAS BEEN reported that more than 95% of controllers in the process control applications are PID (Proportional-Integral-Derivative) type controllers [1]. However, it has also been reported that 75% of all PID based control loops are out of tune. Therefore, researchers are still studying on developing new design methods for calculating the setting parameters of PID controllers.

Design of PID controllers to control inverse response processes is interesting and challenging. Hence, in recent decades, researchers have given many efforts to design PID controllers for inverse response processes. Control of stable processes with inverse response and dead time was given by Luyben [2]. It was stated that the method could give good responses up to dead time value of 3.2 [2]. Luyben suggested an identification approach for modelling integrating processes with inverse response and a design method for tuning a PID controller for controlling it [3]. The response obtained by their method was very sluggish. The use of direct synthesis approach for designing PID controllers to control time delay stable processes with inverse response was studied in [4]. was Pai et al. [5] also used direct synthesis method to obtain analytical expressions for calculating PI/PID controller settings for controlling integrating processes with time delay and inverse response. Simple tuning rules were provided, however, obtained closed loop responses were very oscillatory. Jeng and Lin [6] proposed a Smith-type control structure for controlling both stable and integrating processes with time delay and inverse response. Hamamci [7] suggested design of PID controllers based on graphical optimization for stable, integrating and unstable processes without inverse response. Kaya and Cengiz [8] designed PI/PID controllers using analytical rules for controlling time delay stable processes with inverse response. Authors extended their method to controlling integrating processes with inverse response and time delay, as well. A similar study were later conducted by Irshad and Ali [9], too.

Control of a process becomes more troublesome by inclusion of inverse response characteristic, and the use of conventional PID control, which is the case for the above given references, may lead to unacceptable closed loop responses. Therefore, a PI-PD controller, which has proven to give rise to much better closed loop responses, in the Smith predictor scheme was suggested for controlling stable processes with inverse response [10]. Two difficulties with this method can be expressed. First, the Smith predictor scheme is sensitive to modelling errors and parameter variations. Second, determination of tuning parameters of the forward path controller, PI, includes a trade-off and they must be limited to a value by the designer.

I-PD control has a similar structure to the PI-PD control configuration. PI-PD control configuration has a PI controller on the forward path, whereas I-PD control has an I only controller on the forward path. Having only three tuning parameters to be calculated simplifies the design procedure. Additionally, I-PD controllers can result in very similar closed loop responses that can be achieved with PI-PD controllers.

In this study, simple analytical expressions have been provided to calculate optimum settings of an I-PD controller for improving closed loop responses of stable processes with inverse response and time delay. It is assumed that the process can be identified as a first order plus dead time with inverse response (FOPDT-IR) transfer function. Then, repetitive optimizations in the sense of time weighted integral performance criteria were performed on the error signal of the

IBRAHIM KAYA is with Department of Electrical and Electronics Engineering, Dicle University, Diyarbakır, Turkey, (e-mail: ikaya@dicle.edu.tr).

https://orcid.org/0000-0002-8393-1358

Manuscript received June 01, 2020; accepted July 30, 2020.
DOI: 10.17694/bajece.746352

I-PD control configuration. Thereby, simple analytical expressions have been obtained in terms of parameters of the I-PD controller and the FOPDT model transfer function. Several simulation examples have been given to illustrate the much improved closed loop responses achieved with proposed I-PD controller design method.

The remaining parts of the paper is organized as follows: A very short survey of integral performance criteria is provided in Section II. Section III explains the design of optimum I-PD controllers for controlling FOPDT-IR processes. Simulation examples are supplied in Section IV to show effectiveness of the proposed I-PD controller design method. Finally, conclusions are given in Section V.

II. INTEGRAL PERFORMANCE CRITERIA

In this paper, the following general form of integral performance criteria is used in the optimization.

$$J_n(\eta)=\int_0^\infty [t^n e(\eta,t)]^2\,dt, \qquad n=1,2,3 \tag{1}$$

Here, η stands for the settings of I-PD controller to minimize the performance criteria given in Eq. (1). Selecting various n values, various performance criteria can be obtained. For example, selecting $n=1$ the criteria is named as ISTE, selecting $n=2$ the criteria is named as IST^{2}E, and selecting $n=3$ the criteria is named as IST^{3}E. Increasing the value of n, results in improved closed loop performance in the sense of lower overshoots. Larger n value may slightly slow down the speed of response and increase the settling time.

For minimization of the integral given by Eq. (1), PSO (Particle Swarm Optimization), which is a metaheuristic optimization algorithm, is used [11], [12]. The PSO algorithm works as follows: all particles are randomly distributed in the search space at the beginning. The best position of a particle itself and the best positions of its neighbors are used to update the position at each step. The process is repeated for all particles. The algorithm runs continuously in this manner until the best solution has been obtained [12], [13].

III. I-PD CONTROLLER DESIGN

I-PD controller structure used to control open loop stable processes with inverse response is shown in Fig. 1. In the figure, $G(s)$ is the process transfer function to be controlled. I and PD controllers, respectively, are given by $G_{c1}(s)$ and $G_{c2}(s)$.

The following transfer function is used to identify a stable processes with inverse response and time delay:

$$G(s)=\frac{K(-T_0 s+1)e^{-\theta s}}{(Ts+1)} \tag{2}$$

I-PD controller transfer functions, $G_{c1}(s)$ and $G_{c2}(s)$, are assumed to be given by the following ideal transfer functions:

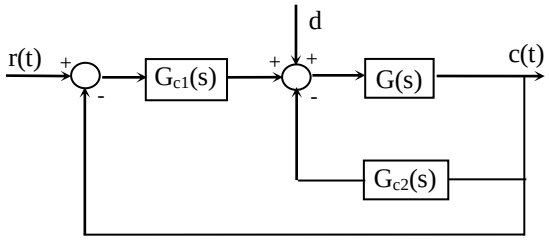

Fig. 1. I-PD Control Structure

$$G_{c1}(s)=\frac{K_c}{T_i s} \tag{3}$$

$$G_{c2}(s)=K_c(1+T_d s) \tag{4}$$

In order to find correlations between the I-PD controller parameters and process transfer function model parameters, $sT=\bar{s}$ normalization is used in Eqs. (2), (3) and (4). 3/3 Pade approximation was used for the normalized time delay. For a specified value of T_0/T, a unit step reference input $r(t)$ was applied to the closed loop system shown in Fig. 1. Then for various values of normalized time delay θ/T, repeated optimizations were carried out by using the PSO algorithm to minimize the error in closed loop system, illustrated in Fig. 1. In the PSO algorithm, number of the particles was selected as 33, and number of iterations for each θ/T value was selected as 300.

For chosen values of T_0/T (0.7 and 1.0), correlations between KK_c, T_i/T and T_d/T and varying values of θ/T (in the range of 0.1 to 1.0 and 1.1 to 2.0) are given in Fig. 2 and Fig. 3 for the ISTE criterion. Tuning parameters obtained from the optimization are shown by asterisk. Then, a curve fitting method has been used to find expressions that fits to obtained tuning parameters. Results of expressions obtained from curve fitting are shown by solid lines. It is observed that very satisfactory fittings have been achieved.

Formulas obtained from the curve fitting method are given below:

$$KK_c=a_1+b_1\left(\frac{\theta}{T}\right)+c_1\left(\frac{T_0}{T}\right)+d_1\left(\frac{\theta}{T}\right)^2+e_1\left(\frac{\theta}{T}\right)\left(\frac{T_0}{T}\right) \tag{5}$$

$$\frac{T_i}{T}=a_2+b_2\left(\frac{\theta}{T}\right)+c_2\left(\frac{T_0}{T}\right)+d_2\left(\frac{\theta}{T}\right)^2+e_2\left(\frac{\theta}{T}\right)\left(\frac{T_0}{T}\right) \tag{6}$$

$$\frac{T_d}{T}=a_3+b_3\left(\frac{\theta}{T}\right)+c_3\left(\frac{T_0}{T}\right)+d_3\left(\frac{\theta}{T}\right)^2+e_3\left(\frac{\theta}{T}\right)\left(\frac{T_0}{T}\right) \tag{7}$$

It has been observed that these expressions can be used for both ranges, that is, $0.1\le\theta/T\le1.0$ and $1.1\le\theta/T\le2.0$, as long as convenient constants are used.

The procedure given above can be repeated for IST^{2}E and IST^{3}E criteria too. Interestingly, it was found that above given expressions can be used for IST^{2}E and IST^{3}E criteria with

appropriate constants, as well. Constants in these expressions for different integral performance criteria and different normalized time delay ratio ranges are summarized in Table I and Table II.

Therefore, once the model transfer function of open loop stable process with inverse response is known, given by Eq. (2), then normalized θ/T and T_0/T ratios can be found and substituted into Eqs. (5)-(7) to calculate optimum I-PD controller settings by selecting appropriate constants from Table I or Table II.

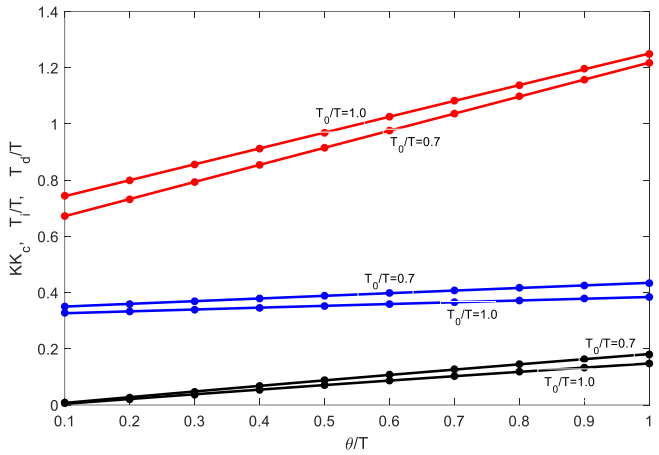

Fig. 2. I-PD parameters over range $0.1 \le \theta/T \le 1.0$ for ISTE criterion (red: T_i/T, blue: KK_c, black: T_d/T)

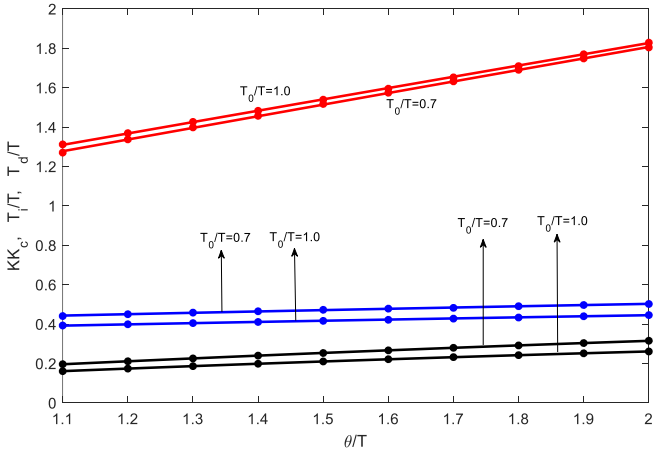

Fig. 3. I-PD parameters over range $1.1 \le \theta/T \le 2.0$ for ISTE criterion (red: T_i/T, blue: KK_c, black: T_d/T)

IV. Simulations And Results

In this section several simulation examples are provided to show the effectiveness of the suggested I-PD controller design method. Irshad and Ali [9], Chien et al. [4] and Jeng and Lin [6] suggested PID controller design methods for controlling stable processes with inverse response and time delay, as well. Therefore, their design methods have been used to evaluate the closed loop performance of suggested I-PD controller design method.

TABLE I
I-PD CONTROLLER PARAMETERS FOR $0.1 \le \theta/T \le 1.0$

		ISTE	IST²E	IST³E
KK_c	a_1	0.38910	0.40550	0.35780
	b_1	0.16670	0.07243	0.04696
	c_1	-0.06931	-0.10900	-0.06851
	d_1	-0.00343	-0.00551	0.02534
	e_1	-0.09871	-0.01586	-0.04792
T_i/T	a_2	0.34300	0.53490	0.52450
	b_2	0.71270	0.57540	0.52200
	c_2	0.25240	0.15130	0.15960
	d_2	-0.00375	0.00148	0.03913
	e_2	-0.14470	-0.05475	-0.08905
T_d/T	a_3	-0.01359	-0.01958	-0.01971
	b_3	0.28810	0.32870	0.37070
	c_3	0.000244	0.00520	0.00269
	d_3	-0.14940	-0.01275	-0.01877
	e_3	-0.11200	-0.13560	-0.15000

TABLE II
I-PD CONTROLLER PARAMETERS FOR $1.1 \le \theta/T \le 2.0$

		ISTE	IST²E	IST³E
KK_c	a_1	0.45520	0.40960	0.34210
	b_1	0.10410	0.07709	0.09369
	c_1	-0.14300	-0.11150	-0.08028
	d_1	-0.00670	-0.00121	-0.00533
	e_1	-0.02445	-0.02727	-0.03791
T_i/T	a_2	0.50700	0.56760	0.49330
	b_2	0.63880	0.55120	0.59280
	c_2	0.15690	0.12810	0.15330
	d_2	-0.00614	0.01095	0.00096
	e_2	-0.04533	-0.04985	-0.08645
T_d/T	a_3	0.02686	0.03825	0.07456
	b_3	0.25310	0.28430	0.28550
	c_3	-0.03932	-0.05992	-0.08782
	d_3	-0.02317	-0.02780	-0.02632
	e_3	-0.07018	-0.06979	-0.06130

Example 1:

Consider an inverse response process transfer function given by

$$G(s) = \frac{0.5848(-0.3546s+1)e^{-0.3567s}}{(0.6302s+1)}.$$

This transfer function was studied by Irshad and Ali [9]. It was derived for an isothermal CSTR exhibiting multiple steady state solutions. For this example comparisons are given only with design method of Irshad and Ali [9] because design methods of Chien et al. [4] and Jeng and Lin [6] requires a

second order stable process transfer function with a positive zero and time delay, hence they cannot be used for this case. Irshad and Ali [9] suggested a PI controller which its tuning parameters found from optimum tuning rules. This process transfer function has a normalized time delay ratio of $\theta/T=0.566$ and $T_0/T=0.563$. Using these values in Eqs. (5)-(6), calculated settings of the proposed I-PD controller and PI controller of Irshad and Ali [9] are given in Table III for various integral performance criteria. A unity step input and a disturbance having magnitude of 0.5 were applied to closed loop control system. It was assumed that the disturbance exist in the system at time $t=10$ s. Obtained closed loop responses for both design methods are illustrated in Fig. 4.

For the I-PD controller, it is observed that there is not much difference in the closed loop performances for ISTE, ISTE2E and IST3E criteria based designs. Thus, in the following examples comparisons will be performed for I-PD controller that is designed based on ISTE criterion. For the PI controller design suggested by Irshad and Ali [9] ISTE criterion results in slightly oscillatory response. Also, PI controller designs suggested by Irshad and Ali [9] lead to larger initial inverse responses.

Closed loop responses for both design methods are depicted in Fig. 5 for +20% change in all parameters (K, T_0, T and θ) of the model transfer function. It is observed that the proposed I-PD provides less overshoot and slightly shorter settling time for both set point tracking and disturbance rejection. Actually, this example verifies the better performance of an I-PD controller than classical PID type controller, because the proposed design method the design method of Irshad and Ali [9] are both rely on the integral performance criteria. Thus, improved response is due to the control structure of I-PD controller.

TABLE III
CONTROLLER PARAMETERS FOR EXAMPLE 1

	Proposed I-PD			PI (Irshad and Ali)		
	ISTE	IST^{2}E	IST^{3}E	ISTE	IST^{2}E	IST^{3}E
K_c	0.704	0.647	0.579	1.270	1.003	0.857
T_i	0.587	0.585	0.563	0.890	0.773	0.718
T_d	0.069	0.077	0.087	-	-	-

Example 2:

Here, the following higher order stable process with inverse response and time delay, which was studied by Jeng and Lin [6], is considered:

$$G(s)=\frac{(-2s+1)e^{-0.5s}}{(2s+1)(s+1)(0.5s+1)}.$$

To identify settings of the I-PD controller, FOPDT-IR model given in Eq. (2) must be determined. For simplicity, approximation method suggested in [14] is used in this study.

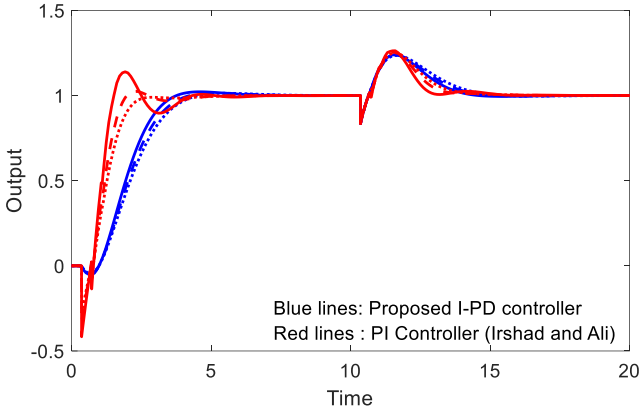

Fig. 4. Closed loop responses for example 1 (solid line: ISTE, dashed line: IST^{2}E, dotted line: IST^{3}E)

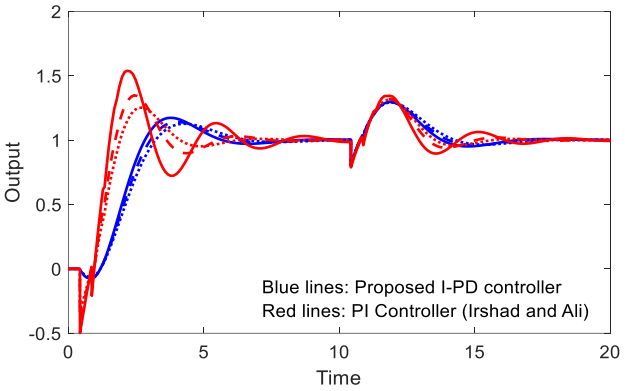

Fig. 5. Closed loop responses for perturbed for example 1 (solid line: ISTE, dashed line: IST^{2}E, dotted line: IST^{3}E)

This approach suggests the use of a first order Taylor series expansion for the smaller poles in order to approximate them. Thus, applying this approach to the two smaller poles, one can obtain the following model:

$$G_m(s)=\frac{(-2s+1)e^{-2s}}{(2s+1)}.$$

This model has a normalized time delay ratio of $\theta/T=1.0$ and $T_0/T=1.0$. Substituting these values in Eqs. (5)-(6) with proper constants selected from Table I, the proposed I-PD controller settings were calculated and given in Table VI together with tuning parameters for other design methods. Additional tuning parameter, λ, of design method suggested by Jeng and Lin [6] has also been supplied in the table.

A unity step input and a disturbance having magnitude of -1 were applied to closed loop control system. It was assumed that the disturbance exist in the system at time $t=40$ s. Obtained closed loop responses for all design approaches are given in Fig. 6. It is observed from figure that proposed I-PD controller design gives the most satisfactory closed loop responses for both the set point tracking and disturbance rejection in the sense of less overshoot and oscillations. Also, unlike the proposed one, others have large initial inverse responses. Corresponding process inputs are shown Fig. 7, which reveals that the proposed I-PD controller has the

smallest control signal magnitude. Design method suggested by Chien et al. [4] requires very large initial control effort.

TABLE VI
CONTROLLER PARAMETERS FOR EXAMPLE 2

Design Methods	K_c	T_i	T_d	λ
Proposed I-PD	0.384	2.501	0.296	-
Irshad and Ali	0.549	3.512	-	-
Jeng and Lin	0.826	4.283	1.011	3.3
Chien et al.	0.596	2.706	1.500	-

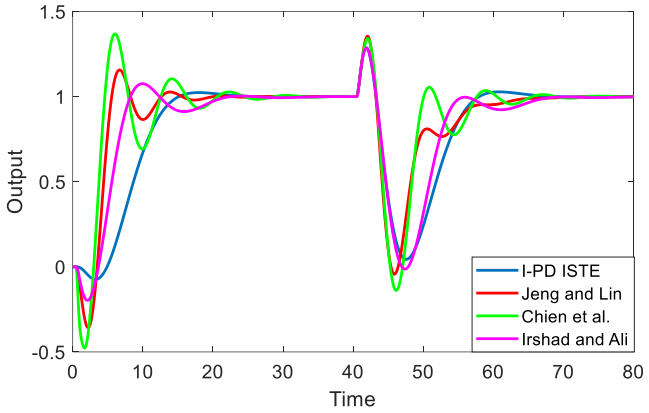

Fig. 6. Output responses for example 2

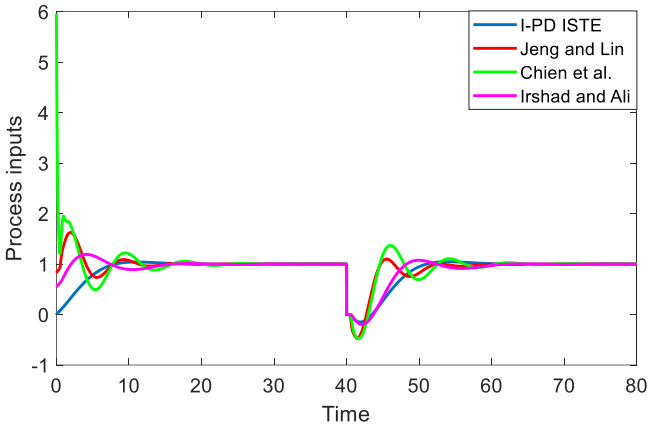

Fig. 7. Process inputs for example 2

Example 3:

Here, a high order stable process with inverse response without time delay given below

$$G(s)=\frac{(-2s+1)}{(s+1)^5}$$

is studied. This process transfer function was also studied by Jeng and Lin [6]. Again, to evaluate setting of the proposed I-PD controller, FOPDT-IR model given in Eq. (2) must be identified. Using the approach explained in example 2, the following model

$$G_m(s)=\frac{(-2s+1)e^{-3s}}{(2s+1)}.$$

which has $\theta/T=1.5$ and $T_0/T=1.0$, can be obtained. Replacing these normalized values into Eqs. (5)-(6) with appropriate constants chosen from Table II, the proposed I-PD controller tuning parameters were evaluated and are provided in Table V. The table gives tuning parameters of design methods used for comparison, as well.

A unity step input and a disturbance having magnitude of -1 were applied to closed loop control system. It was assumed that the disturbance exists in the system at time $t=50$ s. Closed loop responses for all design methods are depicted in Fig. 8. It is seen from the figure that proposed I-PD controller design has much superior performance than others, which all have large overshoots for set point tracking. Additionally, design method suggested by Irshad and Ali [9] has large oscillations for set point tracking and disturbance rejection. Process inputs for all design methods are shown Fig. 9. Similar to example 2, proposed I-PD controller has a smaller control signal magnitude when compared to others.

TABLE V
CONTROLLER PARAMETERS FOR EXAMPLE 3

Design Methods	K_c	T_i	T_d	λ
Proposed I-PD	0.417	3.081	0.420	-
Irshad and Ali	0.632	3.112	-	-
Jeng and Lin	0.795	4.038	1.287	3.7
Chien et al.	0.831	3.681	1.095	-

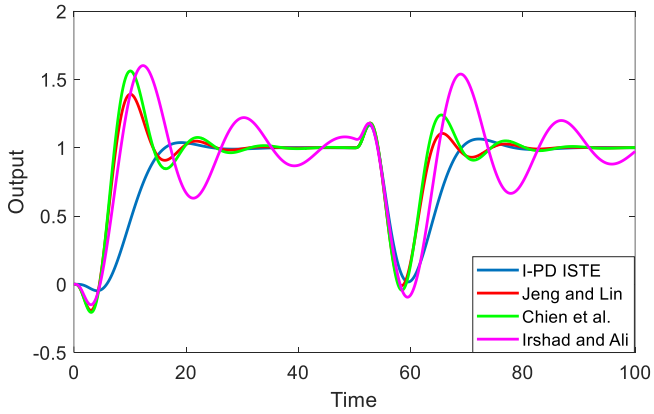

Fig. 8. Output responses for example 3

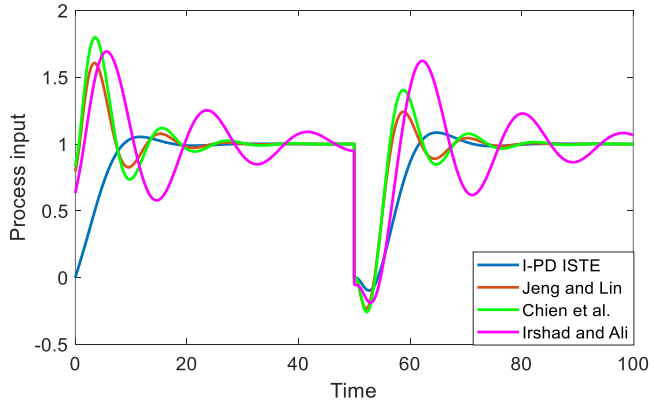

Fig. 9. Process inputs for example 3

V. CONCLUSIONS

Analytical expressions enabling one to calculate optimum tuning parameters of an I-PD controller for controlling stable processes with inverse response and dead time have been

provided. ISTE, IST^{2}E and IST^{3}E criteria were exploited to derive those expressions. As there is not much difference between the closed loop performances obtained from ISTE, IST^{2}E and IST^{3}E criteria for the case studied in this paper, but slightly faster response can be achieved with ISTE criterion, for the comparisons ISTE based rules were used. Provided simulation results exhibited the much better performance of the proposed I-PD controller design for both set point tracking and disturbance rejection.

REFERENCES

[1] K. J. Åström and T. Hägglund, *PID controllers: theory, design and tuning*. 1995.

[2] W. L. Luyben, "Tuning Proprotional-Integral Controllers for Processes with Both Inverse Response and Deadtime," *Ind. Eng. Chem. Res.*, vol. 39, no. 4, pp. 973–976, 2000.

[3] W. L. Luyben, "Identification and Tuning of Integrating Processes with Deadtime and Inverse Response," *Ind. Eng. Chem. Res.*, vol. 42, no. 13, pp. 3030–3035, 2003.

[4] I.-L. Chien, Y.-C. Chung, B.-S. Chen, and C.-Y. Chuang, "Simple PID Controller Tuning Method for Processes with Inverse Response Plus Dead Time or Large Overshoot Response Plus Dead Time," *Ind. Eng. Chem. Res.*, vol. 42, no. 20, pp. 4461–4477, 2003.

[5] N. S. Pai, S. C. Chang, and C. T. Huang, "Tuning PI/PID controllers for integrating processes with deadtime and inverse response by simple calculations," *J. Process Control*, vol. 20, no. 6, pp. 726–733, 2010, doi: 10.1016/j.jprocont.2010.04.003.

[6] J. C. Jeng and S. W. Lin, "Robust proportional-integral-derivative controller design for stable/integrating processes with inverse response and time delay," *Ind. Eng. Chem. Res.*, vol. 51, no. 6, pp. 2652–2665, 2012, doi: 10.1021/ie201449m.

[7] S. E. Hamamci, "A New PID Tuning Method Based on Transient Response Control," *Balk. J. Electr. Comput. Eng.*, vol. 2, no. 3, pp. 132–138, 2014.

[8] I. Kaya and H. Cengiz, "Optimal Analytical PI and PID Tuning Rules for Controlling Stable Processes with Inverse Response," in *10th International Conference on Electrical and Electronics Engineering Conference, ELECO 2017*, 2017, pp. 1355–1359.

[9] M. Irshad and A. Ali, "Optimal tuning rules for PI/PID controllers for inverse response processes," *IFAC-PapersOnLine*, vol. 51, no. 1, pp. 413–418, 2018, doi: 10.1016/j.ifacol.2018.05.063.

[10] I. Kaya, "PI-PD controllers for controlling stable processes with inverse response and dead time," *Electr. Eng.*, vol. 98, no. 1, pp. 299–305, 2016, doi: 10.1007/s00202-015-0352-3.

[11] R. Eberhart and James Kennedy, "A New Optimizer Using Particle Swarm Theory," *Sixth Int. Symp. Micro Mach. Hum. Sci.*, 1999, doi: 10.1.1.470.3577.

[12] M. T. Özdemir, D. Öztürk, I. Eke, V. Çelik, and K. Y. Lee, "Tuning of Optimal Classical and Fractional Order PID Parameters for Automatic Generation Control Based on the Bacterial Swarm Optimization," *IFAC-PapersOnLine*, 2015, doi: 10.1016/j.ifacol.2015.12.429.

[13] R. Eberhart and J. Kennedy, "A new optimizer using particle swarm theory," pp. 39–43, 2002, doi: 10.1109/mhs.1995.494215.

[14] D. E. Seborg, T. F. Edgar, D. A. Mellichamp, and F. J. Doyle III, *Process Dynamics and Control*, 3rd ed. John Wiley & Sons, Inc., 2011.

BIOGRAPHY

Ibrahim KAYA was born in Diyarbakır, Turkey, in 1971. He received BSc degree in electrical and electronics engineering from Gaziantep University, Turkey in 1994 and a DPhil degree in control engineering from University of Sussex, Brighton, UK in 1999. He is currently working as a professor in the department of electrical and electronics engineering at Dicle University, Diyarbakır, Turkey. His primary research interest lies in systems and control.

Comparison of Support Vector Machine Models in the Classification of Susceptibility to Schistosomiasis

D. OLANLOYE, R. OLASUNKANMI and E. ODUNTAN

***Abstract*— Schistosomiasis has become epidemic sending millions of people into untimely graves. A lot of contributing efforts in term of research have been made to eradicate or reduce the rate of this dangerous infection. In this research work, the concept of Machine Learning as one of the sub-division of Artificial Intelligence is being used to determine the level of susceptibility of Schistosomiasis. The research made a comparison of the various support vector machine models - Linear, Quadratic, Cubic, Fine Gaussian, Medium Gaussian and Coarse Gaussian model to determine the level of susceptibility to Schistosomiasis. The results obtained which include Confusion Matrix (CM), Receiver Operating Character (ROC) and Parallel Coordinate Plots (PCP) were interpreted in the form of accuracy, processing speed and execution time. It was finally concluded that Medium Gaussian is the best of all the six models.**

Index Terms— **Artificial Intelligence, Classification, Machine Learning, Schistosomiasis, SVM**

I. INTRODUCTION

ONE OF the major problems in the Africa sub-region is the high mortality and morbidity rate in connection with the disease known as schistosomiasis. Schistosomiasis is a blood dwelling parasitic worm that represents a series of health problems in a tropical region. More than two hundred million people have been infected. It is one of the widely spread and prevalent parasitic diseases in the world today (Makolo and Akinyemi, 2016).

Since the beginning of 20th century, this has been found endemic in several countries and its discontinuous geographical distribution determine to a great extent by the occurrence of its intermediate hosts (freshwater snail) of Biomphalaria (Reynold and ArveLee, 2019). This call for strong measures, aimed at managing the scourge.

A lot of research work has been carried out in this area using various approaches or methods. Computer Scientists are putting in their best yet, enough has not been done to manage the scourge. This research is out to measure and to compare the performance of Support Vector Machine models at the various level of susceptibility of the scourge. The models will be implemented using MatLab Machine Learning (ML) tools.

A. Schistosomiasis

This is a typical type of disease also called bilharzia. It is caused by parasitic worm released by snail into a river. A victim is infected when in contact with contaminated water and the worm penetrated the skin of the victim. It enters into the body system where it continues to grow for several weeks and become an adult worm. The adult worm lives in the blood vessels where the female type continues to produce eggs. The egg when hatched releases free-swimming larva called miracidia into freshwater. The lava finds its way into a freshwater snail and the victim is infected when in contact with such water. The freshwater can also be contaminated when an already infected animal is in contact with freshwater through its urine or faeces. The worm when absorbed into the bloodstream find its level into the liver, intestine or other vital organs in the body system. Possible symptoms include muscular aches, itching skin, persistence cough, headache, stomach pain, joint pain etc. If not treated on time, the patient starts releasing blood in the urine or stew. This leads to retarded growth, especially in children. It can also cause bladder cancer as well as kidney or liver problem. Some other major complications include high blood pressure (hypertension), urinary problem and destruction of vital organs etc. It is a chronic communicable disease that can lead to death.

B. The Concept of Artificial Intelligence and Machine Learning

Between 1940 and 1950, Artificial Intelligence(AI) emerged as a separate and independent field of study. Though, earlier before this time, literature revealed that there has been in existence of different areas of research which studied different concept that form the basis of AI. Those areas were integrated to shape AI as one of the major and independent areas of study.

An attempt to create an "Artificial Intelligence" in a machine such that the machine too can think and solve real-life problems in a humanlike manner is what is being described as Artificial Intelligence. It is a field where systems are made to cope with a certain degree of uncertainty like the accuracy of unexpected events such as unpredictable changes in the world in which the system operates. AI can be defined as the simulation of human intelligence on a machine, to make the machine efficient to identify and use the

ODUNAYO OLANLOYE is with the Department of Computer and Information System Bowen University, Iwo, Nigeria, (e-mail: odun.olanloye@bowenuniversity.edu.ng).

https://orcid.org/0000-0002-3564-774X

OLAWUMI OLASUNKANMI, is with the Department of Computer Science, Ladoke Akintola University of Technology, Ogbomoso, Nigeria, (e-mail: roolasunkanmi20@lautech.edu.ng).

https://orcid.org/0000-0002-8652-0626

ESTHER ODUNTAN, is with the Department of Computer Science, The Federal Polytechnic, Ilaro Ogun State, Nigeria, (e-mail: esteemviac@gmail.com).

https://orcid.org/0000-0003-3522-0356

Manuscript received November 28, 2019; accepted July 08, 2020.
DOI: 10.17694/bajece.651784

right piece of knowledge at a given step of solving a problem. Amint Konar (1999). One major subfield of AI is ML.

Learning could simply be defined as the process of acquiring knowledge or skill which could be applied in some application areas in futures. The process of making a machine to learn through codes or algorithm to acquire enough skill or knowledge to solve future problems is described as Machines Learning. So, the machine learns whenever it changes its structure, programme or data (based on its input or in response to external information) in such a manner that its expected future performance improves. (Kelvin, 2008).

C. *Support Vector Machine*

SVM is a typical example of ML algorithm. Support Vector Machine (SVM) was introduced by Boser, Guyon and Vapink in COLT 92. It is a supervised learning algorithm used for classification and regression. It is referred to as generalized linear classifier. In other words, it is a classification and regression tool that uses machine learning theory to maximize predictive accuracy while automatically avoiding overfitting of the data. (Vikramadiya, 2006).

Support vector machine (SVM) is a Machine Learning algorithm that learns by examples to assign labels to objects. For instances, an SVM can identify a non-fraudulent and fraudulent card (William, 2006). It maximizes a particular mathematical function for a given collection of data. Eventually, the algorithm presents an appropriate classification.

D. *Related Works*

Machine Learning Principles or tools have been used to carry out a series of research work in the area of disease classification or detection.

Stefanie et.al (2013) presented a comprehensive overview of schistosomiasis and explained the latest trend in the diagnosis and treatment of the disease most especially in children. It also revealed the number of people including young and old, recently treated with praziquantel. The article was a review and hence did not propose a specific methodology in detecting or diagnosing the disease.

Makolo and Akinyemi (2016) researched prediction of the risk of infection of schistosomiasis using machine learning approach. The methodology used was based on Neural Network with a single layer but with little variation in transformation function. The algorithm was implemented using JAVA Programming Language.

Guo Li et.al (2018) made use of three different machine learning models to diagnose patient with advance schistosomiasis residing in Hubei province. The data was collected from a previous study based on Hubei population sample including 4136 advanced schistosomiasis cases. Multivariate Logic Regression (MLR), Artificial Neural Network (ANN), Decision Tree (DT) were used for implementation. Hence, in term of sensitivity, the author established the fact that ANN outperformed the other two models.

Noura (2015) was able to apply Neural Networks in the diagnosis and treatment of heart diseases. The author specifically used backpropagation approach for the classification of two of groups – presence or absence of the diseases. Eventually, about 88% of the testing data set were classified successfully.

Bakpo and Kabari (2015) also presented a research work using Neural Network for diagnosis of skin diseases. Feedforward backpropagation was used to classify the absence or presence of the disease. When supplied with the relevant data, the system was able to record about 90% success.

Amosa et.al (2015) also developed an expert system for diagnosis and management of kidney disease making use of CLIPS expert system version 6.3. The system has about 76 rules and can detect various types of renal disease.

Ramya and Radha (2016) also diagnosed chronic kidney disease using Machine Learning algorithm. The classification model was able to classify different stages of chronic kidney diseases. The result showed that Radial basic function is better than others with 85% level of accuracy.

Again, Support Vector Machine (SVM) as one of the major tools of Machine Learning has been applied in solving different medical problems.

Deepti and Sheetal (2013) used SVM and ANN for classification of heart disease in an attempt to assist the physicians to achieve a speedy diagnosis with accurate result. The diagnosis time is reduced with more accuracy in the result obtained. It was finally concluded that SVM performs better than ANN.

Prashasti and Disha (2016) predicted the spread of cardiovascular diseases using SVM and Bayesian classification. The research work predicted accuracy, and sensitivity using SVM and Bayesian classification. The research was able to predict whether a person has heart disease or not. Accuracy graph shows that SVM is better than Naive Bayes.

Shanshikant, Cheta and Ashak (2011) developed a heart disease diagnosis system using SVM. It is an expert system that can decide what type of heart disease a patient suffers for. In the research work, it was established that SVM with sequential minimum optimization is as good as Radial Basis function for diagnosis of heart disease.

E. *Significance of the Research*

This work analyses the predictive factors in the dataset to establish the spread of scistosomiasis amongst different age groups, across continents and maximally evaluates the six (6) SVM models in term of speed, accuracy and processing time.The result obtained will serve as an eye opener to the researchers working in the area of machine learning,especially those that are interested in using SVM models to carry out further research work in the area of identification, classification and prediction of scistosomiasis and othet related diseases. The result obtained, will serve as a good platform for further research. work.

II. METHODOLOGY

A. *Data*

The research data was compiled across 4 age groups (5 - 24, 25 - 49, 50 – 74, above 74), sex (male and female), 3 different levels of exposure (2, 5, 10 for low, average and high). Following this trend, 3, 2, and 1 were assigned to age group 25 to 49, 50 to 74 and 1 to 4 respectively. 1 was also assigned to those that are above 74 years of age. This means that age groups 1 to 4 and those above 74 are in the same group simply because they are too young or too old to make attempt to swim in the river where they can easily be infected with schistosomiasis. In term of gender, males are perceived to swim in rivers than females and therefore stand a higher risk of contracting the disease and therefore assigned a higher risk value of 2 while female gender was assigned 1.

Considering the continent's level of development, Africa is at the highest risk of contracting the disease from the river and therefore assigned the highest risk factor of 4, followed by Asia, South America and others with risk factors of 3, 2 and 1 respectively. For the level of exposure, the values used are 2, 5 and 10 for low, average and high level of exposure.

B. *Method*

We tested various SVM models using MATLAB machine learning toolbox to classify the susceptibility of man to schistosomiasis infection. Five different predictors which include – age, location, sex, exposure and calculated score were used. The predictors were used as input in the classification learner. The scatter dot plot of the predictors.i.e. the plot of the calculated score against the other four predictors are shown in fig1. The six SVM models used are Linear, Quadratic, Cubic, Fine Gaussian, Medium Gaussian and Coarse Gaussian. We selected the six SVM models and used MATLAB to implement the classification model. Each algorithm was trained using the data set and the result of the training for each model was evaluated using ROC curve, Confusion matrix and parallel coordinate plot.

III. RESULTS

Evaluation results obtained from each model using ROC curve, Confusion matrix and parallel coordinate plot are shown in fig 2-7. The performance of the models was also compared using accuracy, speed and training time as shown in table1. Table 1 further explains the model performance with further details depicted in fig 8-10.

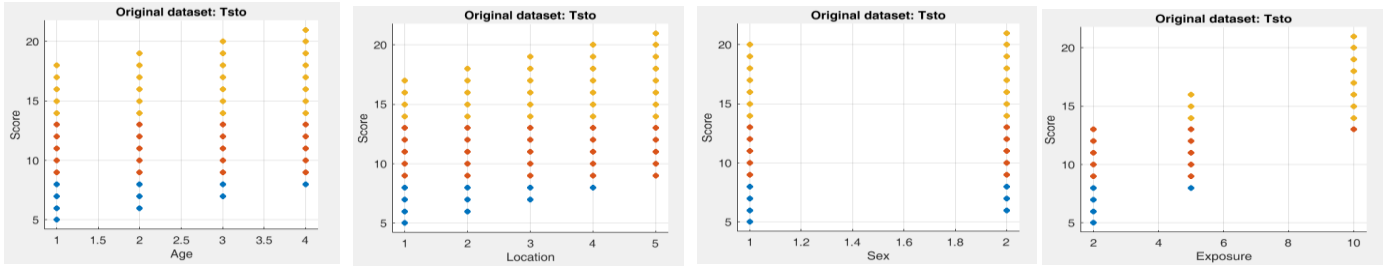

(a) Age (b) Location (c) Sex (d) Exposure

Fig.1. The Scatter Dot Plot of the Predictors

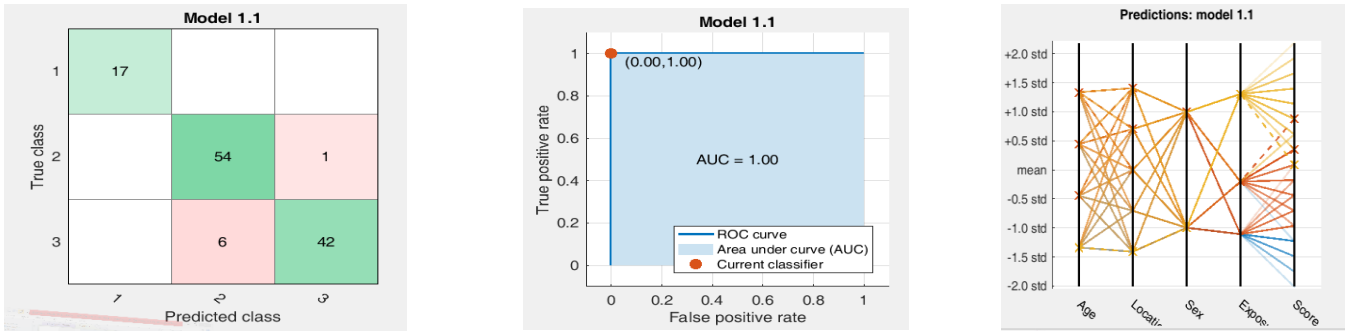

Confusion Matrix ROC Curve Parallel Coordinate Plot

Fig.2. Confusion Matrix, ROC Curve and Parallel Coordinate Plot of the Linear Model

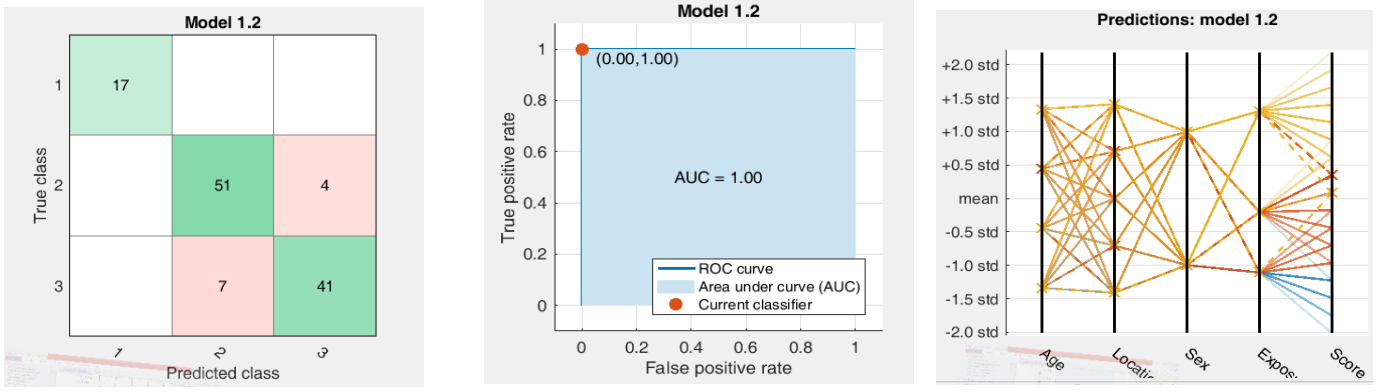

Confusion Matrix ROC Curve Parallel Coordinate Plot

Fig.3. Confusion Matrix, ROC Curve and Parallel Coordinate Plot of the Quadratic Model

Confusion Matrix

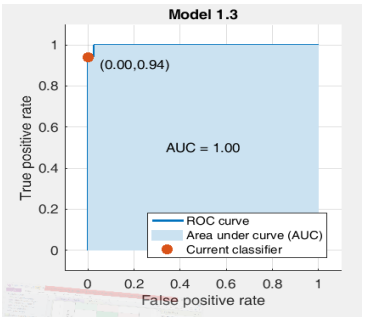

ROC Curve

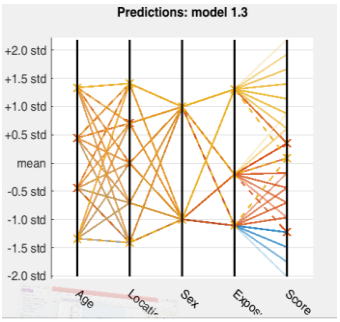

Parallel Coordinate Plot

Fig.4. Confusion Matrix, ROC Curve and Parallel Coordinate Plot of the Cubic Model

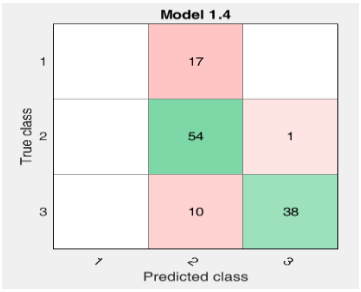

Confusion Matrix

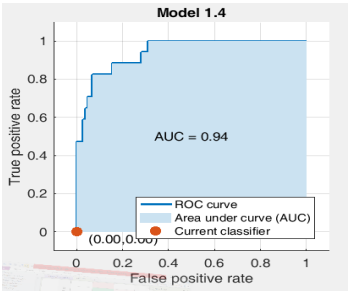

ROC Curve

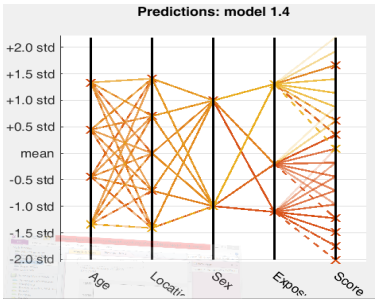

Parallel Coordinate Plot

Fig.5. Confusion Matrix, ROC Curve and Parallel Coordinate Plot of the Fine Gaussian Model

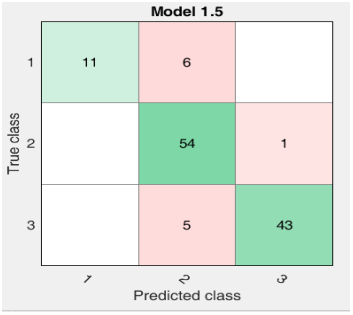

Confusion Matrix

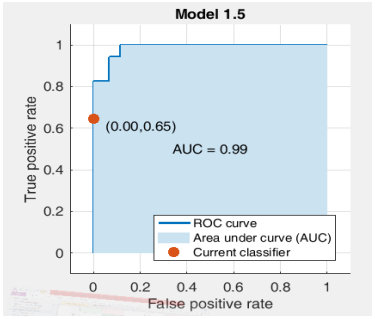

ROC Curve

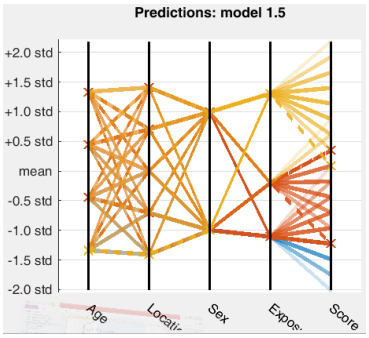

Parallel Coordinate Plot

Fig.6. Confusion Matrix, ROC Curve and Parallel Coordinate Plot of the Medium Gaussian Model

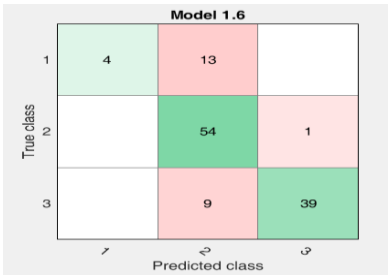

Confusion Matrix

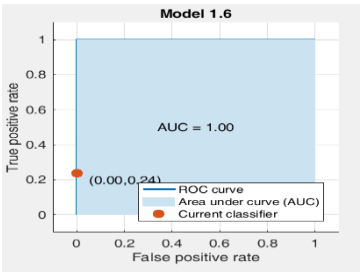

ROC Curve

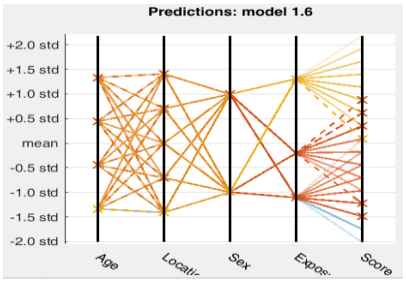

Parallel Coordinate Plot

Fig.7. Confusion Matrix, ROC Curve and Parallel Coordinate Plot of the Coarse Gaussian Model

Table I. Model Performance (Accuracy, Prediction Speed and Training Time)

Model No	Model's Type	Accuracy (%)	Prediction Speed (Obs/sec)	Training Time (sec)
1.1	**Linear**	**94.2 (1)**	**630 (5)**	**7.98 (5)**
1.2	**Quadratic**	**90.8 (2)**	**1400 (3)**	**1.34 (4)**
1.3	**Cubic**	**90.8 (2)**	**1700 (1)**	**1.06 (2)**
1.4	**Fine Gaussian**	**76.7 (5)**	**1600 (2)**	**1.12 (3)**
1.5	**Medium Gaussian**	**90.0 (3)**	**1700 (1)**	**1.03 (1)**
1.6	**Coarse Gaussian**	**80.8 (4)**	**1300 (4)**	**1.06 (2)**

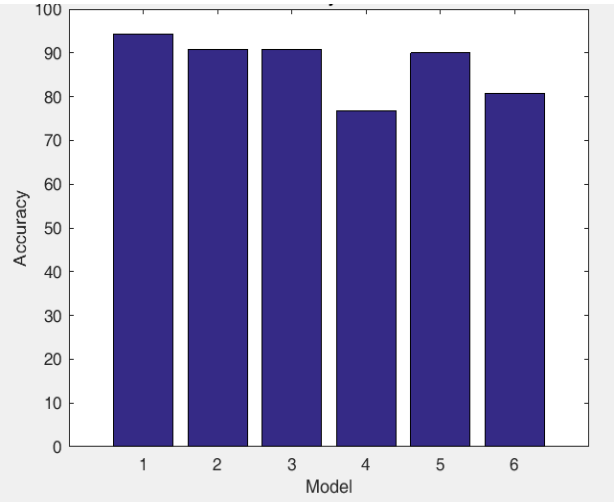

Fig.8. Plot of Accuracy for each Model

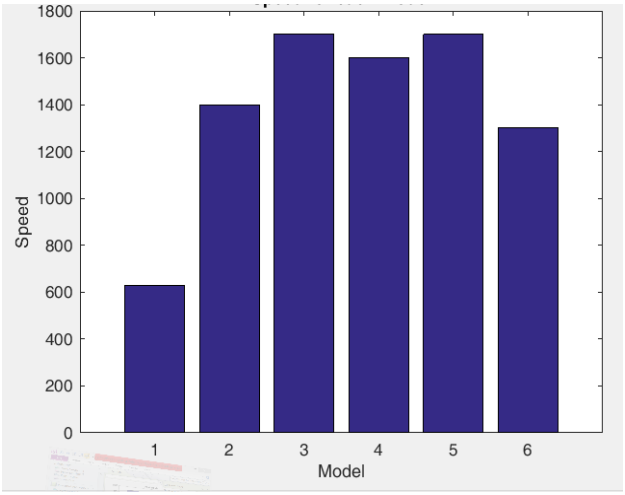

Fig.9. Speed for each Model

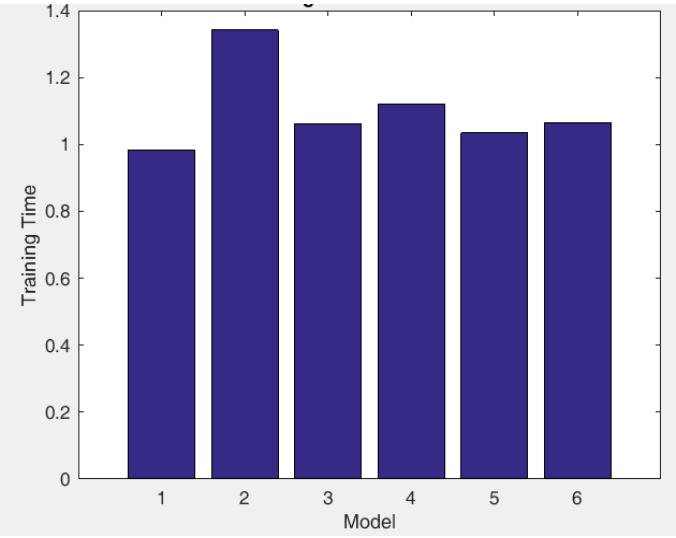

Fig.10. Training Time for each Model

IV. DISCUSSION OF RESULTS

In fig 1 (the scatter plot of the predictors) -yellow, brown and blue points indicates a high, average and low risk of schistosomiasis infection. In Fig 1a, age group 6-24 has the highest tendency of being infected with the disease followed by those between 25 – 49 since the two groups are the most active ones that can easily swim in rivers. The other two groups 1-4 and 50-74 are too young or too old to swim in rivers and hence, they are less susceptible to the infection. In fig 1b Africa (5) being an underdeveloped continent has the highest risk of contracting the disease compared to other continents. It is followed by Asia (4), South America (3), Developed countries (2) and others (1). Fig 1c shows that males (1) stand at higher risk of being infected compared to female (2). There is a high tendency for males to swim in a river compared to female. The level of exposure is expressed by fig 1d. (5) is the highest level followed by medium (5) and the lowest level of exposure (2).

Fig 2-7 expressed the result obtained after the training with the behaviour of model 1.1, 1.2, 1.3, 1.4, 1.5, and 1.6 respectively. The plots are in the form of CM, ROC, and PCP and table 1 explains the behaviour of the models better. The table was expressed in term of Accuracy, Prediction Speed and Training Time for each of the models. It is clear from the ranking that none of the models is perfect in terms of the accuracy, speed and time. For instance, the Linear model came first in term of accuracy, while cubic and the Medium Gaussian outperforms others in prediction speed.

Medium Gaussian requires lower training Time. It can be observed that only Medium Gaussian performs best in term of Prediction Speed and Training Time but managed to come up at the third position under Accuracy. Therefore, it appears to be the best of all.

V. CONCLUSION

Schistosomiasis is presently one of the diseases that is spreading all over the world especially in the Africa sub-region. The disease has in recent time become endemic and destroying the lives of innocent people all over the world. A lot of research is going on to determine how to manage or eradicate or reduce this scourge.

In this research, efforts were made to look into the behaviour of support Vector Machine models in determining the likelihood of being infected. Six models were trained and the result obtained in term of CM, ROC and PCP were interpreted clearly in term of

accuracy, processing, speed and execution time. It was finally concluded that none of the models was perfect but Medium Gaussian appeared to be better than others.

REFERENCES

[1] K. Amit (1999). Artificial Intelligence and Soft Computing Behavioural and Cognitive Modelling of the Human Brain CRIC Press, Boca ration London, New York, Washington, D. C

[2] B. M. G. Amosa, O. K. Olalere, K. A. Kawonise, A. O. Fabiyi, and A. A. Fabiyi (2015). Expert System for Diagnosis and Management of Kidney Diseases. International Journal of Computer Trends and Technology (IJCTT) Volume 20 Number 3, December 2015

[3] F. S. Bakpo and L. G Kabari (2005). Diagnosing Skin Diseases Using an Artificial Neural Network. Available at: http://cdn.intechopen.com/pdfs-wm/14893.pdf P. Saville, *Review of Radar Absorbing Materials*, Defence R&D Canada – Atlantic.

[4] V. Deepti and S. Sheetal (2013). Classification of Heart Diseases using SVM and ANN. International Journal of Research in IJRCCT Computer & Communication Technology Vol.2, Issue 9

[5] L. Guo, Z. Xiaorong, L. Jianbiy, H. Z. Yhanqichen, C. Yanyan, L. Jianhua, J. Hengbo, Y. Junsing, and N. Shaofa (2018) PLOS Neglected Tropical Diseases

[6] P. M. Kelvin (2008). Machine Learning a Probabilistic Perspective. The MIT Press Cambridge, Massachusetts, London, England

[7] U. A. Makolo and M. O. Akinyemi (2016) Predicting the Risk of Infection with SCHISTOSOMA HEAMATOBIUM using ML. International Journal of Computer Application (0975 – 8887) Volume 136, No 8 February 2016

[8] A. Noura (2015). Heart Diseases Diagnoses using Artificial Neural Network, Network and Complex Systems, ISSN 2224-610X (Paper) ISSN 2225-0603 (Online), Vol.5, No.4, 2015

[9] K. Prashasti and R. S. Disha (2016). Prediction of Cardiovascular Diseased using Support Vector Machine and Bayesian Classification. International Journal of Computer Application (0975 – 8887) Vol 156, No 2

[10] H. Reynold and W. ArveLee (2019). Station of Schistomiasis Elimination in the Caribbean Region. Tropical Medical and Infection Disease.

[11] S. Ramya and N. Radha (2016). Diagnosis of Chronic Kidney Disease using ML Algorithm. International Journal of Innovative Research in Computer and Communication Engineering. Vol. 4, Issues 1,

[12] G. Shashikant, P. Chetan, and G. Ashok (2011). Heart Disease Diagnosis using Support Vector. International Conference on Computer Science and Information Technology (ICCSIT'2011) Pattaya.

[13] K. Stefanie, L. B. Soren, J. I. Katrin, K. Jennifer and U. Jurg (2013). Diagnosis and Treatment of Schistosomiasis in Children in the Era of Intensified Central Expert Reviews.

[14] J. Vikramadiya (2006). Support Vector Machine. School of FFCS Washington State University, Pulman 99164.

[15] S. N. William (2006). What is a Support Vector Machine PRIMEK: Computation Biology/Mature Biotechnology Volume 24, No 12 .

BIOGRAPHIES

OLANLOYE ODUNAYO received B.Sc. Mathematical Science (Computer Science option) from University of Agriculture, Abeokuta in 1994 and M.Sc. and P.hD. in Computer Science from Nnamdi Azikiwe University Awka in 2002 and 2017 respectively. He also received Post Graduate Diploma in Education from University of Ibadan in 2004. He has authored and co-authored various books in Computer Science and has published quite a no of articles in reputable local and international journals. He is highly experienced in teaching Computer Science courses at various levels. He is currently a Senior Lecturer in the Department of Computer Science and Information Technology, Bowen University, Iwo. Osun State, His research interest include neural network, fuzzy logic, machine learning, deep learning.

.

OLASUNKANMI OLAWUMI bagged a B.Tech. Computer Science at Ladoke Akintola University of Technology, in 2018 and N.C.E. (Computer Science) from Emmanuel Alayande College of Education Oyo, in 2010. In 2019, She was a Program Assistant and Machine Learning Researcher at Data Science Nigeria. She is currently a Network Administrator and Machine Learning Researcher at Ladoke Akintola University of Technology. Her research interests include data mining, machine learning, deep learning and health informatics.

ODUNTAN ODUNAYO is a researcher and academia in Computer Science. She is blessed with PhD (Computer Science) from Ladoke Akintola University of Technology Ogbomoso; M.Sc. (Computer Science) from University of Lagos, Akoka; B.Sc.(Computer Science) from Ogun State University Ago -Iwoye and N.C.E. (Computer Science) from St. Andrews College of Education Oyo. A Principal Lecturer in the Department of Computer Science, The Federal Polytechnic, Ilaro Ogun State. She has published innovating scholar articles in reputable international and local journals including a book of readings. She is experienced in teaching computer science at all levels of education with the use of simple terms that enables students to understand difficult concepts in computing. She is a Full member of Computer Professionals of Nigeria (CPN), Nigeria Computer Society (p89908NCS), and a Professional Member of Nigerian Women in Information Technology (NIWIT). She happily married and blessed with children.

Effect of RSU Placement on Autonomous Vehicle V2I Scenarios

B. KARA and A. ÖZGÖVDE

***Abstract*— Edge computing has become a prominent computing strategy as mobile devices and Internet of Things (IoT) became popular in the last decade where cloud computing proved partly insufficient meeting the computational requirements of these devices/applications. Unlike cloud, edge computing can provide low latency in communication, high quality of service, and support for high mobility. Connected and autonomous vehicles scenarios can be considered as an important application field for edge computing as these are the key requirements to implement a vehicular network. In this paper, we aim to present a remedy to one of the crucial problems in vehicular networks: efficient RSU placement by addressing network coverage and computational demand. We propose an RSU placement framework for generating placement models based on traffic characteristics of a target area. Our work differs from previous studies in that we focus on both communication coverage and the computational demand aspects simultaneously. The proposed framework in this study can be used by infrastructure providers for designing an efficient RSU placement while building a smart city. Moreover, our work includes extending capabilities of a simulation framework designed for edge computing scenarios. To demonstrate the effectiveness of our proposal we evaluated the performance of various placement models in realistic settings.**

Index Terms— **Road Side Unit (RSU), Edge Computing, V2I (Vehicle to Infrastructure)**

I. INTRODUCTION

WITH THE increasing popularity of mobile devices and Internet of Things (IoT) during the last decade, cloud computing had been leveraged to solve the problem of making complex computations with limited device resources by provisioning remote computing and storage resources. Edge computing, on the other hand, was suggested as a new computing paradigm when the limitations of the centralised data centres started to emerge. Satyanarayanan et al. describe these limitations as long WAN latencies and bandwidth-induced delays [1]. Because of these limitations, cloud computing is not a suitable computing strategy for scenarios which requires real-time data processing and relies on fast feedback. Edge computing is a good candidate to solve these problems by bringing computing resources to the edge of the network, usually one hop away from the user. The features of low latency in communication, high quality of service and support for high mobility makes edge computing an optimal solution for the computational requirements of a wide range of applications in different domains. Connected and autonomous vehicles scenarios are considered as a good application field for edge computing [2]. Fig. 1 shows the system components in a reference scenario.

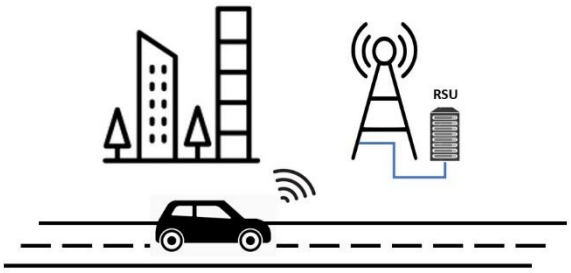

Fig.1. System components for the reference scenario

Using their advanced sensors, connected vehicles collect data from their environments. In current state of automotive technology, vehicles process this data to interpret their environment and enable assisted and autonomous driving for a safe navigation. For example, using their ultrasound, infrared, radar and video sensors, vehicles can detect other vehicles on the road, stop for pedestrians, and handle any unexpected circumstances [3]. On the other hand, the automotive industry is working to develop Vehicular Ad-hoc Networks (VANETs), to enable vehicles to share information with other vehicles and road side units (RSUs) through vehicle-to-vehicle (V2V) and vehicle-to-infrastructure (V2I) communication channels [4]. VANET is an essential part of Intelligent Transportation Systems (ITS) which are defined as the future of transportation.VANETs can be utilized for a broad range of safety and non-safety applications, allow for value added services such as vehicle safety, automated toll payment, traffic management, enhanced navigation, location-based services such as finding the closest fuel station, and infotainment applications such as providing access to the internet [5].

Dedicated short-range communication (DSRC), which is a candidate for use in a VANET, offers the potential to

BARIŞ KARA, is with Department of Computer Engineering Galatasaray University, Istanbul, Turkey,(e-mail: bariskara35@gmail.com).

https://orcid.org/ 0000-0002-2759-7447

ATAY ÖZGÖVDE, is with Department of Computer Engineering Galatasaray University, Istanbul, Turkey,(e-mail: aozgovde@gsu.edu.tr).

https://orcid.org/ 0000-0001-9688-766X

Manuscript received December 31, 2019; accepted June 11, 2020.
DOI: 10.17694/bajece.668615

effectively support V2V and V2I safety communications by providing high data transfer rates with minimum latency [6]. The primary motivation for deploying DSRC is to enable collision prevention applications. These applications depend on frequent data exchanges among vehicles, and between vehicles and roadside infrastructure.

Road Side Units (RSU) are the communication units in VANET which are fixed along the road side or in dedicated locations such as at the junctions or near parking spaces [7]. They are equipped with an antenna to enable wireless communication based on IEEE 802.11p radio technology, a processor, and a read/write memory [8]. Barskar et al. describe main functions and procedures associated with the RSUs as follows [7]:

- To extend the communication range of the ad hoc network for redistributing the information to other vehicles
- Running safety applications and acting as an information source
- Providing internet connectivity to the vehicles

The components of the V2I scenarios can be mapped to edge computing elements as follows:

- RSUs are the edge computing units because of their proximity to the vehicles, providing computational, storage resources and high bandwidth link, and transfer data with minimum latency
- Vehicles are the resource poor clients as they have limited computation and storage resources due to the requirements of small-size and low-cost hardware systems (Yu et al., 2013)
- Vehicular applications are edge applications as they demand complex computation and large storage

Applications collecting information from multiple vehicles have a great potential of increasing road safety and improving quality of traffic. Satyanarayanan proposes a scenario in which crowd sourcing and edge computing can be harnessed to create a shared real-time information system for situational awareness [9]. They claim that collected information can be used to detect critical situations such as accidents, icy road conditions, fallen rocks and advisory messages can be conveyed to the other drivers. Another study proposes an application for intelligent traffic management at intersections to minimize accidents, traffic congestion and environmental costs of road traffic using V2V and V2I communications [10]. Katsaros et al. also design an application that could improve fuel consumption and reduce traffic congestion in junctions using vehicular data through same communication channels [11]. Another study proposes a merging algorithm that optimizes the performance of connected fully automated vehicles through a freeway merging segment for a scenario relying on V2V and V2I communications [12].

All these applications deployed into RSUs receive data from vehicular applications such as trajectory, speed, destination coordinates, etc. in short intervals, aggregate and process it in real time and send response back to senders or to the relevant vehicles within the network range. Here again, low latency and high quality of service are the key factors to build this ecosystem.

RSUs placed in an area should meet two requirements. First, network coverage of the area should be maximised, so that vehicles can stay connected to the RSUs at any time during their journeys and edge applications can work without excluding any territories. Second, edge computing units have limited resource capacities compared to the cloud datacentres [13] and computational demand of the edge applications should be met by the RSUs. It is expected to observe different levels of traffic density in different parts of an area. Placing insufficient number of RSUs in a territory with high traffic volume creates computational demand more than RSUs can handle and this could result in system failure. On the other hand, placing more RSUs than required in a territory with low traffic volume could result in waste of resources and loss of money.

Deploying a specific number of RSUs into an area is a challenging work since satisfying two requirements at the same time brings us to a trade-off problem. RSUs should be placed in an area in a way that satisfies both network coverage for vehicles and computational demand for the edge applications at maximum level considering the traffic density on the road network.

As to be mentioned in Section II, majority of the existing works address RSU placement problem from communication aspect without considering resource consumption of the edge applications. On their survey addressing Mobile Edge Computing, Mach et al. describe the issue of finding an optimal way where to physically place the computation depending on expected user demands as an open research challenge [14].

The objective of this study is to implement an RSU placement framework for generating RSU placement models based on traffic characteristics of an area. We aim to provide a flexible tool that can be configured for designing a placement model in favour of network coverage or computational demand. Additionally, our work includes extending capabilities of an open source simulation framework, EdgeCloudSim[1], proposed to evaluate the performance of edge computing scenarios. By adding new modules to support simulations for V2I scenarios and designing realistic traffic scenarios for a target area in London city centre, we evaluate the performance of the generated placement models and validate their functionality [15].

Simulation results show that generated models satisfy network coverage and resource demand in different levels, and can be used to find the optimal placement of the RSUs in the target area. Therefore, our framework can serve as a reliable tool to be used as part of RSU deployment process by infrastructure providers.

The rest of the paper is organised as follows: Section II explains previous RSU studies addressing RSU placement and Edge Computing in Vehicular Networks. In Section III, we describe preliminary work including processing target area map and generating traffic dataset, then, our reference scenario, proposed placement framework and simulation environment is explained. Section II discusses the simulation

[1] https://github.com/CagataySonmez/EdgeCloudSim

results and validity of the proposed framework. Finally, we conclude the paper and outline the future work in section III.

II. Literature Review

A. RSU placement

Trullols et al. suggest a maximum coverage approach to the problem of information dissemination in intelligent transportation systems in their study, which can be considered as one of the earliest works addressing this topic as most of the research efforts had focused on the development of protocols and applications suitable for VANET until that period of time [16]. In their study, they propose a heuristic algorithm to solve the problem of maximizing the number of vehicles that get in contact with the Dissemination Points (DPs). Their results also show that, their suggested heuristics can be successfully employed to plan a deployment capable of informing more than 95% of vehicles with a few DPs.

Aslam et al. present two different solutions to the RSUs placement problem with objective of maximizing the information flow from vehicles to RSUs in an urban environment: Binary Integer Programming (BIP) method and a novel Balloon Expansion Heuristic (BEH) method [17]. BIP method utilizes branch and bound method to find optimal solution, whereas, BEH method uses balloon expansion analogy to find optimal solution. Both optimization methods were used to solve the optimization problem of minimizing the average reporting time. They have shown that the novel BEH method is more versatile and can be used to solve the optimization problem.

Balouchzahi et al. also propose an optimization method addressing RSU placement by formulating the problem using BIP [18]. In their work, highway and urban scenarios are separately formulated to improve the model scalability. Their simulation results show that the proposed model reduces the receiving time of traffic information and can reach to a satisfactory level of coverage using less RSUs.

Wu et al. tackle the same problem by presenting a placement strategy referred as Capacity Maximization Placement (CMP) based on Integer Linear Programming (ILP). Apart from direct communication of RSUs and vehicles, their study also covers multi-hop relaying, which takes place when the vehicle is out of RSU's transmission range [19]. To validate their findings, they compare the results of CMP with two other models: uniformly distributed placement and hot spot placement. The simulation result shows that the proposed model leads to the best performance among all mentioned models.

Our study differs from aforementioned works in a way that they only address the problem from communication and network coverage aspects without taking resource consumption and computational demand of the RSUs into account. Although a placement model can be optimized enough for a cost efficient RSU deployment in an area and provide a quality of communication at a certain level, it is not guaranteed that it can handle computational demand of the edge applications.

B. Edge Computing in Vehicular Networks

Yu et al. propose a hierarchical cloud architecture for vehicular networks [20]. Their architecture consists of central clouds, roadside cloud and vehicular cloud. Central clouds have sufficient cloud resources but large end-to-end communications delay. On the contrary, roadside and vehicular clouds have limited cloud resources but satisfy communications quality. In their study, they focus on efficient resource management in the proposed architecture and they formulate and solve resource competition among virtual machines in a game-theoretical framework

In their study, Datta et al. seek an alternative of cloud platform to support real time connected vehicular scenarios [21]. They design an IoT framework that includes an edge computing system for the connected vehicles to offer consumer centric services. Their framework primarily utilizes an edge computing platform to support network switching, resource discovery, provisioning, local processing for data fusion and storage of the high-level intelligence for vehicular scenarios. Salahuddin et al. present RSU Clouds as a novel way to offer non-safety application with QoS for VANETs [22]. RSU Clouds consist of traditional RSUs and micro datacentres. Their system can be reconfigured, at a cost, to meet the fluctuating service demands like cloud datacentres. They also focus on concepts such as resource management, minimizing VM migrations, control plane overhead, number of service hosts and infrastructure delay for their proposed architecture.

Although the research described in this section address edge computing in vehicular networks, the researchers mostly suggest new frameworks and architectures in which cloud and edge processing units, and mobile devices/vehicles are integrated into a new ecosystem. Then, they suggest solutions for computational challenges such as resource allocation, scheduling, VM migration, etc. for the computational resources. Our work can be considered as a complementary study in which we focus on provisioning a V2I infrastructure built on top of an existing architecture. Therefore, we assume that low-level computation and communication problems are resolved and we can propose solutions for higher level challenges such as efficient RSU placement

II. Materials and Methods

A. Reference Scenario

In our reference scenario, we consider a smart city equipped with RSUs and support V2I communication. All the vehicles are smart or connected with the ability of running vehicular applications that connect to edge applications deployed into RSUs. Vehicular applications send one task to the nearest RSU per second in case the vehicle is in the network coverage of any RSU. When the task is successfully processed, RSU sends a response back to the vehicular application. There are 4 cases a task can fail:

• Coverage: Vehicle is not in range of any RSU's network

• Capacity: RSU is out of capacity and cannot process incoming task
• Bandwidth: Task cannot be sent through network due to congestion
• Mobility: Vehicle leaves the RSU network coverage after sending the task

We assume all RSUs have same hardware resources and the tasks sent by the applications are identical. In our scenario, each RSU has 1 Mbps bandwidth. Average task payload size is 1024 bytes for both upload and download operations. We also assume that each RSU has an equipped server with 600Mhz CPU and 500MB RAM, and average task length is 300 MI. Table 1 shows the parameters and their values for RSU and task configurations.

TABLE I
RSU AND TASK PARAMETERS AND VALUES

Parameter	Value
RSU Network Range	300m
RSU Bandwidth	1 Mbps
CPU	600 Mhz
Memory	500 MB
Average Task Payload Size	1024 byte
Average Task Length	300 MI
Task arrival rate	1 Hz

The simulations we run are based on these assumptions and parameters.

B. Preliminary Work

1) Target Area

For our scenario, we chose London city centre as the target area for deploying RSUs which covers an area of 3 by 3 kilometres. To be able to run traffic simulations and calculate RSU locations, we needed to extract the road network of the target area. To obtain the road network, we outlined the target area on OpenStreetMap which is a free collaborative map application, then we exported it in xml format. Since the map data includes a variety of information such as buildings, parks, restaurants, etc., we processed the file to only include road network elements such as motorways, intersections and traffic lights. Fig. 2 shows the map of the target area.

2) Traffic Dataset

Due to the lack of publicly available vehicle trajectory dataset for the target area, we used Simulation of Urban Mobility (SUMO) framework to generate realistic traffic dataset. SUMO is an open source, microscopic and continuous road traffic simulation framework designed to handle large road networks [23].

Apart from its simulation capabilities, SUMO includes several scripts for traffic and road network operations. We converted the map data into a network file, which is the SUMO input format that defines the road network. Then, we used randomTrips tool, which is a python script that takes place in SUMO library, to generate the vehicle routes randomly on the road network. The output route file, along with the network file should be provided to SUMO to run the traffic simulation.

We defined two important parameters during route generation: simulation time and vehicle arrival rate. The simulation time we chose as 1 hour, aligns with the time of V2I simulation we conducted in the following steps. Vehicle arrival rate, on the other hand, defines the number of vehicles in the simulation and SUMO generates one specific route for each vehicle. This parameter is set to 1 by default. In our study, traffic density plays an important role on RSU placement process as the load on the RSUs depends on number of vehicles in the system. Thus, to cover scenarios with different traffic volumes, we run the script using different arrival rates. As a result, we generated 8 route files which include 500, 1000, 1500, 2000, 2500, 3000, 3500, and 4000 vehicles routes.

After that, by running SUMO traffic simulation for each route file for a simulation time of 1 hour, we produced 8 traffic output files which comprise our traffic dataset. Each file contains traffic data logged for each simulation second such as vehicle id, type, coordinates, speed, angle, lane, etc. As a result, 8 million logs were produced in total for the traffic dataset.

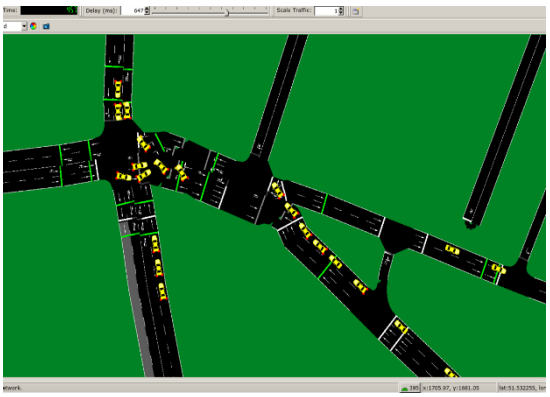

Fig. 2. SUMO traffic simulation

C. RSU Distribution Models

In this study, we propose 3 RSU distribution models: Uniform, Weighted, and Optimized. This section outlines the algorithms, implementations and results of the models.

1) Uniform RSU Distribution

This placement model only aims for full RSU network coverage by placing RSUs equidistant from each other without considering computational demand. Network range of the RSUs can reach up to 1000 meters ifthere are no obstructions, and 250-350 meters in cluttered urban areas [24]. For this model, we assumed that each RSU works best with a coverage of 150 meters due to the shadowing effect of the buildings, and we decided to place RSUs 300 meters far from each other. Therefore, to cover an area of 9 km² with RSUs working in their best performances, we needed to have 100 RSUs.

We developed a Java application as the implementation of the algorithm and referred it to *RSU Distributor*. In this application, we generated a grid on the area map by dividing it into cells each with the size of 300x300 meters. We referred to these cells as territories. Then, we placed one RSU into the centre of each territory, therefore 100 RSUs were evenly distributed to the area. Fig. 3. shows the RSU locations on the target area map based on the uniform distribution. It should be noted that, as its name suggests, an RSU should be placed on the road side to ensure the proximity to the vehicles. However, in an urban scenario in which a complex road structure exists, a territory includes multiple roads and we expect the placed RSU to serve to the vehicles across multiple roads within the coverage area.

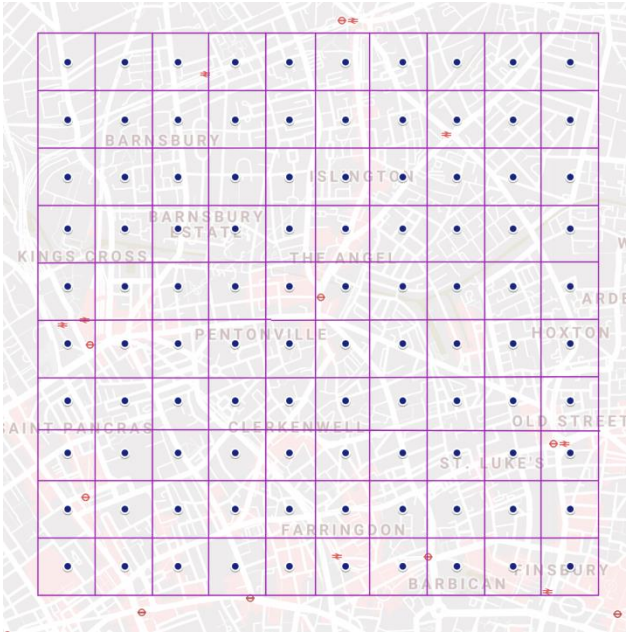

Fig. 3. RSU locations on uniform distribution model

2) Weighted RSU Distribution

We used Uniform Distribution model as base model to generate Weighted RSU distribution with a heuristic approach. This model addresses refining RSU locations set up for uniform distribution model by taking computational demand into account. In the uniform distribution model, despite of the full network coverage, we might have high task failure rates since RSUs might not meet the high computational demand using their limited resources. We may especially experience this problem in territories with higher traffic volumes i.e. traffic congestions. An external parameter, θ, is the relocation factor and determines number of the RSUs to be relocated. Relocation step addresses selecting θ% least utilized RSUs and move them to the territories where more computational resources are needed.

Thus, we aim to decrease resource originated task failures by bringing additional computational resources to meet the higher demand. On the other hand, relocated RSUs will cause coverage originated task failures as no RSUs will serve to vehicles at these territories. Value of θ should be assigned considering the difference of traffic volumes in different territories as this trade-off is only reasonable if total number of task failures decreases after the relocation.

a) Algorithm

The algorithm for this placement model consists of 4 steps:

- **RSU Selection:** This step addresses finding the RSUs placed at the territories with lower traffic volume, thus have low utilization rates. To detect these RSUs, we calculate task assignment rates for each RSUs in the uniform distribution. The RSUs with less task assignment rates are marked to be moved in the territories with higher resource demand. We select θ% least utilized RSUs in this step.
- **Territory Selection:** To detect the territories that need additional resources to meet the high computational demand, we analyse the performance of the RSUs in uniform distribution model under a heavy load. The territories containing the RSUs with higher task failure rates due to insufficient capacity are the candidates to support with additional RSUs.
- **RSU Distribution:** In this step, we first calculate a weight factor using task failure rates for each candidate territory. Then using the weight factor, we calculate number of RSUs to be assigned into each territory. Finally, we distribute the selected RSUs into these territories.
- **RSU Placement:** This step addresses placing selected RSUs into the candidate territories. The first RSU is placed in the middle of territory centre and neighbour territory centre with the highest computational demand among all neighbours. The second RSU is placed between the territory centre and neighbour territory centre with the second highest computational demand, and so on.

As explained above, to refine RSU locations using weighted distribution algorithm, we need to have two metrics from uniform distribution model: task assignment rates and task failure rates of the RSUs. To gather these results, we run V2I simulations on the target area using uniform distribution model and traffic dataset.

b) Simulation Framework

We used EdgeCloudSim as simulation framework which is an open source tool developed by Sonmez et al. [15] to conduct experiments for edge computing scenarios. We extended the capabilities of the framework by defining components and modules specific to V2I scenarios and we referred to this extended simulation environment as V2ISim.

The simulation environment served for two purposes in our study: first, by running simulations for uniform distribution model, we generated the inputs required for weighted distribution algorithm. Second, we needed a simulation environment to make experiments with generated distribution models, therefore we can evaluate the system performance and compare results in the following steps of the study.

TABLE II
SIMULATION PROPERTIES

Property	Value
Total number of traffic logs	8.147.468
Total number of RSUs	100
RSU placement model	Uniform
Simulation time	1 hour

c) Simulation for Uniform Distribution Model

The simulation environment requires two input files: vehicle trajectory data and RSU coordinates. As traffic input data, we provided the traffic dataset we generated using SUMO and as RSU coordinates, we used the coordinates we calculated for uniform distribution model.

We also configured RSU and task characteristics by providing parameters listed in Table 2. We set simulation time to 1 hour and 8.147.468 traffic logs were provided in the traffic dataset as total. Some important simulation properties can be seen in Table 2.

d) Simulation Results

It took 6 hours 10 minutes to run the simulation for uniform distribution model on a laptop with Intel Core i7-8850H CPU and 16GB RAM.

As a result of a simulation 3 output files are generated per traffic input file from the traffic dataset:

- **Generic logs:** this file includes most important simulation results such as number of successfully processed tasks, number of failed tasks, average service time, average network delay and average RSU utilization rate. The values logged in this file are used as metrics while comparing system performances for different RSU placement models.
- **RSU utilization logs:** this file keeps the utilization rates for each RSU logged for each simulation second. This values are used as metrics while comparing system performances from utilization aspect for different RSU placement models.
- **Task assignment logs:** this file is only generated for uniform distribution model simulation and it keeps the logs of number of assigned and failed tasks for each RSU. By processing these values, we can generate the 2 inputs required for weighted distribution algorithm: task assignment rates and task failure rates of the RSUs

e) Weighted Distribution Algorithm Implementation

We extended *RSU Distributor* Java application to implement weighted distribution algorithm. From 500 to 4000 vehicles, the simulation run once for each traffic input file and as a result, 8 task assignment log files which include more than 8 million task logs were produced in total. In the application, these logs were aggregated and processed to find the values of task assignment rates and task failure rates of the RSUs.

The number of RSUs we want to select and distribute into new cells are based on the value of θ, relocation factor. By providing 10, 20, and 30 for θ, we run the application and generated 3 different set of RSU placement models for weighted algorithm. For each value of θ, Table 3 shows the selected RSUs for relocation and Table 4 shows number of RSUs to be assigned to each territory.

TABLE III
RSU IDS SELECTED FOR RELOCATION

θ	RSU ids
10	3, 11, 39, 4, 9, 49, 5, 90, 88, 2
20	3, 11, 39, 4, 9, 49, 5, 90, 88, 2, 74, 89, 79, 69, 1, 91, 6, 70, 93, 12
30	3, 11, 39, 4, 9, 49, 5, 90, 88, 2, 74, 89, 79, 69, 1, 91, 6, 70, 93, 12, 84, 98, 92, 87, 8, 99, 14, 59, 80, 19

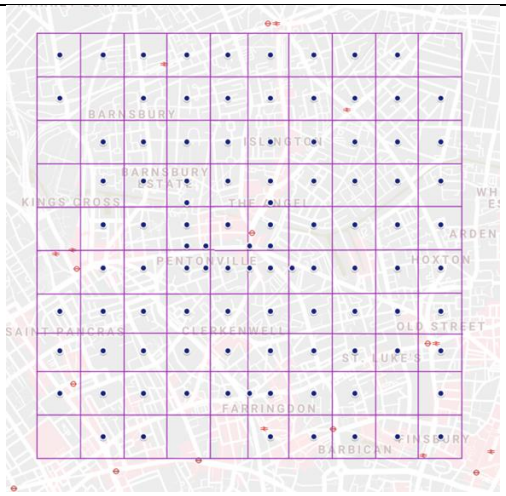

Fig. 4. RSU locations on weighted distribution model for θ = 10

TABLE IV

TERRITORY IDS AND NUMBER OF RSUS TO ASSIGN

θ	Territory ids and number of RSUs to assign
10	55(2), 54(1), 45(1), 35(1), 48(1), 33(1), 34(1), 65(1), 53(1)
20	55(3), 54(2), 45(2), 35(2), 48(2), 33(1), 34(1), 65(1), 53(1), 58(1), 47(1), 46(1), 75(1), 36(1)
30	55(4), 54(3), 45(3), 35(3), 48(3), 33(2), 34(1), 65(1), 53(1), 58(1), 47(1), 46(1), 75(1), 36(1), 25(1), 71(1), 38(1), 63(1)

Fig 3-5 shows the weighted distribution RSU placements for θ=10, 20, and 30, respectively.

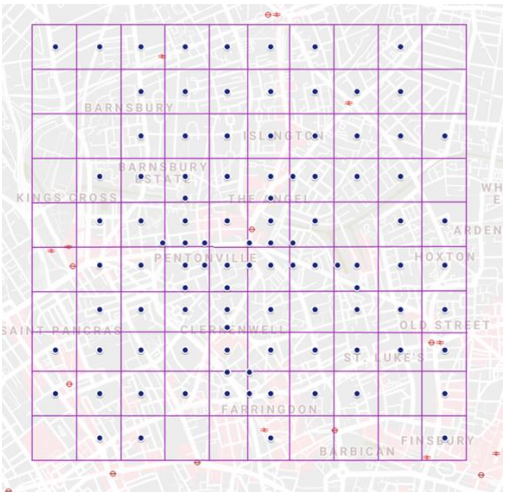

Fig. 5. RSU locations on weighted distribution model for θ = 20

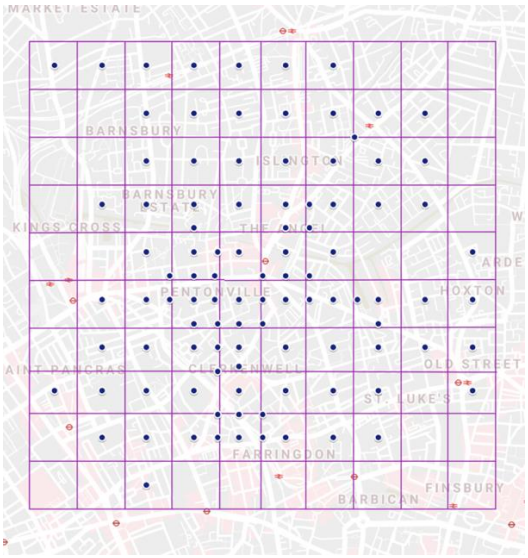

Fig. 6. RSU locations on weighted distribution model for θ = 30

3) Optimized RSU Distribution

As previously discussed, we have two criteria to fulfill while solving the RSU placement problem efficiently: network coverage and computational demand. Our approach for the optimized placement model is to use *Linear Programming* (LP) to address both of the requirements.

a) Algorithm

Similar to other models, optimized RSU distribution model also does its calculations on a grid generated on the target area map. For this purpose, we used the same grid as we generated for the uniform RSU distribution model to provide consistency. It should be noted that, working with smaller cell size would provide fine-grained results, however this results in an exponential growth on the number of formulations to define the mathematical model on LP.

Binary Integer Programming (BIP), is a subtype of Linear Programming in which all decision variables are defined as binary. In our problem, each cell is a candidate for placing an RSU, meaning that we want to solve the problem that decides whether a cell has an RSU or not. Therefore, our decision variables refer to the condition of each cell having the value of 1 or 0, where 1 states that RSU should be placed, and 0 should not. As a result, we formulated the RSU placement problem using BIP.

b) Problem Formulation

For the grid consisting of 100 cells, the we define the decision variables as follows:

$$x_0, x_1, x_2, \dots, x_{99}$$

In the second step, we define the objective function using the decision variables. Our objective is fulfilling the constraints using minimum number of RSUs. Thus, the objective function is:

$$min \sum_{i=0}^{99} x_i$$

Finally, we define the constraints in which we model network coverage and resource demand as well as the criteria we want to set as their minimum values.

(1) Network Coverage

We start by formulating the total coverage (R) of the RSUs using the decision variables. As previously stated, the network range of an RSU is between 250-350 meters in the urban areas (Ligo et al., 2015). The cells have the size of 300x300 meters, whereas we consider the network range of an RSU as also 300 meters. Fig. 7 depicts the positioning of an RSU within a cell along with its network range. As it can be seen in the figure, the area of the RSU's network coverage exceeds the area of the cell. In this situation, when two RSUs are placed within

the neighbour cells, there will be an overlap on the area coverage, and an optimized placement solution should minimize these overlaps. Total coverage is defined with this equation:

$$R = \sum_{i=0}^{99} x_i r_i - \sum_{i=0}^{99}\sum_{j=0}^{99} x_i x_j p_{i,j} + \sum_{i=0}^{99}\sum_{j=0}^{99}\sum_{k=0}^{99} x_i x_j x_k p_{i,j,k}$$

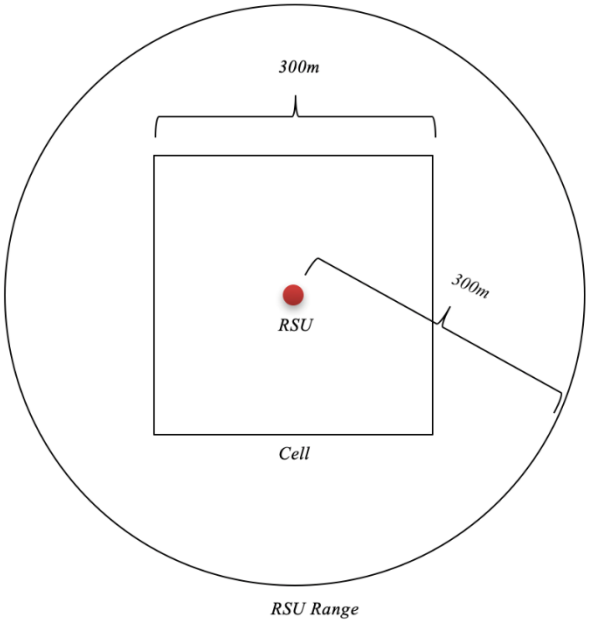

Fig. 7. The positioning of RSU within a cell

In the equation, first summation operation denotes addition of network coverage for all the placed RSUs (*i*). Then, as explained above, the overlapped areas as a result of neighbourhood should be subtracted from this sum, and the double summation operation indicates that (*ii*). According to this Fig. 8 which shows 4 example cells, the neighbourhood, which causes network overlapping, exists when RSUs are placed into these cells: A-B, A-C, A-D, B-C, B-D and C-D. Lastly, when there is a case of "L" shape neighbourhood, we need to add the overlapped area of these 3 cells to the equation as dual neighbourhoods takes out that amount of size from the sum as extra. For example, when RSUs are placed into A, B and D cells, the subtract operations defined at step *ii* will remove the overlapped areas for A-B, A-D and B-D neighbourhoods, and this will result in subtracting an extra overlapped area for A-B-D neighbourhood. The triple summation operation adds this area back to the equation (*iii*).

A	B
C	D

Fig. 8. The neighbour cells

(2) Resource Demand

We followed a similar strategy to network coverage while formulating the resource demand (*D*). The main difference is, we had to calculate the resource demand for each cell using the traffic dataset. Then, the same rules we used for the neighbourhood also apply here.

Therefore, total demand is defined with this equation:

$$D = \sum_{i=0}^{99} x_i d_i - \sum_{i=0}^{99}\sum_{j=0}^{99} x_i x_j s_{i,j} + \sum_{i=0}^{99}\sum_{j=0}^{99}\sum_{k=0}^{99} x_i x_j x_k s_{i,j,k}$$

(3) Constraints

Lastly, we define the constraints. The constraints below suggest that minimum network coverage and resource demand are user defined parameters and denoted by γ and λ. And all the decision variables are binary.

$$R \geq \gamma$$

$$D \geq \lambda$$

$$x_0, x_1, x_2, \dots, x_{99} = 1 \mid 0$$

Table 5 depicts the notations used in the mathematical formulations.

TABLE V
SUMMARY OF NOTATIONS IN THE MATHEMATICAL FORMULATIONS

Symbol	Description
i	Candidate grid cell for RSU placement
x_i	Binary variable for RSU placed at cell i
R	Total network coverage
D	Total resource demand
r_i	Network coverage for RSU placed at cell i
d_i	Satisfied resource demand for RSU placed at cell i
$p_{i,j}$	Overlapped network coverage for the RSUs at neighbour cells i and y
$s_{i,j}$	Overlapped supply for the RSUs at neighbour cells i and y
$p_{i,j,k}$	Overlapped network coverage for the RSUs at neighbour cells i , y and k
$s_{i,j,k}$	Overlapped supply for the RSUs at neighbour cells i , y and k

a) Implementation

We defined the formulations on an open source LP Solver. We solved the problem by assigning different values for γ and λ. When we targeted for for full network coverage (γ = 100) and full resource supply (λ = 100), it resulted that 79 RSUs needed to be placed. However, when we decreased both of the values to 99%, the outcome changed to 52 RSUs. For 90% coverage and supply, the problem was solved with 42 RSUs.

Since this tool is designed to serve as a framework to the infrastructure providers, the company will be free to use any values as parameters based on their financial and technical requirements. While they can set high values γ and λ, they can also aim for maximum coverage whereas they ignore the demand, or vice versa. For our simulation in which we compare the performances of the placement models, we use the values γ = 99 and λ = 99 since this combination result in a very efficient outcome..

To compare system performances and validate functionalities of the RSU placements we generated using RSU placement framework, we run a set of simulations on V2ISim. To achieve this, we processed the simulation output logs and plotted several graphs using *Python matplotlib* library.

Fig. 8 shows the final placement of the optimized distribution model.

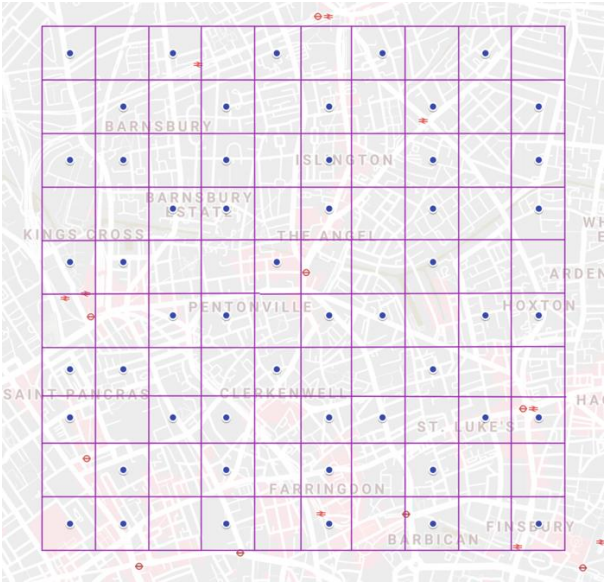

Fig. 8. RSU locations on optimized distribution model

We generated 3 distribution models: uniform, weighted, and optimized. The weighted model has 3 variations for the values of θ = 10, 20 and 30. Since we already had the results for uniform distribution model, we run the simulation for weighted and optimized placements. The simulation took 9 hours 6 minutes, 6 hours 36 minutes, and 6 hours 19 minutes for the weighted placement model respectively, and 7 hours 41 minutes for the optimized placement model. All the simulations were run on a laptop with Intel Core i7-8850H CPU and 16GB RAM.

We used same traffic dataset for all of the simulations. The dataset includes vehicle trajectory data files which represent different traffic densities. Therefore, we can evaluate system behavior under different loads. We classified the traffic densities into 3 categories:

- Number of vehicles below 1500 as low traffic volume
- Number of vehicles between 1500 and 3000 as medium traffic volume
- Number of vehicles more than 3000 as high traffic volume

The graph in Fig. 9 shows the comparison of task failure rates for uniform distribution, weighted distribution for θ = 10, 20, and 30, and optimized distribution. This can be considered as our most important metric while evaluating system performance. A system with low task failure rates is more reliable and functions better.

We can observe that the system functions best for the optimized distribution model under any traffic volumes, therefore we can suggest that optimized distribution model provides the best results among all models. The graph also shows that when the number of vehicles in the system increases, task failure rates also increase for all RSU distribution models consistently except for the optimized model. Considering the sharp increase between 3500 and 4000 vehicles for all models, we can claim that if the traffic density is over a threshold, RSUs will have difficulty handling the load and the system might even crash.

The graph shows us below 1000 vehicles, there is no significant gap between weighted distribution model for θ = 10 and uniform distribution model, however after this point we can observe an increase on this gap.

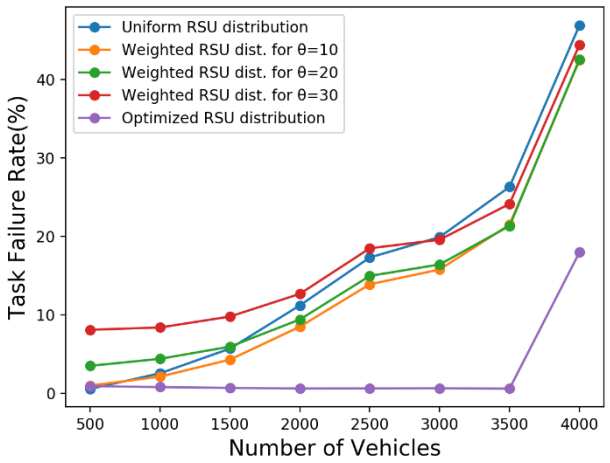

Fig. 9. Task failure rates

On the other hand, while uniform distribution model performs better than the weighted distribution models for θ = 20 and 30 under low traffic volume, weighted distribution model for θ = 20 outperforms it for medium traffic volume and weighted distribution model for θ = 30 outperforms it for high traffic volume. This is because while network coverage is a more important factor for the low traffic volume, resource capacity becomes more critical than the other factors when traffic density increases.

Lastly, the graph shows that relocating less utilized RSUs to the territories with higher load improves the system to a certain point. Weighted distribution model for θ = 10 outperforms uniform model for low, medium and high traffic volumes and it is the most optimal relocation factor among all the others. However, for θ = 20, weighted model only performs better for medium and high traffic volumes, and for θ = 30, it only functions better for high traffic volume. The reason for this is the trade-off between network coverage and resource capacity. When a less demanded RSU is relocated into a position to share the load in a busy area, capacity originated failure rates will decrease for the RSUs in the target territory, however coverage originated failure rates will increase for the original source territory.

As a result, by evaluating the results of Task Failure Rate graph, we can conclude that:

- optimized distribution model outperforms all others under any traffic load.
- uniform distribution model can be used for low traffic volume
- weighted model for θ = 20 can be used for medium and high traffic volumes
- weighted model for θ = 30 does not perform well under any traffic load

Fig. 10 shows the comparison of average service time of the RSUs in the unit of seconds. The service time is sum of download and upload delays and task processing time. As can be seen on the graph, increasing load is positively related to RSU service times for all distribution models except for the optimized model. Optimized distribution model performed better than the other models for all traffic volumes, and all weighted distribution models produced better results than the uniform model. The reason is, both download and upload delays and processing time depend on the demand on the RSU in that particular time. When an RSU needs to serve to higher number vehicles, they experience more delays on network and processing time. And as a result of sharing the high load with relocated RSUs, all weighted models provide better results in terms of service time.

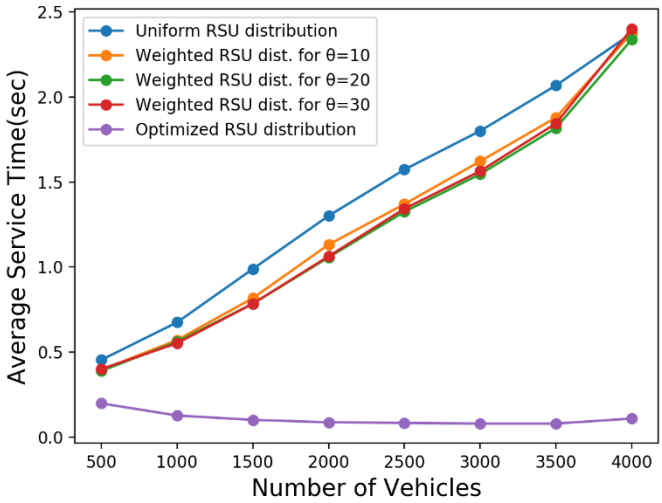

Fig. 10. Average service time

While measuring system performance, another important metric is the average utilizations of the RSUs. A system in which RSUs run with a low capacity is less efficient than another system with higher RSU utilization. On the other hand, a system with RSUs running in full capacity for a certain level of computational demand, is not able to sustain higher loads. Since the simulations we run with low and medium traffic volumes do not create significant load on majority of the RSUs, we compared utilization of the RSUs using only the results of the simulations run with 3500 vehicles. 3500 is the number which creates the highest traffic volume without breaking the system. Fig. 11 shows the histogram of average RSU utilization for uniform, weighted for θ=10, and optimized distribution models. The histogram shows that optimized model performs best in terms of RSU utilization because of two reasons: first, number of RSUs running in the lowest capacity (<10%) is lower than the other models, therefore RSU resources were used more efficiently. Second, number of RSUs running in high capacity (>%80) is also lower, therefore the load is distributed more evenly among the RSUs.

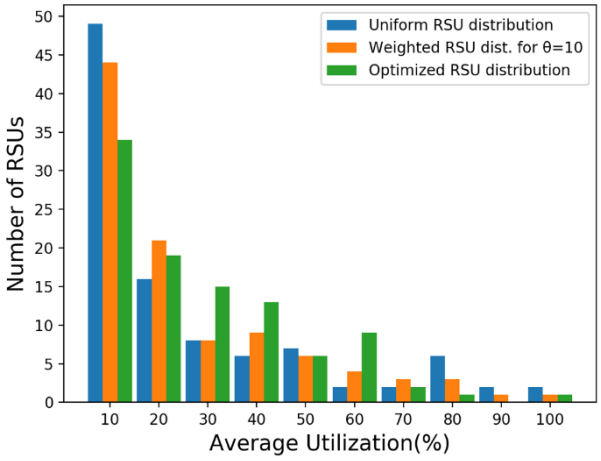

Fig. 11. Average utilization histogram

Fig. 12 (a), (b) and (c) show task failure reasons and breakdowns for uniform, weighted for θ=10, and optimized distribution models respectively. In uniform distribution no task failure due to network coverage can be observed since it was designed for the full network coverage. For uniform model when the traffic volume is low, vehicle mobility is the reason for the majority of the task failures. However, when traffic density increases, mobility failure rate decreases and RSU capacity failure becomes the main reason of the task failures. For weighted model, especially for the low traffic volume, network coverage failure is a significant failure reason as a result of RSU relocation. However, when traffic density increases, coverage and mobility failure rates decrease and RSU capacity failure becomes the main reason of the task failures. Lastly, for optimized model, network coverage is the main reason of the task failures for all traffic density levels, and we observe a spike on the bandwidth failures for 4000 vehicles.

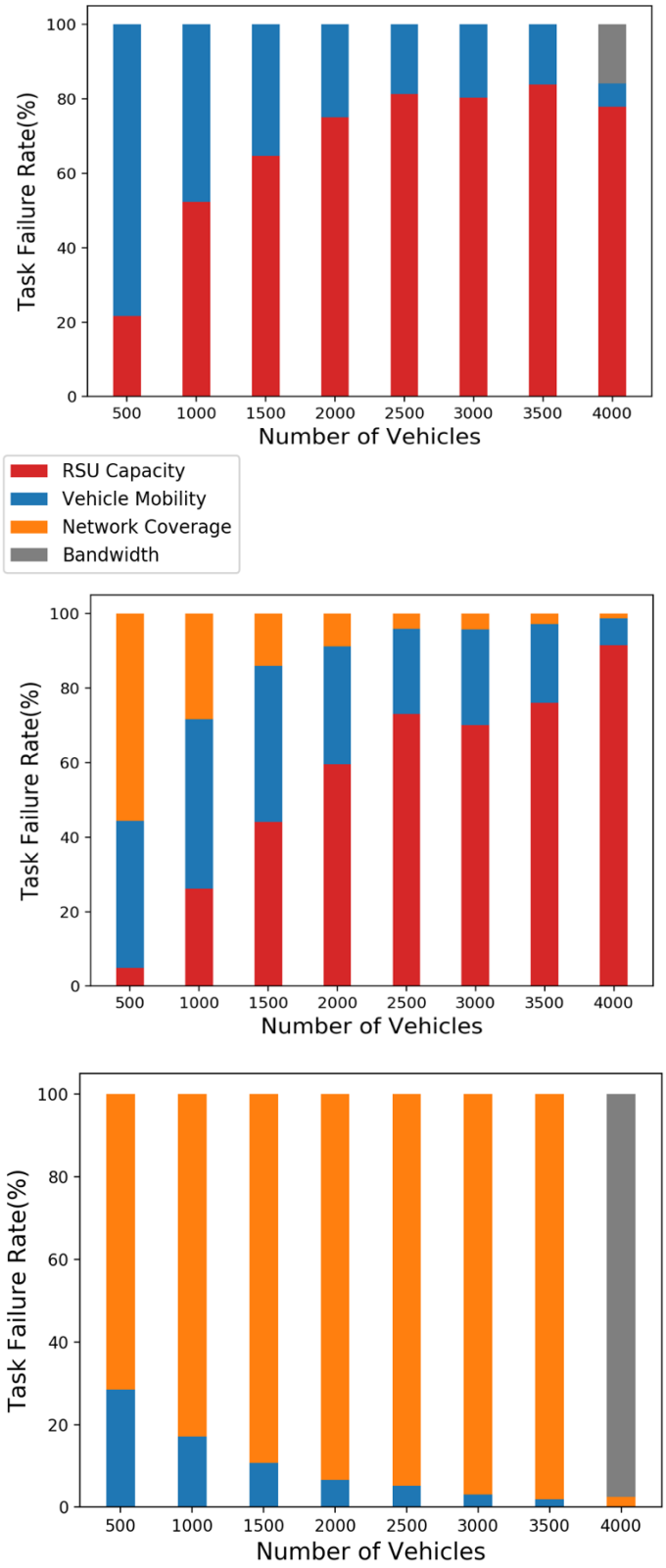

Fig. 12. Task failure breakdown (a) Uniform distribution model
(b) Weighted distribution model (θ = 10)
(c) Optimized distribution model

III. CONCLUSION

In this study, we propose an RSU placement framework to be used for generating optimal RSU placement models based on traffic characteristics of a target area. Two criteria should be satisfied for an RSU placement problem: network coverage and computational demand. The proposed framework includes 3 distribution models: uniform, weighted and optimized. Uniform distribution model addresses full network coverage and do not consider computational demand. This can serve as a suitable model for a road network in which sparse and evenly distributed traffic is observed on the road network. Weighted distribution is a heuristic model which uses uniform model as the base model. It addresses making improvements by considering the computational demand. The relocation factor (θ), which is an external parameter, is provided to this model to update RSU locations in favour of the computational demand. For a scenario with high traffic volume, it is expected to experience congestions on the road network and this might result in extra load on the RSUs serving in those territories. When the computational demand exceeds the capacity of an RSUs, they may become dysfunctional and this eventually would result a system crush. This scenario can be prevented by providing a meaningful value for θ. Thus, for an effective utilization of the framework, traffic characteristics of the target area should be carefully examined, and a suitable value should be assigned for θ. Lastly, optimized distribution model uses Linear Programming to generate an optimized RSU distribution. This solution guarantees a certain level of network coverage and resource supply using minimum number of RSUs. The constraints are defined with external parameters, γ and λ, and denotes coverage constraint level and and resource supply constraint level respectively. Thus, the company that uses this framework will be free to use any values as parameters based on their financial and technical requirements. While they can set high values γ and λ, they can also aim for maximum coverage whereas they ignore the demand, or vice versa.

We needed a simulation environment to test performance of the RSU placement models and validate their functionality. Since we could not find a simulation tool designed for V2I scenarios, we extended the capabilities of EdgeCloudSim, which is a simulation framework designed for edge scenarios. We introduced components and modules specific to V2I scenarios and referred to this extended simulation environment as V2ISim.

In our experiments, we used uniform, optimized, and weighted placement models. For the weighted model, we generated 3 variations for θ=10, 20 and 30. Also we generated a traffic dataset consisting of 8 vehicle trajectory files each representing a different traffic volume. Then, we run a simulation for each placement model using this dataset on V2ISim. The simulation results showed that optimized model outperforms all others under any traffic load. Also, we concluded that uniform distribution model can be used for low traffic volume, weighted model for θ=20 can be used for medium and high, and θ=30 can be used for high traffic volumes. These results align with our expectations and the

experiments validate the functionality of the proposed RSU placement framework.

As future work, we plan to improve our communication model. In this study, we had our main focus on the communication between vehicle and RSU, however inter-RSU communication is an accepted form of communication in Vehicular ad-hoc network (VANET) in which RSUs can exchange data with each other [7]. By implementing this in V2ISim, task transfers between RSUs will be possible and task failures due to vehicle mobility will be prevented. Moreover, some technical factors that can impact the communication between vehicles and RSUs should be studied and findings should be reflected to the study. These can be determining the noise level for the RSUs in close proximity and shadowing effect of the buildings.

ACKNOWLEDGMENT

This work is supported by the Galatasaray University Research Fund under the grant number 18.401.003.

REFERENCES

[1] M. Satyanarayanan, P. Bahl, R. Cáceres and N. Davies, "The case for VM-based cloudlets in mobile computing," *IEEE Pervasive Computing*, 2009.

[2] P. Corcoran and S. K. Datta, "Mobile-Edge Computing and the Internet of Things for Consumers: Extending cloud computing and services to the edge of the network.," *IEEE Consumer Electronics Magazine*, 2016.

[3] E. Uhlemann, "Introducing connected vehicles [Connected vehicles]," *IEEE Vehicular Technology Magazine*, 2015.

[4] J. Santa, A. Moragón and A. F. Gómez-Skarmeta, "Experimental evaluation of a novel vehicular communication paradigm based on cellular networks," in *IEEE Intelligent Vehicles Symposium, Proceedings*, 2008.

[5] S. Zeadally, R. Hunt, Y.-S. Chen, A. Irwin and A. Hassan, "Vehicular ad hoc networks (VANETS): status, results, and challenges," *Telecommunication Systems*, vol. 50, no. 4, pp. 217-241, 2012.

[6] C. Y. Chang, "MAC protocols in vehicular ad hoc networks," in *Telematics Communication Technologies and Vehicular Networks: Wireless Architectures and Applications*, 2009.

[7] R. Barskar and M. Chawla, "Vehicular Ad hoc Networks and its Applications in Diversified Fields," *International Journal of Computer Applications*, 2015.

[8] M. Saini, A. Alelaiwi and A. El Saddik, "How close are we to realizing a pragmatic VANET solution? A meta-survey," *ACM Computing Surveys*, 2015.

[9] M. Satyanarayanan, "Edge computing for situational awareness," in *IEEE Workshop on Local and Metropolitan Area Networks*, 2017.

[10] L. C. Bento, R. Parafita and U. Nunes, "Intelligent traffic management at intersections supported by V2V and V2I communications," in *IEEE Conference on Intelligent Transportation Systems, Proceedings, ITSC*, 2012.

[11] K. Katsaros, R. Kernchen, M. Dianati and D. Rieck, "Performance study of a Green Light Optimized Speed Advisory (GLOSA) application using an integrated cooperative ITS simulation platform," in *IWCMC 2011 - 7th International Wireless Communications and Mobile Computing Conference*, 2011.

[12] C. Letter and L. Elefteriadou, "Efficient control of fully automated connected vehicles at freeway merge segments," *Transportation Research Part C: Emerging Technologies*, vol. 80, pp. 190-205, 1 7 2017.

[13] C.-H. Hong and B. Varghese, "Resource Management in Fog/Edge Computing: A Survey on Architectures, Infrastructure, and Algorithms," *ACM Comput. Surv.*, vol. 52, no. 5, 9 2019.

[14] P. Mach and Z. Becvar, *Mobile Edge Computing: A Survey on Architecture and Computation Offloading*, 2017.

[15] C. Sonmez, A. Ozgovde and C. Ersoy, "EdgeCloudSim: An environment for performance evaluation of edge computing systems," *Transactions on Emerging Telecommunications Technologies*, 2018.

[16] O. Trullols, M. Fiore, C. Casetti, C. F. Chiasserini and J. M. Barcelo Ordinas, "Planning roadside infrastructure for information dissemination in intelligent transportation systems," *Computer Communications*, 2010.

[17] B. Aslam, F. Amjad and C. C. Zou, "Optimal roadside units placement in urban areas for vehicular networks," in *Proceedings - IEEE Symposium on Computers and Communications*, 2012.

[18] N. M. Balouchzahi, M. Fathy and A. Akbari, "Optimal road side units placement model based on binary integer programming for efficient traffic information advertisement and discovery in vehicular environment," *IET Intelligent Transport Systems*, 2015.

[19] T. J. Wu, W. Liao and C. J. Chang, "A cost-effective strategy for road-side unit placement in vehicular networks," *IEEE Transactions on Communications*, 2012.

[20] R. Yu, Y. Zhang, S. Gjessing, W. Xia and K. Yang, "Toward Cloud-based vehicular networks with efficient resource management," *IEEE Network*, 2013.

[21] S. K. Datta, R. P. F. Da Costa, J. Harri and C. Bonnet, "Integrating connected vehicles in Internet of Things ecosystems: Challenges and solutions," in *WoWMoM 2016 - 17th International Symposium on a World of Wireless, Mobile and Multimedia Networks*, 2016.

[22] M. A. Salahuddin, A. Al-Fuqaha, M. Guizani and S. Cherkaoui, "RSU cloud and its resource management in support of enhanced vehicular applications," in *2014 IEEE Globecom Workshops, GC Wkshps 2014*, 2014.

[23] P. A. Lopez, M. Behrisch, L. Bieker-Walz, J. Erdmann, Y. P. Flotterod, R. Hilbrich, L. Lucken, J. Rummel, P. Wagner and E. Wiebner, "Microscopic Traffic Simulation using SUMO," in *IEEE Conference on Intelligent Transportation Systems, Proceedings, ITSC*,

2018.

[24] A. K. Ligo, J. M. Peha, P. Ferreira and J. Barros, "Comparison between Benefits and Costs of Offload of Mobile Internet Traffic Via Vehicular Networks," in *43rd Telecommunications Policy Research Conference*, 2015.

BIOGRAPHIES

BARIŞ KARA received his B.S. degree in computer engineering from 9 Eylül University, İzmir,Turkey in 2010 and the M.S. degree in computer engineering from Galatasaray University, İstanbul, Turkey, in 2019.

Barış Kara is a senior software developer with 10 years of experience. He has been providing software development and IT consultancy services in the UK since 2016. He played major roles in design and development of many enterprise projects. Contributed to software projects of high-profile international and Turkish companies such as HSBC, O2, SKY, ATOS and Borsa Istanbul.

ATAY ÖZGÖVDE received BS, MS and PhD degrees from Bogazici University, Istanbul, in 1995, 1998 and 2009. He worked for Nortel Networks as an R&D engineer in various telecommunications projects between 1998 and 2001. In 2002, he started working as a research assistant in the Computer Engineering Department, Bogazici University. Currently, he is an assistant professor in the Computer Engineering Department, Galatasaray University. His research interests include wireless sensor networks, embedded systems, distributed systems, pervasive computing, SDN and Edge Computing. Atay Ozgovde is a senior member of IEEE.

Publication Ethics

The journal publishes original papers in the extensive field of Electrical-electronics and Computer engineering. To that end, it is essential that all who participate in producing the journal conduct themselves as authors, reviewers, editors, and publishers in accord with the highest level of professional ethics and standards. Plagiarism or self-plagiarism constitutes unethical scientific behavior and is never acceptable.
By submitting a manuscript to this journal, each author explicitly confirms that the manuscript meets the highest ethical standards for authors and coauthors
The undersigned hereby assign(s) to *Balkan Journal of Electrical & Computer Engineering* (BAJECE) copyright ownership in the above Paper, effective if and when the Paper is accepted for publication by BAJECE and to the extent transferable under applicable national law. This assignment gives BAJECE the right to register copyright to the Paper in its name as claimant and to publish the Paper in any print or electronic medium.

Authors, or their employers in the case of works made for hire, retain the following rights:

1. All proprietary rights other than copyright, including patent rights.
2. The right to make and distribute copies of the Paper for internal purposes.
3. The right to use the material for lecture or classroom purposes.
4. The right to prepare derivative publications based on the Paper, including books or book chapters, journal papers, and magazine articles, provided that publication of a derivative work occurs subsequent to the official date of publication by BAJECE.
5. The right to post an author-prepared version or an of ficial version (preferred version) of the published paper on an i nternal or external server controlled exclusively by t he author/employer, pr ovided that (a) such posting is noncommercial in nature and the paper is made available to users without charge; (b) a copyright notice and full citation appear with the paper, and (c) a link to BAJECE's official online version of the abstract is provided using the DOI (Document Object Identifier) link.

Balkan Journal of Electrical & Computer Engineering
An International Peer Reviewed, Indexed and Open Access Journal

ISSN: 2147- 284X
Year: July 2020
Volume: 8
Issue: 3

CONTENTS

M. A. Gungor; Analyzing the Fluid Flow of Transit-Time Ultrasonic Flowmeter with Image Processing Technique and Developing a Quality Metric Depending on Pipe Profile,.....**193-200**

V. Ozduran; LDPCC and OFDM Based Cooperative Communication for Wireless Sensor Networks, ...**201-208**

O. Aydin and R.G. Cinbis; Single-Image Super-Resolution Analysis in DCT Spectral Domain,.....**209-217**

H. Yetis, T. Goktas; Comparative Design of Permanent Magnet Synchronous Motors for Low-Power Industrial Applications, ...**218-224**

A. Gundogdu, F. Ata, B. Dandil;Design of Neuro-Fuzzy Based Torque Controller for Torque Ripple Reduction of Asynchronous Motor,**225-234**

H. Oğraş and Ş. Fidan; Performance Comparison of ACM and GRP Methods for Image Permutation, ...**235-241**

E. Buber, O.K. Sahingoz; Blockchain Based Information Sharing Mechanism for Cyber Threat Intelligence,.....**242-253**

G. Boztas; Optimization of an Input Filter for a Three-Phase Matrix Converter,.....**254-259**

I. Kaya; Optimal and Analytical Tuning of I-PD Controllers for Controlling Stable Processes with Inverse Response,.....**260-265**

D. Olanloye, R. Olasunkanmi and E. Oduntan; Comparison of Support Vector Machine Models in the Classification of Susceptibility to Schistosomiasis,.....**266-271**

B. Kara and A. Özgövde; Effect of RSU Placement on Autonomous Vehicle V2I Scenarios,.....**272-284**

BALKAN JOURNAL OF
ELECTRICAL & COMPUTER ENGINEERING
(An International Peer Reviewed, Indexed and Open Access Journal)

Contact
Batman University
Department of Electrical-Electronics Engineering
Bati Raman Campus Batman-Turkey

Web: http://dergipark.gov.tr/bajece
http://www.bajece.com
e-mail: bajece@hotmail.com